CASI

Numerical Simulation of High-Speed Turbulent Reacting Flows

by

P. Givi, D.B. Taulbee, C.K. Madnia, F.A. Jaberi, P.J. Colucci
L.Y.M. Gicquel, V. Adumitroaie and S. James
Department of Mechanical and Aerospace Engineering
State University of New York at Buffalo
Buffalo, NY 14260-4400

Final Report
for Grant NAG-1-1122

August 1999

1846

Prepared for
Dr. J. Philip Drummond
Hypersonic Airbreathing Propulsion Branch
NASA Langley Research Center
Mail Stop 197
Hampton, VA 23681-2199

Numerical Simulation of High-Speed Turbulent Reacting Flows

P. Givi, D.B. Taulbee, C.K. Madnia, F.A. Jaberi, P.J. Colucci,
L.Y.M. Gicquel, V. Adumitroaie and S. James
Department of Mechanical and Aerospace Engineering
State University of New York at Buffalo
Buffalo, NY 14260-4400

Abstract

The objectives of this research are: (1) to develop and implement a new methodology for large eddy simulation of (LES) of high-speed reacting turbulent flows. (2) To develop algebraic turbulence closures for statistical description of chemically reacting turbulent flows. We have just completed the third year of Phase III of this research. This is the Final Report of our activities on this research sponsored by the NASA LaRC under Grant NAG-1-1122.

Technical Monitor

Dr. J. Philip Drummond (Hypersonics Air-Breathing Propulsion Branch, NASA LaRC, Mail Stop 197, Tel: 757-864-2298) is the Technical Monitor of this Grant.

I Summary of Achievements

We just completed Year 3 of the Phase III activities on this NASA LaRC sponsored project (Grant NAG-1-1122). The total time allotted for this phase is three years; this phase was followed at the conclusion of Phase II activities (also for three years). In total we have completed 9 years of LaRC supported research. This is the Final Report and provides a summary of our accomplishments in Phase III of this research (August 1, 1996 - July 31, 1999). Our work in this phase consists of the following two constituents: (1) development of LES methodologies via probability density function (PDF) methods and numerical solution of the PDF via Monte Carlo schemes, , and (2) Development of algebraic turbulence closures for statistical description chemically reacting turbulent flows. Each of these two constituents are discussed below in order:

I.1 LES of Turbulent Reacting Flow

A methodology termed the "filtered density function" (FDF) is developed and implemented for LES of chemically reacting turbulent flows [1]. In this methodology, the effects of the unresolved scalar fluctuations are taken into account by PDF of subgrid scale (SGS) scalar quantities. A transport equation is derived for the FDF in which the effect of chemical reactions appears in a closed form. The influences of scalar mixing and convection within the subgrid are modeled. The FDF transport equation is solved numerically via a Lagrangian Monte Carlo scheme [2] in which the solutions of the equivalent stochastic differential equations (SDEs) are obtained. These solutions preserve the Itô-Gikhman nature of the SDEs. The consistency of the FDF approach, the convergence of its Monte Carlo solution and the performance of the closures employed in the FDF transport equation are assessed by comparisons with results obtained by direct numerical simulation (DNS) and by conventional LES procedures in which the first two SGS scalar moments are obtained by a finite difference method (LES-FD). These comparative assessments are conducted by implementations of all three schemes (FDF, DNS and LES-FD) in a temporally developing mixing layer and a spatially developing planar jet under both non-reacting and reacting conditions. In non-reacting flows, the Monte Carlo solution of the FDF yields results similar to those via LES-FD. The advantage of the FDF is demonstrated by its use in reacting flows. In the absence of a closure for the subgrid scalar fluctuations, the LES-FD results are significantly different from those based on DNS. The FDF results show a much closer agreement with filtered DNS results. The results of this work are published in Refs. [3,4] and are provided in Appendix I and Appendix II.

We have also developed a methodology, termed the "filtered mass density function" (FMDF) for LES of variable density chemically reacting turbulent flows. This methodology is based on the extension of the FDF and represents the joint probability density function of the subgrid scale (SGS) scalar quantities. The FMDF is obtained by solution of its modeled transport equation. In this equation, the effect of chemical reactions appears in a closed form and the influences of SGS mixing and convection are modeled. The stochastic differential equations (SDEs) which yield statistically equivalent results to that of the FMDF transport equation are derived and are solved via a Lagrangian Monte Carlo scheme. The consistency, convergence, and accuracy of the FMDF and the Monte Carlo solution of its equivalent SDEs are assessed. In non-reacting flows, it is shown that the filtered results via the FMDF agree well with those obtained by LES-FD. The advantage of the FMDF is demonstrated in LES of reacting shear flows with nonpremixed reactants. The FMDF results are appraised by comparisons with data generated by direct numerical simulation (DNS) and with experimental measurements. In the absence of a closure for the SGS scalar correlations, the results based on the LES-FD are significantly different from those obtained by DNS. The FMDF results show a closer agreement with DNS. These results also agree favorably with laboratory data of exothermic reacting turbulent shear flows, and portray several of the features observed experimentally. This work is described in detail in Appendix III. This appendix is scheduled to be published in *Journal of Fluid Mechanics* [5].

We have recently extended the FDF methodology to also include the velocity field. Some preliminary results are provided in Appendix IV. In this portion of our work, the joint-velocity filtered density function of the velocity (VFDF) is considered. A transport equation is proposed for the VFDF in which the unclosed terms are modeled in a manner analogous to conventional second order subgrid scales closures [6]. The modeled VFDF transport equation is solved numerically via a Lagrangian Monte Carlo scheme in which the solutions of the equivalent stochastic differential equations are obtained. The consistency and the convergence of the simulated results are assessed by comparison with results obtained by LES-FD in which the equivalent transport equations of the subgrid scale moments are solved. The accuracy and reliability of the velocity FDF are also assessed via comparison with DNS and experimental data. The DNS data are those for a three-dimensional ($3D$) temporal mixing layer, and experimental data are those of a $3D$ turbulent jet.

I.2 Algebraic Modeling

In this work, explicit algebraic scalar flux models which are valid for three-dimensional turbulent flows are derived from a hierarchy of second-order moment closures. The mathematical procedure is based on the *Cayley-Hamilton* theorem and is an extension of the scheme developed by Taulbee [7]. Several closures for the pressure-scalar gradient correlations are considered and explicit algebraic relations are provided for the velocity-scalar correlations in both nonreacting and reacting flows. In the latter, the role of the Damkohler number is explicitly exhibited in isothermal turbulent flows with nonpremixed reactants. The relationship between these closures and traditional models based on the linear gradient diffusion approximation is theoretically established. The results of model predictions are assessed via comparison with available laboratory data in turbulent jet flows. This work is published in Ref. [8], which is included here as Appendix V.

The extension of the methodology above for high speed flow has also been completed. In this part of our work, closure for the compressible portion of the pressure-strain covariance is developed. It is shown that, within the context of a pressure-strain closure assumption linear in the Reynolds stresses, an expression for the pressure-dilatation can be used to construct a representation for the pressure-strain. Additional closures for the unclosed terms in the Favré-Reynolds stress equations involving the mean acceleration are also constructed. The closures accommodate compressibility corrections depending on the magnitude of the turbulent Mach number, the mean density gradient, the mean pressure gradient, the mean dilatation, and, of course, the mean velocity gradients. The effects of the compressibility corrections on the Favré-Reynolds stresses are consistent with current DNS results. Using the compressible pressure-strain and mean acceleration closures in the Favré-Reynolds stress equations an algebraic closure for the Favré-Reynolds stresses is constructed. Noteworthy is the fact that, in the absence of mean velocity gradients, the mean density gradient produces Favré-Reynolds stresses in accelerating mean flows. Computations of the mixing layer using the compressible closures developed are described. Favré-Reynolds stress closure and two-equation algebraic models are compared to laboratory data for the mixing layer. Experimental data from diverse laboratories for the Favré-Reynolds stresses appears inconsistent and, as a consequence, comparison of the Reynolds stress predictions to the data is not conclusive. Reductions of the kinetic energy and the spread rate are consistent with the sizable decreases seen in these classes of flows. Appendix VI provides a complete description of this portion of our activities. This Appendix is to be published in *Physics Fluids* in September 1999.

II Personnel

Dr. Peyman Givi is the PI of this project. Drs. Dale B. Taulbee and Cyrus K. Madnia are the Co-PIs. The following students worked on various aspects of this research program, and were partially supported by this Grant:

1. Dr. Virgil Adumitroaie (Graduate Research Assistant), Ph.D. in Mechanical Engineering [9]. Current Position: Research Scientist, CFD Research Corp., Huntsville, AL.

2. Dr. Paul J. Colucci (Graduate Research Assistant). Ph.D. in Mechanical Engineering [10]. Current Position: Technical Support Engineer, Fluent Inc., Ann Arbor, MI.

3. Dr. Sean C. Garrick (Graduate Research Assistant). Ph.D. in Mechanical Engineering [11]. Current Position: Nelson Assistant Professor of Mechanical Engineering, The University of Minnesota-Twin Cities, Minneapolis, MN.

4. Dr. Farhad A. Jaberi (Postdoctoral Fellow). Current Position: Associate Professor of Mechanical Engineering, Kansas State University, Manhattan, KS.

5. Dr. Sunil James (Graduate Research Assistant). Ph.D. in Mechanical Engineering [12]. Current Position: Senior Project Engineer, Rolls-Royce Allison, Indianapolis, IN.

References

[1] Givi, P., Spectral and Random Vortex Methods in Turbulent Reacting Flows, in Libby, P. A. and Williams, F. A., editors, *Turbulent Reacting Flows*, chapter 8, pp. 475–572, Academic Press, London, England, 1994.

[2] Pope, S. B., Lagrangian PDF Methods for Turbulent Flows, *Ann. Rev. Fluid Mech.*, **26**:23–63 (1994).

[3] Colucci, P. J., Jaberi, F. A., Givi, P., and Pope, S. B., Filtered Density Function for Large Eddy Simulation of Turbulent Reacting Flows, *Phys. Fluids*, **10**(2):499–515 (1998).

[4] Garrick, S. C., Jaberi, F. A., and Givi, P., Large Eddy Simulation of Scalar Transport in a Turbulent Jet Flow, in *Proceedings of Second AFOSR Conference on DNS and LES*, Kluwer Academic Publishers, The Netherlands, 1999, in press.

[5] Jaberi, F. A., Colucci, P. J., James, S., Givi, P., and Pope, S. B., Filtered Mass Density Function for Large Eddy Simulation of Turbulent Reacting Flows, *J. Fluid Mech.*, (1999), in press.

[6] Pope, S. B., On the Relation Between Stochastic Lagrangian Models of Turbulence and Second-Moment Closures, *Phys. Fluids*, **6**(2):973–985 (1994).

[7] Taulbee, D. B., An Improved Algebraic Reynolds Stress Model and Corresponding Nonlinear Stress Model, *Phys. Fluids A*, **4**(11):2555–2561 (1992).

[8] Adumitroaie, V., Taulbee, D. B., and Givi, P., Algebraic Scalar Flux Models for Turbulent Reacting Flows, *AIChE Journal*, **43**(8):1935–1946 (1997).

[9] Adumitroaie, V., Quasi-Explicit Algebraic Turbulence Closures for Compressible Reacting Flows, Ph.D. Thesis, Department of Mechanical and Aerospace Engineering, State University of New York at Buffalo, Buffalo, NY, 1997.

[10] Colucci, P. J., Large Eddy Simulation of Turbulent Reactive Flows: Stochastic Representation of the Subgrid Scale Scalar Fluctuations, Ph.D. Thesis, Department of Mechanical and Aerospace Engineering, State University of New York at Buffalo, Buffalo, NY, 1998.

[11] Garrick, S. C., Large Eddy Simulations of Turbulent Reacting Jets, Ph.D. Thesis, Department of Mechanical and Aerospace Engineering, State University of New York at Buffalo, Buffalo, NY, 1998.

[12] James, S., Realistic Chemistry in Large Scale Numerical Simulations of Methane Diffusion Flames, Ph.D. Thesis, Department of Mechanical and Aerospace Engineering, State University of New York at Buffalo, Buffalo, NY, 1998.

Appendix I

Filtered Density Function for Large Eddy Simulation of Turbulent Reacting Flows

PHYSICS OF FLUIDS VOLUME 10, NUMBER 2 FEBRUARY 1998

Filtered density function for large eddy simulation of turbulent reacting flows

P. J. Colucci, F. A. Jaberi, and P. Givi
Department of Mechanical and Aerospace Engineering, State University of New York at Buffalo, Buffalo, New York 14260-4400

S. B. Pope
Sibley School of Mechanical and Aerospace Engineering, Cornell University, Ithaca, New York 14853-1301

(Received 16 December 1996; accepted 29 September 1997)

A methodology termed the "filtered density function" (FDF) is developed and implemented for large eddy simulation (LES) of chemically reacting turbulent flows. In this methodology, the effects of the unresolved scalar fluctuations are taken into account by considering the probability density function (PDF) of subgrid scale (SGS) scalar quantities. A transport equation is derived for the FDF in which the effect of chemical reactions appears in a closed form. The influences of scalar mixing and convection within the subgrid are modeled. The FDF transport equation is solved numerically via a Lagrangian Monte Carlo scheme in which the solutions of the equivalent stochastic differential equations (SDEs) are obtained. These solutions preserve the Itô-Gikhman nature of the SDEs. The consistency of the FDF approach, the convergence of its Monte Carlo solution and the performance of the closures employed in the FDF transport equation are assessed by comparisons with results obtained by direct numerical simulation (DNS) and by conventional LES procedures in which the first two SGS scalar moments are obtained by a finite difference method (LES-FD). These comparative assessments are conducted by implementations of all three schemes (FDF, DNS and LES-FD) in a temporally developing mixing layer and a spatially developing planar jet under both non-reacting and reacting conditions. In non-reacting flows, the Monte Carlo solution of the FDF yields results similar to those via LES-FD. The advantage of the FDF is demonstrated by its use in reacting flows. In the absence of a closure for the SGS scalar fluctuations, the LES-FD results are significantly different from those based on DNS. The FDF results show a much closer agreement with filtered DNS results. [S1070-6631(98)01402-0]

I. INTRODUCTION

Over the past 30 years since the early work of Smagorinsky,[1] significant efforts have been devoted to large eddy simulation (LES) of turbulent flows.[2–12] The most prominent model has been the Smagorinsky eddy viscosity closure which relates the unknown subgrid scale (SGS) Reynolds stresses to the local large scale rate of flow strain.[13] This viscosity is aimed to provide the role of mimicking the dissipative behavior of the unresolved small scales. The extensions to "dynamic" models[14,15] have shown some improvements. This is particularly the case in transitional flow simulations where the dynamic evaluations of the empirical model "constant" result in (somewhat) better predictions of the large scale flow features.

A survey of combustion literature reveals relatively little work in LES of chemically reacting turbulent flows.[7,16] It appears that Schumann[17] was one of the first to conduct LES of a reacting flow. However, the assumption made in this work simply to neglect the contribution of the SGS scalar fluctuations to the filtered reaction rate needs to be justified for general applications. The importance of such fluctuations is well recognized in Reynolds averaged procedures in both combustion[18–20] and chemical engineering[21–24] problems. Therefore, it is natural to believe that these fluctuations are also important in LES. McMurtry *et al.*,[25,26] Sykes *et al.*,[27] Liou *et al.*,[28] Menon *et al.*,[29] Boris *et al.*,[30] Fureby *et al.*,[31,32] Cook *et al.*,[33,34] Mathey and Chollet,[35] Branley and Jones[36] and others provide several means of conducting LES of turbulent reacting flows.

Modeling of scalar fluctuations in Reynolds averaged methods has been the subject of broad investigations since the pioneering work of Toor.[37] An approach which has proven particularly useful is based on the probability density function (PDF) or the joint PDF of scalar quantities.[38–41] The systematic approach for determining the PDF is by means of solving the transport equation governing its evolution.[42] In this equation, the effects of chemical reaction appear in a closed form; this constitutes the primary advantage of the PDF schemes in comparison to other statistical procedures. The use of PDF for LES was suggested by Givi[7] and its first application is due to Madnia and Givi.[43] In this work, the *Pearson* family of distributions are assumed to characterize PDF of SGS scalars in homogeneous flows under chemical equilibrium conditions. This procedure was also used by Cook and Riley.[44] The extension of assumed PDF methods for LES of non-equilibrium reacting shear flows is reported by Frankel *et al.*[45] While the generated results are encouraging, they do reveal the need for more systematic schemes in which the transport of the PDF of SGS scalar quantities are considered. Pope[16] introduced the concept of "filtered density function" (FDF) which is essentially the PDF of SGS scalar variables. With a formal mathematical definition of the FDF, Pope[16] demonstrates that the effects of chemical reaction appear in a closed form in the FDF transport, thus making it a viable candidate for LES of chemically reacting flows. Gao and O'Brien[46] develop a transport equation for the FDF and offer suggestions for modeling of the unclosed terms in this equation.

The objective of the present work is to further demonstrate the applicability of the FDF and to provide results based on its implementation for LES of chemically reacting turbulent flows. Only the FDF of scalar quantities is considered; probability treatment of the subgrid velocity fluctuations is postponed for future work.

II. FORMULATION

We consider an incompressible (unit density), isothermal, turbulent reacting flow involving N_s species. For the mathematical description of this flow, the primary transport variables are the velocity vector $u_i(\mathbf{x},t)$ $(i=1,2,3)$, the pressure $p(\mathbf{x},t)$, and the species' mass fractions $\phi_\alpha(\mathbf{x},t)$ $(\alpha=1,2,\ldots,N_s)$. The equations which govern the transport of these variables in space (x_i) and time (t) are

$$\frac{\partial u_i}{\partial x_i}=0, \tag{1}$$

$$\frac{\partial u_j}{\partial t}+\frac{\partial u_i u_j}{\partial x_i}=-\frac{\partial p}{\partial x_j}+\frac{\partial \tau_{ij}}{\partial x_i}, \tag{2}$$

$$\frac{\partial \phi_\alpha}{\partial t}+\frac{\partial u_i \phi_\alpha}{\partial x_i}=-\frac{\partial J_i^\alpha}{\partial x_i}+\omega_\alpha, \tag{3}$$

where $\omega_\alpha(\mathbf{x},t)\equiv\hat{\omega}_\alpha(\mathbf{\Phi}(\mathbf{x},t))$ denotes the chemical reaction term for species α, and $\mathbf{\Phi}\equiv[\phi_1,\phi_2,\ldots,\phi_{N_s}]$ denotes the scalar array. Assuming a Newtonian flow with Fick's law of diffusion, the viscous stress tensor τ_{ij} and mass flux J_i^α are represented by

$$\tau_{ij}=\nu\left(\frac{\partial u_i}{\partial x_j}+\frac{\partial u_j}{\partial x_i}\right), \quad J_i^\alpha=-\Gamma\frac{\partial \phi_\alpha}{\partial x_i}, \tag{4}$$

where ν is the fluid viscosity and Γ is the diffusion coefficient, $\Gamma=\nu/\mathrm{Sc}$, and Sc is the molecular Schmidt number.

Large eddy simulation involves the use of the spatial filtering operation[47]

$$\langle f(\mathbf{x},t)\rangle_L=\int_{-\infty}^{+\infty} f(\mathbf{x}',t)\mathcal{G}(\mathbf{x}',\mathbf{x})d\mathbf{x}', \tag{5}$$

where $\mathcal{G}$ denotes the filter function, $\langle f(\mathbf{x},t)\rangle_L$ represents the filtered value of the transport variable $f(\mathbf{x},t)$, and $f'=f-\langle f\rangle_L$ denotes the fluctuations of f from the filtered value. We consider spatially and temporally invariant and localized filter functions, thus $\mathcal{G}(\mathbf{x}',\mathbf{x})\equiv G(\mathbf{x}'-\mathbf{x})$ with the properties,[47] $G(\mathbf{x})=G(-\mathbf{x})$, and $\int_{-\infty}^{\infty}G(\mathbf{x})d\mathbf{x}=1$. Moreover, we only consider "positive" filter functions as defined by Verman *et al.*[48] for which all the moments $\int_{-\infty}^{\infty}x^m G(x)dx$ exist for $m\geqslant 0$. The application of the filtering operation to the transport equations yields

$$\frac{\partial\langle u_i\rangle_L}{\partial x_i}=0, \tag{6}$$

$$\frac{\partial\langle u_j\rangle_L}{\partial t}+\frac{\partial\langle u_i\rangle_L\langle u_j\rangle_L}{\partial x_i}=-\frac{\partial\langle p\rangle_L}{\partial x_j}+\frac{\partial\langle \tau_{ij}\rangle_L}{\partial x_i}-\frac{\partial T_{ij}}{\partial x_i}, \tag{7}$$

$$\frac{\partial\langle \phi_\alpha\rangle_L}{\partial t}+\frac{\partial\langle u_i\rangle_L\langle \phi_\alpha\rangle_L}{\partial x_i}=-\frac{\partial\langle J_i^\alpha\rangle_L}{\partial x_i}-\frac{\partial M_i^\alpha}{\partial x_i}+\langle\omega_\alpha\rangle_L. \tag{8}$$

where $T_{ij}=\langle u_i u_j\rangle_L-\langle u_i\rangle_L\langle u_j\rangle_L$ and $M_i^\alpha=\langle u_i\phi_\alpha\rangle_L-\langle u_i\rangle_L\langle\phi_\alpha\rangle_L$ denote the subgrid stress and the subgrid mass flux, respectively.

III. CLOSURE STRATEGY

In LES of non-reacting flows the closure problem is associated with[3] $T_{ij}=\langle u_i u_j\rangle_L-\langle u_i\rangle_L\langle u_j\rangle_L$ and $M_i^\alpha=\langle u_i\phi_\alpha\rangle_L-\langle u_i\rangle_L\langle\phi_\alpha\rangle_L$. In reacting flows, an additional model is required for $\langle\omega_\alpha\rangle_L$. Here, modeling of $\langle\omega_\alpha\rangle_L$ is the subject of the probability formulation as described in the next section. For the former two, we make use of currently available closures which are well-established in non-reacting flows. The subgrid stress is modeled via

$$T_{ij}-(\delta_{ij}/3)T_{kk}=-2\nu_t\langle S_{ij}\rangle_L, \tag{9}$$

where $\langle S_{ij}\rangle_L$ is the resolved strain rate tensor and ν_t is the subgrid viscosity. We use two closures to represent this viscosity. The first is the same as that in the conventional Smagorinsky closure[3]

$$\nu_t=C_s\Delta_G^2\sqrt{\langle S_{ij}\rangle_L\langle S_{ij}\rangle_L}, \tag{10}$$

where Δ_G is the filter size and C_s is an empirical constant. The drawbacks of this closure are well-recognized.[49,50] In an attempt to overcome some of these drawbacks, we also make use of a second closure in which the subgrid viscosity is determined based on the modified subgrid kinetic energy

$$\nu_t=C_k\Delta_G\sqrt{|\langle u_i^*\rangle_L\langle u_i^*\rangle_L-\langle\langle u_i^*\rangle_L\rangle_{L'}\langle\langle u_i^*\rangle_L\rangle_{L'}|}, \tag{11}$$

where $u_i^*=u_i-\mathcal{U}_i$ and $\mathcal{U}_i$ is a reference velocity in the x_i direction. The subscript L' denotes the filter at the secondary level which has a characteristic size (denoted by $\Delta_{G'}$) larger than that of grid level filter. This model is essentially a modified version of that proposed by Bardina *et al.*,[51] which utilize equal sizes for the grid and secondary filters. We refer to this as the modified kinetic energy viscosity (MKEV) closure.

A similar model is used for the closure of the subgrid mass fluxes[52]

$$M_i^\alpha=-\Gamma_t\frac{\partial\langle\phi_\alpha\rangle_L}{\partial x_i}, \tag{12}$$

where $\Gamma_t=\nu_t/\mathrm{Sc}_t$, and Sc_t is the subgrid Schmidt number and is assumed constant.

IV. FILTERED DENSITY FUNCTION (FDF)

The key point in this formulation is to consider the scalar fluctuations of the underlying scalars' array $\Phi(\mathbf{x},t)$ in a probabilistic manner. For that, we define the "filtered density function" (FDF), denoted by P_L, as[16]

$$P_L(\Psi;\mathbf{x},t)=\int_{-\infty}^{+\infty}\varrho[\Psi,\Phi(\mathbf{x}',t)]G(\mathbf{x}'-\mathbf{x})d\mathbf{x}', \tag{13}$$

$$\varrho[\Psi,\Phi(\mathbf{x},t)]=\delta[\Psi-\Phi(\mathbf{x},t)]=\prod_{\alpha=1}^{N_s}\delta[\psi_\alpha-\phi_\alpha(\mathbf{x},t)], \tag{14}$$

where δ denotes the delta function and Ψ denotes the composition domain of the scalar array. The term $\varrho[\Phi-\Psi(\mathbf{x},t)]$ is the "fine-grained" density,[39,40] and Eq. (13) implies that the FDF is the *spatially filtered* value of the fine-grained density. Thus, P_L gives the density in the composition space of the fluid around $\mathbf{x}$ weighted by the filter G. With the condition of a positive filter kernel,[48] P_L has all the properties of the PDF.[40]

For further developments, it is useful to define the "conditional filtered value" of the variable $Q(\mathbf{x},t)$ by

$$\langle Q(\mathbf{x},t)|\Psi\rangle_L=\frac{\int_{-\infty}^{+\infty}Q(\mathbf{x}',t)\varrho[\Psi,\Phi(\mathbf{x}',t)]G(\mathbf{x}'-\mathbf{x})d\mathbf{x}'}{P_L(\Psi;\mathbf{x},t)}, \tag{15}$$

where $\langle\alpha|\beta\rangle_L$ denotes the filtered value of α conditioned on β. Equation (15) implies

(i) For $Q(\mathbf{x},t)=c$, $\langle Q(\mathbf{x},t)|\Psi\rangle_L=c$, (16)

(ii) For $Q(\mathbf{x},t)\equiv\hat{Q}(\Phi(\mathbf{x},t))$, $\langle Q(\mathbf{x},t)|\Psi\rangle_L=\hat{Q}(\Psi)$, (17)

(iii) Integral property: $\langle Q(\mathbf{x},t)\rangle_L$

$$=\int_{-\infty}^{+\infty}\langle Q(\mathbf{x},t)|\Psi\rangle_L P_L(\Psi;\mathbf{x},t)d\Psi, \tag{18}$$

where c is a constant, and $\hat{Q}(\Phi(\mathbf{x},t))\equiv Q(\mathbf{x},t)$ denotes the case where the variable Q can be completely described by the compositional variable $\Phi(\mathbf{x},t)$. From these properties it follows that the filtered value of any function of the scalar variables (such as the reaction rate) is obtained by integration over the composition space

$$\langle Q(\mathbf{x},t)\rangle_L=\int_{-\infty}^{+\infty}\hat{Q}(\Psi)P_L(\Psi;\mathbf{x},t)d\Psi. \tag{19}$$

To develop a transport equation for the FDF, the time-derivative of Eq. (13) is considered

$$\begin{aligned}\frac{\partial P_L(\Psi;\mathbf{x},t)}{\partial t}&=-\int_{-\infty}^{\infty}\frac{\partial\phi_\alpha(\mathbf{x}',t)}{\partial t}\frac{\partial\varrho[\Psi,\Phi(\mathbf{x}',t)]}{\partial\psi_\alpha}\\&\quad\times G(\mathbf{x}'-\mathbf{x})d\mathbf{x}'\\&=-\frac{\partial}{\partial\psi_\alpha}\int_{-\infty}^{\infty}\frac{\partial\phi_\alpha(\mathbf{x}',t)}{\partial t}\\&\quad\times\varrho[\Psi,\Phi(\mathbf{x}',t)]G(\mathbf{x}'-\mathbf{x})d\mathbf{x}',\end{aligned} \tag{20}$$

where the summation convention applies to the species suffix, α. This combined with Eq. (15) yields

$$\frac{\partial P_L(\Psi;\mathbf{x},t)}{\partial t}=-\frac{\partial}{\partial\psi_\alpha}\left[\left\langle\frac{\partial\phi_\alpha}{\partial t}\middle|\Psi\right\rangle_L P_L(\Psi;\mathbf{x},t)\right]. \tag{21}$$

Substituting Eq. (3) into Eq. (21) yields

$$\begin{aligned}\frac{\partial P_L(\Psi;\mathbf{x},t)}{\partial t}=\frac{\partial}{\partial\psi_\alpha}\Bigg\{\Bigg[\left\langle\frac{\partial u_i\phi_\alpha}{\partial x_i}\middle|\Psi\right\rangle_L+\left\langle\frac{\partial J_i^\alpha}{\partial x_i}\middle|\Psi\right\rangle_L\\-\langle\hat{\omega}_\alpha(\Phi)|\Psi\rangle_L\Bigg]P_L(\Psi;\mathbf{x},t)\Bigg\}\end{aligned} \tag{22}$$

in which the convective term can be represented in the form

$$\begin{aligned}&\frac{\partial}{\partial\Psi_\alpha}\left[\left\langle\frac{\partial u_i\phi_\alpha}{\partial x_i}\middle|\Psi\right\rangle_L P_L(\Psi;\mathbf{x},t)\right]\\&=-\frac{\partial\langle u_i|\Psi\rangle_L P_L(\Psi;\mathbf{x},t)}{\partial x_i}.\end{aligned} \tag{23}$$

The unclosed nature of convection is denoted by the conditional filtered value of the velocity which is further decomposed into resolved and subgrid scale components. It is useful to adopt the decomposition

$$\langle u_i|\Psi\rangle_L P_L=\langle u_i\rangle_L P_L+[\langle u_i|\Psi\rangle_L-\langle u_i\rangle_L]P_L, \tag{24}$$

so that Eq. (21) can be expressed as

$$\begin{aligned}\frac{\partial P_L}{\partial t}+\frac{\partial\langle u_i\rangle_L P_L}{\partial x_i}=&-\frac{\partial[\langle u_i|\Psi\rangle_L-\langle u_i\rangle_L]P_L}{\partial x_i}\\&+\frac{\partial}{\partial\psi_\alpha}\left[\left\langle\frac{\partial J_i^\alpha}{\partial x_i}\middle|\Psi\right\rangle_L P_L\right]\\&-\frac{\partial[\hat{\omega}_\alpha(\Psi)P_L]}{\partial\psi_\alpha}.\end{aligned} \tag{25}$$

This is an exact transport equation for the FDF and is similar to that presented by Gao and O'Brien.[46] The last term on the right hand side of this equation is due to chemical reaction and is in a closed form. The second term on the left hand side represents the filtered convection of the FDF in physical space and is also closed (provided $\langle u_i\rangle_L$ is known). The unclosed terms are associated with the first term on the right hand side denoting the effects of unresolved subgrid scale convection, and the second term on the right hand side representing the influence of molecular diffusion.

The subgrid convective flux is modeled via

$$[\langle u_i|\Psi\rangle_L-\langle u_i\rangle_L]P_L=-\Gamma_t\frac{\partial P_L}{\partial x_i}. \tag{26}$$

The advantage of the decomposition (Eq. (24)) and the subsequent model (Eq. (26)) is that they yield results similar to that in conventional LES for the first moment of the FDF. The first moments corresponding to Eqs. (24) and (26) are

$$\langle u_i\phi_\alpha\rangle_L=\langle u_i\rangle_L\langle\phi_\alpha\rangle_L+[\langle u_i\phi_\alpha\rangle_L-\langle u_i\rangle_L\langle\phi_\alpha\rangle_L], \tag{27}$$

$$[\langle u_i\phi_\alpha\rangle_L-\langle u_i\rangle_L\langle\phi_\alpha\rangle_L]=-\Gamma_t\frac{\partial\langle\phi_\alpha\rangle_L}{\partial x_i}, \tag{28}$$

$$dX_i(t)=D_i(\mathbf{X}(t),t)dt+E(\mathbf{X}(t),t)dW_i(t), \qquad (35)$$

where X_i is the Lagrangian position of a stochastic particle, D_i and E are known as the "drift" and "diffusion" coefficients, respectively, and W_i denotes the Wiener-Lévy process.[65] A comparison of the Fokker-Plank equation corresponding to Eq. (35) with the FDF transport equation (32) determines the appropriate specification of the coefficients to be

$$E\equiv\sqrt{2(\Gamma+\Gamma_t)}, \quad D_i\equiv\langle u_i\rangle_L+\frac{\partial(\Gamma+\Gamma_t)}{\partial x_i}. \qquad (36)$$

Thus the SDE which represents the spatial transport of the FDF is

$$dX_i(t)=\left[\langle u_i\rangle_L+\frac{\partial(\Gamma+\Gamma_t)}{\partial x_i}\right]dt+[2(\Gamma+\Gamma_t)]^{1/2}dW_i. \qquad (37)$$

The compositional makeup of the particles evolves simultaneously due to the actions of subgrid mixing and reaction

$$\frac{d\phi_\alpha^+}{dt}=-\Omega_m(\phi_\alpha^+-\langle\phi_\alpha\rangle_L)+\omega_\alpha, \qquad (38)$$

where $\phi_\alpha^+=\phi_\alpha(X_i(t),t)$ denotes the scalar value of the particle with the Lagrangian position vector X_i.

In the numerical implementation, the FDF is represented by an ensemble of Monte Carlo particles, each with a set of scalars $\phi_\alpha^{(n)}(\mathbf{X}^{(n)}(t),t)$ and Lagrangian position vector $\mathbf{X}^{(n)}$. Numerically, a splitting operation is employed in which the transport in the physical and the compositional domains are treated separately. The simplest means of simulating Eq. (37) is via the Euler-Maruyamma approximation[66]

$$X_i^n(t_{k+1})=X_i^n(t_k)+D_i^n(t_k)\Delta t+E^n(t_k)(\Delta t)^{1/2}\xi_i^n(t_k), \qquad (39)$$

where $D_i^n(t_k)=D_i(\mathbf{X}^{(n)}(t_k),t)$, $E^n(t_k)=E(\mathbf{X}^{(n)}(t_k),t)$ and $\xi_i^{(n)}$ is a random variable with the standard Gaussian PDF. This formulation preserves the Markovian character of the diffusion process[67–69] and facilitates affordable computations. Higher order numerical schemes for solving Eq. (37) are available,[66] but one must be cautious in using them for LES since the diffusion term in Eq. (35) depends on the stochastic process $\mathbf{X}(t)$. The numerical scheme must preserve the Itô-Gikhman[70,71] nature of the process. The coefficients D_i and E require the input of the filtered mean velocity and the diffusivity (molecular and subgrid eddy). These are provided by the solution of Eqs. (6)–(12) by a finite difference LES (as described below) on a fixed grid and then interpolated to the particle location.

The compositional values are subject to change due to subgrid mixing and chemical reaction. Equation (38) may be integrated numerically to simulate these effects simultaneously. Alternately, this equation is treated in a split manner. This provides an analytical expression for the subgrid mixing. Subsequently, the influence of chemical reaction is determined by evaluating the fine grained reaction rates ω_α^n and modifying the composition of the elements. The implementation of the SGS mixing and chemical reaction requires the filtered mean values of the scalars. These mean values (and other higher moments of the FDF) at a given point are estimated by consideration of particles within some volume centered at the point of interest. Effectively, this finite volume constitutes an "ensemble domain" characterized by the length scale Δ_E (not to be confused with Δ_G) in which the FDF is represented discretely by stochastic particles. This is necessary as, with probability one, no particles will coincide with the point as considered.[56] Here, a box of size Δ_E is used to construct the ensemble mean values at the finite difference nodes. These values are then interpolated to the particle positions. Since the mixing model only requires the input of the filtered scalar value, and not its derivative, this volume averaging procedure is sufficient. However, from the numerical standpoint, determination of the size of the ensemble domain is an important issue. Ideally, it is desired to obtain the statistics from the Monte Carlo solution when the size of sample domain is infinitely small (i.e., $\Delta_E\rightarrow 0$) and the number of particles within this domain is infinitely large. With a finite number of particles, if Δ_E is small there may not be enough particles to construct the statistics. A larger ensemble domain decreases the statistical error, but may increase the dispersion error which manifests itself in "artificially diffused" statistical results. This compromise between the statistical accuracy and dispersive accuracy as pertaining to Lagrangian Monte Carlo schemes implies that the optimum magnitude of Δ_E cannot, in general, be specified *a priori*.[40] This does not diminish the capability of the procedure, but exemplifies the importance of the parameters which govern the statistics.

The LES of the hydrodynamic variables, which also determines the subgrid viscosity and scalar diffusion coefficients, is conducted with the "compact parameter" finite difference scheme of Carpenter.[72] This is a variant of the McCormack[73] scheme in which a fourth order compact differences are used to approximate the spatial derivatives, and a second order symmetric predictor-corrector sequence is employed for time discretization. The computational scheme is based on a hyperbolic solver which considers a fully compressible flow. Here, the simulations are conducted with a low Mach number ($M\approx 0.3$) to minimize compressibility effects. The procedure involved in the finite difference discretization is independent of the Monte Carlo solver, thus alternative differencing schemes can be used if desired. All the finite difference operations are conducted on fixed and equally sized grid points. The transfer of information from these points to the locations of the Monte Carlo particles is conducted via interpolation. Both fourth-order and second-order (bilinear) interpolation schemes were considered, but no significant differences in SGS statistics were observed. The results presented in the next section are based on simulations with fourth- and second-order interpolations in two-dimensional (2D) and 3D flows, respectively.

VI. RESULTS

A. Flows simulated

To demonstrate the effectiveness of the FDF method, in this section simulation results are presented of a temporally developing mixing layer and a spatially developing planar jet. Both non-reacting and reacting flows are considered. In the latter, a simple reaction of the type $\mathcal{A}+\mathcal{B}\rightarrow\mathcal{P}$ is considered in which the reaction is assumed to be constant rate and non-heat releasing (isothermal flow). Therefore, $\omega_{\mathcal{A}}=\omega_{\mathcal{B}}=-KAB$, where K is a constant and A,B denote the mass fractions of species $\mathcal{A}$, $\mathcal{B}$, respectively. The species $\mathcal{A}$, $\mathcal{B}$, $\mathcal{P}$ are assumed thermodynamically identical and the fluid is assumed to be calorically perfect. Both 2D and 3D simulations are conducted of the temporal mixing layer. The jet simulations are 2D.

The temporal mixing layer consists of two coflowing streams traveling in opposite directions with the same speed.[74–77] The reactants $\mathcal{A}$ and $\mathcal{B}$ are introduced into the top and the bottom streams, respectively. In the planar jet, the reactant $\mathcal{A}$ is injected with a high velocity from a jet of width D into a coflowing stream with a lower velocity carrying reactant $\mathcal{B}$.[76,78] Both these flows are dominated by large scale coherent structures. The formation of these structures are expedited by imposing low amplitude perturbations. In the figures presented below, x,y correspond to the streamwise and cross-stream directions, respectively. In 3D, z denotes the spanwise direction. In the temporal mixing layer, the length in the streamwise direction is chosen to be twice the wavelength of the most unstable mode to allow for the rollup of two large vortices and one (subsequent) pairing of these vortices. In 3D, the lengths in the streamwise and the cross-stream directions are the same as those in 2D. The length in the spanwise direction is 60% of that in the streamwise direction. The forcing is imposed in such a way to provide significant 3D transport.[79,80] The initial values of the mass fractions of reactants $\mathcal{A}$ and $\mathcal{B}$ at each of the spanwise points in 3D are identical to those in 2D. The size of the domain in the jet flow is $0\leqslant x\leqslant 14D$, $-3.5D\leqslant y\leqslant 3.5D$. The velocity ratio of the coflowing stream to that of the inlet jet is kept fixed at 0.5.

Both flows are simulated via both DNS and LES. The procedure in DNS is exclusively based on the finite-difference solution of Eqs. (1)–(4) in which there are sufficient grid points to resolve the flow without a need for subgrid closures. The procedure in LES is based on the Monte Carlo solution of the modeled FDF transport equation (Eq. (32)) for the scalars augmented by the finite difference solution of the modeled equations of the filtered hydrodynamic variables (Eqs. (6)–(7)). In the presentation below, these results are identified by the abbreviation FDF. In addition, another LES is conducted in which the modeled transport equations for the filtered scalar and the generalized subgrid variance are simulated with the finite difference scheme. In these simulations, the hydrodynamic solver and the models for the subgrid stresses and mass fluxes are identical to those employed in FDF, but the effects of SGS fluctuations in the filtered reaction rate are ignored. Effectively, Eqs. (33)–(34) are solved with the assumption $\langle\omega_\alpha(\Phi)\rangle_L=\omega_\alpha(\langle\Phi\rangle_L)$. The results based on this procedure are referred to as LES-FD. (The approximation $\langle\omega_\alpha(\Phi)\rangle_L=\langle\omega_\alpha(\langle\Phi\rangle_L)\rangle_L$ was also considered but did not show an improvement over LES-FD.)

In both FDF and LES-FD simulations, the subgrid stresses are modeled via the Smagorinsky closure (Eqs. (9)–(10)) and the MKEV model (Eq. (11)). The subgrid mass fluxes are modeled via Eq. (12). No attempt is made here to determine the magnitudes of the constants appearing in these models in a dynamic manner.[14] However, several different values are considered for C_s and C_k. The values which give the best overall agreement with DNS in non-reacting flows are $C_s=0.014$, 0.01 and $C_k=0.02$, 0.013, in 2D, 3D, respectively. These values are subsequently used in FDF and LES-FD of scalar quantities in reacting flows. This parameterization is justified since the LES of the hydrodynamic field is not the subject of our FDF closure. The other parameters $\mathrm{Sc}=1$, $\mathrm{Sc}_t=0.7$ are kept fixed. In the MKEV model, the ratio of the filter size at the secondary level to that at the grid level is $\Delta_{G'}/\Delta_G=3$. In the implementation of the MKEV in the shear flows as considered, the magnitude of the reference velocity $\mathcal{U}_i$ is set to zero in the cross-stream direction and to the average of the high and low speed streams in the streamwise direction. The subgrid mixing model requires the input of the constant C_Ω in the mixing frequency which also determines the SGS variances. As will be shown below $C_\Omega\sim 3$ is suggested, but the influence of this parameter is also studied by considering other C_Ω values.

The flow variables are normalized with respect to reference quantities denoted by the subscript r. In the temporal mixing layer the reference quantities are the freestream values and the length L_r is defined such that $(\delta_{v0}/L_r)=2.83$, where δ_{v0} is the initial vorticity thickness. In the planar jet, $L_r=D$ and the reference quantities are those at the high speed jet stream. The reference quantities define the Reynolds number $\mathrm{Re}=(U_rL_r/\nu)$. For the temporal mixing layer, the Reynolds number based on the total velocity difference across the layer ($\Delta U=2U_r$) is given by $\mathrm{Re}_{\delta_{v0}}=5.66\ \mathrm{Re}$. The reaction rate is parameterized by the Damköhler number $\mathrm{Da}=K/(U_r/L_r)$. The non-dimensional time is given by $t^*=(U_rt/L_r)$. In the presentations below, the asterisk is dropped.

B. Numerical specifications

The magnitude of the flow parameters considered in the simulations are dictated by the resolution which can be afforded by DNS. The primary parameters are the flow Reynolds number (Re), the Damköhler number (Da) and the molecular Schmidt number. All finite difference simulations (in both DNS and LES) are conducted on equally-spaced, square ($\Delta x=\Delta y=\Delta z$ (for 3D) $=\Delta$) grids. Since the size of the computational domain is fixed, the number (and the size) of the grids depends on type of simulation being conducted. The highest resolution in DNS of the 2D temporal mixing layer consists of 433×577 grid points which allows reliable DNS with $\mathrm{Re}=500$ and $\mathrm{Da}=2$ (based on the velocity difference and the vorticity thickness at the initial time). The DNS of the 3D temporal mixing layer is conducted on $217\times 289\times 133$ grid points with $\mathrm{Re}=400$, $\mathrm{Da}=1$. The resolution in DNS of the planar jet consists of 721×361 grid points and allows accurate simulations with $\mathrm{Re}=12\,000$ and $\mathrm{Da}=2$ (based on the centerline velocity at the inlet and the jet width).

The FDF and LES-FD are conducted on grids coarser than those in DNS. Unless otherwise specified, the LES resolutions in the mixing layer consist of 37×49 grid points in 2D, and $55\times 73\times 34$ grid points in 3D. For the planar jet, a resolution of 101×51 is used for nonreacting flow simulations with $\mathrm{Re}=5000$, while a 181×91 grid is utilized for reactive flow simulations with $\mathrm{Da}=2$ and $\mathrm{Re}=12\,000$. A top-hat filter function[47] of the form below is used

$$G(\mathbf{x}'-\mathbf{x})=\prod_{i=1}^{N_D}\bar{G}(x_i'-x_i),$$

$$\bar{G}(x_i'-x_i)=\begin{cases}\dfrac{1}{\Delta_G} & |x_i'-x_i|\leq\dfrac{\Delta_G}{2}\\[2ex] 0 & |x_i'-x_i|>\dfrac{\Delta_G}{2}\end{cases}\tag{40}$$

in which N_D denotes the number of dimensions, and $\Delta_G=2\Delta$. No attempt is made to investigate the sensitivity of the results to the filter function[48] or the size of the filter.[81]

In FDF, the Monte Carlo particles are distributed at $t=0$ throughout the domain. In the temporal mixing layer, the particles are distributed evenly throughout the whole computational region. In the FDF of the jet, the particles are supplied initially in the inlet region $-1.75D\leq y\leq 1.75D$. In all the simulations, the particle density is monitored at all times to ensure an approximately uniform distribution throughout the mixing regions. In the temporal mixing layer, due to flow periodicity in the streamwise direction, if the particle leaves the domain at the right or the left boundary, new particles are introduced at the other boundary with the same compositional values. A similar procedure is employed in the spanwise direction in 3D simulations. Due to mirror symmetry at the upper and lower boundaries, particles that exit the top or bottom boundaries return to the domain at the opposite boundary with the mass fractions values associated with $\mathscr{A}$ and $\mathscr{B}$ interchanged. In the spatial jet, new particles are introduced at the inlet at a rate proportional to the local flow velocity and with a compositional makeup dependent on the y coordinate. The density of the Monte Carlo particles is determined by the initial number of particles per grid cell (NPG) of dimension $\Delta\times\Delta$ ($\times\Delta$ in 3D). The magnitude of NPG is varied to assess its affect on statistical convergence of the Monte Carlo results. This assessment is demonstrated in 2D simulations of the temporal mixing layer. The simulations of 3D temporal layer and the spatial jet are based on $\mathrm{NPG}=20$. The size of the "ensemble domain" in the FDF simulations is also varied to assess its influence on the statistical convergence. The following sizes are considered: $\Delta_E=2\Delta, \Delta, \Delta/2$. The number of samples used to construct the FDF is thus controlled by the values of NPG and Δ_E.

An additional parameter which influences the numerical accuracy is the magnitude of the incremental time step. The stability criterion for the finite difference scheme requires[72] $\mathrm{CFL}\leq 1/\sqrt{3}$ and is more stringent than the criterion for the Fourier number. The effect of the time increment on the accuracy of the Euler-Maruyamma scheme is also considered. This is assessed by considering several Δt values (CFL numbers). In the context of Itô calculus,[82,83] this issue is considered by analysis of moments of the FDF up to the second order.

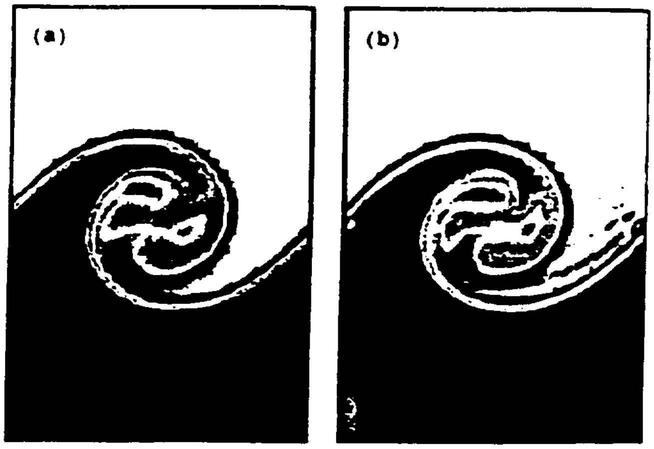

FIG. 1. 2D mixing layer simulation results: Contours of the filtered conserved scalar. (a) FDF and (b) LES-FD.

The simulated results are analyzed both "instantaneously" and "statistically." In the former, the instantaneous contours (snap-shots) of the scalar values are considered. In the latter, the "Reynolds-averaged" statistics constructed from the instantaneous data are considered. In the spatially developing jet flow this averaging procedure is conducted via sampling in time. In the temporal mixing layer, the flow is homogeneous in x (and z in 3D); thus the statistics are generated by constructing the ensemble from all the grid points in the streamwise (and spanwise) directions. These statistics are $y-t$ dependent. All Reynolds averaged results are denoted by an overbar.

C. Consistency of FDF and convergence of the Monte Carlo procedure

The objective in the results presented in this subsection is to demonstrate the consistency of the FDF formulation and the convergence of the Monte Carlo simulations. For this purpose, the LES results via FDF and LES-FD are compared against each other in shear flows under different conditions. In non-reacting flows, any deviations between the FDF and LES-FD results are attributed to the differences in the numerical procedures. Since the accuracy of the finite difference procedure is well-established, this comparative analysis provides a good means of assessing the performance of the Monte Carlo solution of the FDF. Unless specified otherwise, the Smagorinsky model is used to evaluate the eddy viscosity in the simulations considered in this subsection.

In Fig. 1, results are presented of the LES of the nonreacting temporally developing mixing layer. Shown in the figure are the contour plots of $\langle A\rangle_L$ via (a) FDF and (b) LES-FD, with $A=0$, 1 on the bottom and top streams, respectively. These contours correspond to results at a time when the flow has experienced the pairing of two neighboring vortices. This figure provides a simple visual demonstration of the consistency of the FDF as the results via the particle method are in agreement with those obtained by LES-FD. In fact, the Monte Carlo results are somewhat more attractive due the Lagrangian nature of the solution procedure. While the LES-FD results display slight over- and under-shoots, there are no such errors in the Monte Carlo scheme.

A more rigorous means of assessing the FDF results is via consideration of the Reynolds averaged results. Figures 2 and 3 show such results in the non-reacting temporal mixing layer in which the sensitivity of the FDF predictions to several parameters is assessed. Figure 2(a) shows the comparison of FDF and LES-FD results for $\overline{\langle A\rangle_L}$ for several values of Δ_E. It is shown that the first filtered moment of the FDF agrees very well with that obtained by LES-FD, even for large Δ_E values. The differences between the FDF and LES-FD results are more apparent in Figs. 2(b,c,d) where the cross-stream variations of $\overline{\sigma_A}$ are shown for several values of Δ_E and C_Ω and for different LES grid resolutions. As expected, Figs. 2(b,c) show that with increasing C_Ω, the magnitude of the variance decreases. These figures also indicate that the difference between FDF and LES-FD predictions diminish as Δ_E decreases. This is also corroborated in Fig. 2(d) in which the both FDF and LES-FD are conducted on 61×81 grid points. At all Δ_E values, the agreement between FDF and LES-FD is better than those shown in Fig. 2(b) with a lower finite difference resolution. The consistency of the FDF and LES-FD results does not mean that the magnitude of C_Ω can be specified. Hereinafter $C_\Omega=3$ is adopted since it provides the best overall match with DNS data as shown in the next subsection.

The other parameters which influence the accuracy of the Monte Carlo results are the number of Monte Carlo particles per grid cell (NPG) and the magnitude of the incremental time step. Figure 3(a) shows that $\overline{\sigma_A}$ values do not vary significantly for NPG>50. In fact in other cases even smaller NPG values can be used as will be shown. Figure 3(b) verifies the insensitivity of statistics to Δt as long as the stability criterion is satisfied $(\mathrm{CFL}\leq 1/\sqrt{3})$. Hereinafter, CFL=0.5 is used.

The sensitivity of the results to NPG and Δ_E in the FDF simulations of a reacting temporal mixing layer with Da=2 is studied in Fig. 4. In these simulations, the MKEV model is adopted to evaluate the subgrid viscosity because it performs somewhat better than the Smagorinsky model for LES of reactive flows (as assessed by DNS data in the next subsection). Shown in the figure are the Reynolds averaged values of the filtered product mass fraction $(\overline{\langle P\rangle_L})$ at a fixed time (Fig. 4(a)) and the integrated total product $(\delta_P(t) = \int \overline{\langle P\rangle_L}(y,t)dy)$. The convergence of Monte Carlo solution and the independence to NPG and Δ_E are demonstrated by these results (at least for this first moment). Moreover, it is shown that while the mean value of the scalar as used in the mixing model for a given particle should be evaluated at the particle location, the mean value at the nearest finite difference grid point could also be substituted. This eliminates the need for interpolating the mean scalar field to the particle locations.

The consistency and the convergence of the Monte Carlo simulation of the FDF in the nonreacting jet flow are summarized in Figs. 5–6 in which the time averaged (Reynolds)

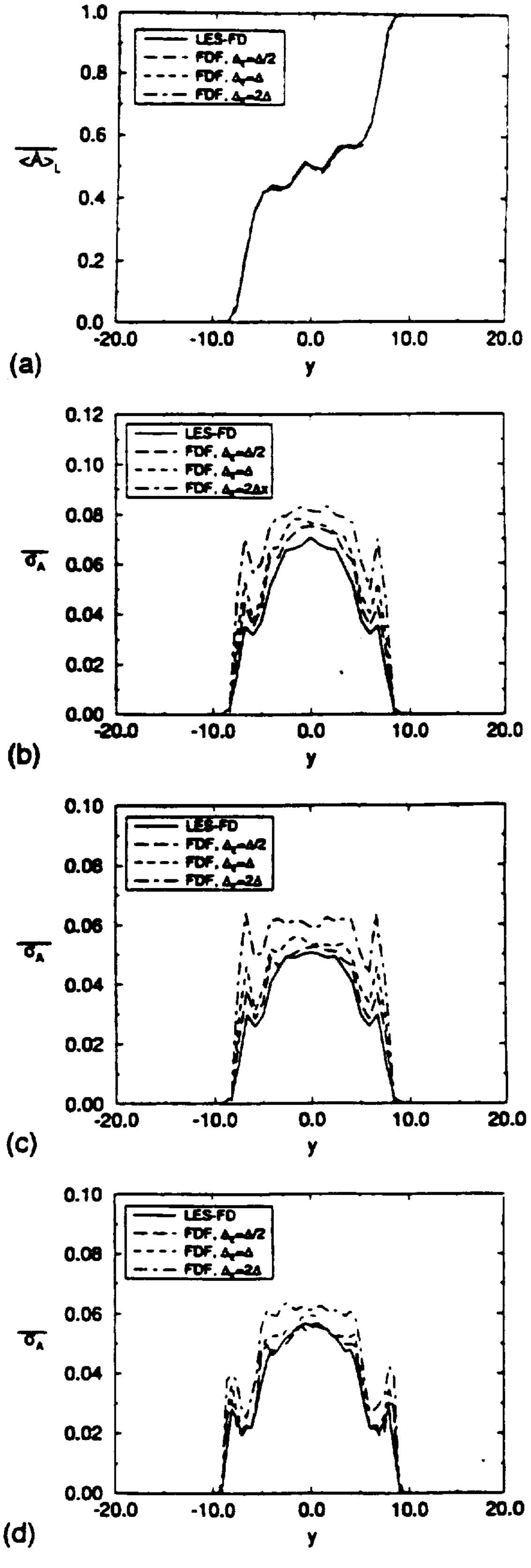

FIG. 2. 2D mixing layer simulation results: (a) Conserved scalar distribution vs. the cross-stream coordinate. Generalized variance vs. cross-stream coordinate at (b) $C_\Omega=1$ and (c) $C_\Omega=3$. (d) Same as (b) but with increased resolution.

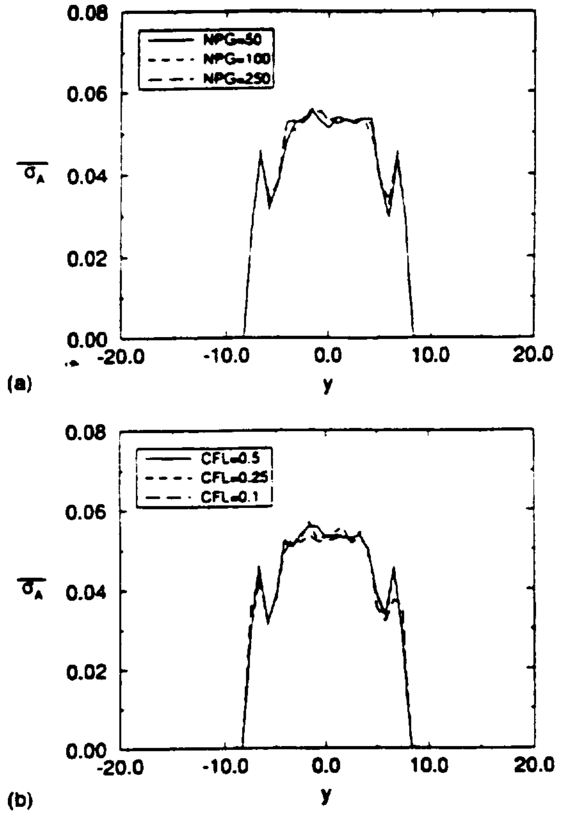

FIG. 3. 2D mixing layer simulation results: (a) Cross-stream variation of the generalized variance for various NPG. (b) Generalized variance vs. cross-stream coordinate at various CFL numbers.

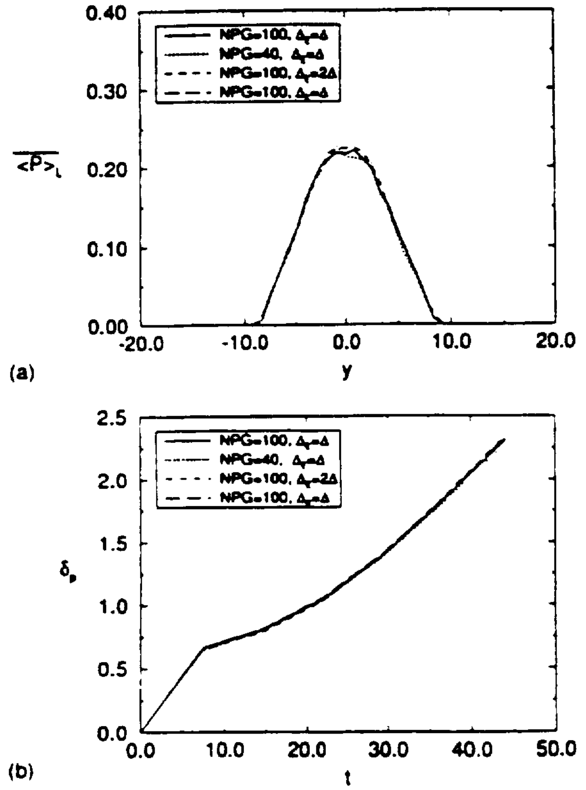

FIG. 4. 2D mixing layer simulation results: (a) Cross-stream variation of the product mass fraction. (b) Total product vs. time. The long-dashed line represent the case where the mean value of the scalar in the mixing model for a particle is set to be equal to the value at the nearest finite difference grid point.

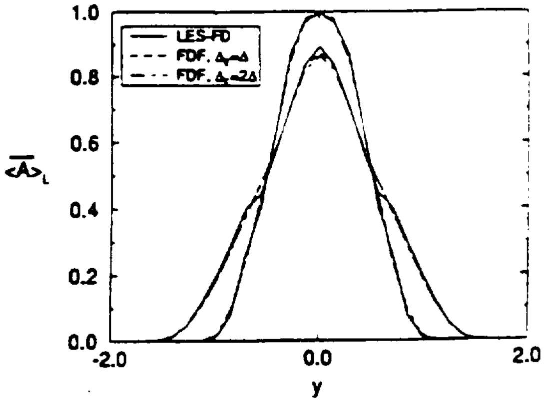

FIG. 5. 2D planar jet results: Conserved scalar distribution vs. cross-stream coordinate at $x=5D, 9D$.

statistics for the first and second subgrid moments of A are presented. Similar to the temporal mixing layer results, Fig. 5 shows the accuracy of the Monte Carlo solver and the insensitivity of results to Δ_E for the first moment of the FDF. Similarly, for the scalar variance, the agreement between the FDF and LES-FD results diminishes as the size of Δ_E is decreased. At $x=5D$, the FDF results with $\Delta_E=\Delta$ are very close to those via LES-FD. With the same Δ_E values the agreement is not as good at $x=9D$ and lower values of Δ_E are needed to achieve a better agreement for the subgrid variance. However, as will be shown below, with this reso-

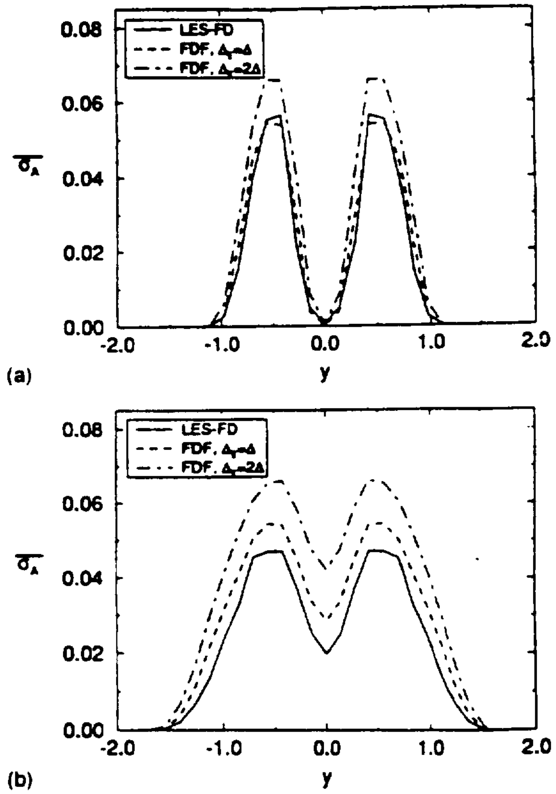

FIG. 6. 2D planar jet results: Generalized variance vs. cross-stream coordinate at (a) $x=5D$ and (b) $x=9D$.

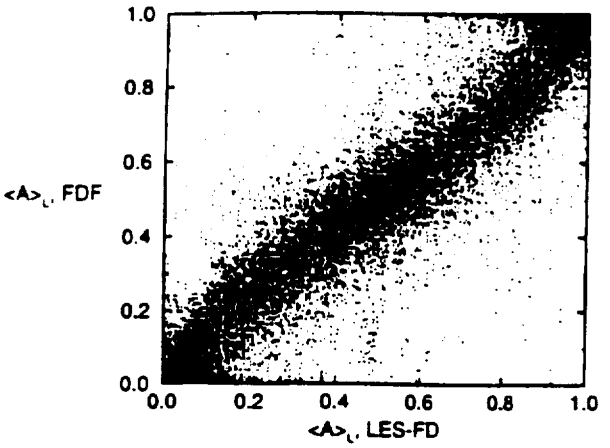

FIG. 7. 3D mixing layer simulation results: Scatter plot of the filtered values of a conserved scalar as obtained by FDF vs. those via LES-FD.

lution the mean filtered values of reacting scalars are predicted reasonably well.

The consistency of the FDF simulation in 3D is demonstrated in Fig. 7 in which the scatter plot is shown of the instantaneous filtered *A* values as obtained by FDF vs. those via LES-FD. The hydrodynamic LES is based on MKEV in both simulations. The correlation coefficient between the data obtained by the two simulations is 0.99. This excellent correlation is also reflected in the cross stream profiles of the Reynolds-averaged filtered quantities in Fig. 8.

D. DNS validations of the FDF

The objective in this section is to assess the overall performance of the FDF and to appraise the validity of the submodels employed in the FDF transport equation. For this objective, the FDF results are compared against DNS of the same flow configuration with the same magnitudes of Re and Da. For a meaningful comparison, the DNS data are filtered and the results on the coarse grids are compared with those on the corresponding coarse grids in the FDF simulations. To illustrate the capability of the FDF, the results are also compared with LES-FD in which the effects of SGS fluctuations on the filtered reaction rate are ignored.

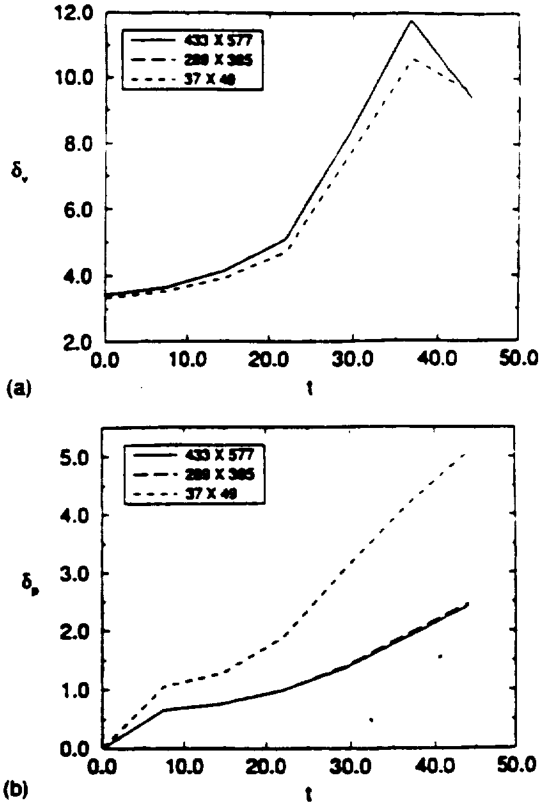

FIG. 9. 2D mixing layer simulation results: Effect of grid resolution on temporal evolution of the (a) vorticity thickness and (b) total product.

First the resolution requirement for DNS is determined. This is demonstrated here for the 2D mixing layer. A similar procedure is followed for the other flow configurations. In Fig. 9 results are presented of the temporal evolution of the vorticity thickness (δ_v) and the total product (δ_P) in a reacting layer with Re=500, Da=2 at several resolutions. It is shown that the results generated via 289×385 are almost identical to those on 433×577 grid points. Analysis of other statistical results (not shown) show a similar behavior. Hereinafter 433×577 grid points are used in all DNS of the 2D mixing layer. The resolution employed in LES (both FDF

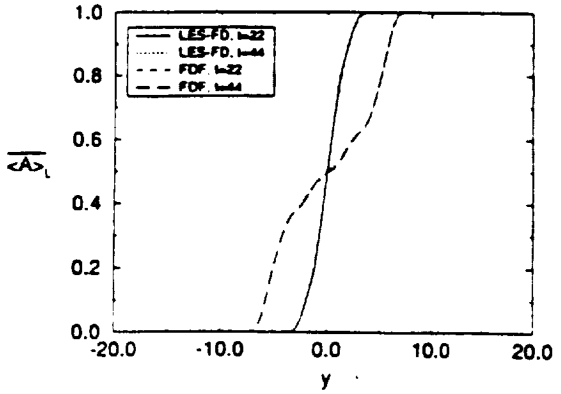

FIG. 8. 3D mixing layer simulation results: Cross-stream variations of the mean value of the filtered mass fraction of a conserved scalar.

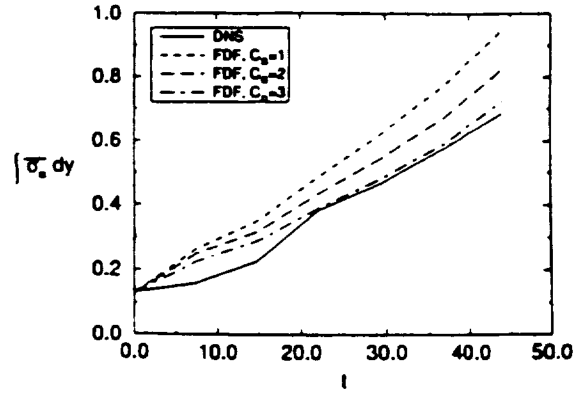

FIG. 10. 2D mixing layer simulation results: The integrated Reynolds averaged values of the filtered scalar's variance vs. time.

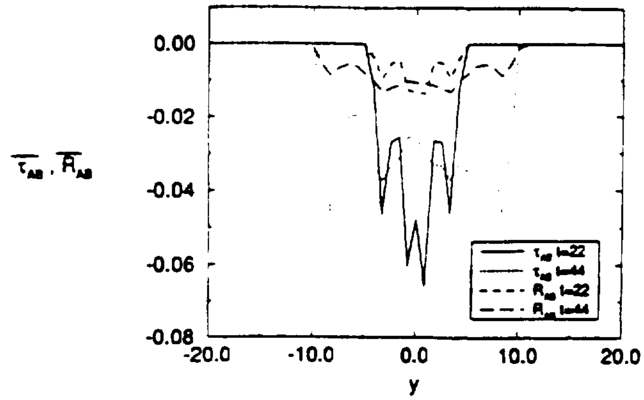

FIG. 11. 2D mixing layer simulation results: Total SGS unmixedness and Reynolds subpart vs. cross-stream coordinate.

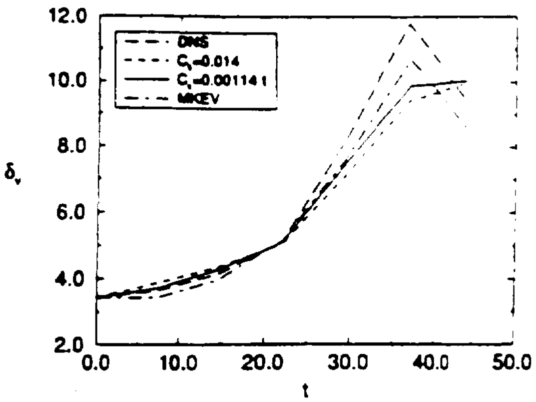

FIG. 13. 2D mixing layer simulation results: Vorticity thickness vs. time.

and LES-FD) is coarser consisting of 37×49 grid points. The results in Fig. 9 indicate the inaccuracy of "DNS" at this resolution.

To determine the magnitude of C_Ω, in Fig. 10 the integrated Reynolds averaged values of the SGS variance ($\int \overline{\sigma_A}(y,t)dy$) of a nonreacting scalar as predicted by FDF are compared with those via DNS. This comparison shows that $C_\Omega \approx 3$ yields a reasonable agreement between the prediction and DNS results. Thus, this value is used in absence of a better model of the subgrid mixing frequency.

To demonstrate the difficulty of modeling the SGS scalar fluctuations in reacting flows, the Reynolds averaged profiles for the "SGS unmixedness" ($\tau_{AB}=\langle AB\rangle_L-\langle A\rangle_L\langle B\rangle_L$) and its "Reynolds" subpart[84,85] $R_{AB}=\langle A'B'\rangle_L-\langle A'\rangle_L\langle B'\rangle_L$ as obtained directly from DNS data are shown in Fig. 11. These results show the importance (non-zero values) of these correlations. They also show that R_{AB} is a fraction of τ_{AB} suggesting that modeling of τ_{AB} in LES is more complex than that in Reynolds procedures.

In Fig. 12, the FDF predictions of the total product are compared with DNS results. The Smagorinsky model is employed in FDF with several values of the parameter C_s. Obviously for a constant C_s value, the agreement between DNS and FDF is not very satisfactory. The subgrid viscosity based on the Smagorinsky closure affects both the resolved hydrodynamic field and the subgrid scalar mixing process. It is known that the Smagorinsky closure sometimes generates excessive damping on the resolved scales in transitional regions.[49] Here, an attempt is made to rectify the situation, albeit in a very *ad hoc* manner. In the temporal mixing later, C_s should be initially zero to reflect the fact that the flow is "laminar." Then its value should increase in time as the flow becomes more "turbulent." The FDF results in Fig. 12 with $C_s \propto t$ agree more favorably with DNS. This is partly due to better predictions of the hydrodynamic field (Fig. 13) but also due to more accurate representation of the subgrid mixing frequency. This better agreement is not sufficient to suggest a new model for C_s; rather it is to demonstrate the importance of the subgrid diffusion in affecting the FDF directly (through the subgrid mixing) and indirectly (through the input of the hydrodynamic parameters).

In order to better predict the subgrid viscosity, the MKEV model (Eq. (11)) is adopted. In Fig. 13 it is shown that the vorticity thickness predicted by the MKEV model compares with DNS data better than that via the Smagorinsky model. The improved prediction of the eddy viscosity also improves the FDF predicted product formation as shown in Fig. 14 for several values of the Damköhler number. Due to the demonstrated superiority, the MKEV closure is utilized in all subsequent simulations unless otherwise noted.

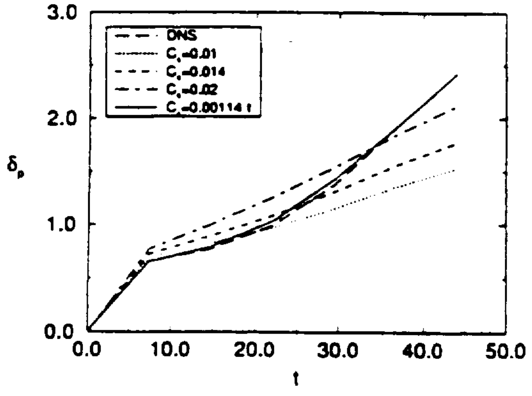

FIG. 12. 2D mixing layer simulation results: Total product variation with time. The Smagorinsky model is used to represent the eddy viscosity for the FDF simulations.

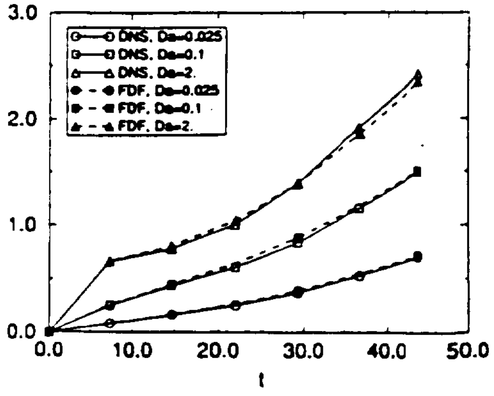

FIG. 14. 2D mixing layer simulation results: Temporal evolution of the total product.

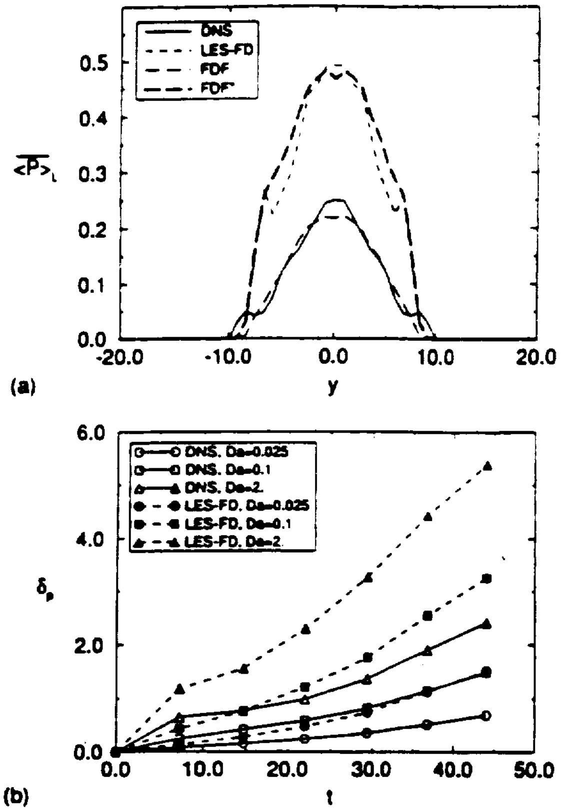

FIG. 15. 2D mixing layer simulation results: (a) Cross-stream variation of the product distribution. (b) Temporal evolution of the total product.

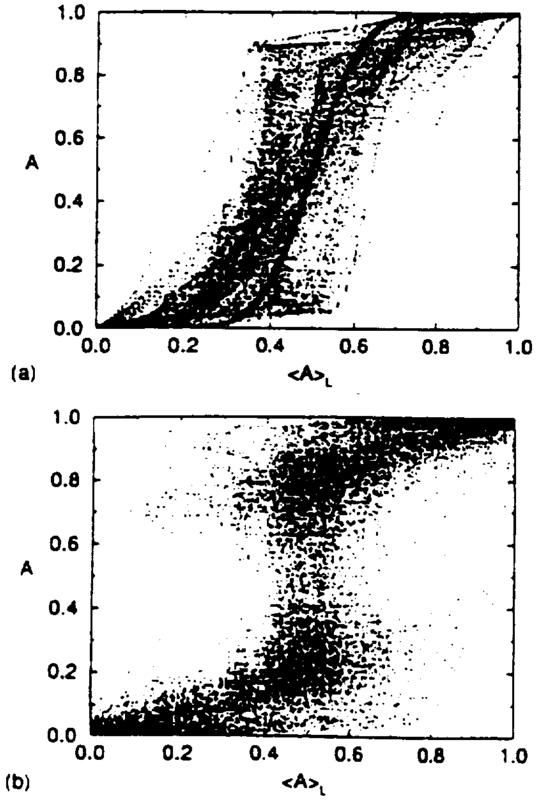

FIG. 16. 2D mixing layer simulation results: Scatter plots of instantaneous value of the conserved scalar vs. the mean value. Data taken from (a) DNS, (b) FDF throughout the computational domain.

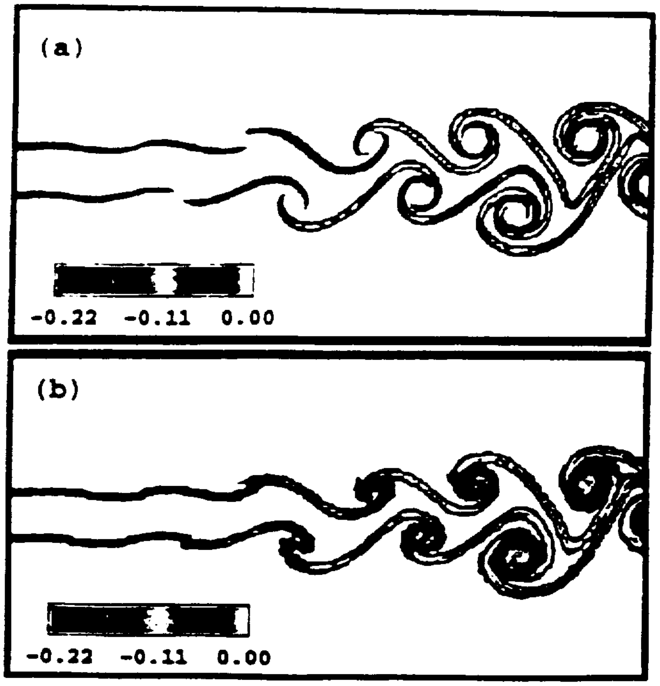

FIG. 17. 2D planar jet simulation results: Contours of the normalized instantaneous subgrid unmixedness (a) DNS, (b) FDF.

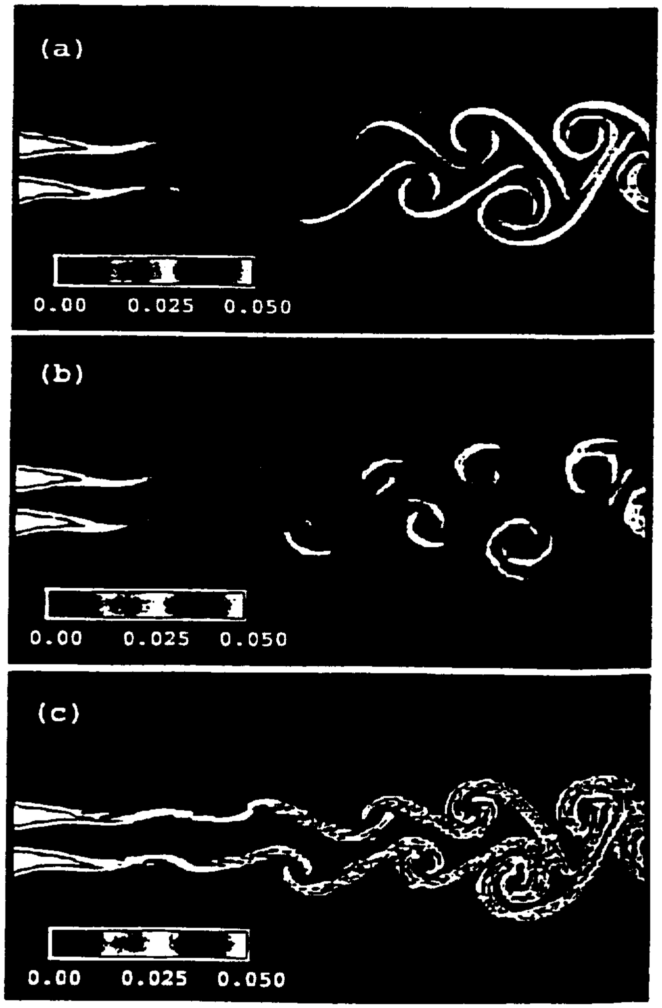

FIG. 18. 2D planar jet simulation results: Instantaneous reaction rate as determined by (a) DNS, (b) FDF, (c) LES-FD.

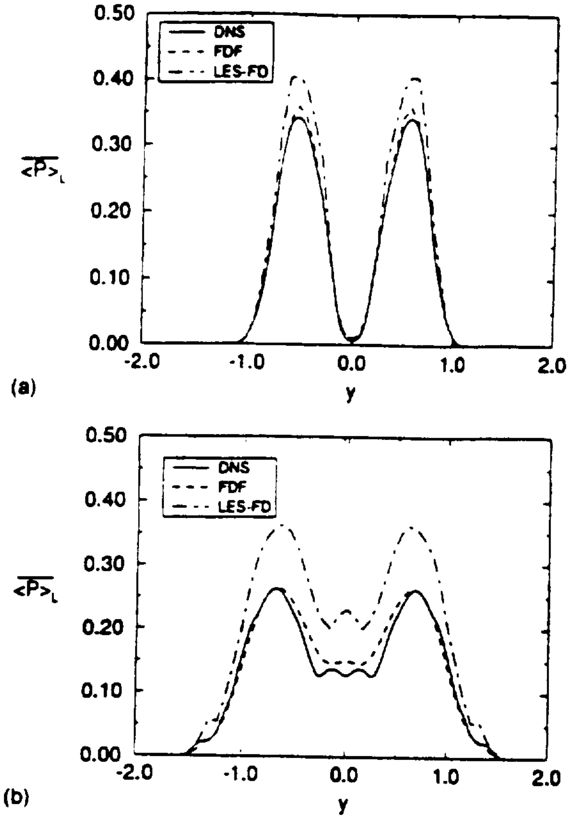

FIG. 19. 2D planar jet simulation results: Cross-stream variation of the mean product mass fraction at (a) $x = 5D$ and (b) $x = 9D$.

To demonstrate the importance of the SGS scalar fluctuations, the results of FDF and LES-FD are compared with DNS results in Fig. 15. This figure shows that the neglect of SGS unmixedness results in significant overpredictions of the product mass fraction. This behavior is observed at all times and all values of the Damköhler number (Fig. 15(b)) and is consistent with that in Reynolds averaging.[18] Moreover, Fig. 15(b) shows that as the magnitude of the Damköhler number increases, the neglect of the SGS unmixedness in LES-FD results in progressively higher deviation of product formation relative to DNS. This is significant since the Da values in practical reacting systems can be quite large. Therefore it is expected that the effects of the SGS unmixedness are very pronounced in such applications. To verify that the enhanced product formation in LES-FD is not associated with the numerical discretization errors, an additional FDF is conducted in which the filtered reaction rate is "incorrectly" calculated in terms of the filtered values of the reactants' mass fractions. The results based on this model are identified by FDF* in Fig. 15(a) and consistent with LES-FD results, overpredict the rate of reactants' conversion.

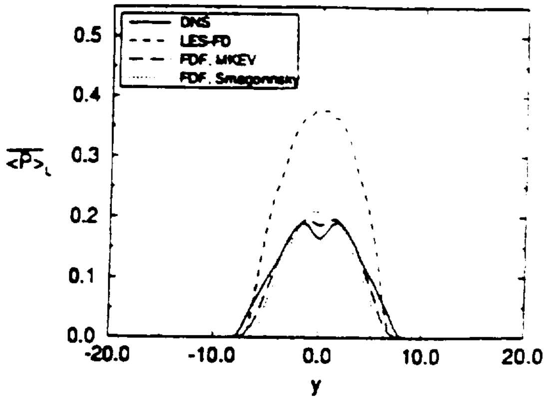

FIG. 21. 3D mixing layer simulation results: Cross-stream variation of the product distribution.

It is useful to compare the DNS results for "fine grid" scalar values with the "fine-grained" values associated with the Monte Carlo particles. The "scatter" plots of the instantaneous fine grid values of A vs. its filtered value $\langle A\rangle_L$ as obtained by DNS are presented in Fig. 16(a) and the scatter plot of fine grained A values vs. $\langle A\rangle_L$ is shown in Fig. 16(b). These results are associated with a non-reacting temporal mixing layer and are taken at a fixed time. The points in Fig. 16(a) correspond to the values at all the grid points employed in DNS within the computation domain. The points in Fig. 16(b) correspond to all Monte Carlo particles occupying the same domain. It is shown that the "density" of scatter is similar in the two plots indicating a qualitative agreement between FDF and DNS. However, the scatter in FDF is expectedly somewhat greater but not with a significant density.

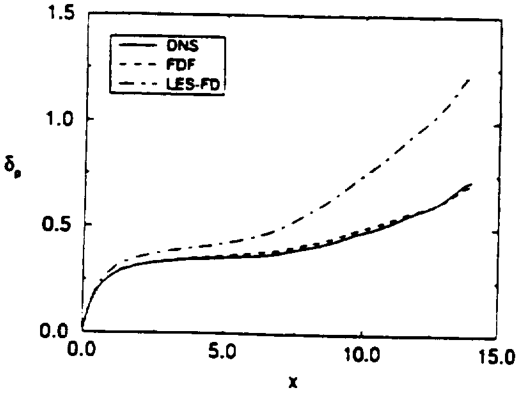

FIG. 20. 2D planar jet simulation results: Total product vs. the downstream coordinate.

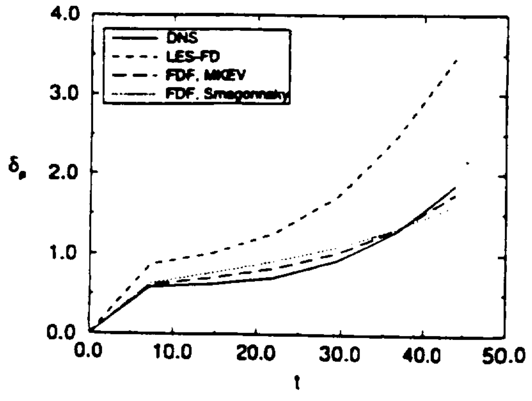

FIG. 22. 3D mixing layer simulation results: Temporal evolution of the total product.

TABLE I. Total computational times for the 2D reacting mixing layer simulations.

Simulation	Grid resolution	NPG	Normalized CPU time[a]	Figure
DNS	433×577	—	285.45	14, 15(b)
FDF	37×49	40	8.45	14
LES-FD	37×49	—	1	15(b)

[a] Unit corresponds to 11 s on a Cray-C90.

TABLE III. Total computational times for the 3D reacting mixing layer simulations.

Simulation	Grid resolution	NPG	Normalized CPU time[a]	Figure
DNS	217×289×133	-	182.71	21, 22
FDF	55×73×34	20	7.64	21, 22
LES-FD	55×73×34	-	1	21, 22

[a] Unit correspond to 655 s on a Cray-C90.

The effectiveness of the FDF to predict the slightly more complex jet flow is summarized in Figs. 17–20. Figure 17 shows the instantaneous contours of the normalized SGS unmixedness as obtained by filtered DNS and FDF. Note that this term is assumed to be identically zero in LES-FD. The SGS unmixedness is negative throughout the reaction zone, thus its effect is manifested in a decrease of the filtered reaction rate. This is readily observed in Fig. 18, where the contour plots of the reaction rates are displayed for the filtered DNS, FDF and LES-FD approaches. While the peak values in the DNS are slightly higher than those observed in the FDF simulations, the reaction zone predicted by the FDF simulation is slightly thicker (due to the finite size of the ensemble domain) therefore yielding a comparable amount of converted products. In contrast, the filtered reaction rates obtained by the finite difference LES procedure in which the SGS unmixedness is neglected are significantly higher. This is reflected in Fig. 19, where the cross-stream variation of the time-averaged filtered values of the product mass fraction are presented at two downstream locations and in Fig. 20, where the streamwise variation of the integrated total product ($\delta_P(x)=\int\langle P\rangle_L(x,y)dy$) is shown. Two additional points are intended by presentations of Figs. 19 and 20. First, the FDF results are compatible with those of DNS at all downstream coordinates. Therefore, there is no "secular" behavior associated with possible modeling errors in the FDF. Second, the differences between the FDF and DNS in predicting the subgrid scalar variances at large x/D values as observed in the variance results in Fig. 6 do not seem to yield significant differences in the amount of product formation as predicted by the FDF. In all the cases the neglect of the SGS fluctuations, as done in LES-FD, results in significant overpredictions of the filtered reactant conversion rate. It is expected that these overpredictions would become even more significant at higher Damköhler and Reynolds numbers.

The major conclusions drawn from the 2D results are confirmed in 3D simulations. The cross-stream variation of the filtered mean products and the temporal variation of the total product in the 3D mixing layer are shown in Figs. 21 and 22. The performances of the Smagorinsky and MKEV closures in predicting the hydrodynamic field are similar to those in 2D. With either closures, the amount of products predicted by LES-FD is higher than those obtained by FDF and DNS. The FDF results are again in a good agreement with DNS data. This agreement also indicates that the mixing model with $C_\Omega=3$ works well in 3D simulations; no attempt was made to find the optimize value of this constant. Future applications to other flow configurations would determine the generality of the model.

TABLE II. Total computational times for the reacting jet simulations.

Simulation	Grid resolution	NPG	Normalized CPU time[a]	Figure
DNS	721×361	—	52.12	18(a)
FDF	181×91	20	12.56	18(b)
LES-FD	181×91	—	1	18(c)

[a] Unit corresponds to 809 s on a Cray-C90.

E. Comparison of computational requirements

The total computational times associated with some of the simulations are shown in Tables I–III. The cases considered in this table are those which give reasonably accurate predictions of the first FDF moments of the reacting scalar field. Expectedly, the overhead associated with the FDF simulation is somewhat extensive as compared to LES-FD; nevertheless the FDF's computational requirement is significantly less that of DNS. While this overhead was tolerated in present simulations, there are several means of reducing it for future applications. A detailed examination of the individual routines utilized in the FDF simulations indicates that the most demanding computation is associated with the particle interpolation procedure. The fourth order interpolation routine consumes about 51.3% of the total CPU time. The bilinear scheme reduces the computational time by 36%. If interpolation can be totally disregarded, i.e., using the results at the nearest finite difference grid point as shown in Fig. 4, the CPU time can be decreased by 50%. In addition, the Lagrangian procedure would benefit from the utilization of parallel architecture, since a significant portion of the time is devoted to computations in large loops dimensioned by the total number of Monte Carlo particles. This has been discussed for use in PDF (Ref. 86) and its utilization is recommended for FDF.

In comparing the computational requirements of FDF with those of DNS, it is important to note that this comparison could be made only in flows for which DNS was possible. The DNS times and the FDF times are as close as they are simply because the DNS had to be done at low Re, Da values. At higher values of these parameters, the difference could be much greater. This warrants further extensions and applications of FDF for more complex turbulent reacting flows for which DNS is not possible.

VII. CONCLUDING REMARKS

It is demonstrated that the filtered density function (FDF) provides a powerful method for large eddy simulation (LES) of turbulent reacting flows. The method is based on the representation of the distribution of the unresolved fluctuations at the subgrid level. This is similar to the probability density function (PDF) methods in Reynolds averaging procedures. Here, the FDF methodology is developed for treatment of scalar variables. Thus, similar to PDF methods it represents the effects of chemical reactions in a closed form.

A modeled transport equation is developed for the FDF by adopting a closure strategy similar to that in PDF methods. It is shown that the Lagrangian Monte Carlo scheme provides an effective means of solving the FDF transport equation. The scheme is exploited for LES of two- and three-dimensional shear flows under both nonreacting and reacting conditions. The simulated results are compared with those based on conventional LES methods in which the effects of subgrid scalar fluctuations are ignored (LES-FD), and those via direct numerical simulation (DNS) of flows with identical values of the physical parameters. The convergence of the Monte Carlo numerical results and the consistency of the FDF formulation are demonstrated by comparisons with the Eulerian results of LES-FD of non-reacting flows. The superiority of the FDF over LES-FD is demonstrated by detailed comparative assessments with DNS results of reacting shear flows. It shown that the subgrid scale scalar fluctuations have a very significant influence on the filtered reaction rate; the neglect of these fluctuations results in overpredictions of the filtered reactant conversion rate.

Although the present methodology is developed for isothermal, constant density, reacting flows with a simple kinetics scheme, the extension to variable density flows, with exothermic reactions imposes no serious mathematical difficulties. With such an extension, it is conceivable that LES of reactive flows with realistic chemical kinetics may be conducted for engineering applications in the near future, if the computational overhead associated with the FDF can be tolerated. In this regard, the scalar FDF methodology is attractive in that the present Monte Carlo solver can be used directly in available CFD codes. Similar to PDF methods, the closure problems associated with the FDF are the correlations involving the velocity field (such as SGS stresses and mass fluxes). This may be overcome by considering the joint velocity-scalar FDF similar to that in PDF.[87]

The computational requirement for FDF is more than that for LES-FD and less than that for DNS. The range of flow parameters (such as the Reynolds and the Damköhler numbers) that can be considered by FDF is significantly larger than can be treated by DNS, and the results are more accurate that those by LES-FD. This comparison of computational requirements could be made here only in flows for which DNS was possible, i.e., low Da, Re values. At higher values of these parameters, the computational cost associated with DNS would be exceedingly higher than that of FDF. Thus for practical flows for which DNS is currently impossible, FDF would be a good alternative. Several means of reducing the FDF's computational requirements are recommended. These could be useful in future applications in complex flows. The FDF methodology will benefit from ongoing and future improvements in PDF schemes from both modeling and computational standpoints.[56]

ACKNOWLEDGMENTS

This work is part of a research program sponsored by the NASA Langley Research Center under Grant No. NAG-1-1122 to SUNY-Buffalo and Grant No. NAG-1-1542 to Cornell University. Dr. J. Philip Drummond is the Technical Monitor of this program. Additional support for the work at Cornell is provided by the AFOSR under Grant No. F49620-94-1-0098. Computational resources are provided by the NAS Program at the NASA Ames Research Center and by the SEAS Computing Center at SUNY-Buffalo.

[1] J. Smagorinsky, "General circulation experiments with the primitive equations. I. The basic experiment," Mon. Weather Rev. 91, 99 (1963).

[2] D. K. Lilly, "The representation of small-scale turbulence in numerical simulation experiments," in *Proceedings of the IBM Scientific Computing Symposium Environmental Sciences*, IBM Form No. 320-1951 (1967), pp. 195–210.

[3] J. H. Ferziger, "Higher level simulations of turbulent flows," Stanford University Report No. TF-16, Department of Mechanical Engineering, Stanford University, Stanford, California, 1981.

[4] P. R. Voke and M. W. Collins, "Large eddy simulation: Retrospect and prospects," PhysicoChem. Hydrodynam. 4, 119 (1983).

[5] R. S. Rogallo and P. Moin, "Numerical simulation of turbulent flow," Annu. Rev. Fluid Mech. 16, 99 (1984).

[6] W.-H. Jou and J. J. Riley, "Progress in direct numerical simulations of turbulent reacting flows," AIAA J. 27, 1543 (1989).

[7] P. Givi, "Model free simulations of turbulent reactive flows," Prog. Energy Combust. Sci. 15, 1 (1989).

[8] *Whither Turbulence? Turbulence at the Crossroads, Lecture Notes in Physics*, edited by J. L. Lumley (Springer, New York, 1990), Vol. 357.

[9] *Numerical Approaches to Combustion Modeling, Progress in Astronautics and Aeronautics*, edited by E. S. Oran and J. P. Boris (AIAA, New York, 1991), Vol. 135.

[10] P. A. McMurtry and P. Givi, "Spectral simulations of reacting turbulent flows," in Ref. 9, Chap. 9, pp. 257–303.

[11] *Large Eddy Simulations of Complex Engineering and Geophysical Flows*, edited by B. Galperin and S. A. Orszag (Cambridge University Press, Cambridge, 1993).

[12] P. Givi, "Spectral and Random vortex methods in turbulent reacting flows," in Ref. 19, Chap. 8, pp. 475–572.

[13] D. K. Lilly, "On the computational stability of numerical solutions of time-dependent non-linear geophysical fluid dynamics problems," Mon. Weather Rev. 93, 11 (1965).

[14] M. Germano, "Turbulence: The filtering appraoch," J. Fluid Mech. 238, 325 (1992).

[15] M. Germano, U. Piomelli, P. Moin, and W. H. Cabot, "A dynamic subgrid-scale eddy viscosity model," Phys. Fluids A 3, 1760 (1991).

[16] S. B. Pope, "Computations of turbulent combustion: Progress and challenges," in *Proceedings of the 23rd Symposium (International) on Combustion* (The Combustion Institute, Pittsburgh, 1990), pp. 591–612.

[17] U. Schumann, "Large eddy simulation of turbulent diffusion with chemical reactions in the convective boundary layer," Atmos. Environ. 23, 1713 (1989).

[18] *Turbulent Reacting Flows, Topics in Applied Physics*, edited by P. A. Libby and F. A. Williams (Springer, Heidelberg, 1980), Vol. 44.

[19] *Turbulent Reacting Flows*, edited by P. A. Libby and F. A. Williams (Academic, London, 1994).

[20] W. P. Jones, "Turbulence Modelling and Numerical Solution Methods for Variable Density and Combusting Flows," in Ref. 19, Chap. 6, pp. 309–374.

[21] *Turbulence in Mixing Operation*, edited by R. S. Brodkey (Academic, New York, 1975).

[22] H. L. Toor, "The non-premixed Reaction: $A+B\rightarrow$products, in Ref. 21, pp. 123–166.

[23] J. C. Hill, "Homogeneous turbulent mixing with chemical reaction," Annu. Rev. Fluid Mech. **8**, 135 (1976).

[24] R. S. Brodkey, "Fundamental of turbulent motion," Chem. Eng. Commun. **8**, 1 (1981).

[25] P. A. McMurtry, S. Menon, and A. R. Kerstein, "A linear eddy sub-grid model for turbulent reacting flows: Application to hydrogen-air combustion," in *Proceedings of the 24th Symposium (International) on Combustion* (The Combustion Institute, Pittsburgh, 1992), pp. 271–278.

[26] P. A. McMurtry, S. Menon, and A. R. Kerstein, "Linear eddy modeling of turbulent combustion," Energy Fuels **7**, 817 (1993).

[27] R. I. Sykes, D. S. Henn, S. F. Parker, and W. S. Lewellen, "Large-eddy simulation of a turbulent reacting plume," Atmos. Environ. **26**, 1713 (1992).

[28] T. M. Liou, W. Y. Lien, and P. W. Hwang, "Large-eddy simulations of turbulent reacting flows in chamber with gaseous ethylene injecting through the porous wall," Combust. Flame **99**, 591 (1994).

[29] S. Menon, P. A. McMurtry, and A. K. Kerstein, "A linear eddy sugbrid model of turbulent combustion," in Ref. 11, Chap. 14, pp. 287–314.

[30] J. P. Boris, F. F. Grinstein, E. S. Oran, and R. L. Kolbe, "New insights into large eddy simulations," NRL Report No. NRL/MR/4400-92-6979, Naval Research Laboratory, Washington, D.C., 1992.

[31] C. Fureby and C. Lofstrom, "Large-eddy simulations of bluff body stabilized flames," in *Proceedings of the 25th Symposium (International) on Combustion* (The Combustion Institute, Pittsburgh, 1994), pp. 1257–1264.

[32] C. Fureby, E. Lundgren, and S. I. Moller, "Large-eddy simulation of combustion," in *Proceedings of the Eighth International Symposium on Transport Phenomena in Combustion*, edited by S. H. Chen (Taylor-Francis, New York, 1996).

[33] A. W. Cook, J. J. Riley, and G. Kosály, "A laminar flamelet approach to subgrid-scale chemistry in turbulent flows," Combust. Flame **109**, 332 (1997).

[34] A. W. Cook, J. J. Riley, and S. M. deBruynKops, "A sub-grid model for nonpremixed turbulent combustion," in *Proceedings of the Eleventh Symposium on Turbulent Shear Flows* (Grenoble, France, 1997), pp. 16.13–16.18.

[35] F. Mathey and J. P. Chollet, "Large eddy simulation of turbulent reactive flows," in *Proceedings of the Eleventh Symposium on Turbulent Shear Flows* (Grenoble, France, 1997), pp. 16.19–16.24.

[36] N. Branley and W. P. Jones, "Large eddy simulation of a turbulent nonpremixed flame," in *Proceedings of the Eleventh Symposium on Turbulent Shear Flows* (Grenoble, France, 1997), pp. 21.1–21.6.

[37] H. L. Toor, "Mass transfer in dilute turbulent and nonturbulent systems with rapid irreversible reactions and equal diffusivities," AIChE J. **8**, 70 (1962).

[38] S. B. Pope, "The statistical theory of turbulent flames," Philos. Trans. R. Soc. London **291**, 529 (1979).

[39] E. E. O'Brien, "The probability density function (PDF) approach to reacting turbulent flows," in Ref. 18, Chap. 5, pp. 185–218.

[40] S. B. Pope, "PDF methods for turbulent reactive flows," Prog. Energy Combust. Sci. **11**, 119 (1985).

[41] C. Dopazo, "Recent Developments in PDF Methods," in Ref. 19, Chap. 7, pp. 375–474.

[42] T. S. Lundgren, "Distribution functions in the statistical theory of turbulence," Phys. Fluids **10**, 969 (1967).

[43] C. K. Madnia and P. Givi, "Direct numerical simulation and large edddy simulation of reacting homogeneous turbulence," in Ref. 11, Chap. 15, pp. 315–346.

[44] A. W. Cook and J. J. Riley, "A subgrid model for equilibrium chemistry in turbulent flows," Phys. Fluids **6**, 2868 (1994).

[45] S. H. Frankel, V. Adumitroaie, C. K. Madnia, and P. Givi, "Large eddy simulations of turbulent reacting flows by assumed PDF methods," edited by S. A. Ragab and U. Piomelli, *Engineering Applications of Large Eddy Simulations* (ASME, New York, 1993), Vol. 162, pp. 81–101.

[46] F. Gao and E. E. O'Brien, "A large-eddy simulation scheme for turbulent reacting flows," Phys. Fluids A **5**, 1282 (1993).

[47] A. A. Aldama, "Filtering techniques for turbulent flow simulations," *Lecture Notes in Engineering* (Springer, New York, 1990), Vol. 49.

[48] B. Vreman, B. Geurts, and H. Kuerten, "Realizability conditions for the turbulent stress tensor in large-eddy simulation," J. Fluid Mech. **278**, 351 (1994).

[49] T. A. Zang and U. Piomelli, "Large eddy simulation of transitional flow," in Ref. 11, Chap. 11, pp. 209–227.

[50] R. M. Kerr, J. A. Domaradzki, and G. Barbier, "Small-scale properties of nonlinear interactions and subgrid-scale energy transfer in isotropic turbulence," Phys. Fluids **8**, 197 (1996).

[51] J. Bardina, J. H. Ferziger, and W. C. Reynolds, "Improved turbulence models based on large eddy simulations of homogeneous, incompressible, turbulent flows," Department of Mechanical Engineering Report No. TF-19, Stanford University, Stanford, California, 1983.

[52] T. M. Eidson, "Numerical simulation of the turbulent Rayleigh-Benard problem using subgrid modelling," J. Fluid Mech. **158**, 245 (1985).

[53] C. Dopazo and E. E. O'Brien, "Statistical treatment of non-isothermal chemical reactions in turbulence," Combust. Sci. Technol. **13**, 99 (1976).

[54] R. Borghi, "Turbulent combustion modeling," Prog. Energy Combust. Sci. **14**, 245 (1988).

[55] S. B. Pope, "A Monte Carlo method for the PDF equations of turbulent reactive flow," Combust. Sci. Technol. **25**, 159 (1981).

[56] S. B. Pope, "Lagrangian PDF methods for turbulent flows," Annu. Rev. Fluid Mech. **26**, 23 (1994).

[57] A. J. Chorin and J. E. Marsden, *A Mathematical Introduction to Fluid Mechanics* (Springer, New York, 1979).

[58] A. Leonard, "Vortex methods for flow simulation," J. Comput. Phys. **37**, 289 (1980).

[59] A. Majda, "Vortex dynamics: Numerical analysis, scientific computing, and mathematical theory," in *ICIAM '87*, edited by J. McKenna and R. Temam (Society for Industrial and Applied Mathematics, Philadelphia, 1988), pp. 153–182.

[60] T. Sarpkaya, "Computational methods with vortices—The 1988 Freeman Scholar Lecture," J. Fluids Eng. **111**, 5 (1989).

[61] A. F. Ghoniem, "Vortex simulation of reacting shear flow," in Ref. 9, Chap. 10, pp. 305–348.

[62] *Vortex Methods and Vortex Motion*, edited by K. E. Gustafson and J. A. Sethian (SIAM, Philadelphia, 1991).

[63] H. Risken, *The Fokker-Planck Equation, Methods of Solution and Applications* (Springer, New York, 1989).

[64] C. W. Gardiner, *Handbook of Stochastic Methods* (Springer, New York, 1990).

[65] S. Karlin and H. M. Taylor, *A Second Course in Stochastic Processes* (Academic, New York, 1981).

[66] P. E. Kloeden and E. Platen, *Numerical Solution of Stochastic Differential Equations, Applications of Mathematics, Stochastic Modelling and Applied Probability* (Springer, New York, 1995), Vol. 23.

[67] P. Billingsly, *Probability and Measure* (Wiley, New York, 1979).

[68] E. Helfand, "Numerical integration of stochastic differential equations," Bell Syst. Tech. J. **58**, 2289 (1979).

[69] D. T. Gillespie, *Markov Processes, An Introduction for Physical Scientists* (Academic, New York, 1992).

[70] K. Itô, *On Stochastic Differential Equations, Memoirs of the American Mathematical Society* (American Math Society, Providence, 1951), Vol. 4.

[71] I. I. Gikhman and A. V. Skorokhod, *Stochastic Differential Equations* (Springer, New York, 1972).

[72] M. H. Carpenter, "A high-order compact numerical algorithm for supersonic flows," in *Proceedings of the Twelfth International Conference on Numerical Methods in Fluid Dynamics, Lecture Notes in Physics*, edited by K. W. Morton (Springer, New York, 1990), Vol. 371, pp. 254–258.

[73] R. W. MacCormack, *The Effect of Viscosity in Hypervelocity Impact Catering*, AIAA Paper 69-354, 1969.

[74] J. J. Riley, R. W. Metcalfe, and S. A. Orszag, "Direct numerical simulations of chemically reacting mixing layers," Phys. Fluids **29**, 406 (1986).

[75] J. J. Riley and P. A. McMurtry, "The use of direct numerical simulation in the study of turbulent chemically reacting flows," edited by R. Borghi and S. N. B. Murthy, *Turbulent Reactive Flows*, Lecture Notes in Engineering (Springer, New York, 1989), pp. 486–514.

[76] P. Givi and J. J. Riley, "Some current issues in the analysis of reacting shear layers: Computational challenges," edited by M. Y. Hussaini, A. Kumar, and R. G. Voigt, *Major Research Topics in Combustion*, (Springer, New York, 1992), pp. 588–650.

[77] P. A. McMurtry and P. Givi, "Direct numerical simulations of a reacting, turbulent mixing layer by a pseudospectral-spectral element method," edited by T. J. Chung, *Finite Elements in Fluids* (Hemisphere, Washington, D.C., 1992), Chap. 14, pp. 361–384.

[78] C. J. Steinberger, T. J. Vidoni, and P. Givi, "The compositional structure and the effects of exothermicity in a nonpremixed planar jet flame," Combust. Flame **94**, 217 (1993).

[79] R. D. Moser and M. M. Rogers, "Mixing transition and the cascade of small scales in a plane mixing layer," Phys. Fluids A **3**, 1128 (1991).

[80] R. S. Miller, C. K. Madnia, and P. Givi, "Structure of a turbulent reacting mixing layer," Combust. Sci. Technol. **99**, 1 (1994).

[81] G. Erlebacher, M. Y. Hussaini, C. G. Speziale, and T. A. Zang, "Toward the large eddy simulation of compressible turbulent flows," J. Fluid Mech. **238**, 155 (1992).

[82] L. Arnold, *Stochastic Differential Equations: Theory and Applications* (Krieger, Malbar, 1974).

[83] T. T. Soong, *Random Differential Equations in Science and Engineering* (Academic, New York, 1973).

[84] A. Leonard, "Energy cascade in large-eddy simulations of turbulent flows," Adv. Geophys. **18A**, 237 (1974).

[85] M. Germano, "A proposal for a redefinition of the turbulent stresses in the filtered Navier-Stokes equations," Phys. Fluids **29**, 2323 (1986).

[86] A. D. Leonard and F. Dai, "Applications of a coupled Monte Carlo PDF/finite volume CFD method for turbulent combustion," AIAA Paper No 94-2904, 1994.

[87] S. B. Pope, "On the relation between stochastic Lagrangian models of turbulence and second-moment closures," Phys. Fluids **6**, 973 (1994).

Appendix II

Filtered Mass Density Function for Large Eddy Simulation of Turbulent Reacting Flows

To appear in JFM (1999

Filtered Mass Density Function for Large Eddy Simulation of Turbulent Reacting Flows

F.A. Jaberi, P.J. Colucci, S. James, P. Givi
Department of Mechanical and Aerospace Engineering
State University of New York
Buffalo, NY 14260-4400

S.B. Pope
Sibley School of Mechanical and Aerospace Engineering
Cornell University
Ithaca, NY 14853-1301

Abstract

A methodology termed the "filtered mass density function" (FMDF) is developed and implemented for large eddy simulation (LES) of variable density chemically reacting turbulent flows at low Mach numbers. This methodology is based on the extension of the "filtered density function" (FDF) scheme recently proposed by Colucci *et al.* (1998) for LES of constant density reacting flows. The FMDF represents the joint probability density function of the subgrid scale (SGS) scalar quantities and is obtained by solution of its modeled transport equation. In this equation, the effect of chemical reactions appears in a closed form and the influences of SGS mixing and convection are modeled. The stochastic differential equations (SDEs) which yield statistically equivalent results to that of the FMDF transport equation are derived and are solved via a Lagrangian Monte Carlo scheme. The consistency, convergence, and accuracy of the FMDF and the Monte Carlo solution of its equivalent SDEs are assessed. In non-reacting flows, it is shown that the filtered results via the FMDF agree well with those obtained by the "conventional" LES in which the finite difference solution of the transport equations of these filtered quantities are obtained. The advantage of the FMDF is demonstrated in LES of reacting shear flows with nonpremixed reactants. The FMDF results are appraised by comparisons with data generated by direct numerical simulation (DNS) and with experimental measurements. In the absence of a closure for the SGS scalar correlations, the results based on the conventional LES are significantly different from those obtained by DNS. The FMDF results show a closer agreement with DNS. These results also agree favorably with laboratory data of exothermic reacting turbulent shear flows, and portray several of the features observed experimentally.

1 Introduction

Within the past decade, large eddy simulation (LES) of turbulent reacting flows has been the subject of widespread investigations (McMurtry *et al.*, 1992; Menon *et al.*, 1993; Gao and O'Brien, 1993; Madnia and Givi, 1993; Frankel *et al.*, 1993; Cook and Riley, 1994; Fureby and Lofstrom, 1994; Möller *et al.*, 1996; Branley and Jones, 1997; Cook *et al.*, 1997a; Cook *et al.*, 1997b; Jiménez *et al.*, 1997; Mathey and Chollet, 1997; Colucci *et al.*, 1998; DesJardin and Frankel, 1998; Jaberi and James, 1998; Réveillon and Vervisch, 1998); see Galperin and Orszag (1993); McMurtry *et al.* (1993); Libby and Williams (1994); Fox (1996); Vervisch and Poinsot (1988) for reviews. Amongst these, Colucci *et al.* (1998) recently developed a methodology, termed the "filtered density function" (FDF) based on an idea originally proposed by Pope (1990). The fundamental property of the FDF is to account for the effects of subgrid scale (SGS) scalar fluctuations in a probabilistic manner. Colucci *et al.* (1998) developed a transport equation for the FDF in constant density flows in which the effects of unresolved convection and subgrid mixing are modeled similarly to those in "conventional" LES, and Reynolds averaging procedures. This transport equation was solved numerically by a Lagrangian Monte Carlo procedure and the results were compared with those obtained by direct numerical simulation (DNS) and by a conventional finite difference LES in which the effects of SGS scalar fluctuations are ignored (LES-FD). It was shown that in non-reacting flows, the first two SGS moments of the FDF as obtained by the Monte Carlo solution are close to those obtained by LES-FD. The advantage of the FDF was demonstrated in reacting flows in which its results were shown to deviate significantly from those obtained by LES-FD but compare favorably with DNS data.

The encouraging results generated by FDF warrant its extension and application to more complex flows. Further assessment of its predictive capability is also in order. The primary objective in this work is to extend the FDF methodology for treatment of variable density reacting flows so that exothermic chemical reactions can be simulated. For that, we introduce the "filtered mass density function" (FMDF). With the definition of the FMDF, the mathematical framework for its implementation in LES of reacting flows is established. A new computational scheme is also developed for the solution of the FMDF transport equation. The results obtained by FMDF are scrutinized by comparisons with DNS and laboratory data in several turbulent reacting flows with nonpremixed reactants. The FMDF deals only with scalar quantities; the hydrodynamic field is obtained via conventional LES. Also, the formulation is based on the assumption of low Mach number. This allows consideration of exothermicity and variable density effects, but the method cannot be used for LES of very high speed flows (Drummond, 1991).

2 Governing Equations

In a compressible flow undergoing chemical reaction, the primary transport variables are the density ρ, the velocity vector u_i, $i = 1,2,3$ along the x_i direction, the total specific enthalpy h, the pressure p, and the species mass fractions Y_α ($\alpha = 1,2,\ldots,N_s$). The conservation equations governing these variables are the continuity, momentum, enthalpy (energy) and species mass fraction equations, along with an equation of state (Williams, 1985)

$$\frac{\partial \rho}{\partial t} + \frac{\partial \rho u_i}{\partial x_i} = 0 \tag{1}$$

$$\frac{\partial \rho u_j}{\partial t} + \frac{\partial \rho u_i u_j}{\partial x_i} = -\frac{\partial p}{\partial x_j} + \frac{\partial \tau_{ij}}{\partial x_i} \tag{2}$$

$$\frac{\partial \rho \phi_\alpha}{\partial t} + \frac{\partial \rho u_i \phi_\alpha}{\partial x_i} = -\frac{\partial J_i^\alpha}{\partial x_i} + \rho S_\alpha, \quad \alpha = 1,2,\ldots,\sigma = N_s + 1 \tag{3}$$

$$p = \rho R^0 T \sum_{\alpha=1}^{N_s} Y_\alpha / \mathcal{M}_\alpha = \rho \mathcal{R} T \tag{4}$$

where t represents time, R^0 is the universal gas constant and $\mathcal{M}_\alpha$ denotes the molecular weight of species α. Equation (4) effectively defines the mixture gas constant $\mathcal{R}$. Equation (3) represents the transport of the species' mass fractions and enthalpy in a common form with

$$\phi_\alpha \equiv Y_\alpha,\ \alpha = 1,2,\ldots,N_s,\quad \phi_\sigma \equiv h = \sum_{\alpha=1}^{N_s} h_\alpha \phi_\alpha \tag{5}$$

with

$$h_\alpha = h_\alpha^0 + \int_{T_0}^{T} c_{p_\alpha}(T')dT' \tag{6}$$

where T denotes the temperature, T_0 is the reference temperature and h_α^0 and c_{p_α} denote the enthalpy at T_0, and the specific heat of species α at constant pressure, respectively. At low Mach numbers and heat release rates, by neglecting the viscous dissipation and thermal radiation the source terms in the enthalpy equation $S_\sigma = \frac{1}{\rho}\frac{Dp}{Dt} \approx \frac{1}{\rho}\frac{\partial p}{\partial t}$ can be assumed to be negligible. Thus, the chemical source terms ($S_\alpha = S_\alpha(\phi), \phi = [Y_1, Y_2, \ldots, Y_{N_s}, h]$) are functions of the composition variables (ϕ). For a Newtonian fluid with zero bulk viscosity and Fickian diffusion, the viscous stress tensor τ_{ij}, mass and heat flux (J_i^α, $\alpha = 1, 2, \ldots, \sigma$) are given by

$$\tau_{ij} = \mu\left(\frac{\partial u_i}{\partial x_j} + \frac{\partial u_j}{\partial x_i} - \frac{2}{3}\frac{\partial u_k}{\partial x_k}\delta_{ij}\right), \tag{7}$$

$$J_i^\alpha = -\gamma\frac{\partial \phi_\alpha}{\partial x_i} \tag{8}$$

where μ is the dynamic viscosity and $\gamma = \rho\Gamma$ denotes the thermal and the mass molecular diffusivity coefficients. Both μ and γ are assumed constant and the Lewis number is assumed to be unity. In reactive flows, molecular processes are much more complicated than portrayed by Eq. (8). But since the molecular diffusion is typically less important than the SGS diffusion (to be defined below), this simple model is adopted with justifications and caveats given by Pope (1985); Bilger (1982).

Large eddy simulation involves the use of the spatial filtering operation (Aldama, 1990)

$$\langle f(\mathrm{x}, t)\rangle_\ell = \int_{-\infty}^{+\infty} f(\mathrm{x}', t)\mathcal{G}(\mathrm{x}', \mathrm{x})d\mathrm{x}' \tag{9}$$

where $\mathcal{G}$ denotes the filter function of width Δ_G, $\langle f(\mathrm{x}, t)\rangle_\ell$ represents the filtered value of the transport variable $f(\mathrm{x}, t)$, and $f' = f - \langle f\rangle_\ell$ denotes the fluctuations of f from the filtered value. In variable density flows it is convenient to consider the Favre filtered quantity $\langle f(\mathrm{x}, t)\rangle_L = \langle \rho f\rangle_\ell / \langle \rho\rangle_\ell$ and the fluctuation $f'' = f - \langle f\rangle_L$. We consider spatially & temporally invariant and localized filter functions, $\mathcal{G}(\mathrm{x}', \mathrm{x}) \equiv G(\mathrm{x}' - \mathrm{x})$ with the properties (Aldama, 1990), $G(\mathrm{x}) = G(-\mathrm{x})$, and $\int_{-\infty}^{\infty} G(\mathrm{x})d\mathrm{x} = 1$. Moreover, we only consider "positive" filter functions as defined by Vreman *et al.* (1994) for which all the moments $\int_{-\infty}^{\infty} x^m G(x)dx$ exist for $m \geq 0$. The application of the filtering operation to the transport equations yields

$$\frac{\partial\langle\rho\rangle_\ell}{\partial t} + \frac{\partial\langle\rho\rangle_\ell\langle u_i\rangle_L}{\partial x_i} = 0 \tag{10}$$

$$\frac{\partial\langle\rho\rangle_\ell\langle u_j\rangle_L}{\partial t} + \frac{\partial\langle\rho\rangle_\ell\langle u_i\rangle_L\langle u_j\rangle_L}{\partial x_i} = -\frac{\partial\langle p\rangle_\ell}{\partial x_j} + \frac{\partial\langle\tau_{ij}\rangle_\ell}{\partial x_i} - \frac{\partial T_{ij}}{\partial x_i} \tag{11}$$

$$\frac{\partial\langle\rho\rangle_\ell\langle\phi_\alpha\rangle_L}{\partial t}+\frac{\partial\langle\rho\rangle_\ell\langle u_i\rangle_L\langle\phi_\alpha\rangle_L}{\partial x_i}=-\frac{\partial\langle J_i^\alpha\rangle_\ell}{\partial x_i}-\frac{\partial M_i^\alpha}{\partial x_i}+\langle\rho S_\alpha\rangle_\ell,\quad \alpha=1,2,\ldots,\sigma \tag{12}$$

where $T_{ij}=\langle\rho\rangle_\ell(\langle u_iu_j\rangle_L-\langle u_i\rangle_L\langle u_j\rangle_L)$ and $M_i^\alpha=\langle\rho\rangle_\ell(\langle u_i\phi_\alpha\rangle_L-\langle u_i\rangle_L\langle\phi_\alpha\rangle_L)$ denote the subgrid stress and the subgrid mass flux, respectively. The filtered reaction source terms are denoted by $\langle\rho S_\alpha\rangle_\ell=\langle\rho\rangle_\ell\langle S_\alpha\rangle_L$ $(\alpha=1,2,\ldots,N_s)$.

Modeling of Hydrodynamic SGS Quantities

In LES of non-reacting flows the closure problem is associated with T_{ij} and M_i^α (Erlebacher *et al.*, 1992; Salvetti and Banerjee, 1995). In reacting flows, an additional model is required for the filtered reaction rate $\langle S_\alpha\rangle_L$. This is the subject of the probability formulation as described in the next section. For T_{ij}, the variable density form of the model used in our previous work (Colucci *et al.*, 1998) is considered:

$$T_{ij}=-2C_R\langle\rho\rangle_\ell\Delta_G\mathcal{E}^{1/2}\left(\langle S_{ij}\rangle_L-\frac{1}{3}\langle S_{kk}\rangle_L\delta_{ij}\right)+\frac{2}{3}C_I\langle\rho\rangle_\ell\mathcal{E}\delta_{ij} \tag{13}$$

where $\langle S_{ij}\rangle_L$ is the resolved strain rate tensor, $\mathcal{E}=|\langle u_i^*\rangle_L\langle u_i^*\rangle_L-\langle\langle u_i^*\rangle_L\rangle_{\ell'}\langle\langle u_i^*\rangle_L\rangle_{\ell'}|$, $u_i^*=u_i-\mathcal{U}_i$ and $\mathcal{U}_i$ is a reference velocity in the x_i direction. The subscript ℓ' denotes the filter at the secondary level of size $\Delta_{G'}>\Delta_G$. This model is essentially a modified version of that proposed by Bardina *et al.* (1983), which utilize equal sizes for the grid and secondary filters. We refer to this as the modified kinetic energy viscosity (MKEV) closure. Accordingly, the subgrid eddy viscosity is expressed as $\nu_t=C_R\Delta_G\mathcal{E}^{\frac{1}{2}}$. A similar diffusivity model is used for the closure of the subgrid mass flux (Eidson, 1985)

$$M_i^\alpha=-\gamma_t\frac{\partial\langle\phi_\alpha\rangle_L}{\partial x_i} \tag{14}$$

where $\gamma_t=\langle\rho\rangle_\ell\Gamma_t$, $\Gamma_t=\nu_t/Sc_t$, and Sc_t is the subgrid Schmidt number, assumed to be constant and equal to the subgrid Prandtl number. It must be emphasized here that these models are not used directly in the FMDF but the modeled FMDF transport equation is constructed to be consistent with them as discussed below.

3 The Filtered Mass Density Function (FMDF)

Let $\boldsymbol{\phi}(\mathbf{x},t)$ denote the scalar array. We define the "filtered mass density function" (FMDF), denoted by F_L, as

$$F_L(\boldsymbol{\psi};\mathbf{x},t) \equiv \int_{-\infty}^{+\infty} \rho(\mathbf{x}',t)\zeta\left[\boldsymbol{\psi},\boldsymbol{\phi}(\mathbf{x}',t)\right] G(\mathbf{x}'-\mathbf{x})d\mathbf{x}', \tag{15}$$

$$\zeta\left[\boldsymbol{\psi},\boldsymbol{\phi}(\mathbf{x},t)\right] = \delta[\boldsymbol{\psi}-\boldsymbol{\phi}(\mathbf{x},t)] \equiv \prod_{\alpha=1}^{\sigma} \delta[\psi_\alpha-\phi_\alpha(\mathbf{x},t)] \tag{16}$$

where δ denotes the delta function and $\boldsymbol{\psi}$ denotes the composition domain of the scalar array. The term $\zeta[\boldsymbol{\phi},\boldsymbol{\psi}(\mathbf{x},t)]$ is the "fine-grained" density (O'Brien, 1980; Pope, 1985), and Eq. (15) implies that the FMDF is the ***mass weighted spatially filtered*** value of the fine-grained density. The integral property of the FMDF is such that

$$\int_{-\infty}^{+\infty} F_L(\boldsymbol{\psi};\mathbf{x},t)d\boldsymbol{\psi} = \int_{-\infty}^{+\infty} \rho(\mathbf{x}',t)G(\mathbf{x}'-\mathbf{x})d\mathbf{x}' = \langle\rho(\mathbf{x},t)\rangle_\ell. \tag{17}$$

For further developments, the mass weighted conditional filtered mean of the variable $Q(\mathbf{x},t)$ is defined as

$$\langle Q(\mathbf{x},t)|\boldsymbol{\psi}\rangle_\ell \equiv \frac{\int_{-\infty}^{+\infty} \rho(\mathbf{x}',t)Q(\mathbf{x}',t)\zeta\left[\boldsymbol{\psi},\boldsymbol{\phi}(\mathbf{x}',t)\right] G(\mathbf{x}'-\mathbf{x})d\mathbf{x}'}{F_L(\boldsymbol{\psi};\mathbf{x},t)}. \tag{18}$$

Equation (18) implies

$$\begin{aligned}
&(i) && \text{For } Q(\mathbf{x},t) = c, && \langle Q(\mathbf{x},t)|\boldsymbol{\psi}\rangle_\ell = c && (19)\\
&(ii) && \text{For } Q(\mathbf{x},t) \equiv \hat{Q}(\boldsymbol{\phi}(\mathbf{x},t)), && \langle Q(\mathbf{x},t)|\boldsymbol{\psi}\rangle_\ell = \hat{Q}(\boldsymbol{\psi}) && (20)\\
&(iii) && \text{Integral property}: && \int_{-\infty}^{+\infty} \langle Q(\mathbf{x},t)|\boldsymbol{\psi}\rangle_\ell F_L(\boldsymbol{\psi};\mathbf{x},t)d\boldsymbol{\psi} && \\
&&&&& \quad = \langle\rho(\mathbf{x},t)\rangle_\ell\langle Q(\mathbf{x},t)\rangle_L && (21)
\end{aligned}$$

where c is a constant, and $\hat{Q}(\boldsymbol{\phi}(\mathbf{x},t)) \equiv Q(\mathbf{x},t)$ denotes the case where the variable Q can be completely described by the compositional variable $\boldsymbol{\phi}(\mathbf{x},t) \equiv [\phi_1,\phi_2,\ldots,\phi_\sigma]$. From these properties, it follows that the filtered value of any function of the scalar variables (such as $\rho \equiv \hat{\rho}[\boldsymbol{\phi}(\mathbf{x},t)]$ and $S_\alpha \equiv \hat{S}_\alpha[\boldsymbol{\phi}(\mathbf{x},t)]$) is obtained by integration over the composition space. It is noted that the mass weighted conditional filtered mean reduces to the conditional filtered mean (Colucci *et al.*, 1998) when the density can be completely expressed in terms of the compositional variables.

By applying the method developed by Lundgren (1969); Pope (1976); O'Brien (1980) to Eq. (3), a transport equation is obtained for the fine-grained density (Colucci *et al.*, 1998). The transport equation for $F_L(\boldsymbol{\psi}; \mathbf{x}, t)$ is obtained by multiplying the equation for the fine grained density by the filter function $G(\mathbf{x}' - \mathbf{x})$ and integrating over $\mathbf{x}'$ space. The final result after some algebraic manipulation is

$$\frac{\partial F_L(\boldsymbol{\psi}; \mathbf{x}, t)}{\partial t} + \frac{\partial[\langle u_i(\mathbf{x}, t)|\boldsymbol{\psi}\rangle_\ell F_L(\boldsymbol{\psi}; \mathbf{x}, t)]}{\partial x_i} = \frac{\partial}{\partial \psi_\alpha}\left[\left\langle \frac{1}{\hat{\rho}(\boldsymbol{\phi})} \frac{\partial J_i^\alpha}{\partial x_i} |\boldsymbol{\psi}\right\rangle_\ell F_L(\boldsymbol{\psi}; \mathbf{x}, t)\right]$$
$$- \frac{\partial[\hat{S}_\alpha(\boldsymbol{\psi}) F_L(\boldsymbol{\psi}; \mathbf{x}, t)]}{\partial \psi_\alpha}. \tag{22}$$

This is an exact transport equation for the FMDF. The last term on the right hand-side of this equation is due to chemical reaction and is in a closed form. The unclosed nature of SGS convection and mixing is indicated by the conditional filtered values. These terms are modeled in a manner consistent with Reynolds averaging and conventional LES in non-reacting flows. The convection term is decomposed via

$$\langle u_i|\boldsymbol{\psi}\rangle_\ell F_L = \langle u_i\rangle_L F_L + [\langle u_i|\boldsymbol{\psi}\rangle_\ell - \langle u_i\rangle_L] F_L. \tag{23}$$

where the second term on the right hand side denotes the influence of SGS convective flux. This term is modeled as

$$[\langle u_i|\boldsymbol{\psi}\rangle_\ell - \langle u_i\rangle_L] F_L = -\gamma_t \frac{\partial (F_L/\langle\rho\rangle_\ell)}{\partial x_i}. \tag{24}$$

The advantage of the decomposition (Eq. (23)) and the subsequent model (Eq. (24)) is that they yield results similar to that in conventional LES (Germano, 1992; Salvetti and Banerjee, 1995). The first Favre moments corresponding to Eqs. (23) and (24) are

$$\langle u_i\phi_\alpha\rangle_L = \langle u_i\rangle_L\langle\phi_\alpha\rangle_L + [\langle u_i\phi_\alpha\rangle_L - \langle u_i\rangle_L\langle\phi_\alpha\rangle_L], \tag{25}$$

$$\langle\rho\rangle_\ell[\langle u_i\phi_\alpha\rangle_L - \langle u_i\rangle_L\langle\phi_\alpha\rangle_L] = -\gamma_t \frac{\partial\langle\phi_\alpha\rangle_L}{\partial x_i}. \tag{26}$$

The term within brackets in Eq. (25) is the generalized scalar flux. This makes Eq. (26) identical to Eq. (14). The closure adopted for the SGS mixing is based on the linear mean square estimation (LMSE) model (O'Brien, 1980; Dopazo and O'Brien, 1976), also known as the IEM (interaction by exchange with the mean) (Borghi, 1988)

$$\frac{\partial}{\partial \psi_\alpha}\left[\left\langle -\frac{1}{\hat{\rho}}\frac{\partial}{\partial x_i}\left(\gamma \frac{\partial \phi_\alpha}{\partial x_i}\right)|\psi\right\rangle_\ell F_L\right] = \frac{\partial}{\partial x_i}\left(\gamma \frac{\partial (F_L/\hat{\rho})}{\partial x_i}\right) + \frac{\partial}{\partial \psi_\alpha}\left[\Omega_m(\psi_\alpha - \langle \phi_\alpha\rangle_L)F_L\right], \quad (27)$$

where $\Omega_m(\mathbf{x}, t)$ is the "frequency of mixing within the subgrid" which is not known *a priori*. This frequency is modeled as $\Omega_m = C_\Omega(\gamma + \gamma_t)/(\langle \rho\rangle_\ell \Delta_G^2)$. For the first term on the right hand side of Eq. (27) an additional minor assumption is made:

$$\frac{\partial}{\partial x_i}\left(\gamma \frac{\partial (F_L/\hat{\rho})}{\partial x_i}\right) \approx \frac{\partial}{\partial x_i}\left(\gamma \frac{\partial (F_L/\langle \rho\rangle_\ell)}{\partial x_i}\right). \quad (28)$$

This assumption is not necessary for the treatment of FMDF and is only adopted to establish consistency between the FMDF and the conventional LES. With these approximations, the modeled FMDF transport equation is

$$\frac{\partial F_L}{\partial t} + \frac{\partial[\langle u_i\rangle_L F_L]}{\partial x_i} = \frac{\partial}{\partial x_i}\left[(\gamma + \gamma_t)\frac{\partial (F_L/\langle \rho\rangle_\ell)}{\partial x_i}\right] + \frac{\partial}{\partial \psi_\alpha}\left[\Omega_m(\psi_\alpha - \langle \phi_\alpha\rangle_L)F_L\right] - \frac{\partial[\hat{S}_\alpha F_L]}{\partial \psi_\alpha}. \quad (29)$$

This equation may be integrated to obtain transport equations for the SGS moments. The equations for the first subgrid Favre moment, $\langle \phi_\alpha\rangle_L$, and the generalized subgrid variance, $\sigma_\alpha^2 = \langle \phi_{(\alpha)}^2\rangle_L - \langle \phi_{(\alpha)}\rangle_L^2$ are

$$\frac{\partial(\langle \rho\rangle_\ell \langle \phi_\alpha\rangle_L)}{\partial t} + \frac{\partial(\langle \rho\rangle_\ell \langle u_i\rangle_L \langle \phi_\alpha\rangle_L)}{\partial x_i} = \frac{\partial}{\partial x_i}\left[(\gamma + \gamma_t)\frac{\partial \langle \phi_\alpha\rangle_L}{\partial x_i}\right] + \langle \rho\rangle_\ell \langle S_\alpha\rangle_L \quad (30)$$

$$\begin{aligned}\frac{\partial(\langle \rho\rangle_\ell \sigma_\alpha^2)}{\partial t} + \frac{\partial(\langle \rho\rangle_\ell \langle u_i\rangle_L \sigma_\alpha^2)}{\partial x_i} &= \frac{\partial}{\partial x_i}\left[(\gamma + \gamma_t)\frac{\partial \sigma_\alpha^2}{\partial x_i}\right] + 2(\gamma + \gamma_t)\left[\frac{\partial \langle \phi_{(\alpha)}\rangle_L}{\partial x_i}\frac{\partial \langle \phi_{(\alpha)}\rangle_L}{\partial x_i}\right] \\ &- 2\Omega_m \langle \rho\rangle_\ell \sigma_\alpha^2 + 2\langle \rho\rangle_\ell \left(\langle \phi_{(\alpha)} S_{(\alpha)}\rangle_L - \langle \phi_{(\alpha)}\rangle_L \langle S_{(\alpha)}\rangle_L\right) \quad (31)\end{aligned}$$

where the subscripts in parenthesis are excluded from the summation convention. These equations are identical to those which can be derived by filtering Eq. (3) directly, and employing consistent closures for the subgrid flux and the dissipation. In such direct moment closure formulation, however, the terms involving $\langle S_\alpha \rangle_L$ remain unclosed.

4 Monte Carlo Solution of the FMDF

The Lagrangian Monte Carlo procedure (Pope, 1985) is employed for the solution of Eq. (29). In this procedure, each of the Monte Carlo elements (particles) obeys certain equations which govern their transport. These particles undergo motion in physical space by convection due to the filtered mean flow velocity and diffusion due to molecular and subgrid diffusivities. The compositional values of each particles are changed due to mixing and reaction. The spatial transport of the FMDF is represented by the general diffusion process governed by the stochastic differential equation (SDE) (Risken, 1989; Gardiner, 1990)

$$dX_i(t) = D_i(\mathbf{X}(t), t)dt + E(\mathbf{X}(t), t)dW_i(t) \tag{32}$$

where X_i is the Lagrangian position of a stochastic particle, D_i and E are the "drift" and "diffusion" coefficients, respectively, and W_i denotes the Wiener process (Karlin and Taylor, 1981). The drift and diffusion coefficients are obtained by comparing the Fokker-Plank equation corresponding to Eq. (32) with the spatial derivative terms in the FMDF transport equation (Eq. (29)),

$$E \equiv \sqrt{2(\gamma + \gamma_t)/\langle \rho \rangle_\ell}, \quad D_i \equiv \langle u_i \rangle_L + \frac{1}{\langle \rho \rangle_\ell} \frac{\partial(\gamma + \gamma_t)}{\partial x_i}. \tag{33}$$

The subgrid mixing and reaction terms are implemented by altering the compositional makeup of the particles

$$\frac{d\phi_\alpha^+}{dt} = -\Omega_m(\phi_\alpha^+ - \langle \phi_\alpha \rangle_L) + \hat{S}_\alpha(\phi^+) \tag{34}$$

where $\phi_\alpha^+ = \phi_\alpha(\mathbf{X}(t), t)$ denotes the scalar value of the particle with the Lagrangian position vector X_i. The solutions of Eqs. (32) and (34) yield the same statistics as those obtained directly from the solution of FMDF transport equation according to the principle of ***equivalent systems*** (Pope, 1985; Pope, 1994).

Numerical Solution Procedure

A new computational algorithm is developed for the solution of the FMDF. While the algorithm is similar to that used in PDF methods (Pope, 1985), it is not exactly the same. Therefore, a detailed description is provided.

The complete numerical solution of the equations governing the resolved field is based on a hybrid scheme in which the hydrodynamic Favre filtered equations (Eqs. (10)-(11)) are integrated by a finite difference method and the filtered scalar field is simulated by the Monte Carlo solution of the FMDF transport equation. The LES of the hydrodynamic variables, which also determines the subgrid viscosity and scalar diffusion coefficients, is conducted with the "compact parameter" scheme of Carpenter (1990). This scheme is based on a hyperbolic solver which considers a fully compressible flow. Here, the simulations are conducted at a low Mach number to minimize compressibility effects. All the finite difference operations are conducted on a fixed and uniform grid. Thus, the filtered values of the hydrodynamic variables are determined on these grid points. The transfer of information from these points to the location of the Monte Carlo particles (described below) is conducted via interpolation. Both fourth-order and second-order (bilinear) interpolations schemes were considered, but no significant differences in filtered quantities were observed. The results presented below utilize fourth- and second-order interpolation for two-dimensional (2D) and 3D simulations, respectively.

The FMDF is represented by an ensemble of Monte Carlo particles, each with a set of scalars $\phi_\alpha^{(n)}(t) = \phi_\alpha(\mathbf{X}^{(n)}(t), t)$ and Lagrangian position vector $\mathbf{X}^{(n)}$. A splitting operation is employed in which transport in the physical and compositional domains are treated separately. The simplest means of simulating Eq. (32) is via the Euler-Maruyamma approximation (Kloeden and Platen, 1995): $X_i^{(n)}(t_{k+1}) = X_i^{(n)}(t_k) + D_i^{(n)}(t_k)\Delta t + E^{(n)}(t_k)(\Delta t)^{1/2}\xi_i^{(n)}(t_k)$, where $\Delta t = t_{k+1} - t_k$ is the computational time increment between two consecutive discretized time levels, $D_i^{(n)}(t) = D_i(\mathbf{X}^{(n)}(t), t)$, $E^{(n)}(t) = E(\mathbf{X}^{(n)}(t), t)$ and $\xi_i^{(n)}$ is a random variable with the standard Gaussian PDF. The coefficients D_i and E require the input of the filtered mean velocity and the diffusivity (molecular and subgrid). These are provided by finite difference solution of Eqs. (10)-(11).

The compositional values are subject to change due to SGS mixing and chemical reaction.

Equation (34) may be integrated numerically to simulate these effects simultaneously. Alternately, this equation is treated in a split manner. This provides an analytical expression for the subgrid mixing. Subsequently, the influence of chemical reaction is determined by evaluating the fine grained reaction rates $S_\alpha^{(n)} = \hat{S}_\alpha(\phi^{(n)})$ and modifying the composition. The mixing model requires the Favre filtered scalar values. These and other higher moments of the FMDF at a given point are estimated by consideration of particles within a volume centered at the point of interest. Effectively, this finite volume constitutes an "ensemble domain" characterized by the length scale Δ_E (not to be confused with Δ_G) in which the FMDF is discretely represented. A box of size Δ_E is used to construct the statistics at the finite difference nodes. These are then interpolated to the particle positions. Since the SGS mixing model only requires the input of the filtered scalar values, and not their derivative, this volume averaging is sufficient. From a numerical standpoint, specification of the size of the ensemble domain is an important issue. Ideally, it is desired to obtain the statistics from the Monte Carlo solution when the size of sample domain is infinitely small ($\Delta_E \to 0$) and the number of particles within this domain is infinitely large. With a finite number of particles, if Δ_E is small there may not be enough particles to construct reliable statistics. A larger ensemble domain decreases the statistical error, but increases the spatial error which manifests itself in artificially diffused statistical results. This compromise between the statistical accuracy and dispersive accuracy as pertaining to Lagrangian Monte Carlo schemes implies that the optimum magnitude of Δ_E cannot, in general, be specified *a priori* (Pope, 1985; Colucci *et al.*, 1998). This does not diminish the capability of the scheme, but exemplifies the importance of the parameters which govern the statistics.

In an attempt to reduce the computational overhead, a procedure involving the use of non-uniform weights is also considered. This procedure allows a smaller number of particles to be imposed in regions where a low degree of variability is expected. Conversely, in regions of highly varying character, a larger number of particles is allowed. This is akin to grid compression in finite difference (or finite volume) schemes. Operationally, the particles evolve with a discrete FMDF,

$$F_N(\psi; \mathbf{x}, t) = \Delta m \sum_{n=1}^{N} w^{(n)} \delta(\psi - \phi^{(n)}) \delta(\mathbf{x} - \mathbf{x}^{(n)}) \tag{35}$$

where $w^{(n)}$ is the weight of the n^{th} particle and Δm is the mass of a particle with unit weight.

The FMDF is the expectation of the discrete FMDF

$$
\begin{aligned}
F_L(\psi; \mathbf{x}, t) &= \Delta m \sum_{n=1}^{N} \langle w^{(n)} \delta(\psi - \phi^{(n)}) \delta(\mathbf{x} - \mathbf{x}^{(n)}) \rangle \\
&= \Delta m \langle w^{(n)} \delta(\psi - \phi^{(n)}) \delta(\mathbf{x} - \mathbf{x}^{(n)}) \rangle
\end{aligned} \tag{36}
$$

for any n $(1 \leq n \leq N)$. The brackets without the subscript L represent ensemble averaging. With integration of this expression over the composition domain within an infinitesimal volume, it is possible to demonstrate

$$
\langle \rho \rangle_\ell \approx \frac{\Delta m}{\Delta V} \sum_{n \in \Delta_E} w^{(n)}, \tag{37}
$$

where ΔV is the volume of the ensemble domain. The Favre filtered value of a transport quantity $\hat{Q}(\phi)$ is constructed from the weighted average

$$
\langle Q \rangle_L \approx \frac{\sum_{n \in \Delta_E} w^{(n)} \hat{Q}(\phi^{(n)})}{\sum_{n \in \Delta_E} w^{(n)}}. \tag{38}
$$

The approximations in Eqs. (37) - (38) are exact in the limit $\Delta_E \rightarrow 0$ and the number of particles within the ensemble domain becomes infinite (Pope, 1985). Equation (37) implies that the filtered fluid density is directly proportional to the sum of the weights in the ensemble domain. With uniform weights, $\langle \rho \rangle_\ell \approx \frac{\Delta m}{\Delta V} N_E$ and $\langle Q \rangle_L \approx \frac{1}{N_E} \Sigma \hat{Q}(\phi^{(k)})$ (Pope, 1985) where N_E is the number of particles in the ensemble domain. Hence, with uniform weights, the particle number density decreases significantly in regions of high temperature. The implementation of variable weights allows the increase of the particle number density without a need to increase the number density outside of the reaction zone.

To evaluate the chemical source terms, the fine grained values of the temperature $(T^{(n)})$ for all particles are calculated from the composition variable $\phi^{(n)} \equiv [Y_1^{(n)}, Y_2^{(n)}, \ldots, Y_{N_s}^{(n)}, h^{(n)}]$ and the fine grained values of density $(\rho^{(n)})$ are determined from evaluation of the equation of state at the reference pressure p_0. The filtered pressure is obtained by the filtered equation of state, $\langle p \rangle_\ell = \langle \rho \rangle_\ell \langle \mathcal{R} T \rangle_L$. In this equation $\langle \rho \rangle_\ell$ is obtained from the finite difference solver and the correlation $\langle \mathcal{R} T \rangle_L$ is obtained by ensemble averaging in the Monte Carlo solver. In this way, the coupling between the hydrodynamic and the scalar fields is taken into account and allows the investigation of the effects of variable density. The results obtained by this scheme are identified by the label FMDF-1.

The pressure ($\langle p \rangle_\ell$) field as determined by the above procedure exhibits some spatial oscillations caused by statistical error. Since the spatial derivatives of $\langle p \rangle_\ell$ are required in the hydrodynamic solver, these oscillations can cause numerical difficulties. This is particularly exacerbated by the nature of the compressible hydrodynamic code which allows propagation of these oscillations throughout the computational domain. Our results shown below indicate that while the extent of noise in the pressure field is noticeable, it is not significant in the compositional variables. The amplitudes of the oscillations can be decreased by smoothing of the $\langle \mathcal{R}T \rangle_L$ field. An alternate procedure is also followed in which the correlation $\langle \mathcal{R}T \rangle_L$ is evaluated by the finite difference solution of its transport equation. With the assumption of constant $\mathcal{R}$, only the solution of the Favre filtered temperature equation is required. The reaction source term in this equation is evaluated from the Monte Carlo solution. The results obtained by this scheme are identified by the label FMDF-2. While the finite difference solution of the filtered temperature is used to calculate the filtered pressure in FMDF-2, the filtered temperature can also be evaluated directly from the Monte Carlo particles. The results below indicate that the filtered temperature fields obtained by the two methods are nearly identical.

In addition, another LES is also considered in which the modeled transport equations for the filtered scalar and the generalized SGS scalar variance are simulated with the finite difference scheme. The hydrodynamic solver and the models for the subgrid stress and mass flux are identical to those in FMDF, but the effects of SGS fluctuations in the filtered reaction rate are ignored. That is, Eqs. (30)-(31) are solved via the finite difference scheme with the assumption $\langle \hat{S}_\alpha(\phi) \rangle_L = \hat{S}_\alpha(\langle \phi \rangle_L)$. The results based on this scheme are referred to as LES-FD. A variant of this model, in which the filtered reaction rate is modeled by $\langle \hat{S}_\alpha(\phi) \rangle_L = \langle \hat{S}_\alpha(\langle \phi \rangle_L) \rangle_L$ was also considered. However this closure did not show any improvements over LES-FD; thus is not discussed. For non-reacting flows, the LES-FD results are used to demonstrate the consistency of the FMDF results. For reacting flows, the difference between FMDF and LES-FD demonstrates the effects of the SGS fluctuations. However, this comparison does not imply that these two methods are the only means of performing LES of reacting flows; several other schemes are currently available as indicated in Section 1.

Table 1: Attributes of the Computational Methods.

Method	Mean Field Equations	Particle Properties	Particle Fields Used in the Mean Field Equations	Duplicate Fields
LES-FD	$\langle\rho\rangle_\ell$, $\langle u_i\rangle_L$, $\langle\phi\rangle_L$	–	–	–
FMDF-1	$\langle\rho\rangle_\ell$, $\langle u_i\rangle_L$	ϕ, $\hat{\rho}(\phi)$, $\hat{\mathcal{R}}(\phi)$,$\hat{T}(\phi)$	–	$\langle\rho\rangle_\ell$
FMDF-2	$\langle\rho\rangle_\ell$, $\langle u_i\rangle_L$, $\langle\mathcal{R}T\rangle_L$	ϕ, $\hat{\rho}(\phi)$, $\hat{\mathcal{R}}(\phi)$,$\hat{T}(\phi)$	$\langle S_{\mathcal{R}T}\rangle_L$	$\langle\rho\rangle_\ell$, $\langle\mathcal{R}T\rangle_L$

It is noted that the FMDF-1 simulation procedure is similar to that typically used in PDF methods (Pope, 1985; Tolpadi *et al.*, 1995; Tolpadi *et al.*, 1996). The procedure described in FMDF-2 is proposed here for the first time. It is shown below that the pressure field as determined by this method exhibits almost no spatial oscillations, thus no smoothing is required. This scheme is starting to replace the equivalent of FMDF-1 in PDF methods (Pope, 1997). The attributes of the LES-FD, FMDF-1 and FMDF-2 schemes are outlined in Table 1. In this table, $S_{\mathcal{R}T}$ denotes the source term in the equation governing the transport of $\mathcal{R}T$.

5 Results

5.1 Flows Simulated

The simulations of the following flow configurations are considered:

1. A two-dimensional (2D) temporally developing mixing layer.
2. A 3D temporally developing mixing layer.
3. A 2D spatially developing planar jet.
4. A 2D spatially developing mixing layer.

The objectives of the numerical simulations are to: (i) demonstrate the consistency of the Monte Carlo solution procedure, (ii) demonstrate the capabilities of the FMDF, (iii) appraise its overall performance, and (iv) highlight its deficiencies. The flow configurations (1),(3) and (4) are suitable for objectives (i) and (ii) in which 2D simulations are sufficient. However, objectives (iii) requires 3D simulations. All flow configurations are used for objective (iv). The 2D simulations are conducted to allow extensive computations for assessing the consistency and accuracy of the FMDF and the convergence of the Monte Carlo results. Both non-reacting and reacting flows are simulated, and FMDF and LES-FD are applied to the cases itemized in (1)-(3). Some of these cases are also treated by DNS, the results of which are used to assess the performance of the FMDF. Further appraisal is made by comparison with laboratory data for the flow under item (4).

The temporal mixing layer consists of two co-flowing streams traveling in opposite directions with the same speed (Riley *et al.*, 1986; Jou and Riley, 1989; Givi, 1989). The reactants $\mathcal{A}$ and $\mathcal{B}$ are introduced into the top and the bottom streams, respectively. The length in the streamwise direction is large enough to allow for the roll-up of two large vortices and one (subsequent) pairing of these vortices. In 3D simulations, the length of the domain in spanwise direction is 60% of that in the streamwise direction. The layer is forced via both 2D and 3D forcing functions (Moser and Rogers, 1991; Miller *et al.*, 1994; Givi, 1994). The initial values of the reactants $\mathcal{A}$ and $\mathcal{B}$ at each spanwise location in 3D simulations are identical to those in 2D. In the figures presented below, x, y, z correspond to the streamwise, cross-stream and spanwise directions (in 3D), respectively in all the simulations.

In the planar jet, the reactant $\mathcal{A}$ is issued from a jet of width D into a co-flowing stream with a lower velocity carrying reactant $\mathcal{B}$ (Givi and Riley, 1992; Steinberger *et al.*, 1993). The size of the domain in the jet flow is $0 \leq x \leq 14D$, $-3.5D \leq y \leq 3.5D$. The ratio of the co-flowing stream velocity to that of the jet at the inlet is kept fixed at 0.5. A double-hyperbolic tangent profile is utilized to assign the velocity distribution at the inlet plane. The formation of the large scale coherent structures are expedited by imposing low amplitude perturbations at the inlet. The frequency of these perturbations correspond to the most unstable mode and subharmonics of this mode as determined by the linear stability analysis of spatially evolving disturbances (Michalke, 1965; Colucci, 1994). The characteristic boundary condition procedure developed by Poinsot and Lele (1992) is used at the inlet. This procedure facilitates evaluation of incoming waves which are necessary to satisfy the continuity equation. Zero derivative boundary conditions are used at the free-streams and the pressure boundary condition of Rudy and Strikwerda (1980) is used at the outflow.

The flow configuration in (4) is the one considered in the laboratory experiments of Mungal and Dimotakis (1984). In these experiments, a heat releasing reacting planar mixing layer composed of diatomic hydrogen in one stream and diatomic fluorine in the other stream is considered. Both reactants are diluted in nitrogen with the level of dilution determining the extent of heat release. While the laboratory flow, like all turbulent flows, is inherently 3D, it is dominated by large scale 2D structures (Brown and Roshko, 1974; Givi and Riley, 1992; Givi, 1994). We demonstrate that 2D simulations are sufficient to capture the hydrodynamics features of this flow reasonably well. The computational domain considers the region 54.84 *cm* × 27.42 *cm*, which covers the whole region considered experimentally including $x = 45.7$ *cm* where measured data are reported. In order to mimic a "naturally" developing shear layer, a modified variant of the forcing procedure suggested by Sandham and Reynolds (1989) is utilized. The cross-stream velocity component at the inlet is forced at the most unstable mode as well as four harmonics (both sub- and super-) of this mode. A spatial linear stability analysis was performed to determine the most unstable mode of the hyperbolic velocity profile imposed at the inlet. Sandham and Reynolds (1989) suggest the use of a random phase shift to "jitter" the layer and to prevent a periodic behavior. A similar random phase shift procedure is imposed here; a discrete approximation of the Wiener process is applied for the phase shift at each time increment.

The flow variables are normalized with respect to selected reference quantities, denoted by the subscript r. In the temporal mixing layer, the reference quantities are the free-stream values and the reference length L_r is defined such that $\frac{\delta_{v0}}{L_r} = 2.83$, where δ_{v0} is the initial vorticity thickness ($\delta_v = \frac{\Delta U}{\left[\partial \overline{\langle u_1 \rangle_L} / \partial y\right]_{max}}$, where $\overline{\langle u_1 \rangle_L}$ is the Reynolds averaged value of the Favre filtered streamwise velocity and ΔU is the velocity difference across the layer). In the spatial flows, normalization is performed with respect to the values in the high speed stream. In the planar jet $L_r = D$. In the hydrogen-fluorine mixing layer, L_r is equal to the distance from the virtual origin to the downstream measuring station in the experiment. These quantities are used to define the Reynolds number $Re = \frac{\rho_r U_r L_r}{\mu}$. For the temporal mixing layer, the Reynolds number in terms of the total velocity difference across the layer ($\Delta U = 2U_r$) is $Re_{\delta_{v0}} = 5.66 Re$. The non-dimensional time is given by $t^* = \frac{U_r t}{L_r}$.

5.2 Reaction Mechanisms

For the flow configurations (1)-(3), the reaction scheme is of the type $\mathcal{A} + \mathcal{B} \rightarrow \mathcal{P}$ with an Arrhenius reactant conversion, $S_{\mathcal{A}} = S_{\mathcal{B}} = -\rho k_f AB \exp(-E_a/RT)$, where k_f is the pre-exponential factor, E_a is the activation energy, and A, B denote the mass fractions of species $\mathcal{A}$, $\mathcal{B}$, respectively. The species $\mathcal{A}, \mathcal{B}, \mathcal{P}$ are assumed thermodynamically identical and the fluid is assumed to be calorically perfect. The normalized reaction rate is $S^*_{\mathcal{A}} = -\rho^* Da AB \exp(-Ze/T^*)$ in which $Ze = E_a/RT_r$ and $Da = \frac{k_f \rho_r}{U_r/L_r}$ denote the Zeldovich number and the Damköhler number, respectively. T_r denotes the reference ambient temperature. The degree of exothermicity is parameterized by the non-dimensional heat release parameter $Ce = \frac{-\Delta h^0_{\mathcal{P}}}{c_p T_r}$ where $\Delta h^0_{\mathcal{P}}$ is the heat of reaction. Both constant rate and temperature dependent reactions are considered.

The reaction mechanism associated with the mixing layer experiment is more complex. The hydrogen-fluorine reaction can be represented by the reaction (Mungal and Dimotakis, 1984)

$$H_2 + F_2 \rightarrow 2HF, \quad \Delta Q = 65 \text{ kcal/mol}, \tag{39}$$

where ΔQ is the heat of reaction. This reaction belongs to the more general family of hydrogen-halogen reactions (Spalding and Stephenson, 1971; Chelliah, 1989). The heat released in a mixture containing 1% mole fraction of F_2 and 1% mole fraction of H_2 diluted in nitrogen results in an adiabatic temperature of $93K$ above the ambient (Mungal and Dimotakis, 1984). The global representation in Eq. (39) is composed of a pair of second-order chain reactions (Mungal and Dimotakis, 1984)

$$H_2 + F \xrightarrow{k_1} HF + H, \quad \Delta Q = 32 \text{ kcal/mol}, \quad k_1 = 2.6 \times 10^{12} T^{0.5} \exp\left(\frac{-610}{R^0 T}\right), \tag{40}$$

$$H + F_2 \xrightarrow{k_2} HF + F, \quad \Delta Q = 98 \text{ kcal/mol}, \quad k_2 = 3 \times 10^{9} T^{1.5} \exp\left(\frac{-1,680}{R^0 T}\right), \tag{41}$$

where the reaction rate constants k_1 and k_2 are given in units of cm^3/(mol s), T in K, and the universal gas constant R^0 in cal/(mol K). At low concentrations of the H atom, the reverse of the first of these two reactions is slow. Additionally, the rate data suggest that the reverse of the second reaction is also negligible as compared to the forward reaction (Chelliah, 1989).

The explosion limits for the hydrogen-fluorine reaction indicate that a mixture of these two gases at typical ambient conditions is stable (Chen *et al.*, 1975; Gmelin, 1980). Therefore, in order to initiate reaction, a source of F atoms must be provided (Mungal and Dimotakis, 1984). Experimentally, this is accomplished by uniformly mixing a small amount of nitric oxide with the hydrogen-nitrogen mixture. The nitric oxide reacts with the fluorine to produce free fluorine atoms

$$NO + F_2 \xrightarrow{k_3} NOF + F, \quad \Delta Q = 18 \text{ kcal/mol}, \quad k_3 = 4.2 \times 10^{11} \exp\left(\frac{-1150}{T}\right). \qquad (42)$$

The reverse of this reaction may be neglected (Rapp and Johnston, 1960). An additional reaction serves to limit the nitric oxide concentration (Baulch *et al.*, 1981; Cool *et al.*, 1970)

$$F + NO + M \xrightarrow{k_4} NOF + M, \quad \Delta Q = 57 \text{ kcal/mol}, \quad k_4 \approx 3 \times 10^{16} \text{ cm}^6/(\text{mol}^2\text{s}). \qquad (43)$$

While it is necessary to add nitric oxide to initiate reaction, the addition of excessive amounts would deplete the availability of the free F atoms. Mungal and Dimotakis (1984) indicate that keeping the product of nitric oxide and diatomic fluorine molar concentrations at 0.03% results in a rapid combustion. It was also noted that an increase of 50% in the nitric oxide concentration results in no appreciable changes in the temperature. This suggests that the hydrogen-fluorine reaction can be approximated by the limit of infinite rate chemistry. In the simulations, therefore, both finite and infinite rate models are considered. Due to the very fast rate of the reaction, the compositional change due to reaction is implemented in 10 incremental time steps for every hydrodynamic time step. These simulations with stiff reaction rates are obviously computationally intensive. The implementation of the infinite rate chemistry model (Williams, 1985) is significantly less expensive. With this approximation, it may be possible to employ the assumed FDF approach (Madnia and Givi, 1993). However, in order to demonstrate the operationally of the FMDF, here this procedure is employed for both finite and infinite rate models.

5.3 Numerical Specifications

The magnitude of the flow parameters considered in DNS are dictated by the resolution which can be afforded. The primary parameters are Re, Da, Ze, Ce, Sc, and Pr. In all simulations $Sc = Pr = 1$. All finite difference simulations (in both DNS and LES) are conducted on equally-spaced grid points ($\Delta x = \Delta y = \Delta z$ (for 3D) $= \Delta$). The highest resolution in DNS of the 2D temporal mixing layer consists of 433×577 grid points which allows reliable calculations at $Re = 2,000$, $Ce = 5$, $Ze = 8$, and $Da = 11.92$. The DNS of the 3D temporal shear layer is conducted with a resolution of $217 \times 289 \times 133$ grid points with $Re = 400$, $Da = 1$ and $Ce = Ze = 0$. The DNS of the planar jet is performed on 1201×601 grid points and allows accurate simulations with $Re = 10,000$, $Ce = 2.5$, $Ze = 8$ and $Da = 119.2$. The FMDF and LES-FD are conducted with lower grid resolutions. The LES of the temporal mixing layer is conducted on 37×49 and 55×73 grid points for 2D simulations while resolutions of $37 \times 49 \times 23$ and $55 \times 73 \times 34$ are utilized in 3D. The LES of the spatial jet and hydrogen-fluorine mixing layer are conducted on 201×101 grid points. A top-hat filter function (Aldama, 1990) of the form

$$G(\mathbf{x}' - \mathbf{x}) = \prod_{i=1}^{N_d} \hat{G}(x_i' - x_i)$$

$$\hat{G}(x_i' - x_i) = \begin{cases} \frac{1}{\Delta_G} & |x_i' - x_i| \leq \frac{\Delta_G}{2} \\ 0 & |x_i' - x_i| > \frac{\Delta_G}{2} \end{cases} \tag{44}$$

is used with $\Delta_G = 2\Delta$ and N_d denotes the number of dimensions. No attempt is made to investigate the sensitivity of the results to the filter function (Vreman *et al.*, 1994) or the filter size (Erlebacher *et al.*, 1992).

For FMDF simulations of the temporal mixing layer, the Monte Carlo particles are initially distributed throughout the computational region. For the jet flow, the particles are supplied in the inlet region $-1.75D \leq y \leq 1.75D$. As the particles convect downstream, this zone distorts as it conforms to the flow as determined by the hydrodynamic field. In regions populated with particles, $\sum_{n \in \Delta_E} w^{(n)}$ remains proportional to the instantaneous filtered density (within statistical error). In regions without particles, a delta function FDF corresponding to the free-stream composition is enforced. The simulation results are monitored to ensure the particles fully encompass and extend well beyond regions of non-zero vorticity and reaction. In the temporal mixing layer, due to flow periodicity in the streamwise and spanwise directions, if the particle leaves the domain at one of the boundaries new particles are introduced at the other boundary with the same compositional values. In the spatially evolving jet and the planar mixing layer, new particles are introduced at the inlet at a rate corresponding to the desired (imposed) local particle number density and fluid velocity. In some of the planar jet simulations and all of the hydrogen-fluorine mixing layer simulations, variable particle weights are employed. With prescription of the filtered fluid density, the particle weight is adjusted to yield the proper mass flux across the boundary. All other simulations utilize uniform weights. The sensitivity of the statistical results to the number of particles per grid cell (NPG) and the size of the ensemble domain is studied in the temporal mixing layer. The following sizes are considered: $\Delta_E = 2\Delta,\ \Delta, \Delta/2$.

In the FMDF simulation of the experimental mixing layer configuration, initially $NPG = 5$ in the free-streams and gradually increases in the cross steam direction peaking to $NPG = 25$ at the splitter plate ($y = 0$). This yields 20 to 100 sample points per ensemble for $\Delta_E = 2\Delta$. The particles are supplied in the region $-0.12L_r \leq y \leq 0.12L_r$ where $L_r = 45.7\ cm$. The composition of incoming particles is set according to composition of the fluid at the point of entry. The magnitudes of the Reynolds, Peclet, Damköhler and Zeldovich numbers and the velocity ratio across the layer in the simulations are the same as those in the experiment, but the maximum value of the Mach number in the simulations is 0.31 which is higher than that in the experiment. This was necessary in the compressible flow solver employed for the simulations. With the values of the physical parameters in this experiment, it is not possible to employ DNS and LES-FD for this flow, thus only FMDF results are compared with experimental data. For that FMDF-1 is used in which smoothing of $\langle \mathcal{R}T \rangle_L$ is done with a box filter consisting of 3×3 grid points with equal weights.

The simulated results are analyzed both instantaneously and statistically. In the former, the instantaneous contours (snap-shots) and the scatter plots of the scalar values are considered. In the latter, the "Reynolds-averaged" statistics are constructed form the instantaneous data. In the temporal mixing layer, the statistics are constructed by the ensemble from all the grid points in the homogeneous direction(s) x (and z in 3D). In the spatially developing mixing layer and the jet flow, averaging is conducted via time sampling. All Reynolds averaged results are denoted by an overbar. In the presentations below, the asterisk (denoting the normalized quantities) is dropped.

5.4 Model Parameters

In the implementation of the MKEV, the magnitude of the reference velocity $\mathcal{U}_i$ is set to zero in the cross-stream and spanwise directions, and to the average of the high and low speed streams in the streamwise direction. Additionally, the ratio of the filter size at the secondary level to that at the grid level is $\Delta_{G'}/\Delta_G = 3$. In all simulations $C_I = 0.006$. The magnitude of C_R is 0.020 and 0.013 for 2D and 3D, respectively. The subgrid mass flux is modeled via Eq. (14). In all cases except LES of the hydrogen-fluorine mixing layer, $Pr_t = Sc_t = 0.7$. No attempt is made to determine the magnitudes of these model constants in a dynamic manner (Germano, 1992). The subgrid mixing model requires the input of the constant C_Ω which also determines the SGS variances. The value $C_\Omega = 4$ is used in most simulations. In the hydrogen-fluorine configuration $Sc_t = Pr_t = 0.4$ and $C_\Omega = 6$. Some constant density test simulations are also conducted in which $C_\Omega = 3$ as previously used by Colucci *et al.* (1998). The non-universality (flow dependence) of the hydrodynamic model constants (C_I, C_R, Pr_t, Sc_t) has been well recognized and was expected here. The additional constant introduced by FMDF is C_Ω, although this constant also appears if the SGS variance is considered in the conventional LES-FD. This non-universality, in general, diminishes the predictive capability of LES; however the range of the values as considered here is not very broad.

5.5 Consistency of FMDF

The objective in the results presented in this subsection is to demonstrate the consistency of the FMDF formulation. For this purpose, the LES results via FMDF and LES-FD are compared against each other in 2D and 3D temporal mixing layers. Since the accuracy of the finite difference scheme is well-established, this comparative analysis provides a means of assessing the performance of the Monte Carlo solution of the FMDF. For most of the results in this section, $NPG = 50$ in 2D and $NPG = 20$ in 3D at locations where $\langle \rho \rangle_\ell = 1$. In 2D, $\Delta_E = \Delta$ and in 3D, $\Delta_E = 2\Delta$. Several additional simulations are also performed with varying values of NPG and Δ_E to asses their effects.

Simulations of 2D non-reacting temporally developing mixing layers are conducted in which the flow is initiated with non-uniform density and temperature distributions. The initial filtered density is distributed as a "spike" at the middle of the layer. With uniform weights assigned to the Monte Carlo particles, the particle number density must remain proportional to the fluid density. This is observed in Fig. 1, where it is demonstrated that the filtered density evaluated from the Monte Carlo particles matches very well with that of the finite difference calculated values at the Eulerian grid points. The values generated by the finite difference solution are identified by FD and the results generated by ensemble averaging of the Monte Carlo particles are identified by MC. Figure 1 shows that at the final time of the simulation (when the flow has experienced the pairing of two neighboring vortices) the Reynolds averaged filtered density calculated by the finite difference and the Monte Carlo procedures are very close. The particle number density exhibits an appreciable degree of oscillations due to statistical errors associated with a finite sample of particles.

Figure 2 shows the temporal evolution of the vorticity thickness. When the flow starts with uniform density, the effect of thermodynamic quantities on the hydrodynamics is negligible. Thus the δ_v profiles as obtained by FMDF-1 and FMDF-2 are nearly identical. With an initial density spike, the growth of the layer is damped as expected (McMurtry *et al.*, 1989; Jackson, 1992; Colucci, 1994), but the results obtained by FMDF-1 are very close to those by FMDF-2. The slight differences are due to the numerical solution procedures. The results obtained by both procedures are close to those obtained by DNS.

In Fig. 3, the contour plots of the resolved vorticity and temperature at the final time ($t = 44$) as obtained by FMDF-1 and FMDF-2 are shown. This figure provides a visual demonstration of the consistency of the FMDF as the results via the two FMDF procedures are similar. The difference, as expected, is exhibited by the oscillations in FMDF-1. The effect of the baroclinic torque in generating vorticity near the braids is captured by both simulations. To exhibit the extent of the noise more clearly, the Reynolds averaged values of the resolved pressure and the mass fraction of a conserved scalar are shown in Fig. 4. The most significant difference is evident in the filtered pressure field which exhibits appreciable oscillations in FMDF-1. These oscillations are reduced by application of a local least square filter to smooth the Monte Carlo $\langle T\rangle_L$ field. This operation does not modify the other statistical quantities. Several other filter functions are also considered and their influence is summarized in Fig. 5 where the percentages of the differences between the values of $\langle p\rangle_\ell$ via FMDF-2 and FMDF-1 with smoothing are shown. In all cases, the difference is small (less than 2%); the most significant difference is expectedly observed when no smoothing operation is applied. Figure 5 also shows that the difference is significantly decreased as the number of Monte Carlo particles is increased.

To demonstrate the consistency between the FMDF and LES-FD, a comparison is made between the moments of the mass fraction of $\mathcal{A}$ in the non-reacting temporal mixing layer with an initial density spike as obtained by the two procedures. Figure 6 shows the instantaneous contour plots of the Favre filtered mass fraction of species $\mathcal{A}$ and Fig. 7 shows the Reynolds averaged values of the moments of this mass fraction. In these simulations, the filtered temperature is calculated via FMDF-1 without smoothing. The similarity of FMDF and LES-FD results is evident in both figures. The agreement in the first moment (Figs. 7(a,c)) is quite good even for large values of Δ_E and small values of NPG. The difference is more apparent in the subgrid variance values (Figs. 7(b,d)). However, the difference becomes smaller as Δ_E decreases.

In reactive flows, the consistency established above no longer exists since the reaction term appears in a closed form in the FMDF formulation but not in the moment equations of LES-FD. This inconsistency, which motivates the use of FMDF, is illustrated in Fig. 8 where the temporal evolution of the integrated "total product" $\left(\delta_P(t) = \int \overline{\langle P \rangle_L}(y,t)dy\right)$ in a constant density reacting temporal mixing layer with $Da = 2$ and $Ce = Ze = 0$ is shown. In these simulations, the LES resolution is 37×49 and $Re = 500$. The LES results are also compared with those obtained via DNS with 433×577 grid points. It is shown that the FMDF results are very close to those via DNS, but LES-FD significantly overpredicts the amount of products formed. Also shown in Fig. 8 are the results via the constant density filtered density function (FDF) formulation (Colucci *et al.*, 1998) which is suitable for this flow. The close agreement of FMDF, FDF and DNS results indicate both the consistency of the Monte Carlo solution and the relative superiority of FMDF over LES-FD.

To generalize the results above, LES of a 3D temporally developing mixing layer is conducted. In these simulations, a non-reacting flow with a density spike similar to that in 2D is considered. The statistical results in simulations with 3D forcing exhibit significant variations along the spanwise direction. The filtered pressure obtained from FMDF-1 exhibits similar trends to those obtained from FMDF-2 but does portray statistical noise. As is the case for 2D simulations, the filtered mass fraction and temperature calculated by the Monte Carlo solver are close to those obtained by the finite difference simulations. This is illustrated Fig. 9 in which scatter plots of $\langle T\rangle_L$ and $\langle A\rangle_L$ values generated by FMDF-2 are shown. The correlation coefficient between the Monte Carlo (MC) and the finite difference (FD) values is 0.999 for both sets of results shown.

5.6 Validation via DNS Data

The objectives in this subsection are to assess the overall performance of FMDF, to appraise the validity of the submodels employed in the FMDF transport equation, and to demonstrate the capabilities of FMDF for LES of exothermic chemically reacting flows. To meet these objectives, the FMDF results are compared against DNS results of the same flow configurations with the same magnitudes of the physical parameters (Re, Da, *etc.*). For a meaningful comparison, the DNS data are filtered and down-sampled onto coarse grid points corresponding to those employed in FMDF. At this point it is emphasized that FMDF is not claimed to be an alternative to DNS; the comparisons made here are primarily for assessment of the FMDF. For further comparative assessments, the FMDF results are also compared with those via LES-FD. Both 2D and 3D simulations are considered. Unless otherwise specified, all Monte Carlo simulations presented in this section are based on the FMDF-2 formulation.

To quantify the performance of FMDF in LES of the exothermic reacting 2D temporal mixing layer, in Fig. 10 the cross-stream variation of the Reynolds averaged filtered temperature values at $t = 44$ are shown. In this simulation, $Da = 11.92$, $Ze = 8$ and $Ce = 5$. The FMDF results are calculated with both $\Delta_E = \Delta$ and $\Delta_E = 2\Delta$. Initially, the particle number density is set to $NPG = 40$ with initial uniform fluid density. The size of the ensemble domain for the evaluation of the Favre filtered statistics does not have a significant influence on the first filtered moment. The deviation of LES-FD results from those via FMDF and/or DNS is evident. This behavior is observed at all times for all the cases considered. It is expected that the difference between DNS and LES-FD results would be even more as the magnitude of the Damköhler number and/or Reynolds number increases (Colucci *et al.*, 1998). Figure 10 shows that for this flow with a rather significant variation of temperature, the averaged filtered temperature is predicted well by FMDF. Comparatively, LES-FD overpredicts the filtered temperature values. While the finite difference solution of the filtered temperature is used to calculate the filtered pressure in the FMDF-2, the filtered temperature can also be evaluated directly from the ensemble of the Monte Carlo elements. Figure 10 indicates that the evaluation of the filtered temperature in this way (denoted by MC ensemble) is consistent with that obtained by FMDF-2.

The results of the spatially developing jet flow are shown in Figs. 11-17 in which several issues pertaining to the Monte Carlo simulation are addressed. Figures 11 and 12 show the instantaneous contours of the filtered pressure and the filtered temperature values, respectively. Parts (a), (b), and (c) of these figures correspond to results with FMDF-1 without smoothing of the temperature field, FMDF-1 with smoothing, and FMDF-2, respectively. While the temperature fields as obtained by all three procedures are similar, the differences between the pressure fields are noticeable. The behavior portrayed in Fig. 11(c) is physical, whereas the oscillations observed in Figs. 11(a,b) could cause numerical problems. While these oscillations did not cause problems here, Fig. 11 shows that FMDF-2 is more robust and is recommended for both LES and PDF simulations. In Figs. 13 and 14 the influence of the particle weights in the Monte Carlo simulation is exhibited. Figure 13 shows that the instantaneous particle number density and the filtered fluid density calculated by FMDF are highly correlated in these simulations in which uniform particle weights are employed. It is noted that the particle number density is lowest in the high temperature reaction zones. Figure 14 shows the results via variable weights. It is observed in Fig. 14(a) that there is a higher concentration of particles in the reaction zones in comparison to the case with uniform weights. The particle mass density shown in Fig. 14(b) is highly correlated with the filtered fluid density (Fig. 14(c)). A comparison between Figs. 13(b) and 14(c) indicates that despite the significant difference in the total number of particles and particle weighing procedures, the filtered density fields are nearly identical in the two simulations. This similarity is also reflected in the streamwise variations of the total product $\left(\delta_P(x) = \int \overline{\langle P\rangle_L}(x,y)dy\right)$ in Fig. 15. The results via both procedures are nearly identical and are superior to LES-FD in matching with DNS results. The computational time in the simulations with variable weights is about half of that in simulations with equal particle weights.

As indicated previously, the essential difference between FMDF and LES-FD is due to the ability of FMDF in accounting for the SGS scalar fluctuations. To demonstrate this explicitly, in Fig. 16, the contour plots of the "SGS unmixedness" defined as $\langle\rho\rangle_\ell \left[\langle\hat{S}(\phi)\rangle_L - \hat{S}(\langle\phi\rangle_L)\right]$ are shown. It is observed that the FMDF results are in good agreement with DNS. The contribution of the SGS unmixedness to the total filtered reaction rate is expected to increase as the magnitudes of the Re, Da, Ce increase. Therefore, it is anticipated that the difference between DNS and LES-FD results would be even more with increased values of these parameters. Scatter data of the instantaneous product mass fraction $\mathcal{P}$ vs. the mixture fraction Z are presented in Fig. 17. These data are gathered at the final time of the simulations including the results within the region $x \geq 3.5D$. Both the DNS (Fig. 17(a)) and FMDF-2 (Fig. 17(b)) exhibit significant scatters indicative of appreciable finite rate chemistry effects. The FMDF is able to capture the scatter reasonably well. It is important to note that while the fine-grained values associated with the particles may be interpreted as instantaneous realizations, conventional LES cannot offer such "de-filtered" information.

The major conclusions drawn from the 2D results are confirmed in 3D simulations. In Fig. 18, the time-variation of the total product as predicted by FMDF of the constant density temporally developing reacting mixing layer is compared with DNS and LES-FD results. Consistent with the 2D results, the total product predicted by FMDF is closer to DNS in comparison to that of LES-FD. With increased resolution in LES, the difference between DNS and LES-FD is less, but the FMDF results are not significantly modified.

5.7 Validation via Laboratory Data

The experiments of Mungal and Dimotakis (1984) were conducted with several values of the equivalence ratio, $\phi = c_{02}/c_{01}$ where c_0 refers to the free-stream molar concentration and the subscripts 1 and 2 denote the reactants in the high- and the low-speed streams, respectively. Equivalence ratios of 1, 2, 4 and 8 were considered. In addition, "flip" experiments were also conducted in which inverse values of the equivalence ratio ($\phi = 1$, $\frac{1}{2}$, $\frac{1}{4}$ and $\frac{1}{8}$) were considered. All of these cases are considered in the simulations by FMDF-1. The implementations of DNS and LES-FD are not possible for this flow.

Figure 19 displays the contour plots of the instantaneous and the Reynolds averaged temperature field for the case with $\phi = 1$. In this simulation, the finite rate reaction scheme is employed. The peak value of the instantaneous temperature field approaches, but is lower than, the adiabatic flame temperature. This is due to the filtering of the temperature field. The peak values of the time averaged temperature values are considerably lower than that of the adiabatic flame temperature, an intuitive fact indicated by Mungal and Dimotakis (1984) and also by Wallace (1981). However, it is noted that a large number of individual particles (*i.e.* realizations) do indeed approach the adiabatic limit.

The FMDF predictions are compared with experimental results both qualitatively and quantitatively. Figure 20 shows the time history of the temperature at several cross stream locations as obtained by FMDF. Each vertical increment represents temperature values ranging from the ambient to the maximum attained instantaneous temperature (T_{max}). These time traces are qualitatively similar to those measured experimentally (Mungal and Dimotakis, 1984). One notable difference is observed near the middle region of the layer. In this region, there are instances when the simulations exhibit near ambient temperature values (cold fluid). While there is some evidence of this behavior in the experiments, it is more pronounced in the simulations. This is partly attributed to the 2D nature of the simulations as the small scale mixing present in 3D tend to provide a more effective mixing (Miller *et al.*, 1994). For this reason it is expected that the minimum values of the time averaged temperature in the vicinity $y = 0$ to be slightly lower than those measured experimentally. Another reason for this difference is due to the fact that the cold wire probes may include some thermal lag and conduction errors (Scadron and Warshawsky, 1952; Paranthoen *et al.*, 1982; Mungal and Dimotakis, 1984) manifesting in an artificial "smoothing" effect in the measured temperature values.

For a quantitative comparison, in Fig. 21 the cross stream variations of the Reynolds averaged temperature rise normalized by the adiabatic temperature rise (T_a) are shown. The quantity δ_1 denotes the distance between the points where the cross stream mean temperature rise is 1% of the maximum mean temperature rise and y_0 is the cross stream location where the time-averaged streamwise velocity is the average of the high- and low-speed velocities. No attempt is made to de-filter the LES results and $\langle T \rangle_L$ is directly compared to experimental data. The agreement between the FMDF and experimental data is good. Also shown in this figure are the results based on the FMDF with the infinite reaction rate model. As expected, the results are very close to those of the finite rate simulation, but the computational cost is significantly less. In this particular case, the time requirement for FMDF simulations with the infinite rate chemistry is approximately 16% of that for the finite rate chemistry simulations. Due to this lower cost, and the confidence in the infinite rate model, the remaining simulations are conducted with this model.

To demonstrate the flip effect, Fig. 22 shows the cross-stream variation of the normalized temperature for all equivalence ratios (the simulations with $\phi = 1$ are repeated). Two observations are made consistent with the experimental results: (1) the peak value of the mean temperature in each of the experiments is different from that in the corresponding flip experiment, although the adiabatic flame temperature is the same, (2) the peak temperature value shifts toward the lean reactant stream. Since the only difference between each of the two cases is the interchange of the low and high speed reactants, the reason for this behavior is due to the different entrainment processes (Mungal and Dimotakis, 1984). Additionally, with the exception of the two cases with $\phi = 1$, the peak temperature is higher for equivalence ratios greater than one compared to the reciprocal equivalence ratios. Consistent with the experimental results, the peak normalized temperature reaches a maximum for an equivalence ratio in the range $1 \leq \phi \leq 2$. These trends are more clearly portrayed in Fig. 23(a), which Mungal and Dimotakis (1984) refer to as "inferred" temperature profiles. These reflect the temperature if the high speed reactant was fixed at 1 % molar concentration while the low speed stream was varied from $\frac{1}{8}\%$ through 8% to obtain the desired equivalence ratios. This figure supports the conclusion of Mungal and Dimotakis (1984) that there exists an asymptotic limit to the amount of products formed as the high speed reactant is burned to completion. A similar behavior is exhibited in Fig. 23(b) in which the inferred temperature profiles are shown for the situation in which the low stream reactant is fixed at 1% and the high speed reactant is varied to obtain the same equivalence ratios.

Further quantitative comparison between the FMDF and experimental results is made in Fig. 24 which shows the variation of the normalized product thickness with the equivalence ratio. The product thicknesses are defined as (Mungal and Dimotakis, 1984)

$$\delta_{p1} = \int_{-\infty}^{+\infty} \frac{C_p \overline{\langle T(y)\rangle_L}}{c_{01}\Delta Q} dy, \quad \delta_{p2} = \int_{-\infty}^{+\infty} \frac{C_p \overline{\langle T(y)\rangle_L}}{c_{02}\Delta Q} dy \tag{45}$$

where C_p is the molar heat capacity of the carrier gas. Figure 24(a) indicates the FMDF predicts the extent of product formation reasonably well over a wide range of equivalence ratios. At low values of ϕ, the amount of products varies nearly linearly as the low speed reactant is consumed when excessive amounts of the high speed reactant are present. At

Table 2: The computational times for 2D planar jet simulations.

Simulation	Grid resolution	Normalized CPU time†
DNS	1201 × 601	242.5
FMDF	201 × 101	7.62
LES-FD	201 × 101	1

† Unit correspond to 760 seconds on a Cray-C90.

high values of the equivalence ratio, the product thickness approaches an asymptotic value as the reaction progress is inhibited by a lack of high speed reactant relative to the amount of reactant in the low speed stream. Figure 24(b) demonstrates a similar agreement between the experimental and the FMDF results.

5.8 Computational Requirements

To appraise the computational requirements of the FMDF, the computational times for some of the cases are monitored. Tables 2 and 3 list the normalized CPU times required for the simulations of the reacting 2D planar jet and the reacting 3D temporally developing mixing layer, respectively. These cases are selected since simulations via all three schemes (FMDF, LES-FD and DNS) are conducted. The computational times listed for FMDF are those associated with FMDF-2, although the increase in cost over FMDF-1 is insignificant. Obviously the overhead of the FMDF simulation is extensive as compared to LES-FD; nevertheless, the computational time for FMDF simulation is significantly less than that of DNS. Again it is emphasized that FMDF is not claimed to be an alternative to DNS; neither it is claimed that the FMDF is capable of reproducing all DNS results. However, the close proximity of values obtained FMDF and DNS, and the substantial lower computational costs of FMDF makes it as a viable tool for simulations of reacting flow systems for which DNS is not possible.

6 Summary and Concluding Remarks

The basic objective of this work is to develop a methodology for large eddy simulation (LES) of turbulent reacting flows, with inclusion of exothermicity and variable density effects. The

Table 3: The computational times for 3D temporal mixing layer simulations.

Simulation	Grid resolution	Normalized CPU time†
DNS	217 × 289 × 133	182.71
FMDF	55 × 73 × 34	7.64
LES-FD	55 × 73 × 34	1

† Unit correspond to 655 seconds on a Cray-C90.

methodology is termed the "filtered mass density function" (FMDF) and is based on the extension of the "filtered density function" (FDF) developed previously for LES of constant density, reacting, isothermal flows (Colucci *et al.*, 1998). The procedure for this extension is similar to that used in probability density function (PDF) methods in Reynolds averaging procedures (Pope, 1985). Here the FMDF is considered for treatment of scalar variables. A transport equation is developed for the FMDF in which the unclosed terms, similar to PDF methods, are due to SGS convection and mixing. The former is modeled via the gradient diffusion model as done in most LES of non-reacting flows (Galperin and Orszag, 1993); the latter is closed via the IEM model as typically used in PDF methods (Pope, 1985).

The modeled FMDF transport equation is solved numerically via a Lagrangian Monte Carlo scheme in which the solutions of the equivalent stochastic differential equations (SDEs) are obtained. Two Monte Carlo procedures are considered. The first (FMDF-1) is similar to that typically used in PDF methods (Pope, 1985; Tolpadi *et al.*, 1995; Tolpadi *et al.*, 1996). The second (FMDF-2) is new. Both schemes preserve the Itô-Gikhman nature of the SDEs and provide a reliable solution for the FMDF. The second scheme is more robust in dealing with the statistical noise generated by the Monte Carlo scheme. The consistency of the FMDF, the convergence of its Monte Carlo solutions, the advantages and drawbacks of the FMDF as well as the performance of the closures employed in the FMDF transport equation are assessed. This is done via extensive comparisons between the results obtained by the Monte Carlo procedure and the finite difference solution of the transport equations of the first two filtered moments of scalar quantities (LES-FD). In non-reacting flows, the consistency and convergence of the Monte Carlo solution is demonstrated by good agreements of the first two SGS scalar moments with those obtained by LES-FD. The performance of FMDF and its superiority over LES-FD are demonstrated by comparison with direct numerical simulations (DNS) results of two-dimensional (2D) and 3D temporally developing mixing layers, and a 2D spatially developing jet. In all cases the FMDF results are shown to be in closer agreement with the DNS data than are the LES-FD results in which the influence of the SGS fluctuations on the reaction rate are ignored.

The performance of the FMDF is further appraised by comparison against the experimental data of Mungal and Dimotakis (1984) of a spatially developing mixing layer involving the exothermic hydrogen-fluorine reaction. The FMDF is considered via both finite rate and infinitely fast chemistry. The treatment of the former with a stiff reaction source term is computationally expensive, but comparison of the results with those of the latter gives confidence in the less costly infinite rate procedure. The results produced by both methods compare favorably with experimental data and some qualitative features, such as the "flip effect", are captured by the FMDF simulation.

In addition to the those in the hydrodynamic closure, there are three constants for the LES of scalar quantities: Sc_t and Pr_t for the SGS convective fluxes of the mass fraction and the temperature, respectively, and C_Ω as appears in the SGS mixing model. Based on the present results and those of Colucci *et al.* (1998) for a variety of different flows (2D and 3D, constant and variable density, different chemistry schemes, *etc.*) it seems that $Sc_t = Pr_t \approx 0.4 - 0.7$, $C_\Omega \approx 3 - 6$. The predictive capability of the FMDF can be improved by future developments in PDF methods.

While the FMDF method is computationally more expensive than conventional LES method, it is much more advantageous for treating reacting flows. The computational overhead is tolerable for simulations of complex reacting flows for which DNS is not feasible.

Acknowledgment

This work is part of a research program sponsored by the NASA Langley Research Center under Grant NAG-1-1122 to SUNY-Buffalo and Grant NAG-1-1542 to Cornell University. Dr. J. Philip Drummond is the Technical Monitor of this program. Acknowledgment is also made to the Donors of the Petroleum Research Funds administrated by the American Chemical Society for their support under Grant ACS-PRF 32892-AC9 to SUNY-Buffalo. Additional support for the work at Cornell is provided by the AFOSR under Grant F49620-97-1-0126. Computational resources are provided by the NCSA at the University of Illinois and by the SEAS Computing Center at SUNY-Buffalo.

References

Aldama, A. A. (1990). Filtering techniques for turbulent flow simulations. volume 49 of *Lecture Notes in Engineering*. Springer-Verlag, New York, NY.

Bardina, J., Ferziger, J. H., and Reynolds, W. C. (1983). Improved turbulence models based on large eddy simulations of homogeneous, incompressible, turbulent flows. Department of Mechanical Engineering Report TF-19, Stanford University, Stanford, CA.

Baulch, D. L., Duxbury, J., Grant, S. J., and Montague, D. C. (1981). Evaluated kinetic rate data for high temperature reactions, vol. 4. *J. Phys. Chem. Ref. Data* **10**, Suppl. 1.

Bilger, R. W. (1982). Molecular transport effects in turbulent diffusion flames at moderate Reynolds number. *AIAA J.* **20**, 962–970.

Borghi, R. (1988). Turbulent combustion modeling. *Prog. Energy Combust. Sci.* **14**, 245–292.

Branley, N. and Jones, W. P. (1997). Large eddy simulation of a turbulent non-premixed flame. In *Proceedings of the Eleventh Symposium on Turbulent Shear Flows*, pages 21.1–21.6, Grenoble, France.

Brown, G. L. and Roshko, A. (1974). On density effects and large structure in turbulent mixing layers. *J. Fluid Mech.* **64**, 775–816.

Carpenter, M. H. (1990). A high-order compact numerical algorithm for supersonic flows. In Morton, K. W., editor, *Twelfth International Conference on Numerical Methods in Fluid Dynamics*, volume 371 of *Lecture Notes in Physics*, pages 254–258. Springer-Verlag, New York, NY.

Chelliah, H. K. (1989), *Asymptotic Analyses of the Structures and Characteristics of Flames.* Ph.D. Thesis, Department of Mechanical and Aerospace Engineering, Princeton University, Princeton, NJ.

Chen, H., Daugherty, J. D., and Fyfe, W. (1975). TA5-H_2/F_2. Flame propagation and repetitively pulsed Hydrogen Fluoride (HF) chain-reaction laser. *IEEE J. Quantum Electronics* **QE-11**, **8**, 648–653.

Colucci, P. J., Jaberi, F. A., Givi, P., and Pope, S. B. (1998). Filtered density function for large eddy simulation of turbulent reacting flows. *Phys. Fluids* **10**, 499–515.

Colucci, P. J. (1994). Linear stability analysis of density stratified parallel shear flows. AIAA Paper 94-0011.

Cook, A. W. and Riley, J. J. (1994). A subgrid model for equilibrium chemistry in turbulent flows. *Phys. Fluids* **6**, 2868–2870.

Cook, A. W., Riley, J. J., and deBruynKops, S. M. (1997a). A sub-grid model for non-premixed turbulent combustion. In *Proceedings of the Eleventh Symposium on Turbulent Shear Flows*, pages 16.13–16.18, Grenoble, France.

Cook, A. W., Riley, J. J., and Kosály, G. (1997b). A laminar flamelet approach to subgrid-scale chemistry in turbulent flows. *Combust. Flame* **109**, 332–341.

Cool, T. A., Stephens, R. R., and Shirley, J. A. (1970). HCl, HF, and DF partially inverted CW chemical lasers. *J. Appl. Phys.* **41**, 4038–4050.

DesJardin, P. E. and Frankel, S. H. (1998). Large eddy simulation of a turbulent non-premixed reacting jet: Application and assessment of subgrid-scale combustion models. *Phys. Fluids* **10**, 2298–2314.

Dopazo, C. and O'Brien, E. E. (1976). Statistical treatment of non-isothermal chemical reactions in turbulence. *Combust. Sci. and Tech.* **13**, 99–112.

Drummond, J. P. (1991). Supersonic reacting internal flow fields. In Oran, E. S. and Boris, J. P., editors, *Numerical Approaches to Combustion Modeling*, volume 135 of *Progress in Astronautics and Aeronautics*, chapter 12, pages 365–420. AIAA Publishing Co., Washington, D.C.

Eidson, T. M. (1985). Numerical simulation of the turbulent rayleigh-benard problem using subgrid modelling. *J. Fluid Mech.* **158**, 245–268.

Erlebacher, G., Hussaini, M. Y., Speziale, C. G., and Zang, T. A. (1992). Toward the large eddy simulation of compressible turbulent flows. *J. Fluid Mech.* **238**, 155–185.

Fox, R. O. (1996). Computational methods for turbulent reacting flows in chemical process industry. *Revue De L'Institut Francais Du Petrole* **51**, 215–246.

Frankel, S. H., Adumitroaie, V., Madnia, C. K., and Givi, P. (1993). Large eddy simulations of turbulent reacting flows by assumed PDF methods. In Ragab, S. A. and Piomelli, U., editors, *Engineering Applications of Large Eddy Simulations*, pages 81–101. ASME, FED-Vol. 162, New York, NY.

Fureby, C. and Lofstrom, C. (1994). Large-eddy simulations of bluff body stabilized flames. In *Proceedings of 25th Symp. (Int.) on Combustion*, pages 1257–1264. The Combustion Institute, Pittsburgh, PA.

Galperin, B. and Orszag, S. A., editors. (1993). *Large Eddy Simulations of Complex Engineering and Geophysical Flows*. Cambridge University Press, Cambridge, England.

Gao, F. and O'Brien, E. E. (1993). A large-eddy simulation scheme for turbulent reacting flows. *Phys. Fluids A* **5**, 1282–1284.

Gardiner, C. W. (1990). *Handbook of Stochastic Methods*. Springer-Verlag, New York, NY.

Germano, M. (1992). Turbulence: The filtering approach. *J. Fluid Mech.* **238**, 325–336.

Givi, P. and Riley, J. J. (1992). Some current issues in the analysis of reacting shear layers: Computational challenges. In Hussaini et al. (1992), pages 588–650.

Givi, P. (1989). Model free simulations of turbulent reactive flows. *Prog. Energy Combust. Sci.* **15**, 1–107.

Givi, P. (1994). Spectral and random vortex methods in turbulent reacting flows. In Libby and Williams (1994), chapter 8, pages 475–572.

Gmelin, L. (1980). *Handbook of Inorganic Chemistry: Fluorine Suppl., Vol. 2: The Element.* Springer, New York, NY.

Hussaini, M. Y., Kumar, A., and Voigt, R. G., editors. (1992). *Major Research Topics in Combustion.* Springer-Verlag, New York, NY.

Jaberi, F. A. and James, S. (1998). A dynamic similarity model for large eddy simulation of turbulent combustion. *Phys. Fluids* **10**, 1775–1777.

Jackson, T. L. (1992). A review of spatial stability analysis of compressible reacting mixing layers. In Hussaini et al. (1992), pages 131–161.

Jiménez, J., Liñán, A., Rogers, M. M., and Higuera, F. J. (1997). *A Priori* testing of subgrid models for chemically reacting non-premixed turbulent flows. *J. Fluid Mech.* **349**, 149–171.

Jou, W.-H. and Riley, J. J. (1989). Progress in direct numerical simulations of turbulent reacting flows. *AIAA J.* **27**, 1543–1556.

Karlin, S. and Taylor, H. M. (1981). *A Second Course in Stochastic Processes.* Academic Press, New York, NY.

Kloeden, P. E. and Platen, E. (1995). *Numerical Solution of Stochastic Differential Equations*, volume 23 of *Applications of Mathematics, Stochastic Modelling and Applied Probability.* Springer-Verlag, New York, NY.

Libby, P. A. and Williams, F. A., editors. (1994). *Turbulent Reacting Flows.* Academic Press, London, England.

Lundgren, T. S. (1969). Model equation for nonhomogeneous turbulence. *Phys. Fluids* **12**, 485–497.

Madnia, C. K. and Givi, P. (1993). Direct numerical simulation and large eddy simulation of reacting homogeneous turbulence. In Galperin and Orszag (1993), chapter 15, pages 315–346.

Mathey, F. and Chollet, J. P. (1997). Large eddy simulation of turbulent reactive flows. In *Proceedings of the Eleventh Symposium on Turbulent Shear Flows*, pages 16.19–16.24, Grenoble, France.

McMurtry, P. A., Riley, J. J., and Metcalfe, R. W. (1989). Effects of heat release on the large scale structures in a turbulent reacting mixing layer. *J. Fluid Mech.* **199**, 297–332.

McMurtry, P. A., Menon, S., and Kerstein, A. R. (1992). A linear eddy sub-grid model for turbulent reacting flows: Application to hydrogen-air combustion. In *Proceedings of 24th Symp. (Int.) on Combustion*, pages 271–278. The Combustion Institute, Pittsburgh, PA.

McMurtry, P. A., Menon, S., and Kerstein, A. R. (1993). Linear eddy modeling of turbulent combustion. *Energy & Fuels* **7**, 817–826.

Menon, S., McMurtry, P. A., and Kerstein, A. K. (1993). A linear eddy sugbrid model of turbulent combustion. In Galperin and Orszag (1993), chapter 14, pages 287–314.

Michalke, A. (1965). On spatially growing disturbances in an inviscid shear layer. *J. Fluid Mech.* **23**, 521–544.

Miller, R. S., Madnia, C. K., and Givi, P. (1994). Structure of a turbulent reacting mixing layer. *Combust. Sci. and Tech.* **99**, 1–36.

Möller, S. I., Lundgren, E., and Fureby, C. (1996). Large eddy simulations of unsteady combustion. In *Proceedings of 26th Symp. (Int.) on Combustion*, page 241. The Combustion Institute, Pittsburgh, PA.

Moser, R. D. and Rogers, M. M. (1991). Mixing transition and the cascade of small scales in a plane mixing layer. *Phys. Fluids A* **3**, 1128–1134.

Mungal, M. G. and Dimotakis, P. E. (1984). Mixing and combustion with low heat release in a turbulent mixing layer. *J. Fluid Mech.* **148**, 349–382.

O'Brien, E. E. (1980). The probability density function (PDF) approach to reacting turbulent flows. In Libby, P. A. and Williams, F. A., editors, *Turbulent Reacting Flows*, chapter 5, pages 185–218. Springer-Verlag, Heidelberg.

Paranthoen, P., Petit, C., and Lecordier, J. C. (1982). The effect of thermal prong-wire interaction on the response of a cold wire in gaseous flows (air, argon and helium). *J. Fluid Mech.* **124**, 457–473.

Poinsot, T. J. and Lele, S. K. (1992). Boundary conditions for direct simulations of compressible viscous flows. *J. Comp. Phys.* **101**, 104–129.

Pope, S. B. (1976). The probability approach to modeling of turbulent reacting flows. *Combust. Flame* **27**, 299–312.

Pope, S. B. (1985). PDF methods for turbulent reactive flows. *Prog. Energy Combust. Sci.* **11**, 119–192.

Pope, S. B. (1990). Computations of turbulent combustion: Progress and challenges. In *Proceedings of 23rd Symp. (Int.) on Combustion*, pages 591–612. The Combustion Institute, Pittsburgh, PA.

Pope, S. B. (1994). Lagrangian pdf methods for turbulent flows. *Ann. Rev. Fluid Mech.* **26**, 23–63.

Pope, S. B. (1997). Mean field equations in PDF particle methods for turbulent reactive flows. Technical Report FDA 97-06, Cornell University, Ithaca, NY.

Rapp, D. and Johnston, H. S. (1960). Nitric Oxide-Fluorine dilute diffusion flame. *J. Chem. Phys.* **33**, 695–699.

Réveillon, J. and Vervisch, L. (1998). Subgrid-scale turbulent micromixing: Dynamic approach. *AIAA J.* **36**, 336–341.

Riley, J. J., Metcalfe, R. W., and Orszag, S. A. (1986). Direct numerical simulations of chemically reacting mixing layers. *Phys. Fluids* **29**, 406–422.

Risken, H. (1989). *The Fokker-Planck Equation, Methods of Solution and Applications.* Springer-Verlag, New York, NY.

Rudy, D. H. and Strikwerda, J. C. (1980). Boundary conditions for subsonic compressible navier-stokes calculations. *J. Comp. Phys.* **36**, 327–338.

Salvetti, M. V. and Banerjee, S. (1995). A priori tests of a new dynamic subgrid-scale model for finite-difference large-eddy simulations. *Phys. Fluids* **7**, 2831–2847.

Sandham, N. D. and Reynolds, W. C. (1989). Some inlet-plane effects on the numerically simulated spatially-developing mixing layer. In *Turbulent Shear Flows 6*, pages 441–454. Springer-Verlag, New York, NY.

Scadron, M. D. and Warshawsky, I. (1952). Experimental determination of time constants and Nusselt numbers for bare-wire thermocouples in high-velocity air streams and analytic approximation of conduction and radiation errors. NACA TN 2599.

Spalding, D. B. and Stephenson, P. L. (1971). Laminar flame propagation in Hydrogen+Bromine mixtures. *Proc. R. Soc. Lond. A* **324**, 315–337.

Steinberger, C. J., Vidoni, T. J., and Givi, P. (1993). The compositional structure and the effects of exothermicity in a nonpremixed planar jet flame. *Combust. Flame* **94**, 217–232.

Tolpadi, A. K., Correa, S. M., Burrus, D.L., and C., Mongia H. (1995). A Monte Carlo PDF method for the calculation of gas turbine combustor flow fields. AIAA Paper 95-2443.

Tolpadi, A. K., Hu, I. Z., Correa, S. M., and Burrus, D. L. (1996). Coupled Lagrangian Monte Carlo PDF-CFD computation of gas turbine combustor flowfields with finite-rate chemistry. ASME Paper 96-GT-205. presented at the 41st ASME Turbo Expo, Birmingham, England, June 1996.

Vervisch, L. and Poinsot, T. (1988). Direct numerical simulation of non-premixed turbulent flames. *Annu. Rev. Fluid Mech.* **30**, 655–691.

Vreman, B., Geurts, B., and Kuerten, H. (1994). Realizability conditions for the turbulent stress tensor in large-eddy simulation. *J. Fluid Mech.* **278**, 351–362.

Wallace, A. K. (1981), *Experimental Investigation on the Effects of Chemical Heat Release on Shear Layer Growth and Entrainment.* Ph.D. Thesis, University of Adelaide, Australia.

Williams, F. A. (1985). *Combustion Theory.* The Benjamin/Cummings Publishing Company, Menlo Park, CA, 2nd edition.

Figure Captions

Figure 1. Cross-stream variation of the filtered density in the 2D temporal mixing layer obtained by FMDF-1 at $t = 44$.

Figure 2. Vorticity thickness vs. time in the 2D temporal mixing layer.

Figure 3. Contours of the filtered vorticity and temperature in the 2D temporal mixing layer obtained by FMDF-1 (right side) and FMDF-2 (left side) at $t = 44$. Top: vorticity field, bottom: temperature field.

Figure 4. Cross-stream variation of the mean filtered quantities at $t = 44$ in the 2D temporal mixing layer. (a) Pressure, (b) mass fraction of a conserved scalar.

Figure 5. Cross-stream variation of the percentage of the difference in pressure as obtained by FMDF-2 and FMDF-1 with different smoothing in the 2D temporal mixing layer at $t = 44$. Long-dashed line: no smoothing, $NPG = 50$ and $\Delta_E = \Delta$; Dotted-dashed line: smoothed with a Gaussian filter, $NPG = 50$ and $\Delta_E = \Delta$; solid line: smoothed with a box filter, $NPG = 50$ and $\Delta_E = \Delta$; dashed line: smoothed with a local least square filter, $NPG = 50$ and $\Delta_E = \Delta$; Long-dashed thick line: smoothed with a Gaussian filter, $NPG = 200$ and $\Delta_E = \Delta$; Dotted thick line: smoothed with a Gaussian filter, $NPG = 50$ and $\Delta_E = 2\Delta$.

Figure 6. Contours of the filtered values of the conserved scalar at $t = 44$ in the 2D temporal mixing layer as obtained by (a) LES-FD, (b) FMDF.

Figure 7. Cross-stream variation of mean filtered scalar ((a) and (c)) and the generalized variance of the conserved scalar ((b) and (d)) in the 2D temporal mixing layer.

Figure 8. Total product variation with time in the 2D temporal mixing layer.

Figure 9. Scatter plots of the filtered quantities as obtained by the Monte Carlo (MC) solution vs. those via the finite difference (FD) solution in the 3D temporal mixing layer: (a) temperature, (b) the conserved mass fraction.

Figure 10. Cross-stream variation of the normalized filtered temperature in the 2D temporal mixing layer at $t = 44$.

Figure 11. Contours of the normalized filtered pressure in the planar jet: (a) FMDF-1 with

no smoothing of the filtered temperature, (b) FMDF-1 with smoothed filtered temperature with box filter, (c) FMDF-2.

Figure 12. Contours of the normalized filtered temperature in the reactive planar jet: (a) FMDF-1 with no smoothing of the filtered temperature, (b) FMDF-1 with smoothed filtered temperature with box filter, (c) FMDF-2.

Figure 13. Contours of (a) the particle number density, (b) the fluid filtered density in the reactive planar jet simulations with uniform weights.

Figure 14. Contours of (a) the particle number density, (b) the particle mass density, (c) the fluid filtered density in the reactive planar jet simulations with variable weights.

Figure 15. Streamwise variation of the total product in the reactive planar jet.

Figure 16. Contours of the normalized instantaneous SGS unmixedness in the reactive planar jet, (a) DNS, (b) FMDF.

Figure 17. Scatter plot of the product mass fraction vs. the mixture fraction in the reactive planar jet, (a) DNS, (b) FMDF.

Figure 18. Total product vs. time in the 3D temporal mixing layer. (a) lower LES resolution ($37 \times 49 \times 23$), (b) higher LES resolution ($55 \times 73 \times 34$).

Figure 19. Contour plots of (a) instantaneous Favre filtered temperature, (b) time averaged Favre filtered temperature for $\phi = 1$ in the hydrogen-fluorine mixing layer. The values are normalized by T_r.

Figure 20. Time history of the instantaneous Favre filtered temperature in the hydrogen-fluorine mixing layer at several cross stream locations.

Figure 21. Cross stream variation of the normalized mean temperature for $\phi = 1$ in the hydrogen-fluorine mixing layer.

Figure 22. Cross stream variation of the normalized mean temperature for all equivalence ratios in the hydrogen-fluorine mixing layer.

Figure 23. Cross stream variation of the "inferred" mean temperature profiles for (a) 1% high speed mole fraction, (b) 1% low speed mole fraction for all equivalence ratios in the hydrogen-fluorine mixing layer.

Figure 24. Normalized product thickness variation with equivalence ratio in the hydrogen-fluorine mixing layer: (a) δ_{p1} vs. the equivalence ratio, (b) δ_{p2} vs. the inverse equivalence ratio.

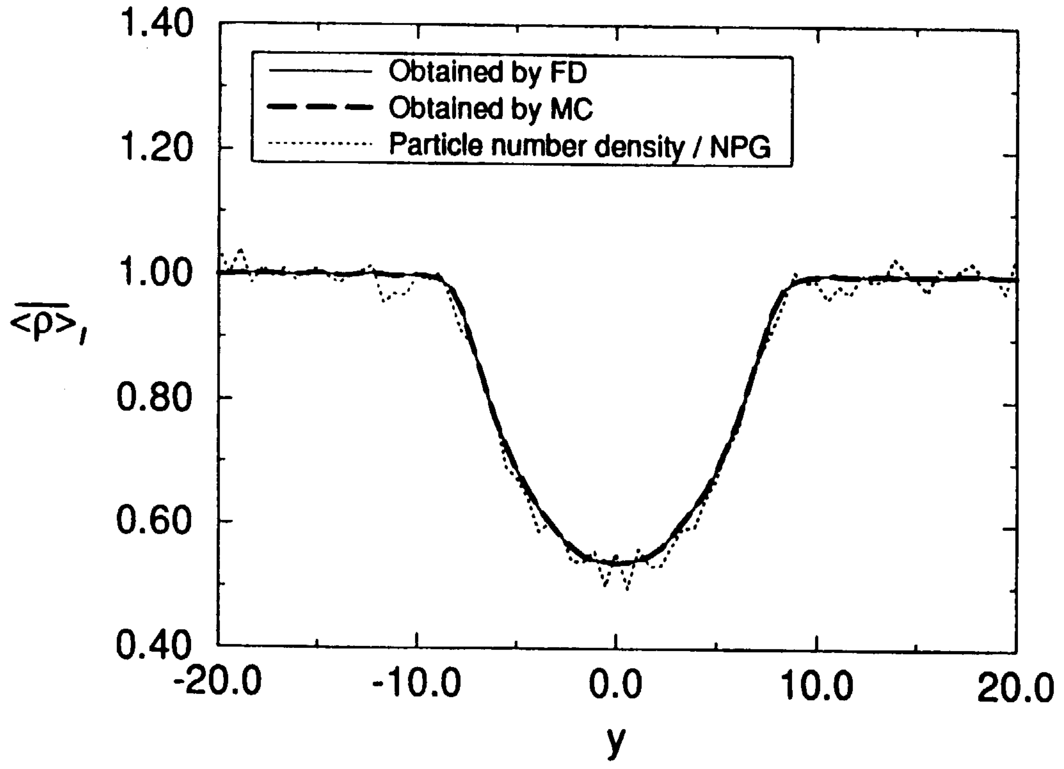
Obtained by FD
Obtained by MC
Particle number density / NPG
$\overline{\langle\rho\rangle}_l$
1.40
1.20
1.00
0.80
0.60
0.40
-20.0
-10.0
0.0
10.0
20.0
y

Figure 1

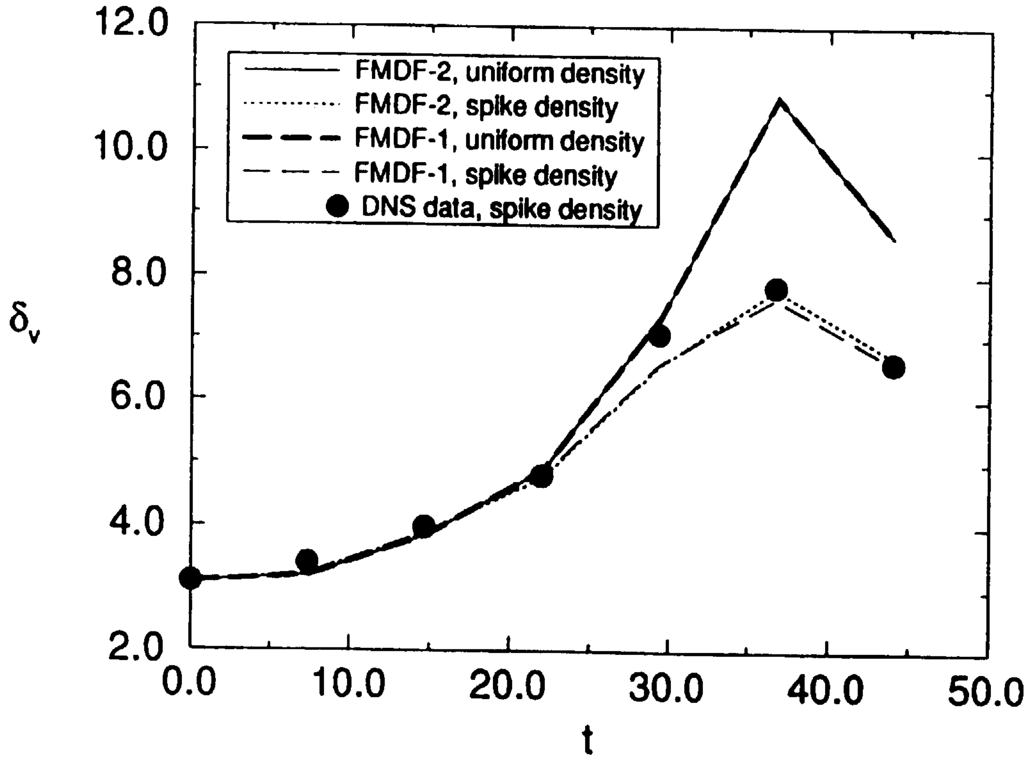
12.0
10.0
8.0
6.0
4.0
2.0
δ_v
0.0
10.0
20.0
30.0
40.0
50.0
t
FMDF-2, uniform density
FMDF-2, spike density
FMDF-1, uniform density
FMDF-1, spike density
DNS data, spike density

Figure 2

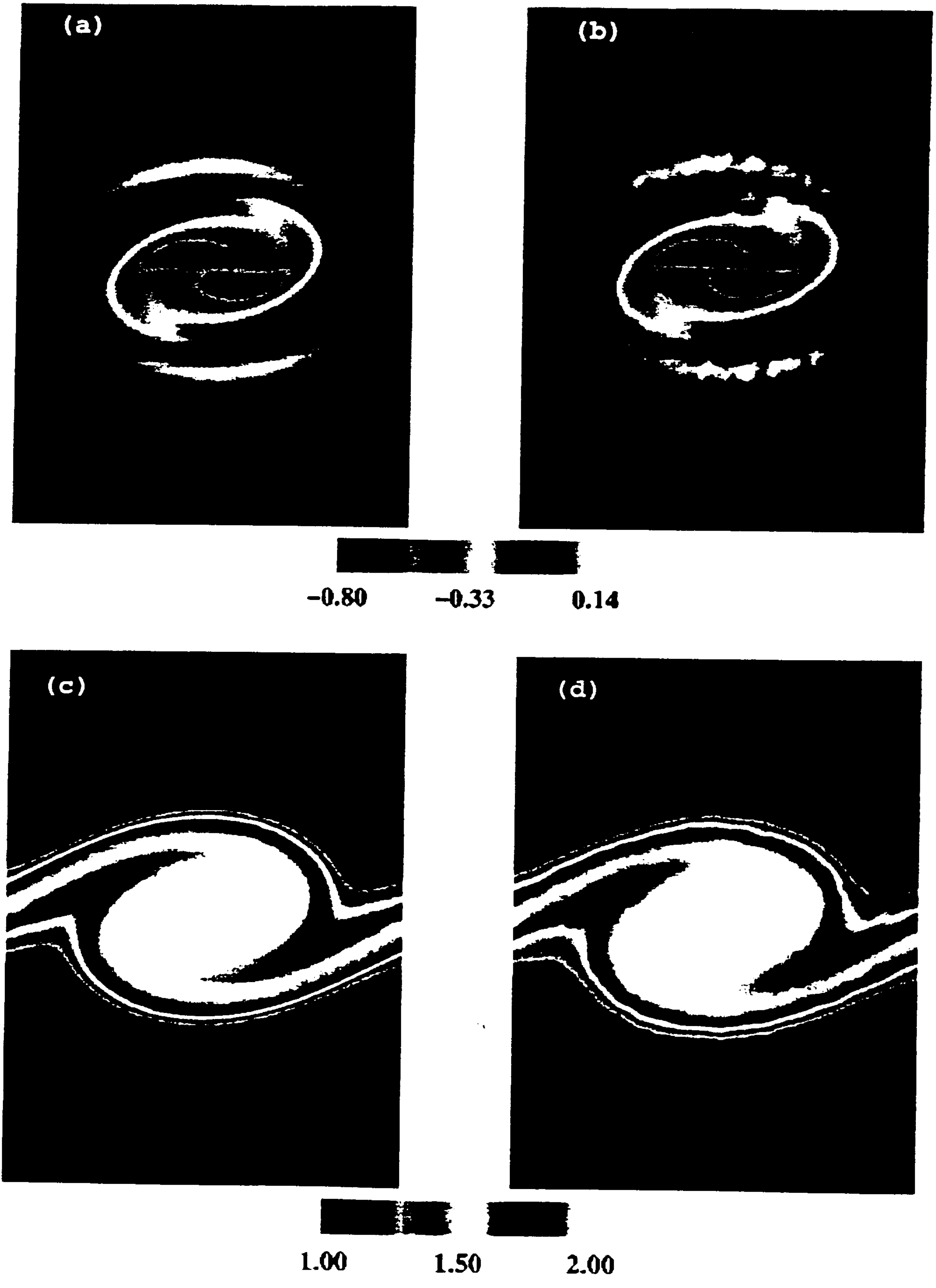

Figure 3

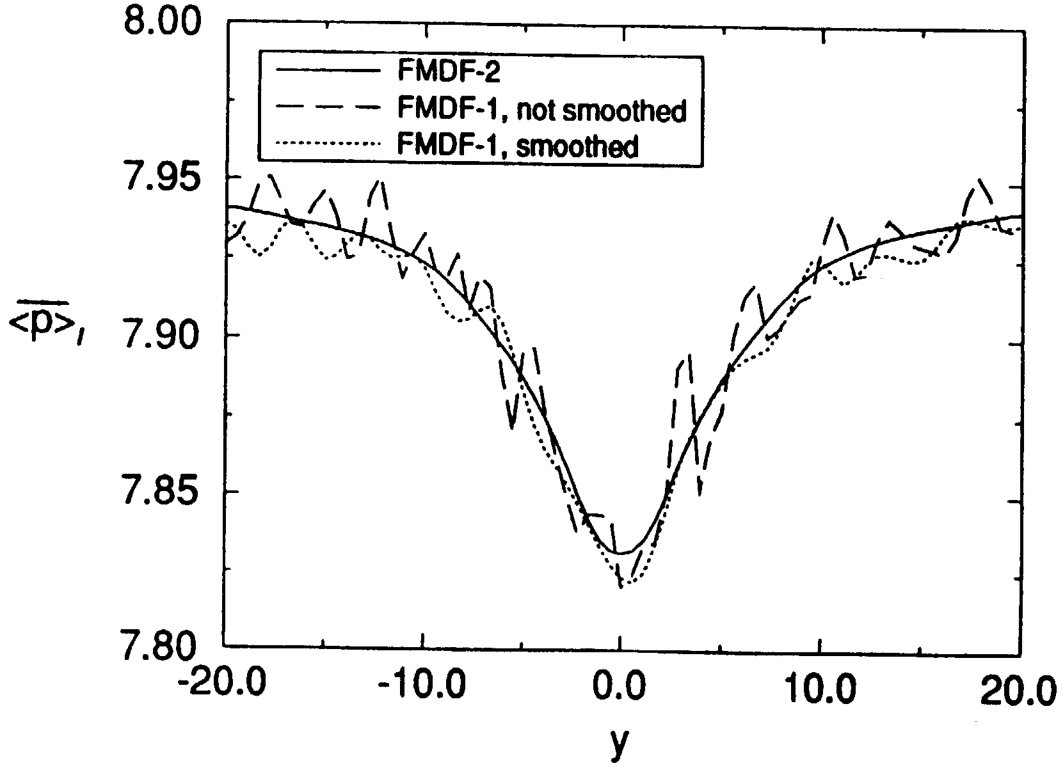
FMDF-2
FMDF-1, not smoothed
FMDF-1, smoothed
$\overline{\langle p\rangle}_l$
8.00
7.95
7.90
7.85
7.80
-20.0
-10.0
0.0
10.0
20.0
y

Figure 4(a)

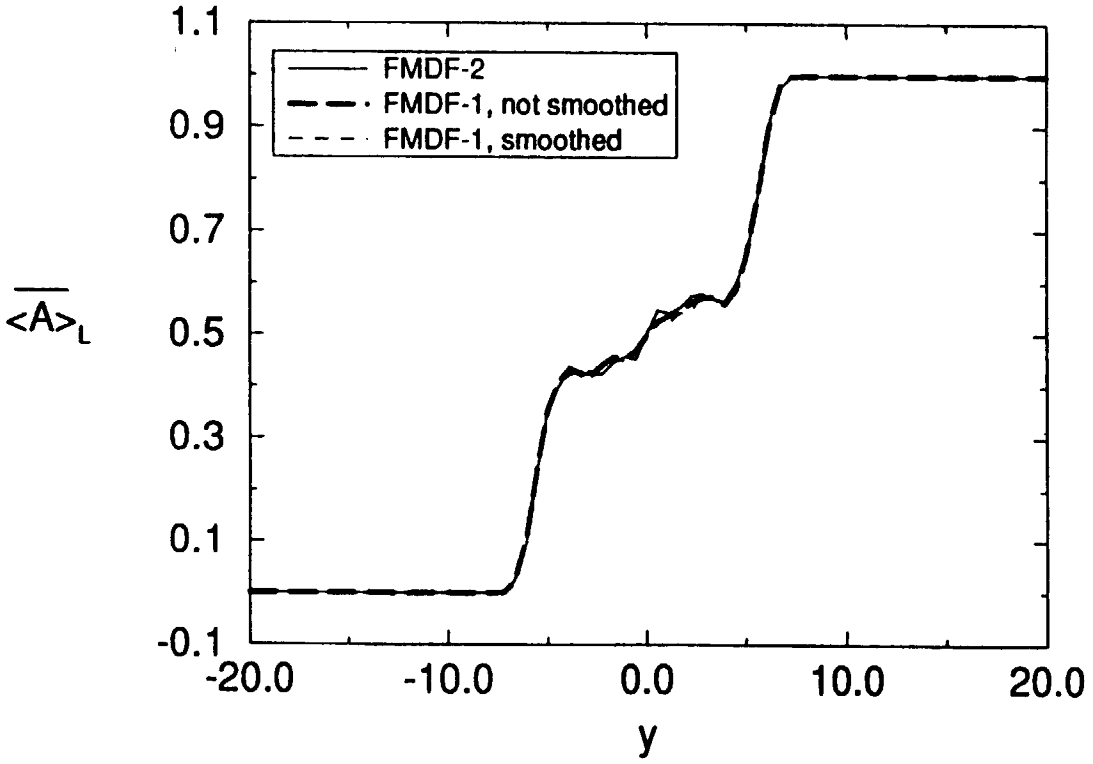
1.1
0.9
0.7
0.5
0.3
0.1
-0.1
$\overline{\langle A \rangle_L}$
-20.0
-10.0
0.0
10.0
20.0
y
FMDF-2
FMDF-1, not smoothed
FMDF-1, smoothed

Figure 4(b)

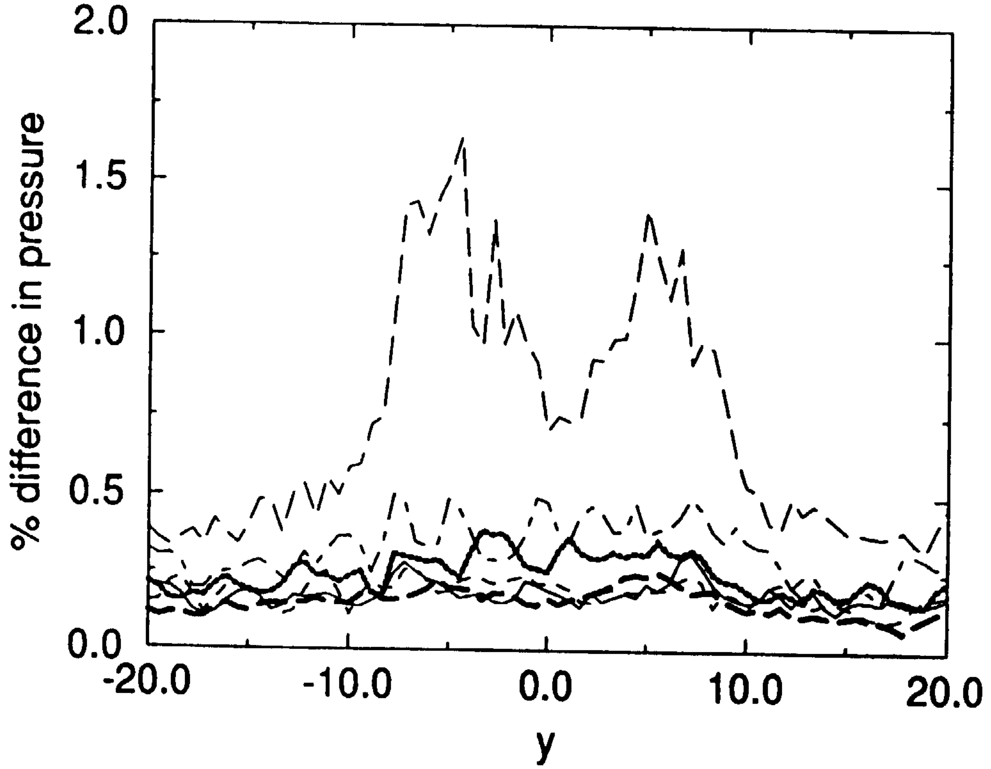

Figure 5

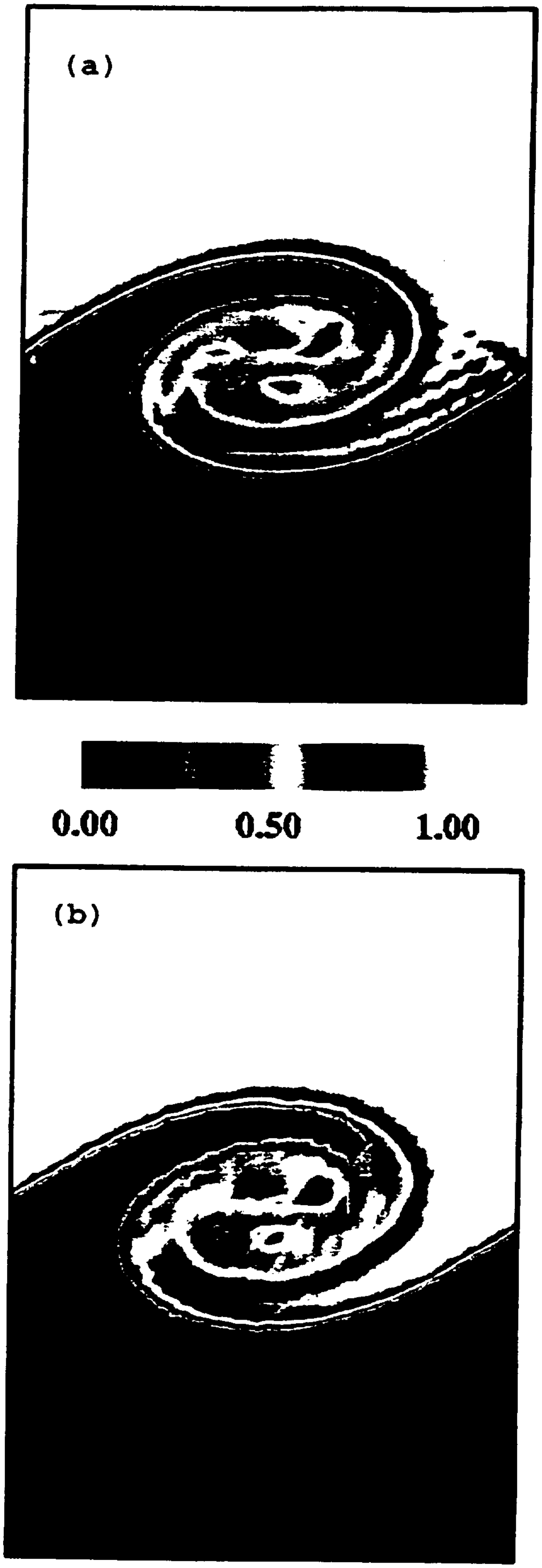

Figure 6

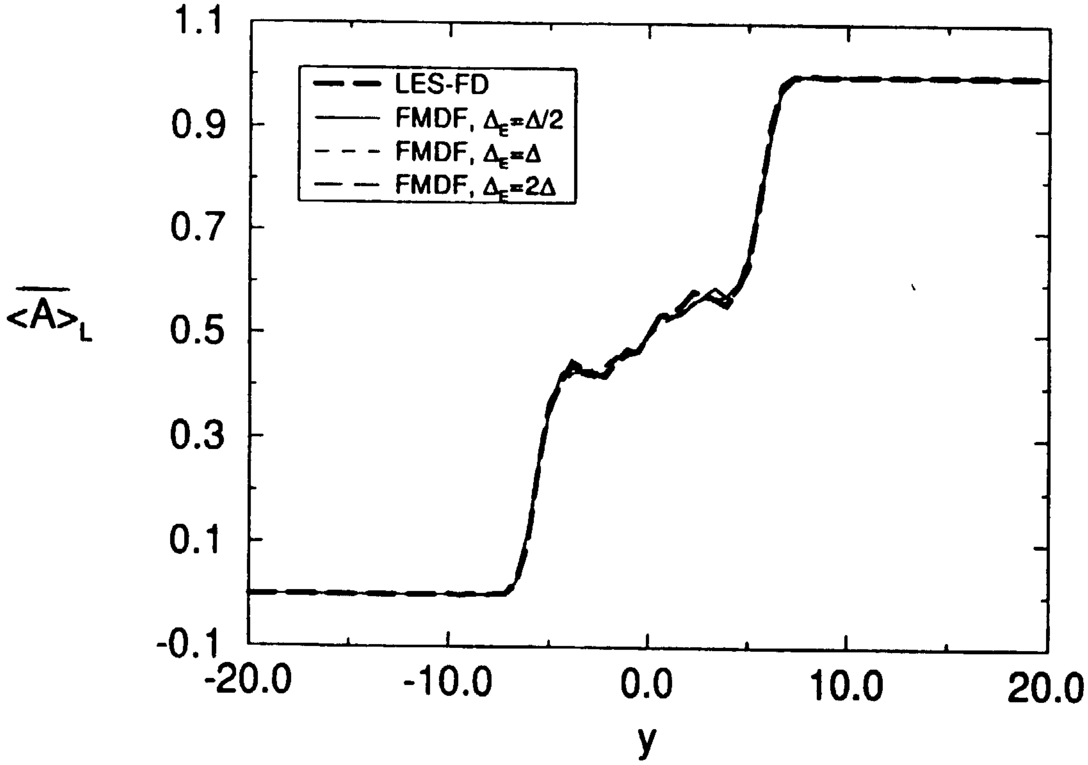
1.1
0.9
0.7
0.5
0.3
0.1
-0.1
$\overline{<A>}_L$
-20.0
-10.0
0.0
10.0
20.0
y
LES-FD
FMDF, $\Delta_E=\Delta/2$
FMDF, $\Delta_E=\Delta$
FMDF, $\Delta_E=2\Delta$

Figure 7(a)

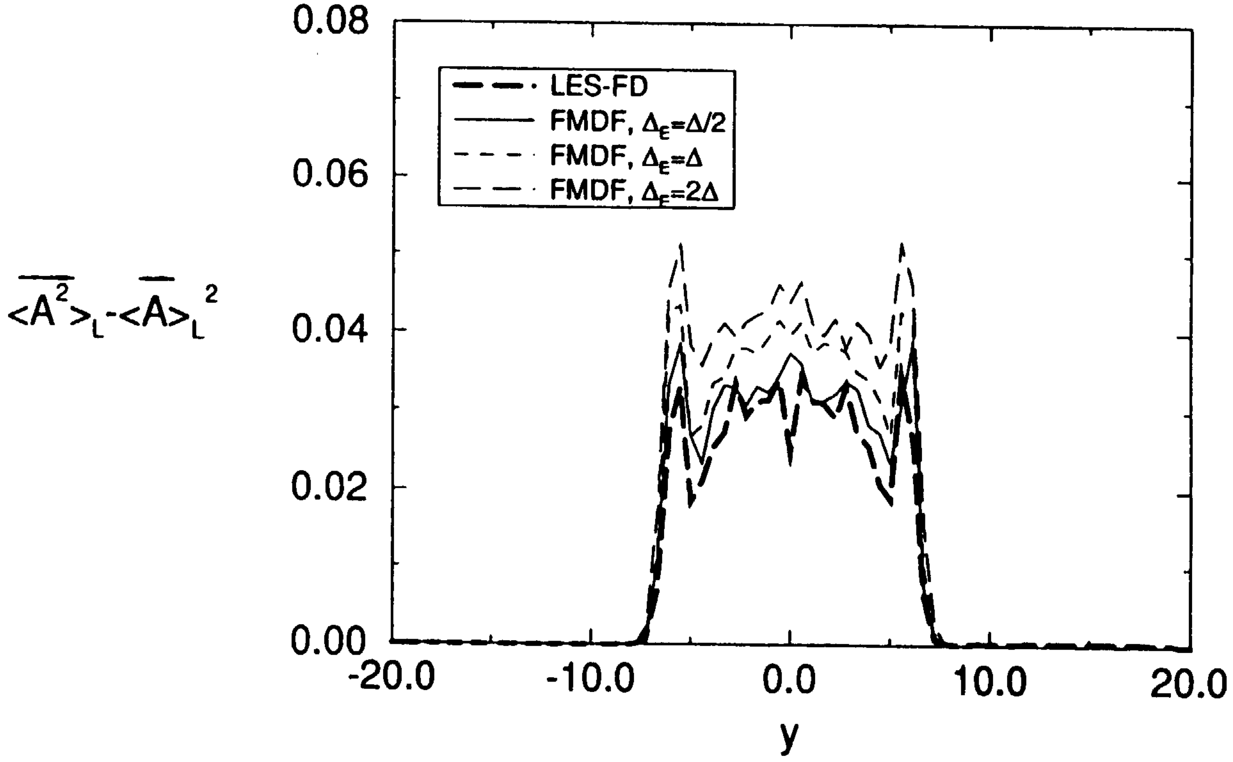

$\overline{\langle A^2 \rangle_L} - \overline{\langle A \rangle_L}^2$
0.08
0.06
0.04
0.02
0.00
-20.0
-10.0
0.0
10.0
20.0
y
LES-FD
FMDF, $\Delta_E=\Delta/2$
FMDF, $\Delta_E=\Delta$
FMDF, $\Delta_E=2\Delta$

Figure 7(b)

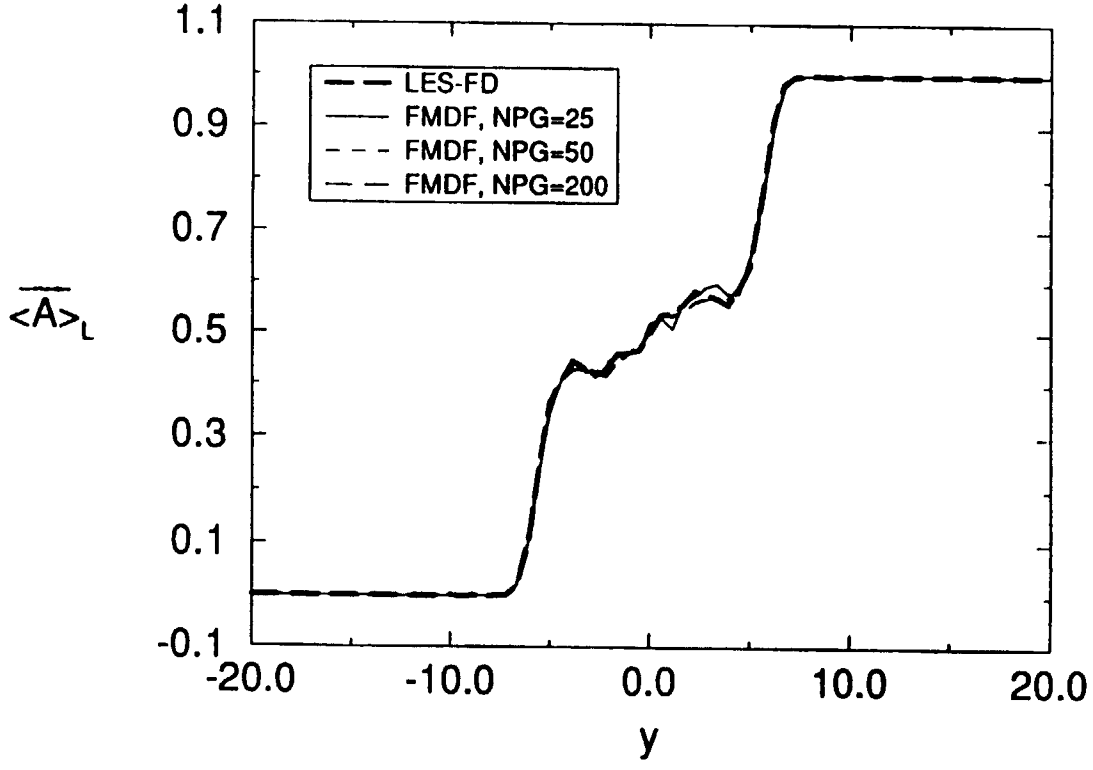
LES-FD
FMDF, NPG=25
FMDF, NPG=50
FMDF, NPG=200
$\overline{\langle A \rangle_L}$
1.1
0.9
0.7
0.5
0.3
0.1
-0.1
-20.0
-10.0
0.0
10.0
20.0
y

Figure 7(c)

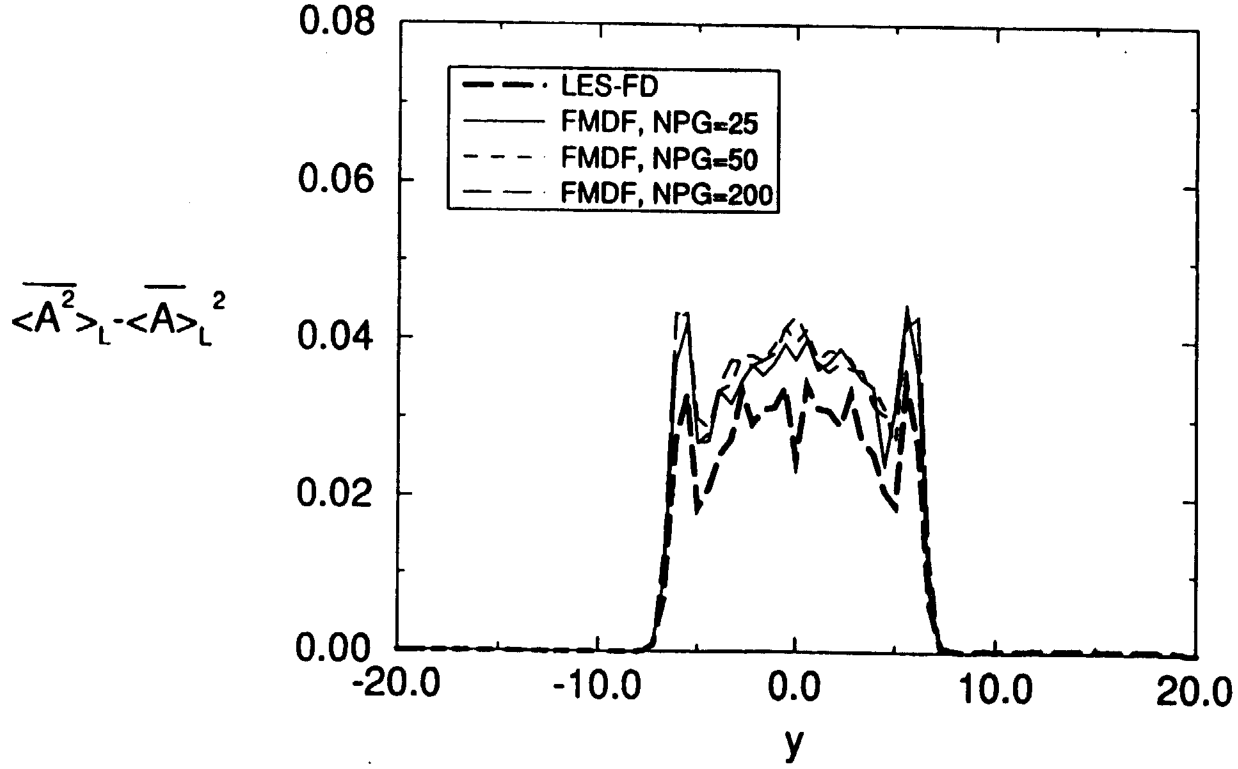
0.08
0.06
0.04
0.02
0.00
$\overline{<A^2>_L} - \overline{<A>_L}^2$
-20.0
-10.0
0.0
10.0
20.0
y
LES-FD
FMDF, NPG=25
FMDF, NPG=50
FMDF, NPG=200

Figure 7(d)

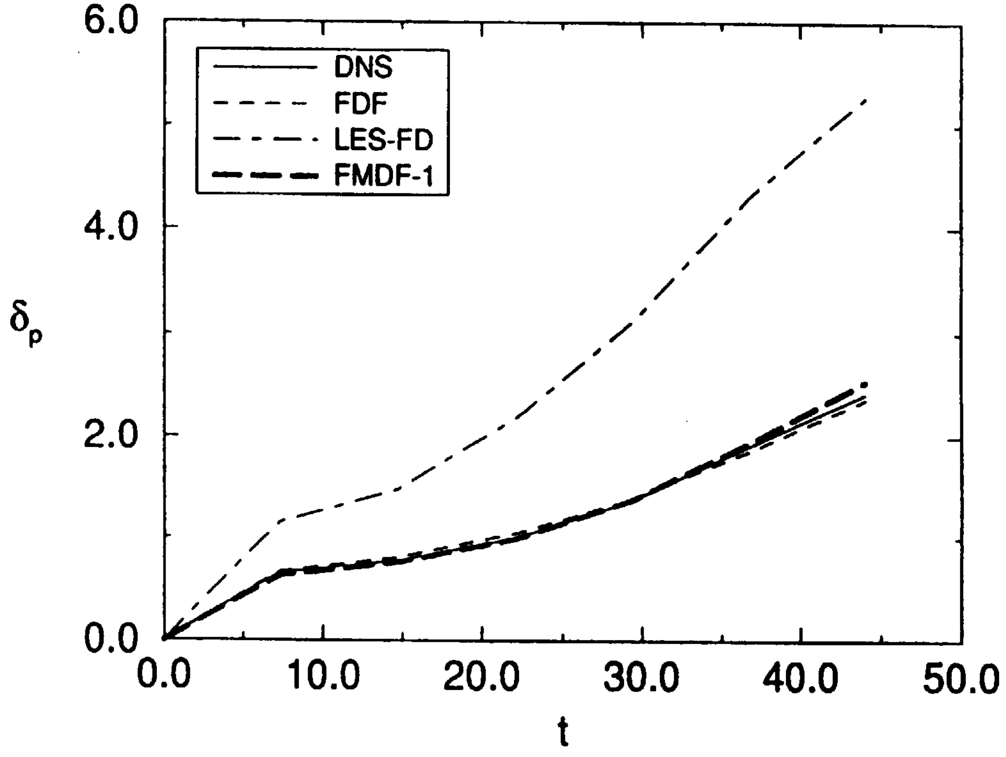

Figure 8

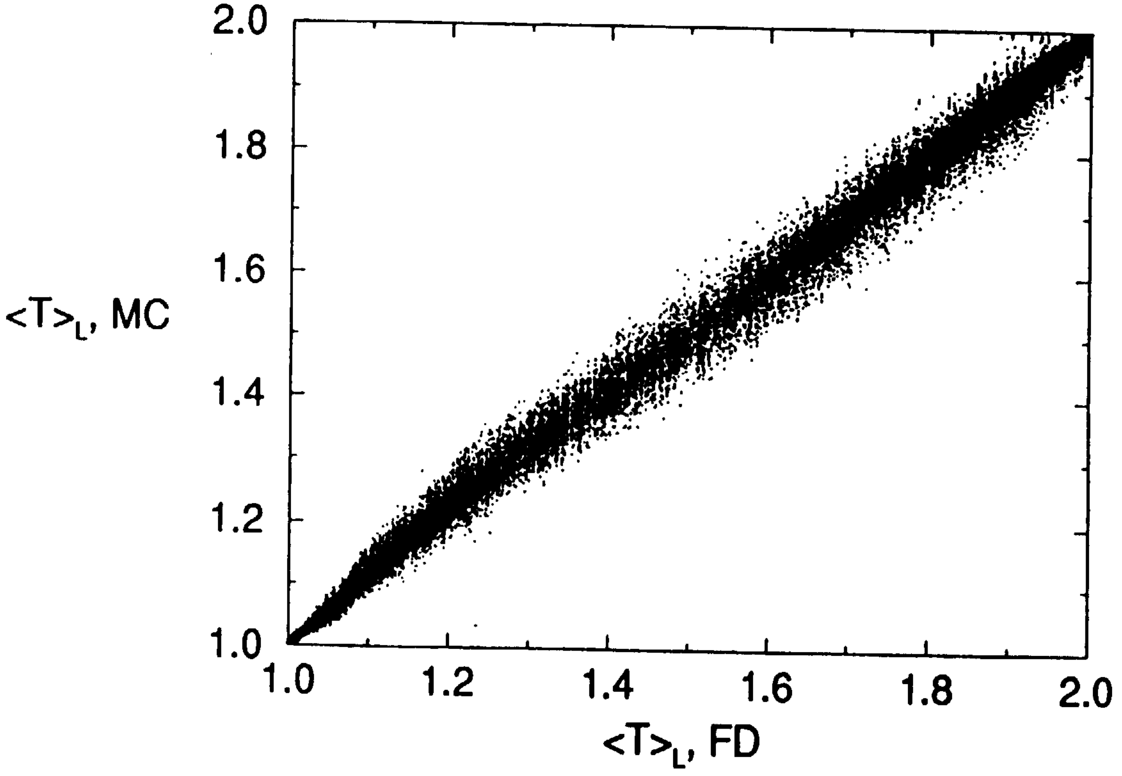

Figure 9(a)

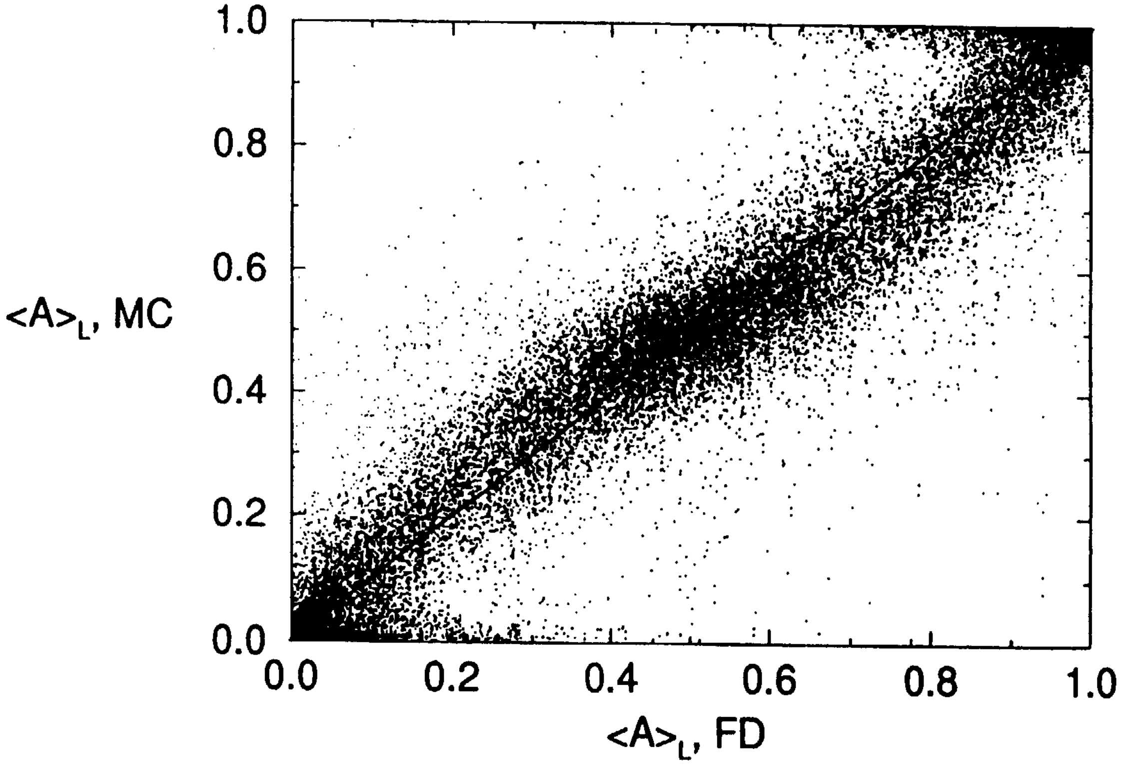
1.0
0.8
0.6
0.4
0.2
0.0
$\langle A \rangle_L$, MC
0.0
0.2
0.4
0.6
0.8
1.0
$\langle A \rangle_L$, FD

Figure 9(b)

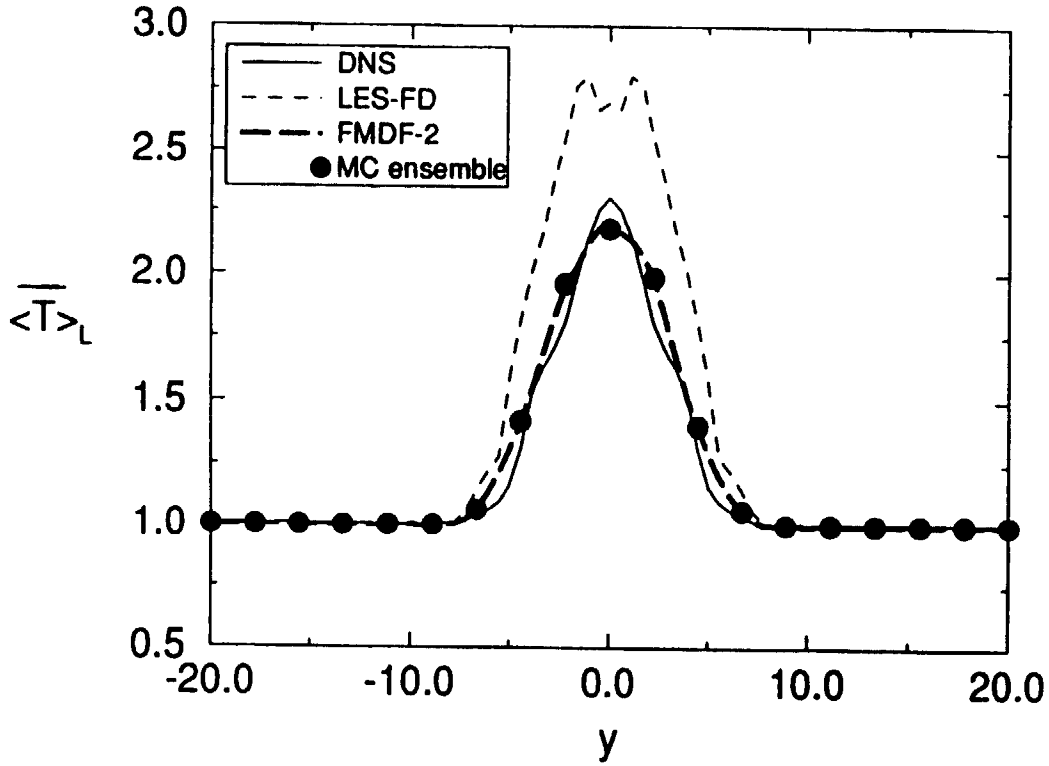
3.0
2.5
2.0
1.5
1.0
0.5
$\overline{\langle T \rangle_L}$
-20.0
-10.0
0.0
10.0
20.0
y
DNS
LES-FD
FMDF-2
MC ensemble

Figure 10

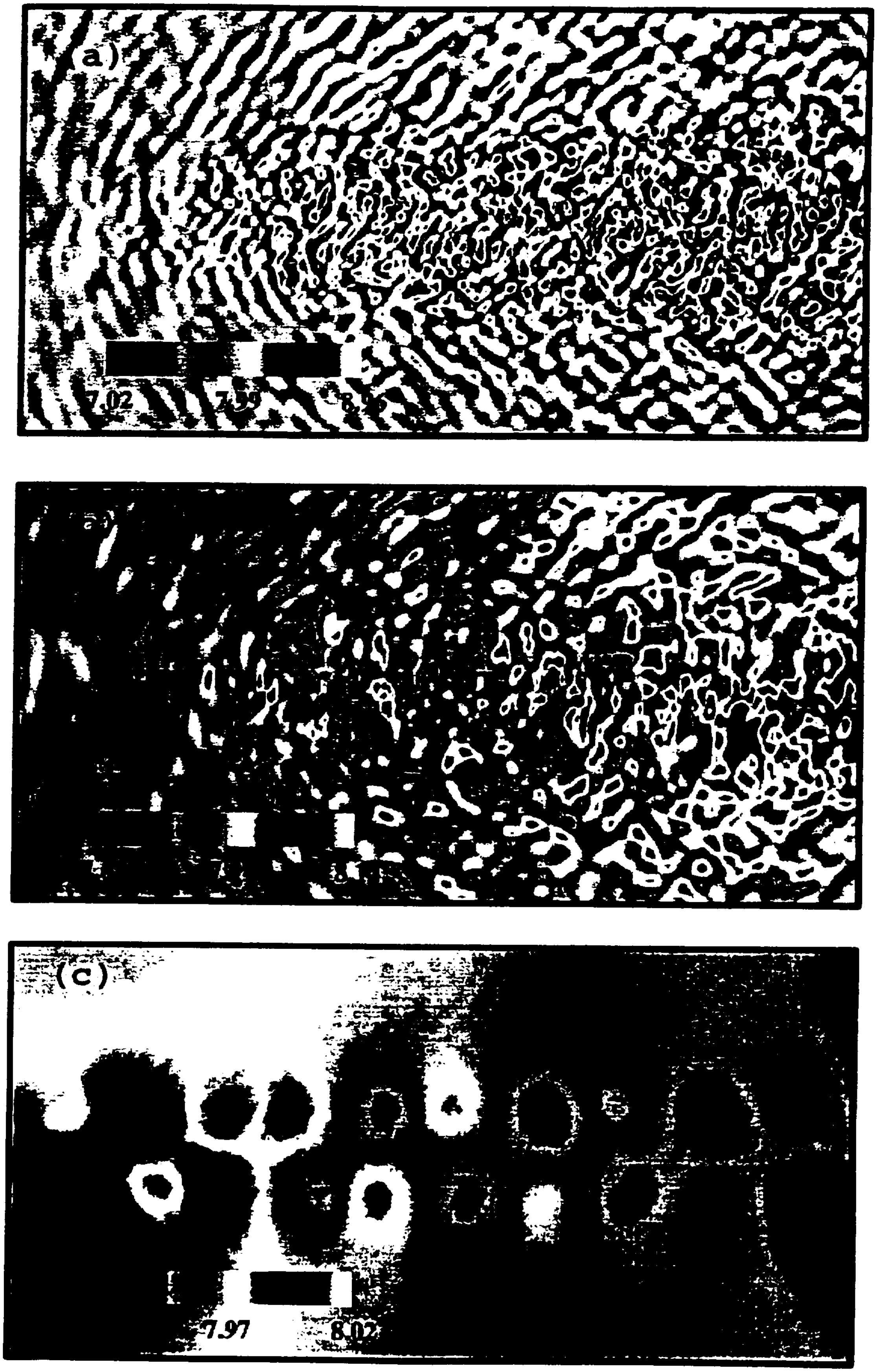

Figure 11

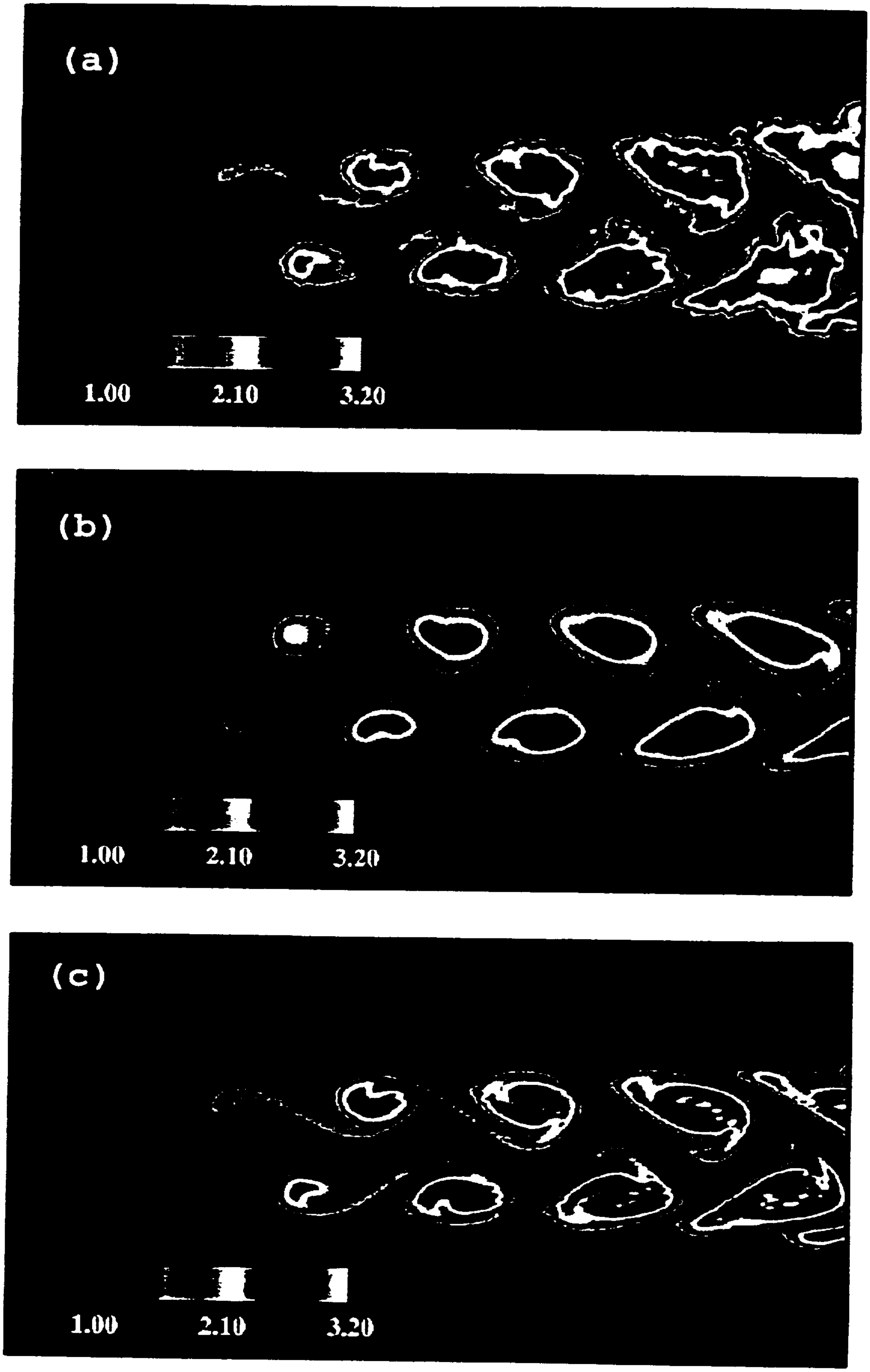

Figure 12

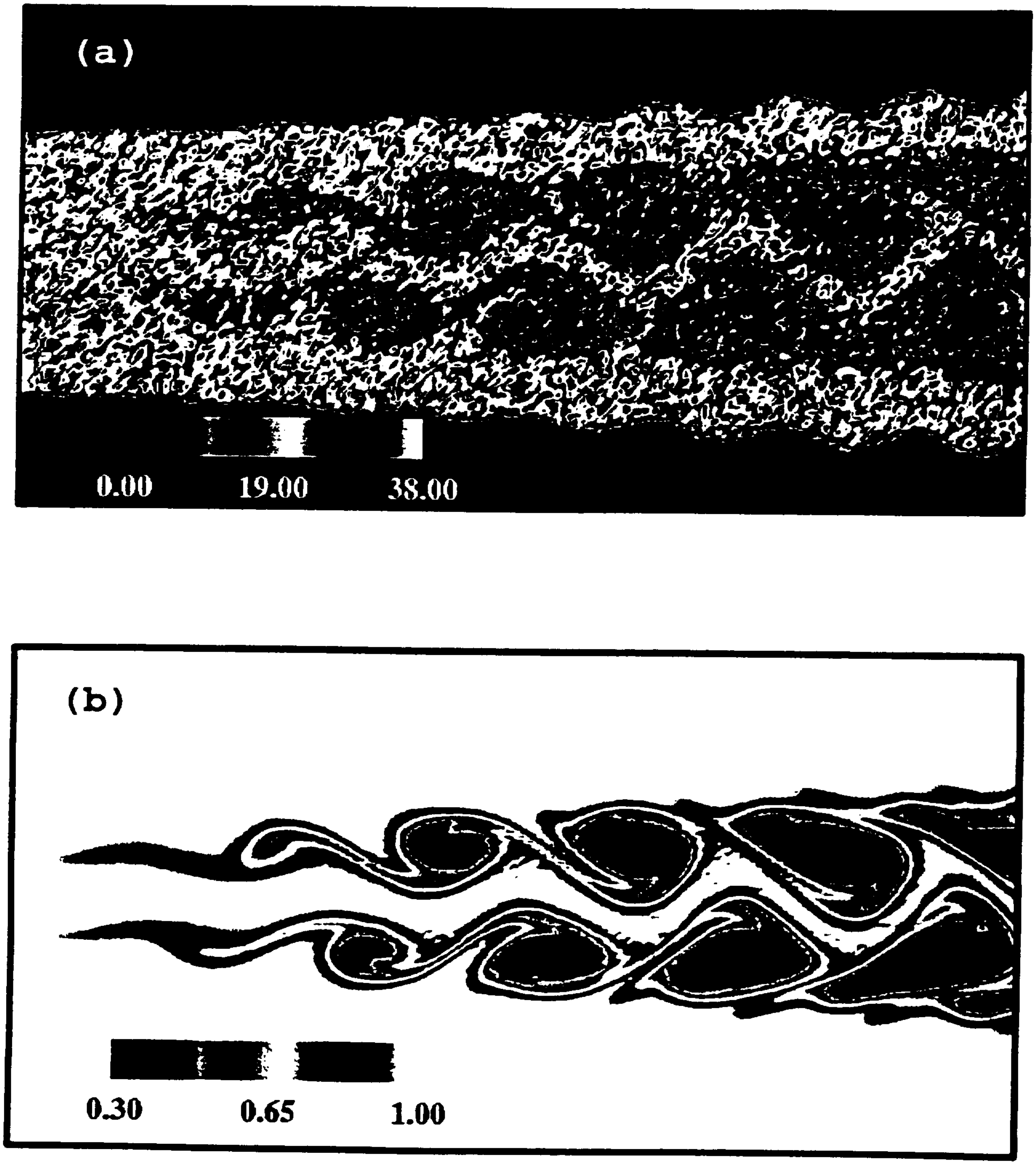

Figure 13

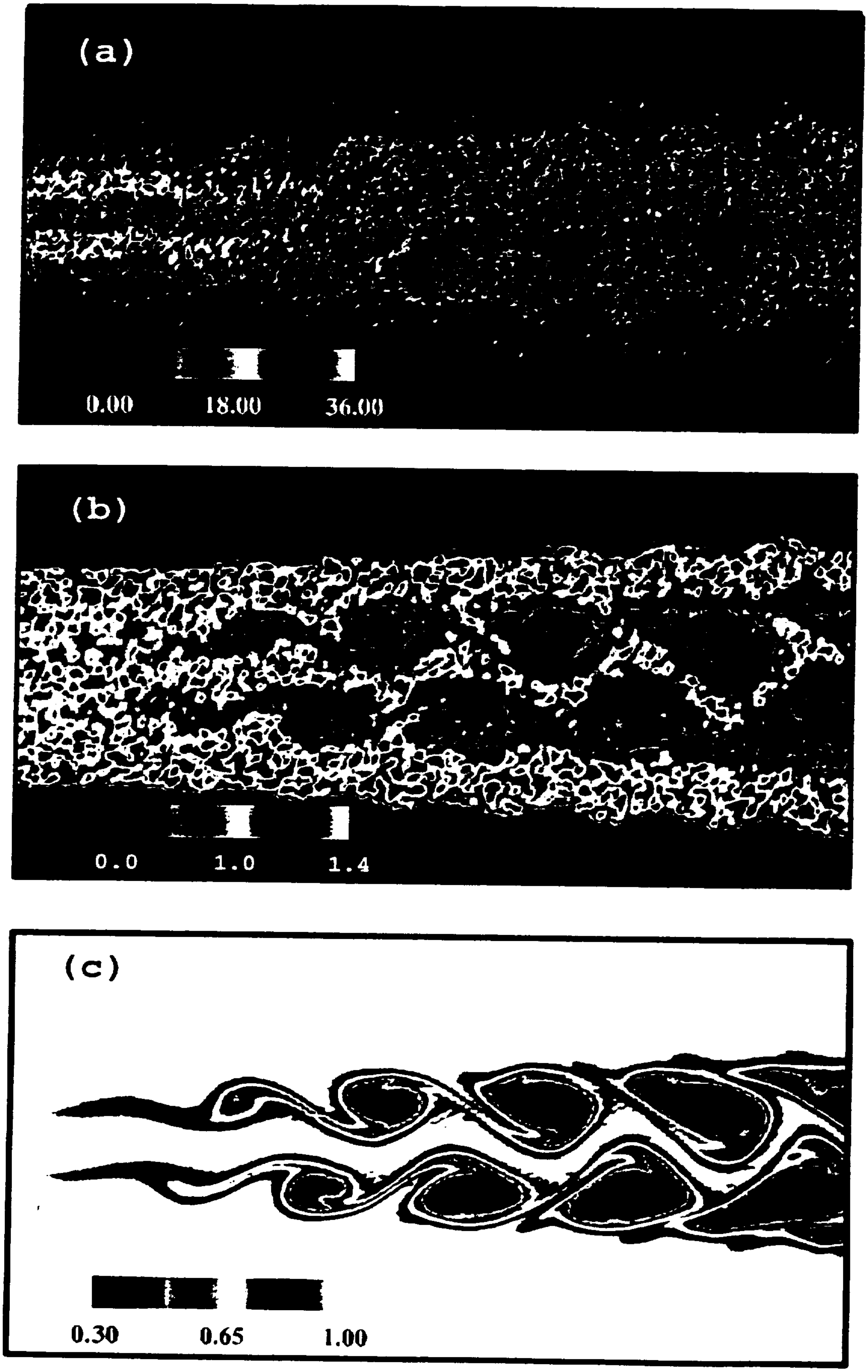

Figure 14

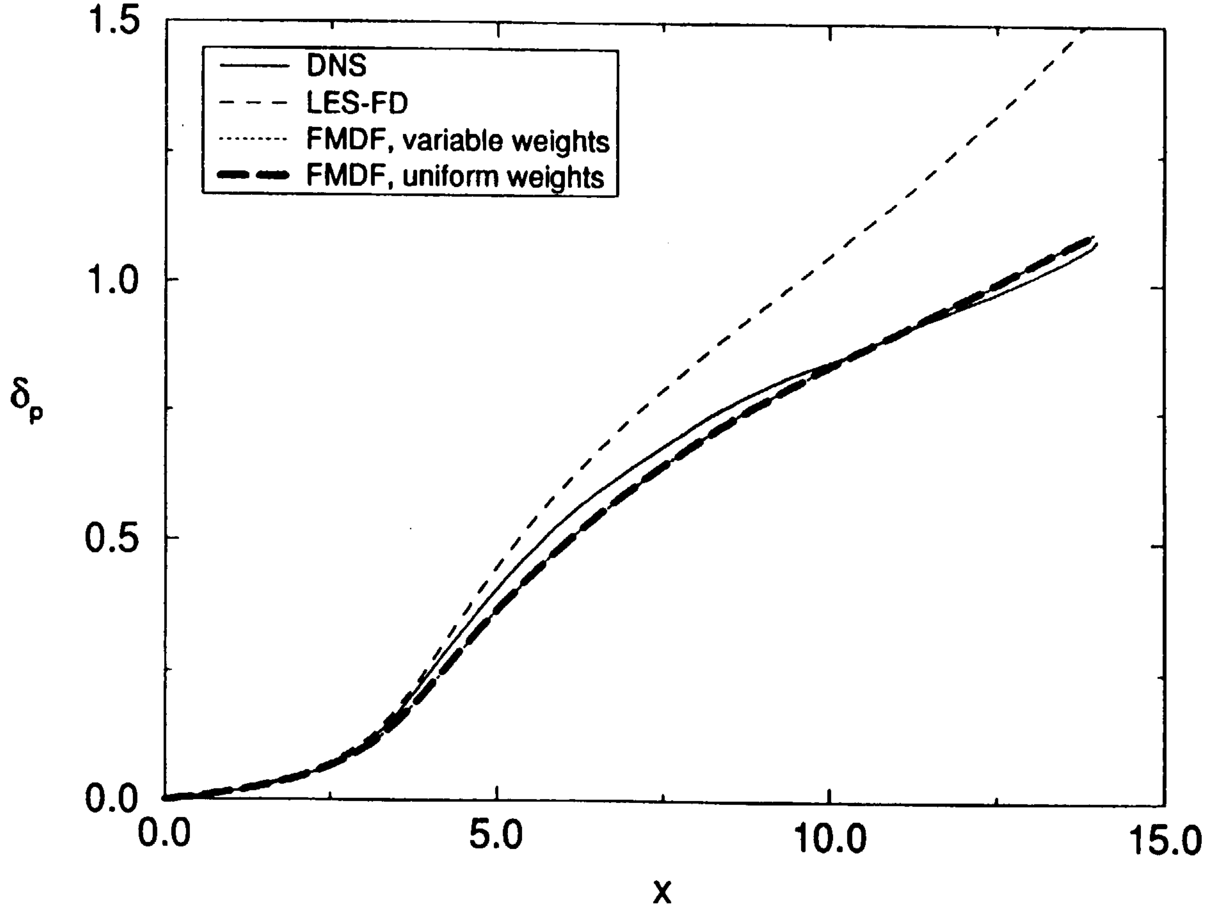
1.5
1.0
0.5
0.0
δ_p
0.0
5.0
10.0
15.0
x
DNS
LES-FD
FMDF, variable weights
FMDF, uniform weights

Figure 15

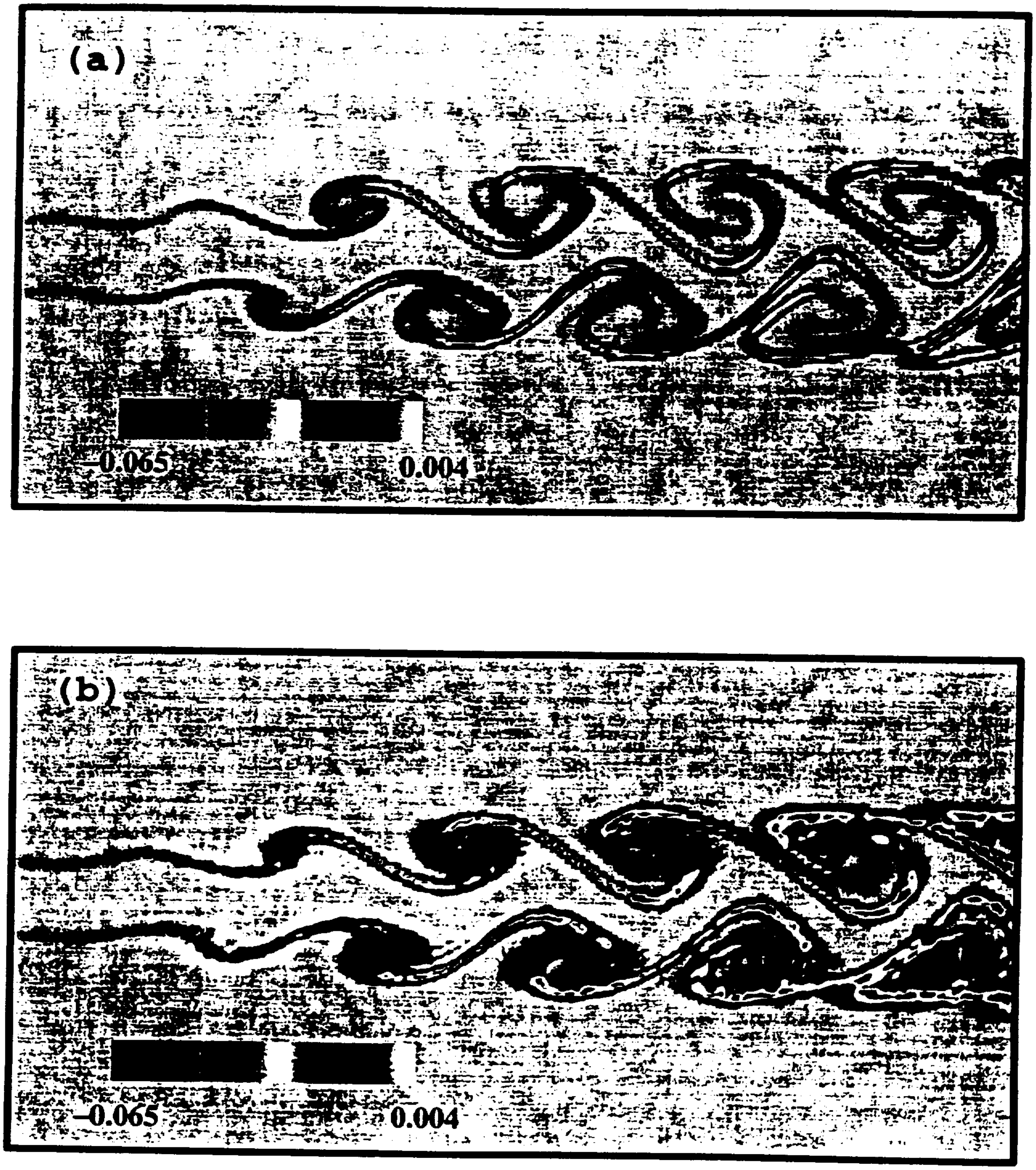

Figure 16

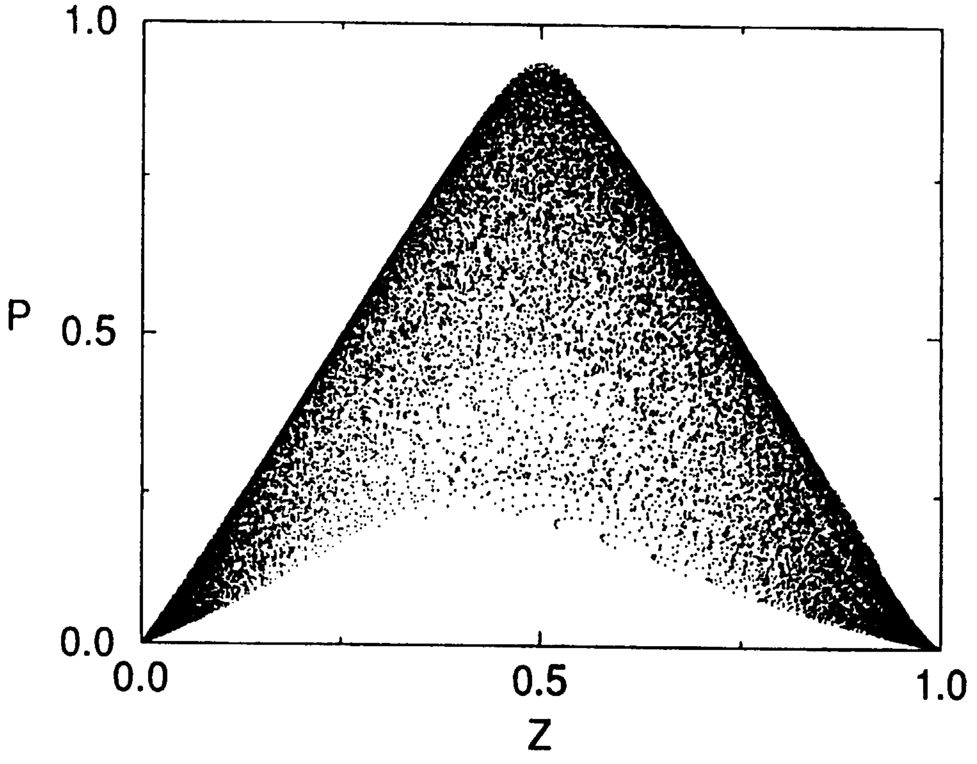

Figure 17(a)

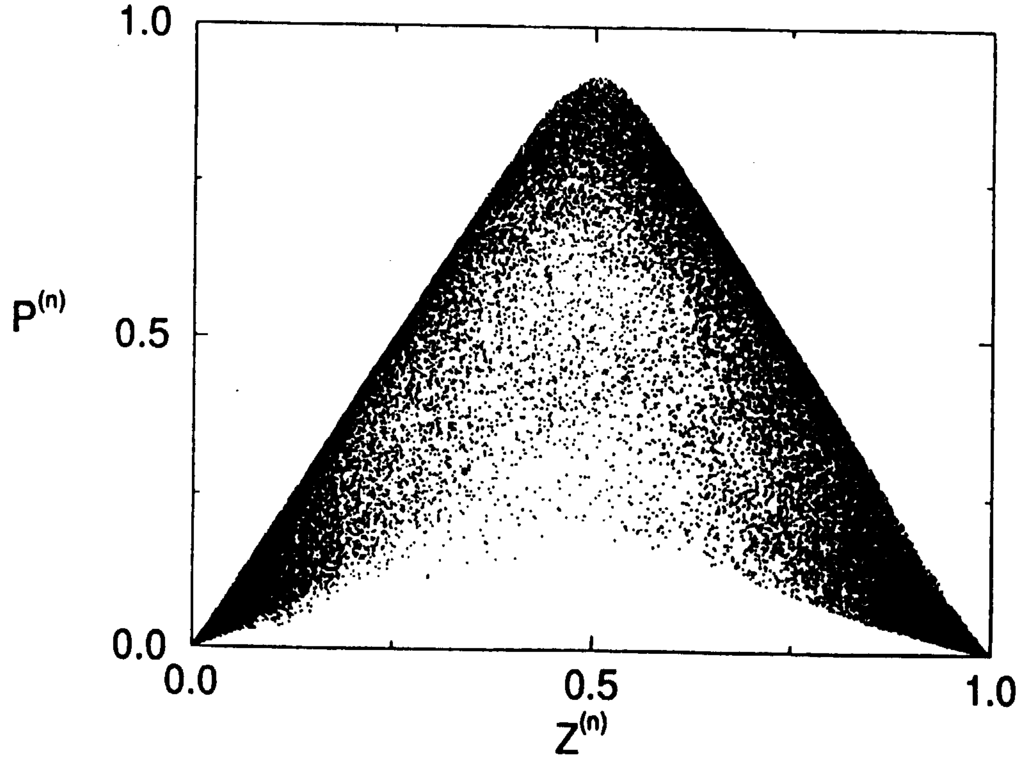

Figure 17(b)

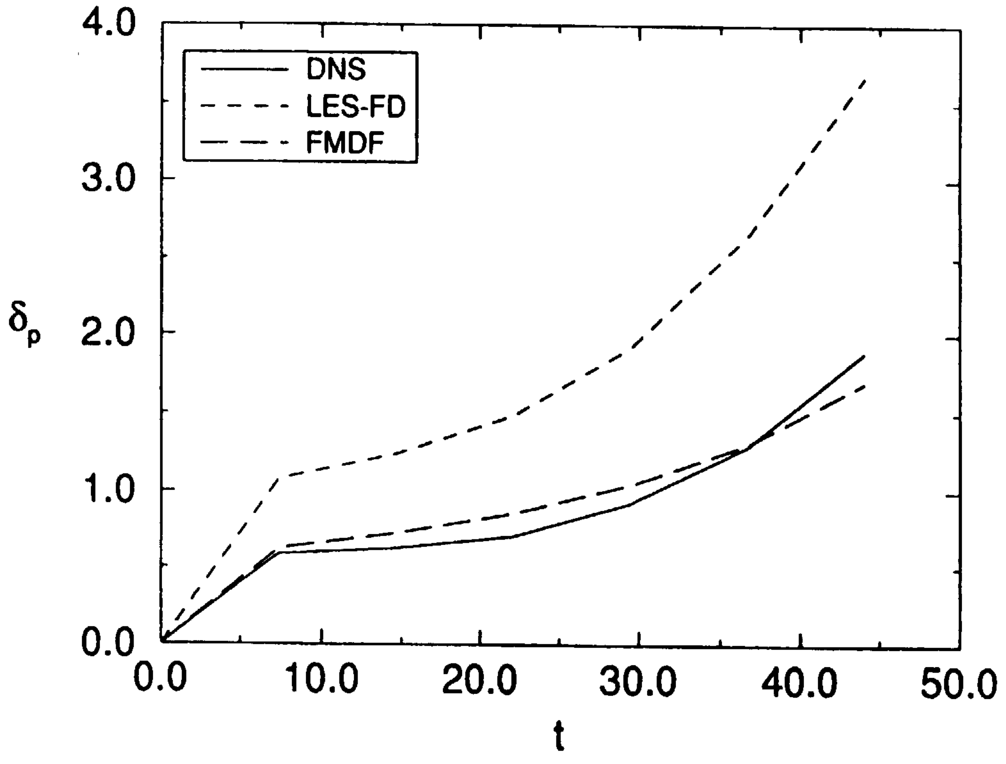

Figure 18(a)

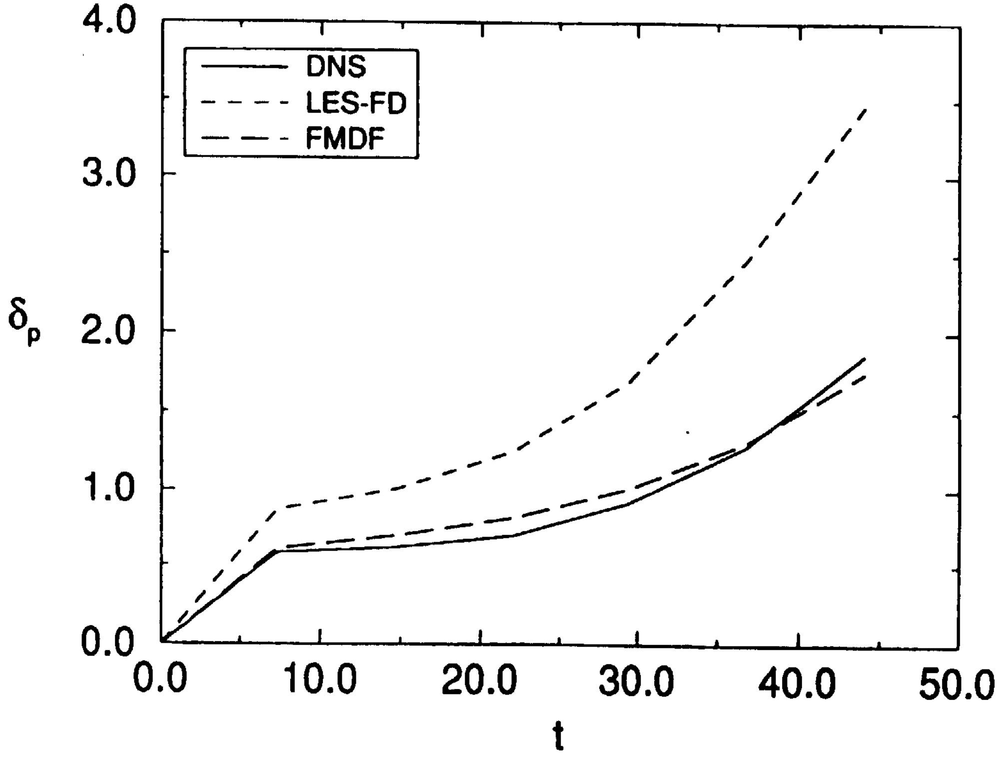

Figure 18(b)

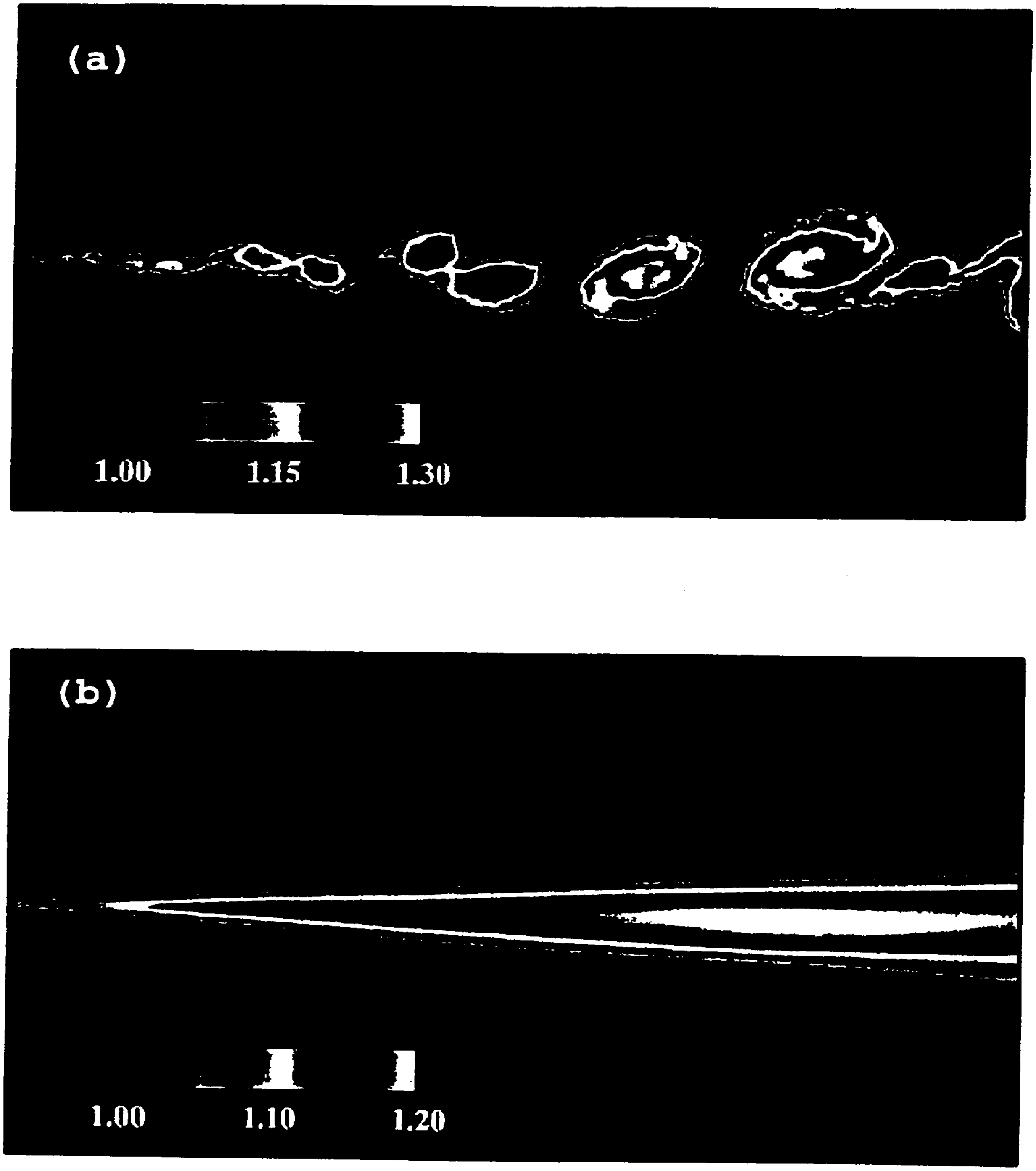

Figure 19

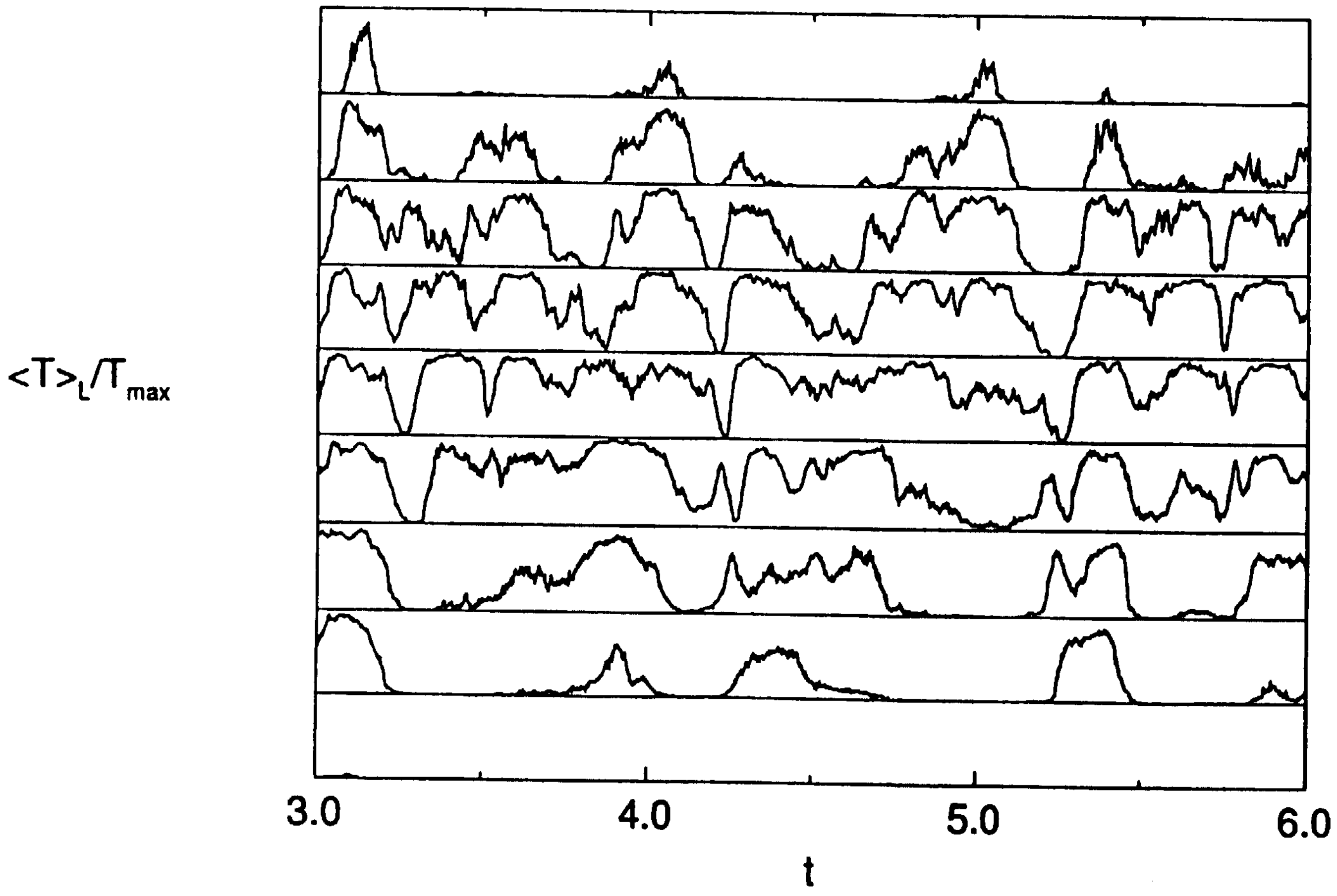

Figure 20

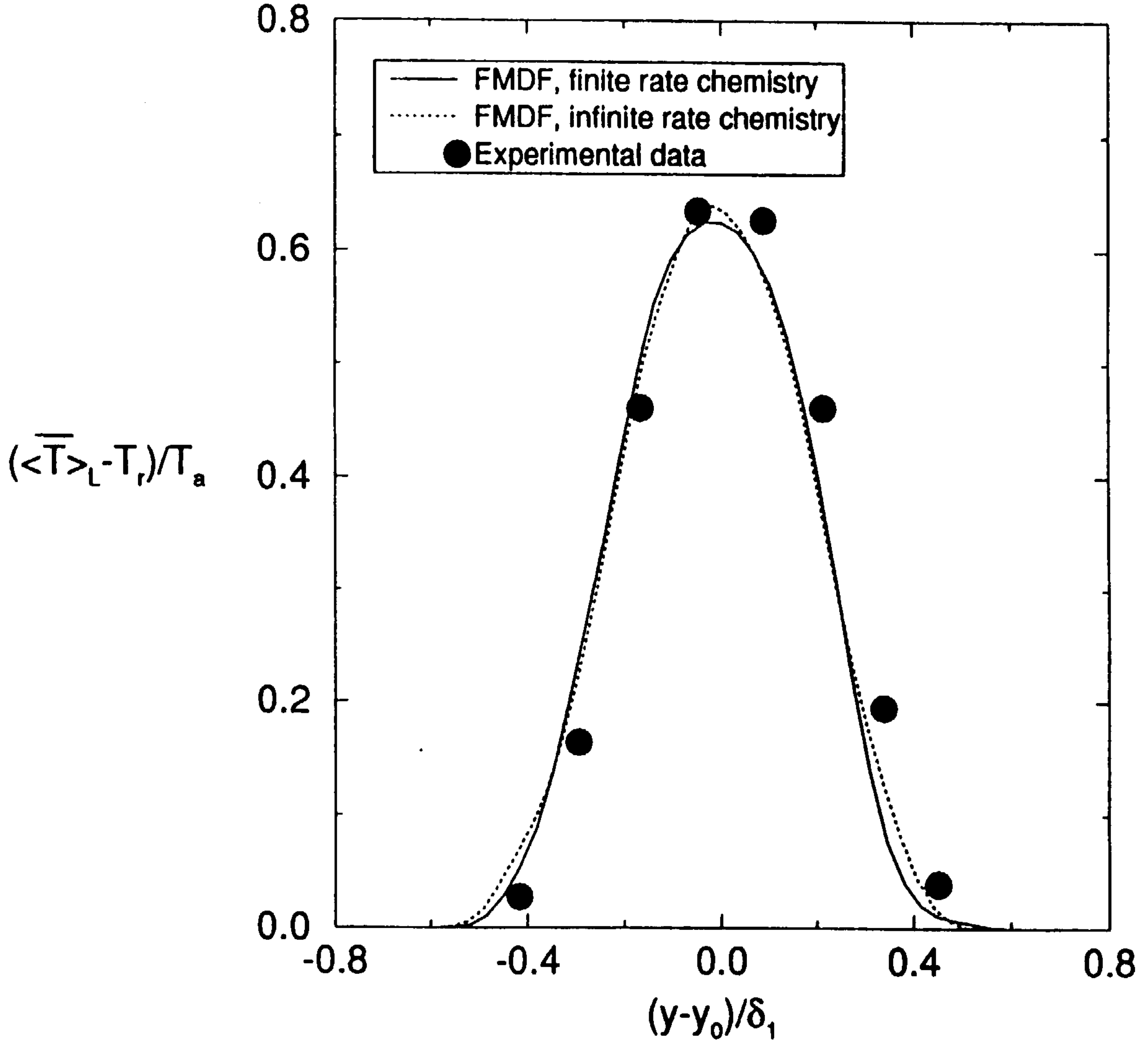

FMDF, finite rate chemistry
FMDF, infinite rate chemistry
Experimental data
0.8
0.6
0.4
0.2
0.0
-0.8
-0.4
0.0
0.4
0.8
$(\langle\overline{T}\rangle_L - T_r)/T_a$
$(y-y_0)/\delta_1$

Figure 21

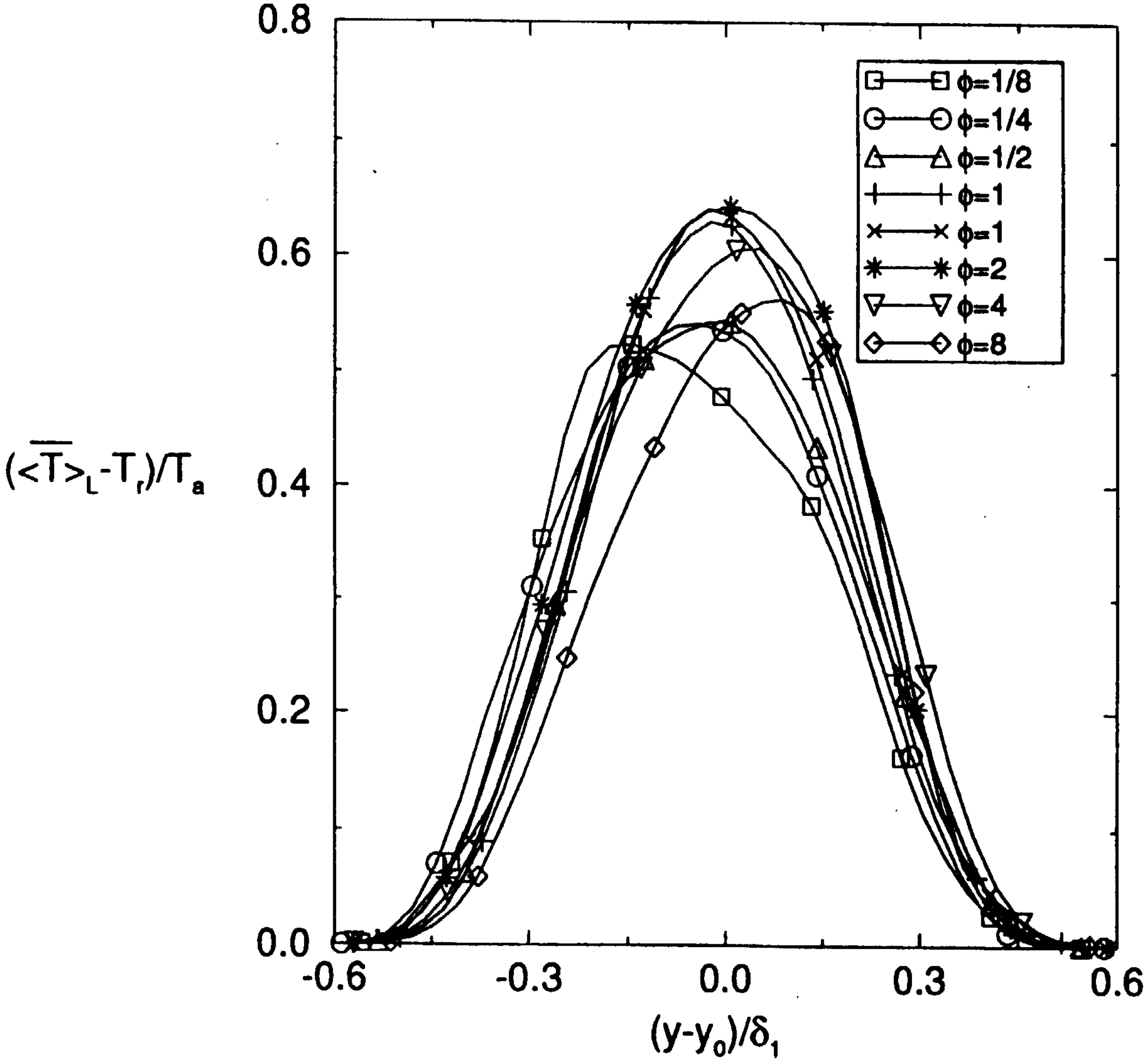

0.8
0.6
0.4
0.2
0.0
-0.6
-0.3
0.0
0.3
0.6
$(\overline{<T>}_L - T_r)/T_a$
$(y-y_0)/\delta_1$
ϕ=1/8
ϕ=1/4
ϕ=1/2
ϕ=1
ϕ=1
ϕ=2
ϕ=4
ϕ=8

Figure 22

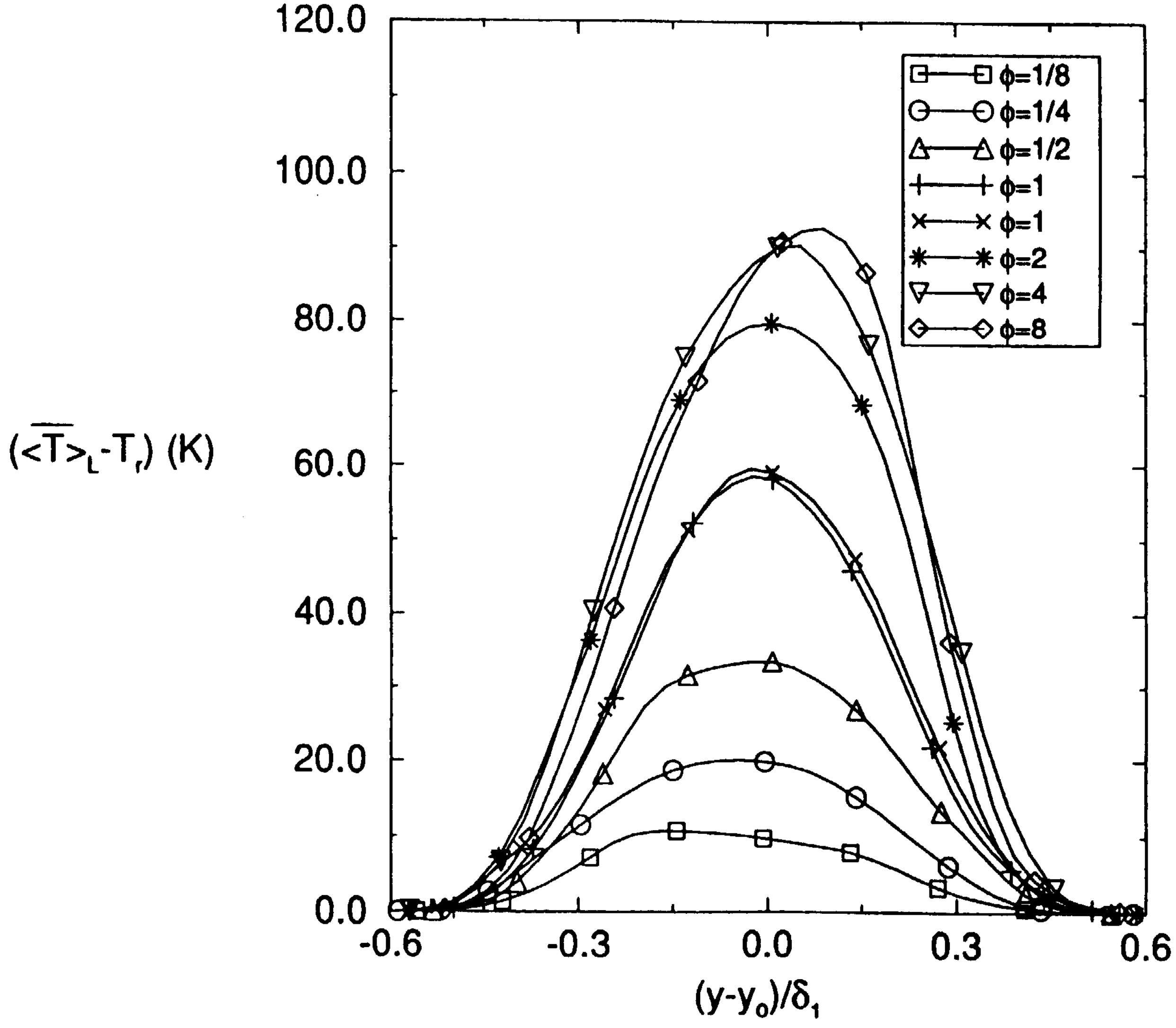
120.0
100.0
80.0
60.0
40.0
20.0
0.0
$(\overline{\langle T\rangle}_L - T_r)$ (K)
-0.6
-0.3
0.0
0.3
0.6
$(y-y_o)/\delta_1$
ϕ=1/8
ϕ=1/4
ϕ=1/2
ϕ=1
ϕ=1
ϕ=2
ϕ=4
ϕ=8

Figure 23(a)

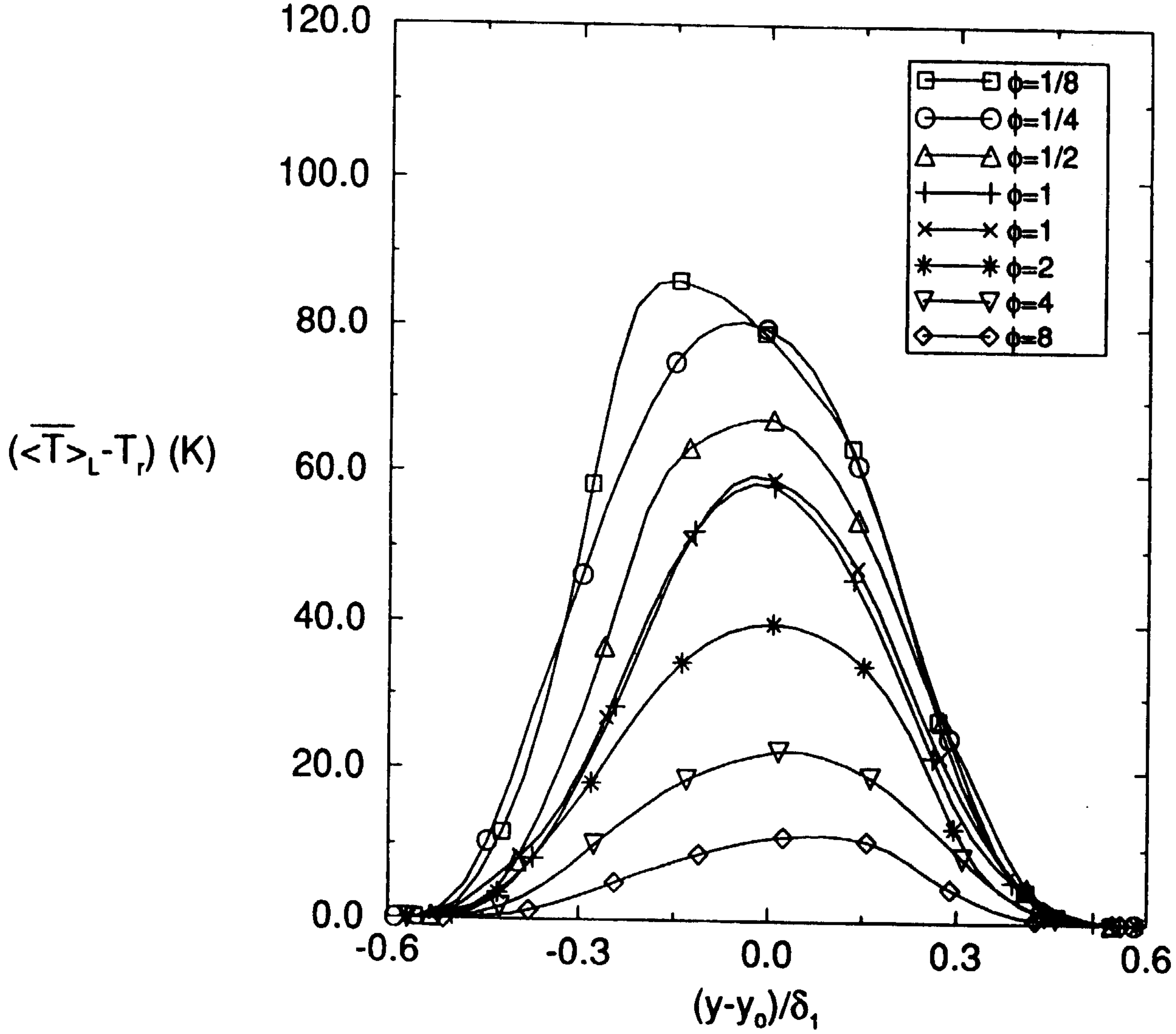
120.0
100.0
80.0
60.0
40.0
20.0
0.0
$(\overline{<T>}_L-T_r)$ (K)
-0.6
-0.3
0.0
0.3
0.6
$(y-y_0)/\delta_1$
ϕ=1/8
ϕ=1/4
ϕ=1/2
ϕ=1
ϕ=1
ϕ=2
ϕ=4
ϕ=8

Figure 23(b)

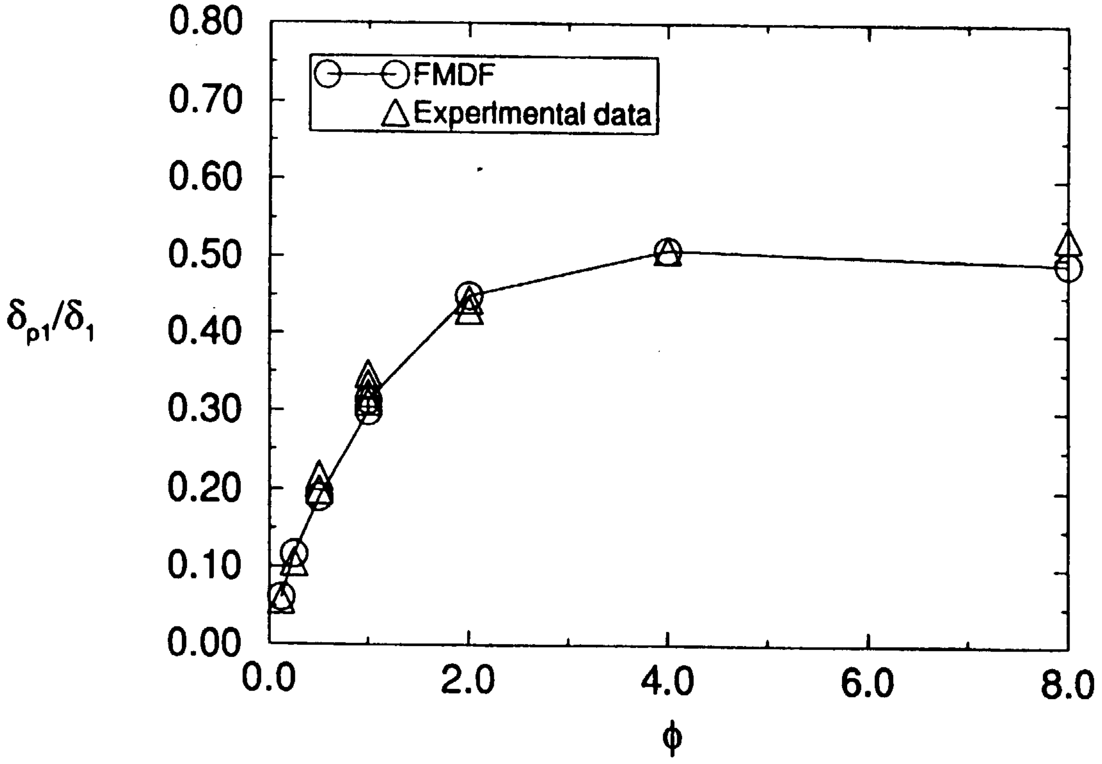
FMDF
Experimental data
0.80
0.70
0.60
0.50
0.40
0.30
0.20
0.10
0.00
δ_{p1}/δ_1
0.0
2.0
4.0
6.0
8.0
ϕ

Figure 24(a)

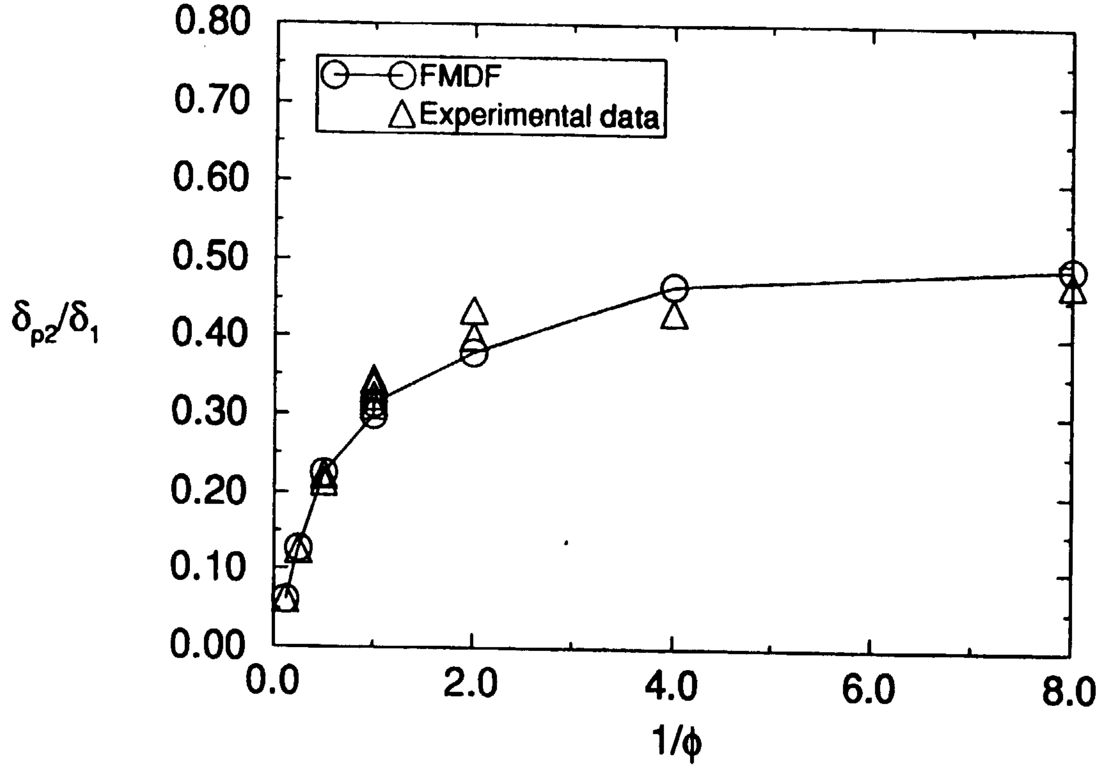

FMDF
Experimental data
δ_{p2}/δ_1
0.80
0.70
0.60
0.50
0.40
0.30
0.20
0.10
0.00
0.0
2.0
4.0
6.0
8.0
$1/\phi$

Figure 24 (b)

Appendix III

Large Eddy Simulation of Scalar Transport in a Turbulent Jet Flow

LARGE EDDY SIMULATION OF SCALAR TRANSPORT IN A TURBULENT JET FLOW

S.C. GARRICK
Department of Mechanical Engineering
University of Minnesota
Minneapolis, MN 55455-0111

AND

F.A. JABERI AND P. GIVI
Department of Mechanical & Aerospace Engineering
State University of New York - Buffalo
Buffalo, NY 14260-4400

1. Introduction

Large eddy simulation (LES) of turbulent reacting flows has been the subject of widespread investigation (McMurtry *et al.*, 1992; Galperin and Orszag, 1993; Menon *et al.*, 1993; McMurtry *et al.*, 1993; Gao and O'Brien, 1993; Madnia and Givi, 1993; Frankel *et al.*, 1993; Cook and Riley, 1994; Givi, 1994; Fureby and Lofstrom, 1994; Möller *et al.*, 1996; Branley and Jones, 1997; Cook *et al.*, 1997; Jiménez *et al.*, 1997; Mathey and Chollet, 1997; Colucci *et al.*, 1998; DesJardin and Frankel, 1998; Jaberi and James, 1998; Réveillon and Vervisch, 1998; Vervisch and Poinsot, 1988). Amongst these, recently Colucci *et al.* (1998) developed a methodology, termed the "filtered density function" (FDF). The fundamental property of the FDF is to account for the effects of subgrid scale (SGS) scalar fluctuations in a probabilistic manner. This is similar to probability density function (PDF) methods which have proven to be very useful in Reynolds averaging procedures (Libby and Williams, 1980; Libby and Williams, 1994; O'Brien, 1980; Pope, 1985; Dopazo, 1994). Colucci *et al.* (1998) developed a transport equation for the FDF in constant density flows in which the effects of unresolved convection and subgrid mixing are modeled similarly to those in "conventional" LES, and Reynolds averaging procedures. This transport equation was solved numerically by a Lagrangian Monte Carlo procedure and the results were compared with those obtained by direct numerical simulation (DNS) and by a conventional finite difference LES in which the effects of SGS scalar fluctuations are ignored (LES-FD). It was shown that in non-reacting flows, the first two SGS moments of the FDF, as obtained by the Monte Carlo solution, are close to those obtained by LES-FD. The advantage of the FDF was demonstrated in reacting flows in which its results were shown to deviate significantly from those obtained by LES-FD but compare favorably with DNS data. The encouraging results generated by FDF warrant its extension and application to more complex flows. Further assessment of its predictive capability is also in order. The primary objective in this work is to extend the FDF methodology for LES of three-dimensional (3D) turbulent reacting jet flows. The FDF deals only with scalar quantities; the hydrodynamic field is obtained via conventional LES.

2. Formulation

We consider constant density turbulent reacting jet flows involving N_s species. The primary transport variables are the velocity vector $u_i(\underline{x}, t)$, $(i = 1, 2, 3)$, the fluid pressure $p(\underline{x}, t)$, and the species' mass fractions $\phi_\alpha(\underline{x}, t)$ $(\alpha = 1, 2, ..., N_s)$. These variables are governed by the conservation equations:

$$\frac{\partial u_j}{\partial x_j} = 0, \tag{1}$$

$$\frac{\partial u_i}{\partial t} + \frac{\partial u_i u_j}{\partial x_j} = -\frac{\partial p}{\partial x_i} + \frac{\partial \tau_{ij}}{\partial x_j}, \tag{2}$$

$$\frac{\partial \phi_\alpha}{\partial t} + \frac{\partial \phi_\alpha u_j}{\partial x_j} = -\frac{\partial J_j{}^\alpha}{\partial x_j} + \omega_\alpha, \tag{3}$$

where ω_α is the chemical source term. Assuming a Newtonian fluid and Fickian diffusion,

$$\tau_{ij} = \nu \left(\frac{\partial u_i}{\partial x_j} + \frac{\partial u_j}{\partial x_i} \right), \quad J_j^\alpha = -\Gamma \frac{\partial \phi_\alpha}{\partial x_j}, \tag{4}$$

where ν is the kinematic viscosity, $\Gamma = \frac{\nu}{Sc}$ is the molecular diffusivity and Sc is the molecular Schmidt Number. Large eddy simulation involves the use of the spatial filtering operation (Aldama, 1990; Moin, 1991)

$$\langle \phi(\underline{x}, t) \rangle_L = \int_{-\infty}^{+\infty} h_s(\underline{x} - \underline{x}') \phi(\underline{x}', t), d\underline{x}' \tag{5}$$

where $h_s(\underline{x})$ denotes the filter function of width Δ_H, and $\langle \phi(\underline{x}, t) \rangle_L$ represents the filtered value of the transport variable $\phi(\underline{x}, t)$. We consider spatially & temporally invariant, localized and "positive" filter functions (Vreman *et al.*, 1994). The application of the filtering operation to the transport equations yields:

$$\frac{\partial \langle u_j \rangle_L}{\partial x_j} = 0 \tag{6}$$

$$\frac{\partial \langle u_i \rangle_L}{\partial t} + \frac{\partial \langle u_i \rangle_L \langle u_j \rangle_L}{\partial x_j} = -\frac{\partial \langle p \rangle_L}{\partial x_i} + \frac{\partial \langle \tau_{ij} \rangle_L}{\partial x_j} - \frac{\partial T_{ij}}{\partial x_j} \tag{7}$$

$$\frac{\partial \langle \phi_\alpha \rangle_L}{\partial t} + \frac{\partial \langle u_j \rangle_L \langle \phi_\alpha \rangle_L}{\partial x_j} = -\frac{\partial \langle J_j^\alpha \rangle_L}{\partial x_j} - \frac{\partial M_j^\alpha}{\partial x_j} + \langle \omega_\alpha \rangle_L \tag{8}$$

where $T_{ij} = \langle u_i u_j \rangle_L - \langle u_i \rangle_L \langle u_j \rangle_L$ and $M_j^\alpha = \langle u_j \phi_\alpha \rangle_L - \langle u_j \rangle_L \langle \phi_\alpha \rangle_L$ denote the SGS stress and the SGS mass flux, respectively.

The closure problem in LES of non-reacting flows is essentially one of representing the unresolved terms T_{ij} and M_j^α. In reacting flows, the problem is compounded by the presence of the chemical source term $\langle \omega_\alpha \rangle_L$, for which an additional model is required. For closure of the hydrodynamic SGS stresses, the gradient-diffusion approximation is invoked:

$$T_{ij} - (\delta_{ij}/3) T_{kk} = -2\nu_t \langle S_{ij} \rangle_L \tag{9}$$

where $\langle S_{ij} \rangle_L$ is the resolved strain rate tensor and ν_t is the SGS viscosity modeled via the modified kinetic energy model (MKEV) (Colucci *et al.*, 1998):

$$\nu_t = C_k \Delta_H \sqrt{|\langle u_i^* \rangle_L \langle u_i^* \rangle_L - \langle \langle u_i^* \rangle_L \rangle_{L'} \langle \langle u_i^* \rangle_L \rangle_{L'}|}, \tag{10}$$

where $u_i^* = u_i - \mathcal{U}_i$ and $\mathcal{U}_i$ is a reference velocity in the x_i direction. The subscript L' denotes the filter at the secondary level which has a characteristic size (denoted by $\Delta_{H'}$) larger than that of grid level filter. The gradient-diffusion approximation is also used for closure of the SGS mass fluxes (Eidson, 1985):

$$M_j^\alpha = -\Gamma_t \frac{\partial \langle \phi_\alpha \rangle_L}{\partial x_j} \tag{11}$$

where $\Gamma_t = \nu_t / Sc_t$, and Sc_t is the SGS Schmidt number and is assumed constant.

The filtered density function (FDF) is utilized to represent the scalars in a probabilistic manner. For the scalar array $\underline{\phi}(\underline{x}, t) = [\phi_1, \phi_2, \ldots \phi_{N_s}]$, the FDF, denoted by f_L, is defined as (Pope, 1990):

$$f_L(\underline{\psi}; \underline{x}, t) \equiv \int_{-\infty}^{+\infty} \varrho \left[\underline{\psi}, \underline{\phi}(\underline{x}', t) \right] h_s(\underline{x}' - \underline{x}) d\underline{x}', \tag{12}$$

$$\varrho \left[\underline{\psi}, \underline{\phi}(\underline{x}, t) \right] = \delta[\underline{\psi} - \underline{\phi}(\underline{x}, t)] \equiv \prod_{\alpha=1}^{N_s} \delta[\psi_\alpha - \phi_\alpha(\underline{x}, t)], \tag{13}$$

where δ denotes the delta function and $\underline{\psi}$ denotes the composition domain counterpart of the scalar vector $\underline{\phi}$. The term $\varepsilon[\underline{\phi} - \underline{\psi}(\underline{x}, t)]$ is the "fine-grained" density (Lundgren, 1967; O'Brien, 1980), and Eq. (12) states that the FDF is the spatially filtered, fine-grained density. Thus, f_L gives the density in the composition space around $\underline{x}$, weighted by the filter h_s. With a positive definite filter (Vreman *et al.*, 1994), f_L has all the properties of the PDF. For further development, it is useful to define the "conditional filtered value" of the variable $Q(\underline{x}, t)$ by

$$\langle Q(\underline{x}, t)|\underline{\psi}\rangle_L \equiv \frac{\int_{-\infty}^{+\infty} Q(\underline{x}', t)\varepsilon\left[\underline{\psi}, \underline{\phi}(\underline{x}', t)\right] h_s(\underline{x}' - \underline{x})d\underline{x}'}{f_L(\underline{\psi}; \underline{x}, t)} \tag{14}$$

where $\langle\alpha|\beta\rangle_L$ denotes the filtered value of α conditioned on β. Equation (14) implies

$$\begin{array}{lll} (i) & \text{For } Q(\underline{x}, t) = c, & \langle Q(\underline{x}, t)|\underline{\psi}\rangle_L = c \\ (ii) & \text{For } Q(\underline{x}, t) \equiv \widehat{Q}(\underline{\phi}(\underline{x}, t)), & \langle Q(\underline{x}, t)|\underline{\psi}\rangle_L = \widehat{Q}(\underline{\psi}) \\ (iii) & \text{Integral property}: & \langle Q(\underline{x}, t)\rangle_L = \displaystyle\int_{-\infty}^{+\infty} \langle Q(\underline{x}, t)|\underline{\psi}\rangle_L f_L(\underline{\psi}; \underline{x}, t)d\underline{\psi} \end{array} \tag{15}$$

where c is a constant, and $\widehat{Q}(\underline{\phi}(\underline{x}, t)) \equiv Q(\underline{x}, t)$ denotes the case where the variable Q can be completely described by the compositional variable $\underline{\phi}(\underline{x}, t)$. These properties, in conjunction with the FDF, facilitate the calculation of the moments involving the scalar variables via integration over composition space,

$$\langle Q(\underline{x}, t)\rangle_L = \int_{-\infty}^{+\infty} \widehat{Q}(\underline{\psi}) f_L(\underline{\psi}; \underline{x}, t)d\underline{\psi}. \tag{16}$$

The FDF transport equation is obtained by taking the time derivative of Eq. (12) and making use of Eq. (3):

$$\begin{aligned} \frac{\partial f_L}{\partial t} + \frac{\partial\langle u_j\rangle_L f_L}{\partial x_j} \quad = \quad & -\frac{\partial[\langle u_j|\underline{\psi}\rangle_L - \langle u_j\rangle_L]f_L}{\partial x_j} \\ & + \frac{\partial}{\partial\psi_\alpha}\left[\left\langle \frac{\partial J_j^\alpha}{\partial x_j}|\underline{\psi}\right\rangle_L f_L\right] - \frac{\partial[\widehat{\omega}_\alpha(\underline{\psi})f_L]}{\partial\psi_\alpha}. \end{aligned} \tag{17}$$

This is an exact transport equation for the FDF. The last term on the RHS is due to chemical reaction and is in a closed form. The second term on the left hand side represents the filtered convection of the FDF in physical space and is also closed (provided $\langle u_i\rangle_L$ is known). The unclosed terms are the first two terms on the RHS which represents the transport of the FDF via SGS convection and the effects of diffusion in composition space. The SGS convective flux is modeled via the gradient-diffusion approximation.

$$[\langle u_j|\underline{\psi}\rangle_L - \langle u_j\rangle_L]f_L = -\Gamma_t \frac{\partial f_L}{\partial x_j}. \tag{18}$$

The closure for the conditional SGS diffusion is based on the linear mean square estimation (LMSE) model (O'Brien, 1980), which is also known as the interaction by exchange with the mean, or the IEM model (Borghi, 1988). Implementation of this model together with Eq. (18) yields the modeled FDF transport equation:

$$\begin{aligned} \frac{\partial f_L}{\partial t} + \frac{\partial[\langle u_i\rangle_L f_L]}{\partial x_i} &= \frac{\partial}{\partial x_i}\left[(\Gamma + \Gamma_t)\frac{\partial f_L}{\partial x_i}\right] \\ &+ \frac{\partial}{\partial \psi_\alpha}[\Omega_m(\psi_\alpha - \langle\phi_\alpha\rangle_L)f_L] - \frac{\partial[\widehat{\omega}_\alpha(\underline{\psi})f_L]}{\partial \psi_\alpha}. \end{aligned} \tag{19}$$

In the second term on the RHS , Ω_m is the frequency of scalar mixing within the subgrid and is modeled via $\Omega_m = C_\Omega(\Gamma+\Gamma_t)/\Delta_H^2$. This equation may be integrated to obtain transport equations for the SGS moments. For example, the first moment, $\langle\phi_\alpha\rangle_L$, or the filtered mean is governed by:

$$\frac{\partial\langle\phi_\alpha\rangle_L}{\partial t} + \frac{\partial\langle u_j\rangle_L\langle\phi_\alpha\rangle_L}{\partial x_j} = \frac{\partial}{\partial x_j}\left[(\Gamma + \Gamma_t)\frac{\partial\langle\phi_\alpha\rangle_L}{\partial x_j}\right] + \langle\omega_\alpha\rangle_L, \tag{20}$$

3. Numerical Formulation

The numerical solution of the hydrodynamic and the scalar fields involves a two step explicit procedure. The first involves the advancement of the hydrodynamic variables and is accomplished via a compact finite difference scheme (Kennedy and Carpenter, 1994). The second involves the time advancement of the FDF for which a Lagrangian Monte Carlo procedure is used. This procedure is based on the idea of "equivalent systems" by considering the random process $X_i(t)$.

$$dX_i(t) = D_i(\underline{X}(t), t)dt + E^{1/2}(\underline{X}(t), t)dW_i(t), \tag{21}$$

where $D_i(\underline{X}, t)$ is the drift vector, $E(\underline{X}, t)$ is the diffusion coefficient and W_i represents the Wiener-Lévy process (Karlin and Taylor, 1981). With the equivalence:

$$E \equiv 2(\Gamma + \Gamma_t), \quad D_i \equiv \langle u_i\rangle_L + \frac{\partial(\Gamma + \Gamma_t)}{\partial x_i}. \tag{22}$$

the Fokker Planck equation corresponding to stochastic differential equation (21) becomes equivalent to the spatial transport equation of the modeled FDF equation (19).

In the the numerical solution, the FDF is represented with a set of scalars $\phi_\alpha^{(n)}(\underline{X}^{(n)}(t), t)$ assigned on the particles throughout the flow-field. The location of the notional particles are given by $\underline{X}^{(n)}$ and Eq. (21) is integrated via the Euler-Maruyamma scheme:

$$X_i^{(n)}(t_{k+1}) = X_i^{(n)}(t_k) + D_i^{(n)}(t_k)\Delta t + \left(E^{(n)}(t_k)\Delta t\right)^{1/2} \xi_i^{(n)}(t_k), \qquad (23)$$

where $D_i^{(n)}(t_k) = D_i(\underline{X}^{(n)}(t_k), t)$, $E^{(n)}(t_k) = E(\underline{X}^{(n)}(t_k), t)$ and $\xi_i^{(n)}$ is a random variable with the standard Gaussian PDF. This schemes preserves the Markovian character of the diffusion process (Gardiner, 1990) and facilitates affordable computations. The coefficients D_i and E require the knowledge of the filtered mean velocity and the diffusivity (molecular and SGS). These are provided by the solution of Eqs. (6)-(7) by a finite difference procedure and then is interpolated to the particle location.

The scalar composition of each particle changes due to the effects of chemical reaction, and mixing (SGS and molecular). Both mechanisms are implemented deterministically and the scalars evolve according to

$$\frac{d\phi_\alpha^+}{dt} = -\Omega_m(\phi_\alpha^+ - \langle\phi_\alpha\rangle_L) + \omega_\alpha, \qquad (24)$$

where ϕ_α^+ denotes the scalar value of a particle.

4. Results

Both FDF and LES-FD are employed for simulations of 3D turbulent round jets under both non-reacting and reacting conditions similar to those considered in the experiments of Shea (1977). In the nonreactive case, the configuration consists of a jet of ozone (O_3) diluted in nitrogen (N_2) issuing into a coflowing stream of N_2. In the reacting flow, the surrounding fluid consists of nitric oxide (NO) diluted in N_2. The chemistry is modeled via the one-step reaction of $O_3 + NO \rightarrow O_2 + NO_2$. The ratio of the reactants' concentration to that of the carrier gas is of order $\mathcal{O}(10^{-4})$. With such dilute reactants, the effects of reaction exothermicity can be neglected (Shea, 1977). In reacting flow simulations via LES-FD, the SGS scalar correlations are neglected.

The streamwise velocity at the inflow boundary is initialized with an approximate top-hat radial distribution. The initial velocity is U_o in the jet, and U_∞ in the co-flow, with a velocity ratio of $U_o/U_\infty = 4$. The Reynolds number based on the jet diameter (D) and the inner jet velocity is $Re_D =$

4, 000. The space coordinates are $\underline{x} = [x, y, z]$, where x is the streamwise direction, and y & z are the radial/cross-stream directions. A mesh consisting of $101 \times 61 \times 61$ grid points in the x, y, z directions, respectively, is used to cover a domain of size $8D \times 4D \times 4D$. The ratio of the secondary filter size to the grid filter size is $\Delta_{H'}/\Delta_H = 3$. The values of the other parameters are: $Sc = 1$, $Sc_t = 0.7$, $C_k = 0.045$, $C_\Omega = 2$. No attempt was made to find the optimum, or the "dynamically" determined (Germano *et al.*, 1991; Germano, 1996) values of the model constants.

The simulation results are statistically analyzed via time averaging over 16, 000 samples. In the FDF simulations, the filtered values of the scalar quantities are determined by performing local averaging. The volume from which an ensemble of particles is constructed is Δ_E^3. By increasing Δ_E, the number of particles in the ensemble increases. This improves the statistical accuracy but increases dispersion. First, LES results of the non-reacting jet flow are considered in which the FDF simulations are conducted with $\Delta_E = 2\Delta_H$. This size facilitates the use of fewer particles while still retaining a large enough sample for reliable statistics. The instantaneous density of the number of the Monte Carlo particles is presented in Fig. 1. This figure provides a visual demonstration of the basic methodology and the flow structure, as captured by the FDF. To establish the consistency of the FDF, its results are compared with those of LES-FD. Shown in Fig. 2 are the contour plots of the filtered ozone mass fraction at planes normal to the streamwise coordinate. The results via FDF are very similar to those obtained by LES-FD; the latter contain slight numerical oscillations which are not present in the Lagrangian Monte Carlo simulations. The comparison between the filtered values as predicted by FDF and LES-FD is quantified by performing a linear regression analysis of data at all the points. This analysis yields a correlation coefficient of 0.99 between the two sets of results which indicates a very good agreement between the LES-FD and the FDF in predicting the filtered mean values.

The radial distributions of the time-averaged, filtered, normalized ozone mass fractions $\overline{\langle Y^*_{O_3}\rangle_L} = \overline{\langle Y_{O_3}\rangle_L}/\overline{\langle Y_{O_3}\rangle_L}(x = y = z = 0)$ are shown in Fig. 3. In the non-reacting case, expectedly, the FDF results agree well with those via LES-FD. Both simulations predict a similar rate of decay for the centerline values of the mass fraction as the flow evolves. In the reacting case, however, there is a significant difference between the results of the two simulations. It is noted that LES-FD predicts a much larger rate of reactant conversion in comparison with FDF. This difference is due to the neglect of the SGS scalar fluctuations in the LES-FD. This trend was observed in all the cases considered and is consistent with that observed in Reynolds-averaged simulations (Bilger, 1980). An attempt was made to compare the results with experimental data of Shea (1977). But there are not sufficient detailed data reported in regard to the initial conditions in this experiments. Also, because of numerical concerns some of the simulation parameters are different from those considered experimentally. Work is in progress to generate DNS data for 3D, turbulent reacting jet flows with simple chemistry schemes of the type considered here. Such data are needed for further assessment of the methodology before it is implemented for simulations of more complex reacting flows.

Although the FDF methodology is presented here for isothermal, constant density, reacting flows with a simple kinetics scheme, the extension to variable density flows, with exothermic reactions imposes no serious mathematical difficulties (Jaberi *et al.*, 1999). For LES of variable density flows, it is convenient to use the filtered mass density function (FMDF), denoted by F_L, defined as

$$F_L(\underline{\psi};\underline{x},t) \equiv \int_{-\infty}^{+\infty} \rho(\underline{x}',t)\varepsilon\left[\underline{\psi},\underline{\phi}(\underline{x}',t)\right] h_s(\underline{x}'-\underline{x})d\underline{x}', \tag{25}$$

where ρ is the fluid density. The integral property of the FMDF is such that

$$\int_{-\infty}^{+\infty} F_L(\underline{\psi};\underline{x},t)d\underline{\psi} = \int_{-\infty}^{+\infty} \rho(\underline{x}',t)h_s(\underline{x}'-\underline{x})d\underline{x}' = \langle\rho(\underline{x},t)\rangle_L. \tag{26}$$

Jaberi *et al.* (1999) developed a transport equation for the FMDF and applied it for LES of several reacting flows. All the results as compared with DNS and laboratory data show significant advantages over LES-FD. With inclusion of efficient numerical integration routines for the treatment of complex chemistry mechanisms (Pope, 1997), it is conceivable that LES of reactive flows with realistic chemical kinetics may be conducted for engineering applications in the near future. In this regard, the scalar FDF methodology is attractive in that the present Monte Carlo solver can be used directly in available CFD codes. Similar to PDF methods, the closure problems associated with the FDF (and FMDF) are the correlations involving the velocity field (such as SGS stresses and mass fluxes). This may be overcome by considering the joint velocity-scalar FDF (FMDF) similar to that in PDF methods (Pope, 1994b). This issue is currently under investigation.

The computational requirement for FDF simulations with 2×10^6 particles is about 2.5 times that of LES-FD. This overhead appears tolerable in view of the attractiveness of the methodology. Also, the computational requirements for FDF is significantly less than that of DNS. But the range of flow parameters (such as the Reynolds and the Damköhler numbers) that can be considered by FDF is significantly larger than can be treated by DNS, and the results are more accurate that those by LES-FD. Colucci *et* *al.* (1998) and Jaberi *et al.* (1999) report a comparison of the computational requirements of LES-FD, FDF and DNS for several flow configurations. This comparison could be made only in flows for which DNS was possible, *i.e.* low Damköhler and Reynolds numbers. At higher values of these parameters, the computational cost associated with DNS would be exceedingly higher than that of FDF. Thus for practical flows for which DNS is currently impossible, the FDF would be a good alternative. Several means of reducing the FDF's computational requirements are possible and should be considered. These could be useful in future applications in complex flows. The FDF method will benefit from ongoing and future improvements in PDF and other LES schemes (Pope, 1994a; Subramaniam and Pope, 1997; Pierce and Moin, 1998) from both modeling and computational standpoints.

5. Acknowledgment

The first author acknowledges the support of HBECC Fellowship provided by the U.S. Office of Naval Research under Grant N000014-92-J-1252-NY-001. This work is part of a research program sponsored by the NASA Langley Research Center under Grant NAG-1-1122 to SUNY-Buffalo, with Dr. J. Philip Drummond serving as the Technical Monitor. Acknowledgment is also made to the Donors of the Petroleum Research Funds administrated by the American Chemical Society for their support under Grant ACS-PRF 32892-AC9. Computational resources are provided by the Minnesota Supercomputing Institute, and the National Center for Supercomputing Applications at the University of Illinois at Urbana.

References

Aldama, A. A. (1990). Filtering techniques for turbulent flow simulations. volume 49 of *Lecture Notes in Engineering*. Springer-Verlag, New York, NY.

Bilger, R. W. (1980). Turbulent flows with nonpremixed reactants. In Libby and Williams (1980), chapter 3, pages 65–113.

Borghi, R. (1988). Turbulent combustion modeling. *Prog. Energy Combust. Sci.* **14**, 245–292.

Branley, N. and Jones, W. P. (1997). Large eddy simulation of a turbulent non-premixed flame. In *Proceedings of the Eleventh Symposium on Turbulent Shear Flows*, pages 21.1–21.6, Grenoble, France.

Colucci, P. J., Jaberi, F. A., Givi, P., and Pope, S. B. (1998). Filtered density function for large eddy simulation of turbulent reacting flows. *Phys. Fluids* **10**, 499–515.

Cook, A. W. and Riley, J. J. (1994). A subgrid model for equilibrium chemistry in turbulent flows. *Phys. Fluids* **6**, 2868–2870.

Cook, A. W., Riley, J. J., and Kosály, G. (1997). A laminar flamelet approach to subgrid-scale chemistry in turbulent flows. *Combust. Flame* **109**, 332–341.

DesJardin, P. E. and Frankel, S. H. (1998). Large eddy simulation of a turbulent nonpremixed reacting jet: Application and assessment of subgrid-scale combustion models. *Phys. Fluids* **10**, 2298–2314.

Dopazo, C. (1994). Recent developments in pdf methods. In Libby and Williams (1994), chapter 7, pages 375–474.

Eidson, T. M. (1985). Numerical simulation of the turbulent rayleigh-benard problem using subgrid modelling. *J. Fluid Mech.* **158**, 245–268.

Frankel, S. H., Adumitroaie, V., Madnia, C. K., and Givi, P. (1993). Large eddy simulations of turbulent reacting flows by assumed PDF methods. In Ragab, S. A. and Piomelli, U., editors, *Engineering Applications of Large Eddy Simulations*, pages 81–101. ASME, FED-Vol. 162, New York, NY.

Fureby, C. and Lofstrom, C. (1994). Large-eddy simulations of bluff body stabilized flames. In *Proceedings of 25th Symp. (Int.) on Combustion*, pages 1257–1264. The Combustion Institute, Pittsburgh, PA.

Galperin, B. and Orszag, S. A., editors. (1993). *Large Eddy Simulations of Complex Engineering and Geophysical Flows.* Cambridge University Press, Cambridge, England.

Gao, F. and O'Brien, E. E. (1993). A large-eddy simulation scheme for turbulent reacting flows. *Phys. Fluids A* **5**, 1282–1284.

Gardiner, C. W. (1990). *Handbook of Stochastic Methods.* Springer-Verlag, New York, NY.

Germano, M., Piomelli, U., Moin, P., and Cabot, W. H. (1991). A dynamic subgrid-scale eddy viscosity model. *Phys. Fluids A* **3**, 1760–1765.

Germano, M. (1996). A statistical formulation of dynamic model. *Phys. Fluids* **8**, 565–570.

Givi, P. (1994). Spectral and random vortex methods in turbulent reacting flows. In Libby and Williams (1994), chapter 8, pages 475–572.

Jaberi, F. A. and James, S. (1998). A dynamic similarity model for large eddy simulation of turbulent combustion. *Phys. Fluids* **10**, 1775–1777.

Jaberi, F. A., Colucci, P. J., James, S., Givi, P., and Pope, S. B. (1999). Filtered mass density function for large eddy simulation of turbulent reacting flows. *J. Fluid Mech.* submitted.

Jiménez, J., Liñán, A., Rogers, M. M., and Higuera, F. J. (1997). *A Priori* testing of subgrid models for chemically reacting non-premixed turbulent flows. *J. Fluid Mech.* **349**, 149–171.

Karlin, S. and Taylor, H. M. (1981). *A Second Course in Stochastic Processes.* Academic Press, New York, NY.

Kennedy, C. A. and Carpenter, M. H. (1994). Several new numerical methods for compressible shear-layer simulations. *Appl. Num. Math.* **14**, 397–433.

Libby, P. A. and Williams, F. A., editors. (1980). *Turbulent Reacting Flows*, volume 44 of *Topics in Applied Physics.* Springer-Verlag, Heidelberg.

Libby, P. A. and Williams, F. A., editors. (1994). *Turbulent Reacting Flows.* Academic Press, London, England.

Lundgren, T. S. (1967). Distribution functions in the statistical theory of turbulence. *Phys. Fluids* **10**, 969–975.

Madnia, C. K. and Givi, P. (1993). Direct numerical simulation and large eddy simulation of reacting homogeneous turbulence. In Galperin and Orszag (1993), chapter 15, pages 315–346.

Mathey, F. and Chollet, J. P. (1997). Large eddy simulation of turbulent reactive flows. In *Proceedings of the Eleventh Symposium on Turbulent Shear Flows*, pages 16.19–16.24, Grenoble, France.

McMurtry, P. A., Menon, S., and Kerstein, A. R. (1992). A linear eddy sub-grid model for turbulent reacting flows: Application to hydrogen-air combustion. In *Proceedings of 24th Symp. (Int.) on Combustion*, pages 271–278. The Combustion Institute, Pittsburgh, PA.

McMurtry, P. A., Menon, S., and Kerstein, A. R. (1993). Linear eddy modeling of turbulent combustion. *Energy & Fuels* **7**, 817–826.

Menon, S., McMurtry, P. A., and Kerstein, A. K. (1993). A linear eddy sugbrid model of turbulent combustion. In Galperin and Orszag (1993), chapter 14, pages 287–314.

Moin, P. (1991). Towards large eddy and direct numerical simulations of complex turbu-

lent flows. *Computer Methods in Applied Mechanics and Engineering* **87**, 329–334.
Möller, S. I., Lundgren, E., and Fureby, C. (1996). Large eddy simulations of unsteady combustion. In *Proceedings of 26th Symp. (Int.) on Combustion*, page 241. The Combustion Institute, Pittsburgh, PA.
O'Brien, E. E. (1980). The probability density function (PDF) approach to reacting turbulent flows. In Libby and Williams (1980), chapter 5, pages 185–218.
Pierce, C. D. and Moin, P. (1998). A dynamic model for subgrid-scale variance and dissipation rate of a conserved scalar. *Phys. Fluids* **10**, 3041–3044.
Pope, S. B. (1985). PDF methods for turbulent reactive flows. *Prog. Energy Combust. Sci.* **11**, 119–192.
Pope, S. B. (1990). Computations of turbulent combustion: Progress and challenges. In *Proceedings of 23rd Symp. (Int.) on Combustion*, pages 591–612. The Combustion Institute, Pittsburgh, PA.
Pope, S. B. (1994a). Lagrangian pdf methods for turbulent flows. *Ann. Rev. Fluid Mech.* **26**, 23–63.
Pope, S. B. (1994b). On the relation between stochastic Lagrangian models of turbulence and second-moment closures. *Phys. Fluids* **6**, 973–985.
Pope, S. B. (1997). Computationally efficient implementation of combustion chemistry using *in situ* adaptive tabulation. *Combust. Theo. Modelling* **1**, 41.
Réveillon, J. and Vervisch, L. (1998). Subgrid-scale turbulent micromixing: Dynamic approach. *AIAA J.* **36**, 336–341.
Shea, J. R. (1977). A chemical reaction in a turbulent jet. *J. Fluid Mech.* **81**, 317–333.
Subramaniam, S. and Pope, S. B. (1997). Comparison of PDF mixing models for non-premixed turbulent reacting flow. Technical Report FDA 97-03, Cornell University, Ithaca, NY.
Vervisch, L. and Poinsot, T. (1988). Direct numerical simulation of non-premixed turbulent flames. *Annu. Rev. Fluid Mech.* **30**, 655–691.
Vreman, B., Geurts, B., and Kuerten, H. (1994). Realizability conditions for the turbulent stress tensor in large-eddy simulation. *J. Fluid Mech.* **278**, 351–362.

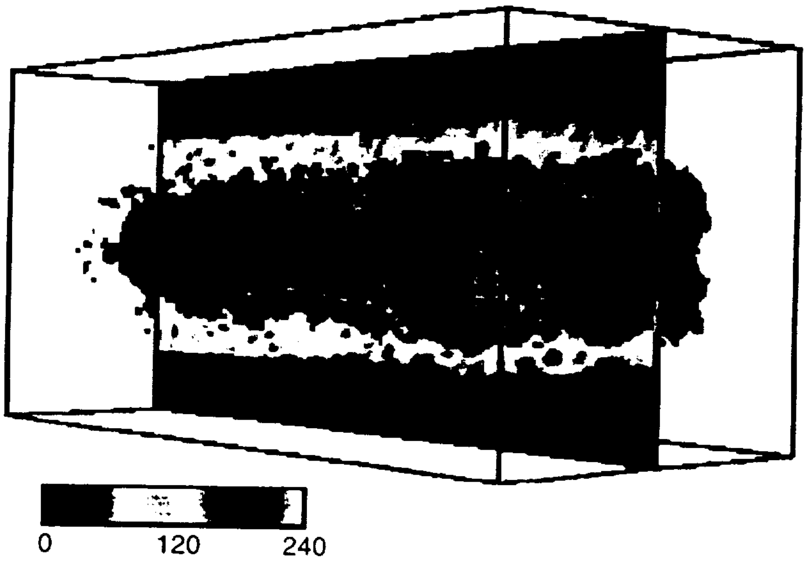

Figure 1. Monte Carlo particle number density.

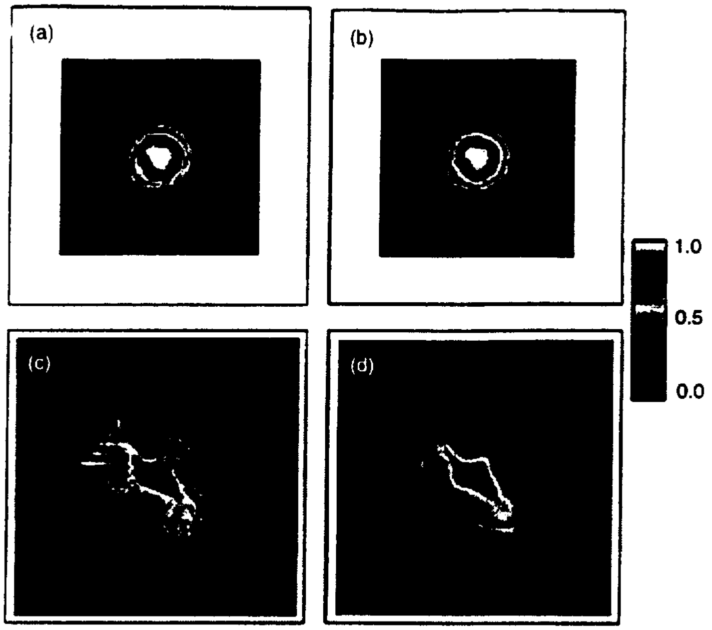

Figure 2. Instantaneous filtered mean ozone mass fraction contours at streamwise planes: (a) LES-FD, $x/D = 2.5$; (b) FDF, $x/D = 2.5$; (c) LES-FD, $x/D = 7.5$;(d) FDF, $x/D = 7.5$.

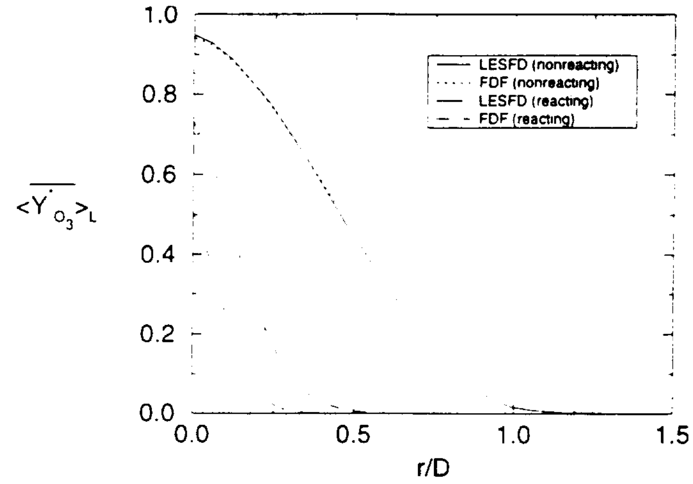

Figure 3. Time-averaged filtered mean ozone mass fraction.

Appendix IV

Velocity Filtered Density Function for Large Eddy Simulation of Turbulent Flows

Please Note: The materials provided in this Appendix (IV) are very preliminary and work is still in progress on this portion of our activities.

Velocity Filtered Density Function for Large Eddy Simulation of Turbulent Flows

I Introduction

Modeling of the Sub-Grid Scale (SGS) correlations in large eddy simulations (LES) of turbulent flows is continuing to be an active area of research in fluid dynamics.[1–11] The most prominent model has been the Smagorinsky eddy viscosity closure[12] which relates the unknown subgrid scale Reynolds stresses to the local large scale rate of flow strain.[13] This viscosity is aimed to provide to a zeroth order approximation the role of mimicking the dissipative behavior of the unresolved small scales. The extensions to "dynamic" and "mixed" models[14–19] have shown some improvements. This is particularly the case in transitional flow simulations where the dynamic evolutions of the empirical model "constant" result in (somewhat) better predictions of the large scale flow features. More recent investigations and developments for more accurate SGS closures[20–27] imply the resolution of subgrid transport equations. The motivation in these cases is the desire to reduce the dissipative effect found in fixed length scale approaches and to predict the now famous problem of "back-scatter" by evaluating a proper velocity subgrid scale. Here again the "dynamic" approach is feasible to evaluate the required closure coefficients.[23] Two classes emerge in the subgrid velocity scale approach. The one equation type of approach investigated by Menon *et al.*[20,21] solves for the subgrid kinetic energy, while the second one originally proposed by Deadorff *et al.*[25] and studied by Fureby *et al.*[27] directly solve for the SGS transport equations. The latter model is theoretically more attractive as it has the ability of resolving anisotropy in the SGS.

In a recent study Colucci *et al.* develop a new methodology for LES of turbulent reacting flows.[28] In this new approach the definition of "Filtered Density Function"[28,29] (FDF) and "Filtered Mass Density Function"[30] (FMDF) are defined for the scalars and allow an exact representation of the chemical source terms appearing in the LES equations of turbulent reacting flows. While the applicability of the scalar FDF for LES of chemically reacting turbulent flows has been successfully demonstrated by Colucci *et al.*,[28,30] the hydrodynamic part of the problem was limited to conventional Smagorinsky hydrodynamic closures[12] and of now well known limitations.[31,32]

The objective of the present work is to derive a higher order type of hydrodynamics closure through the modeling of the joint-velocity FDF and to demonstrate its applicability by providing results based on its implementation for LES of turbulent flows. Assessment of the methodology is obtained at first through consistency simulations as explained later. Only the FDF of the joint-velocity vector is considered here; probabilistic treatment of the velocity-scalar fluctuations is postponed to future work but is the long term goal of the present investigation.

II Formulation

The primary transport variables for the mathematical description of incompressible (unit density) turbulent flows are the velocity vector $u_i(\mathbf{x},t)$ $(i = 1,2,3)$ and the pressure $p(\mathbf{x},t)$. The equations which govern the transport of these variables in space (x_i) and time (t) are

$$\begin{gathered}\frac{\partial u_i}{\partial x_i} = 0, \\ \frac{\partial u_j}{\partial t} + \frac{\partial u_i u_j}{\partial x_i} = -\frac{\partial p}{\partial x_j} + \frac{\partial \sigma_{ij}}{\partial x_i}.\end{gathered} \tag{1}$$

Assuming a Newtonian flow, the viscous stress tensor σ_{ij} is represented by

$$\sigma_{ij} = \nu\left(\frac{\partial u_i}{\partial x_j} + \frac{\partial u_j}{\partial x_i}\right), \tag{2}$$

where ν is the fluid viscosity and is assumed to be constant.

Large eddy simulation involves the use of the spatial filtering operation[33]

$$\langle f(\mathbf{x},t)\rangle_L = \int_{-\infty}^{+\infty} f(\mathbf{x}',t)\mathcal{G}(\mathbf{x}',\mathbf{x})d\mathbf{x}', \tag{3}$$

where $\mathcal{G}$ denotes the filter function, $\langle f(\mathbf{x},t)\rangle_L$ represents the filtered value of the transport variable $f(\mathbf{x},t)$, and $f' = f - \langle f\rangle_L$ denotes the fluctuations of f from the filtered value. We consider spatially & temporally invariant and localized filter functions, thus $\mathcal{G}(\mathbf{x}',\mathbf{x}) \equiv G(\mathbf{x}' - \mathbf{x})$ with the properties,[33] $G(\mathbf{x}) = G(-\mathbf{x})$, and $\int_{-\infty}^{\infty} G(\mathbf{x})d\mathbf{x} = 1$. Moreover, we only consider "positive" filter functions as defined by Vreman *et al.*[34] for which all the moments $\int_{-\infty}^{\infty} x^m G(x)dx$ exist for $m \geq 0$.

The application of the filtering operation to the instantaneous transport equations yields

$$
\begin{aligned}
&\frac{\partial \langle u_i \rangle_L}{\partial x_i} = 0, \\
&\frac{\partial \langle u_j \rangle_L}{\partial t} + \frac{\partial \langle u_i \rangle_L \langle u_j \rangle_L}{\partial x_i} = -\frac{\partial \langle p \rangle_L}{\partial x_j} + \frac{\partial \langle \sigma_{ij} \rangle_L}{\partial x_i} - \frac{\partial \tau_L(u_i, u_j)}{\partial x_i}.
\end{aligned}
\tag{4}
$$

where $\tau_L(u_i, u_j) = \langle u_i u_j \rangle_L - \langle u_i \rangle_L \langle u_j \rangle_L$ denotes the "generalized subgrid stresses" as defined by Germano.[14]

III Deterministic modeling

In LES the closure problem is associated with $\tau_L(u_i, u_j)$.[2] Here, this term is modeled with a probabilistic and deterministic closures. The former is based on the velocity filtered density function and is discussed in the next section. For the later, several existing closures are given and used for comparison with the VFDF.

The most famous deterministic LES model is probably the Smagorinsky model[12] which assumes equilibrium between the energy production and dissipation rates in the small scales. The model reads,[12]

$$
\begin{aligned}
\tau_L(u_i, u_j) &= -2\,\nu_t\, S_{ij} + \frac{2}{3} k \delta_{ij}, \\
S_{ij} &= \frac{1}{2}\left(\frac{\partial \langle u_i \rangle_L}{\partial x_j} + \frac{\partial \langle u_j \rangle_L}{\partial x_i}\right), \\
\nu_t &= C_{\nu 1}\, \Delta_L^2\, S.
\end{aligned}
\tag{5}
$$

$C_{\nu 1}$ is a constant of order 0.01, $S = \sqrt{S_{ij} S_{ij}}$ and Δ_L is the characteristic length of the LES filter.

A more appropriate closure was proposed by Menon *et al.*[20,21] in which the SGS are given by,

$$\begin{aligned} \tau_L(u_i, u_j) &= -2\,\nu_t\,S_{ij} + \frac{2}{3}k\,\delta_{ij}, \\ \nu_t &= C_{\nu 1}\,\Delta_L\,\sqrt{k}, \\ \frac{\partial}{\partial t}[k] + \frac{\partial}{\partial x_k}[\langle u_k\rangle_L k] &= -\frac{\partial}{\partial x_k}\left[(\nu+\nu_t)\frac{\partial k}{\partial x_k}\right] - \tau_L(u_i, u_j)\frac{\partial\langle u_i\rangle_L}{\partial x_j} - \varepsilon, \\ \varepsilon &= C_\varepsilon\,\frac{k^{\frac{3}{2}}}{\Delta_L}. \end{aligned} \tag{6}$$

and for which the introduction of $k = 1/2\ \tau_L(u_k, u_k)$ as a subgrid velocity scale removes the equilibrium assumption allowing more realistic flow predictions.

For our purpose we are interested in the transport equation of the SGS stresses,[14]

$$\frac{\partial}{\partial t}[\tau_L(u_i, u_j)] + \frac{\partial}{\partial x_k}[\langle u_k\rangle_L \tau_L(u_i, u_j)] = -\frac{\partial T_{ijk}}{\partial x_k} - \Pi_{ij} + P_{ij} - \varepsilon_{ij}. \tag{7}$$

to allow resolution of the anisotropy present in the small scales. In this equation, $T_{ijk} = \tau_L(u_i, u_j, u_k) - \nu\frac{\partial}{\partial x_k}[\tau_L(u_i, u_j)]$ is the subgrid turbulent transport tensor where $\tau_L(u_i, u_j, u_k) = \langle u_i u_j u_k\rangle_L - \langle u_i\rangle_L\tau_L(u_j, u_k) - \langle u_j\rangle_L\tau_L(u_i, u_k) - \langle u_k\rangle_L\tau_L(u_i, u_j) - \langle u_i\rangle_L\langle u_j\rangle_L\langle u_K\rangle_L$.[14] The other terms are, the subgrid pressure-velocity scrambling tensor, $\Pi_{ij} = \tau_L(u_i, \frac{\partial p}{\partial x_j}) + \tau_L(u_j, \frac{\partial p}{\partial x_i})$, the subgrid production rate tensor, $P_{ij} = -\tau_L(u_i, u_k)\frac{\partial\langle u_j\rangle_L}{\partial x_k} - \tau_L(u_j, u_k)\frac{\partial\langle u_i\rangle_L}{\partial x_k}$, and the subgrid dissipation rate tensor, $\varepsilon_{ij} = 2\nu\tau_L(\frac{\partial u_i}{\partial x_k}, \frac{\partial u_j}{\partial x_k})$. At this closure level a deterministic approach requires models for $\tau_L(u_i, u_j, u_k)$, Π_{ij} and ε_{ij}.

Consistent with the models used in Reynolds averaged (RAS) calculations; the subgrid velocity-pressure scrambling tensor and anisotropic part of the subgrid dissipation rate tensor are combined and modeled via a Rotta type closure.[35] The resulting model is,[25,27]

$$-\Pi_{ij} - (\varepsilon_{ij} - \frac{2}{3}\varepsilon\,\delta_{ij}) = -C_1\,\omega\left[\tau_L(u_i, u_j) - \frac{2}{3}k\,\delta_{ij}\right]. \tag{8}$$

where $\omega = \frac{\varepsilon}{k}$ is the subgrid mixing frequency, $k = \frac{1}{2}\tau_L(u_i, u_i)$ is the subgrid kinetic energy, and $\varepsilon = \frac{1}{2}\varepsilon_{ii}$ is the subgrid kinetic energy dissipation rate. The dissipation rate is related to the characteristic length of the filter, Δ_L, and the subgrid kinetic energy according to the same expression as in Eq. (6),[25,27]

The third order term, $\tau_L(u_i, u_j, u_k)$, needs also to be modeled in a deterministic approach which is done using,[25,27]

$$\tau_L(u_i, u_j, u_k) = -C_{\nu 2}\, \Delta_L \sqrt{k}\, \frac{\partial}{\partial x_k} [\tau_L(u_i, u_j)]. \tag{9}$$

All the coefficients $C_1, C_\epsilon, C_{\nu 1}, \ldots$ have to be provided externally or may be calculated via dynamic methods.[14–18] Note also that more elaborate closures similar to those used in RAS could be used but they are beyond the scope of the present work.

IV The velocity filtered density function (VFDF)

The key point in this formulation is to consider the velocity vector $U(\mathbf{x}, t)$ in a probabilistic manner. For that, we define the " velocity filtered density function" (VFDF), denoted by P_L, as

$$\begin{gathered} P_L(\boldsymbol{V}; \mathbf{x}, t) \equiv \int_{-\infty}^{+\infty} \varrho[\boldsymbol{V}, \boldsymbol{U}(\mathbf{x}', t)]\, G(\mathbf{x}' - \mathbf{x}) d\mathbf{x}', \\ \varrho[\boldsymbol{V}, \boldsymbol{U}(\mathbf{x}, t)] = \delta[\boldsymbol{V} - \boldsymbol{U}(\mathbf{x}, t)] \equiv \prod_{i=1}^{3} \delta[V_i - u_i(\mathbf{x}, t)] \end{gathered} \tag{10}$$

where δ denotes the delta function and $\boldsymbol{V}$ is the velocity state vector. The term $\varrho[\boldsymbol{V}; \boldsymbol{U}(\mathbf{x}, t)]$ is the "fine-grained" density,[36,37] and Eq. (10) implies that the VFDF is the *spatially filtered* value of the fine-grained density. Thus, P_L gives the one point, one time density distribution in the velocity space of the fluid state weighted by the filter G. With the condition of a positive filter kernel,[34] P_L has all the properties of the PDF.[37]

For further developments, it is useful to define the "conditional filtered value" of the variable $Q(\mathbf{x}, t)$ by

$$\langle Q(\mathbf{x}, t) | \boldsymbol{V} \rangle_L \equiv \frac{\int_{-\infty}^{+\infty} Q(\mathbf{x}', t)\, \varrho[\boldsymbol{V}, \boldsymbol{U}(\mathbf{x}', t)]\, G(\mathbf{x}' - \mathbf{x}) d\mathbf{x}'}{P_L(\boldsymbol{V}; \mathbf{x}, t)}. \tag{11}$$

where $\langle \alpha | \beta \rangle_L$ denotes the filtered value of α conditioned on β. Equation (11) implies

$$\begin{array}{lll} (i) & \text{For } Q(\mathbf{x},t) = c, & \langle Q(\mathbf{x},t) | \boldsymbol{V} \rangle_L = c, \\ (ii) & \text{For } Q(\mathbf{x},t) \equiv \hat{Q}(\boldsymbol{U}(\mathbf{x},t)), & \langle Q(\mathbf{x},t) | \boldsymbol{V} \rangle_L = \hat{Q}(\boldsymbol{V}), \\ (iii) & \text{Integral property}: & \langle Q(\mathbf{x},t) \rangle_L = \int_{-\infty}^{+\infty} \langle Q(\mathbf{x},t) | \boldsymbol{V} \rangle_L P_L(\boldsymbol{V}:\mathbf{x},t) d\boldsymbol{V}, \end{array} \tag{12}$$

where c is a constant, and $\hat{Q}(\boldsymbol{U}(\mathbf{x},t)) \equiv Q(\mathbf{x},t)$ denotes the case where the variable Q can be completely described by the variable $\boldsymbol{U}(\mathbf{x},t)$. Note that for simplicity the following abbreviation is used: $\langle A | \boldsymbol{V} \rangle_L \equiv \langle A | \boldsymbol{U}(\mathbf{x},t) = \boldsymbol{V} \rangle_L$. From these properties it follows that the filtered value of any function of the velocity variable is obtained by integration over the velocity space

$$\langle Q(\mathbf{x},t) \rangle_L = \int_{-\infty}^{+\infty} \hat{Q}(\boldsymbol{V}) P_L(\boldsymbol{V}:\mathbf{x},t) d\boldsymbol{V}. \tag{13}$$

To develop a transport equation for the VFDF, the time-derivative of Eq. (10) is considered

$$\begin{aligned} \frac{\partial P_L(\boldsymbol{V}:\mathbf{x},t)}{\partial t} &= - \int_{-\infty}^{\infty} \frac{\partial u_i(\mathbf{x}',t)}{\partial t} \frac{\partial \varrho[\boldsymbol{V},\boldsymbol{U}(\mathbf{x}',t)]}{\partial V_i} G(\mathbf{x}' - \mathbf{x})\, d\mathbf{x}' \\ &= - \frac{\partial}{\partial V_i} \int_{-\infty}^{\infty} \frac{\partial u_i(\mathbf{x}',t)}{\partial t} \varrho[\boldsymbol{V},\boldsymbol{U}(\mathbf{x}',t)]\; G(\mathbf{x}' - \mathbf{x})\, d\mathbf{x}'. \end{aligned} \tag{14}$$

This combined with Eq. (11) yields

$$\frac{\partial P_L(\boldsymbol{V}:\mathbf{x},t)}{\partial t} = - \frac{\partial}{\partial V_i} \left[\left\langle \frac{\partial u_i}{\partial t} | \boldsymbol{V} \right\rangle_L P_L(\boldsymbol{V}:\mathbf{x},t) \right]. \tag{15}$$

Substituting Eq. (1) into Eq. (15) yields

$$\frac{\partial P_L(\boldsymbol{V}:\mathbf{x},t)}{\partial t} = - \frac{\partial}{\partial V_i} \left\{ \left[- \left\langle \frac{\partial u_i u_k}{\partial x_k} | \boldsymbol{V} \right\rangle_L - \left\langle \frac{\partial p}{\partial x_i} | \boldsymbol{V} \right\rangle_L + \left\langle \frac{\partial \sigma_{ik}}{\partial x_k} | \boldsymbol{V} \right\rangle_L \right] P_L(\boldsymbol{V}:\mathbf{x},t) \right\}. \tag{16}$$

in which the convective term can be represented in the form

$$\frac{\partial}{\partial V_i} \left[\left\langle \frac{\partial u_i u_k}{\partial x_k} | \boldsymbol{V} \right\rangle_L P_L(\boldsymbol{V}:\mathbf{x},t) \right] = - V_k \frac{\partial P_L(\boldsymbol{V}:\mathbf{x},t)}{\partial x_k}. \tag{17}$$

Substitution of Eq. (2) for the conditional diffusion and some algebraic manipulations yield,

$$\frac{\partial}{\partial V_i}\left[\left\langle \frac{\partial \sigma_{ik}}{\partial x_k}|\mathbf{V}\right\rangle_L P_L(\mathbf{V}:\mathbf{x},t)\right] = -\nu\frac{\partial^2 P_L(\mathbf{V}:\mathbf{x},t)}{\partial x_k \partial x_k} + \frac{\partial^2}{\partial V_i \partial V_j}\left[\left\langle \nu\frac{\partial u_i}{\partial x_k}\frac{\partial u_j}{\partial x_k}|\mathbf{V}\right\rangle_L P_L(\mathbf{V}:\mathbf{x},t)\right]. \tag{18}$$

The conditional filtered values of the pressure gradient and dissipation rate can be further decomposed into resolved and deviatory components from the mean (filtered) values. It is useful to adopt the following decompositions,

$$\begin{aligned}
V_k P_L &= \langle u_k\rangle_L P_L + [V_k - \langle u_k\rangle_L]P_L. \\
\left\langle \frac{\partial p}{\partial x_i}|\mathbf{V}\right\rangle_L P_L &= \frac{\partial\langle p\rangle_L}{\partial x_i}P_L + \left[\left\langle \frac{\partial p}{\partial x_i}|\mathbf{V}\right\rangle_L - \frac{\partial\langle p\rangle_L}{\partial x_i}\right]P_L. \\
\left\langle \nu\frac{\partial u_i}{\partial x_k}\frac{\partial u_j}{\partial x_k}|\mathbf{V}\right\rangle_L P_L &= \nu\frac{\partial\langle u_i\rangle_L}{\partial x_k}\frac{\partial\langle u_j\rangle_L}{\partial x_k}P_L + \left[\left\langle \nu\frac{\partial u_i}{\partial x_k}\frac{\partial u_j}{\partial x_k}|\mathbf{V}\right\rangle_L - \nu\frac{\partial\langle u_i\rangle_L}{\partial x_k}\frac{\partial\langle u_j\rangle_L}{\partial x_k}\right]P_L.
\end{aligned} \tag{19}$$

so that Eq. (15) can be expressed as

$$\begin{aligned}
\frac{DP_L}{Dt} = &-\frac{\partial}{\partial x_k}[(V_k - \langle u_k\rangle_L)P_L] + \frac{\partial\langle p\rangle_L}{\partial x_i}\frac{\partial P_L}{\partial V_i} + \nu\frac{\partial^2 P_L}{\partial x_k \partial x_k} - \nu\frac{\partial\langle u_i\rangle_L}{\partial x_k}\frac{\partial\langle u_j\rangle_L}{\partial x_k}\frac{\partial^2 P_L}{\partial V_i \partial V_j} \\
&-\frac{\partial}{\partial V_i}\left[\left(\left(\left\langle \frac{\partial p}{\partial x_i}|\mathbf{V}\right\rangle_L - \frac{\partial\langle p\rangle_L}{\partial x_i}\right)P_L\right] - \frac{\partial^2}{\partial V_i \partial V_j}\left[\left(\left(\left\langle \nu\frac{\partial u_i}{\partial x_k}\frac{\partial u_j}{\partial x_k}|\mathbf{V}\right\rangle_L - \nu\frac{\partial\langle u_i\rangle_L}{\partial x_k}\frac{\partial\langle u_j\rangle_L}{\partial x_k}\right)P_L\right].
\end{aligned} \tag{20}$$

where $\frac{D}{Dt} = \frac{\partial}{\partial t} - \langle u_k\rangle_L\frac{\partial}{\partial x_k}$ denotes the filtered material derivative.

Equation (20) is an exact transport equation for the joint-velocity FDF. The first term on the right hand side represents the deviatory/subgrid convection of the VFDF in physical space and is closed (provided that $\langle u_k\rangle_L$ is known). The second term corresponds to the convection in the velocity space due to the resolved pressure gradient. The third term is the diffusion of the VFDF in physical space due to the molecular effects, and the fourth term is the diffusion in velocity space due to the resolved dissipation rate. The unclosed terms are associated with the last two terms on the RHS of Eq. (20). These terms represent the convection in velocity space by the unresolved subgrid/deviatory pressure gradient and the diffusion in velocity space by the unresolved subgrid/deviatory dissipation rate.

The subgrid pressure gradient and the subgrid dissipation rate are modeled via the generalized Langevin model[38–40]

$$\frac{\partial}{\partial V_i}\left[\left(\left\langle\frac{\partial p}{\partial x_i}\middle|\mathbf{V}\right\rangle_L - \frac{\partial\langle p\rangle_L}{\partial x_i}\right)P_L\right] - \frac{\partial^2}{\partial V_i\partial V_j}\left[\left(\left\langle\nu\frac{\partial u_i}{\partial x_k}\frac{\partial u_j}{\partial x_k}\middle|\mathbf{V}\right\rangle_L - \nu\frac{\partial\langle u_i\rangle_L}{\partial x_k}\frac{\partial\langle u_j\rangle_L}{\partial x_k}\right)P_L\right]$$
$$\approx -\frac{\partial}{\partial V_i}\left[\,G_{ij}\,(V_j - \langle u_j\rangle_L)\,P_L\,\right] + \frac{1}{2}\,C_0\,\varepsilon\,\frac{\partial^2 P_L}{\partial V_i\partial V_i}. \tag{21}$$

The advantage of the decomposition in Eq. (20) and the subsequent model in Eq. (21) is that they yield results "nearly" similar to those in "conventional" LES for the first two moments of the VFDF. To show this mathematically the moment equations are evaluated by integrating Eqs. (20 & 21) in velocity space. These moment equations are read as,

$$\begin{aligned}
&\frac{\partial\langle u_i\rangle_L}{\partial x_i} = 0,\\
&\frac{\partial\langle u_j\rangle_L}{\partial t} + \frac{\partial\langle u_i\rangle_L\langle u_j\rangle_L}{\partial x_i} = -\frac{\partial\langle p\rangle_L}{\partial x_j} + \nu\frac{\partial^2\langle u_j\rangle_L}{\partial x_i\partial x_i} - \frac{\partial\tau_L(u_i,u_j)}{\partial x_i}.
\end{aligned} \tag{22}$$

$$\begin{aligned}
\frac{\partial}{\partial t}[\tau_L(u_i,u_j)] + \frac{\partial}{\partial x_k}[\langle u_k\rangle_L\tau_L(u_i,u_j)] &= -\frac{\partial}{\partial x_k}\left[\tau_L(u_i,u_j,u_k) - \nu\frac{\partial}{\partial x_k}[\tau_L(u_i,u_j)]\right]\\
&+ G_{ik}\tau_L(u_j,u_k) + G_{jk}\tau_L(u_i,u_k) - \tau_L(u_i,u_k)\,\frac{\partial\langle u_j\rangle_L}{\partial x_k} - \tau_L(u_j,u_k)\,\frac{\partial\langle u_i\rangle_L}{\partial x_k}\\
&+ C_0\,\varepsilon\,\delta_{ij}.
\end{aligned} \tag{23}$$

The advantage of the VFDF approach is seen in Eqs. (22,23) where the subgrid stresses appear in a closed form without the need of solving subgrid transport equations. Moreover, the third order quantities, $\tau_L(u_i,u_j,u_k)$, appears as a consequence of the VFDF model and do not need to be modeled separately as in a deterministic closure, i.e. Eq. (9). The accuracy of the subgrid stresses as obtained from the modeled VFDF transport equation for Eq. (20) need nonetheless to be validated.

To make the second moment equation derived from the VFDF transport equations more similar to the one derived directly from the instantaneous equation (7), we define G_{ij} as,[41]

$$G_{ij} = -\omega\left(\frac{1}{2} + \frac{3}{4}C_0\right)\delta_{ij} = -\omega\,\frac{C_1}{2}\,\delta_{ij}. \tag{24}$$

With this, the resulting transport equation for the modeled VFDF becomes,

$$\frac{DP_L}{Dt} = -\frac{\partial}{\partial x_k}\left[(V_k - \langle u_k \rangle_L)\, P_L \right] + \frac{\partial \langle p \rangle_L}{\partial x_i}\frac{\partial P_L}{\partial V_i} - \nu \frac{\partial \langle u_i \rangle_L}{\partial x_k}\frac{\partial \langle u_j \rangle_L}{\partial x_k}\frac{\partial^2 P_L}{\partial V_i \partial V_j} + \nu \frac{\partial^2 P_L}{\partial x_k \partial x_k}$$
$$- \frac{\partial}{\partial V_i}\left[G_{ij}\, (V_j - \langle u_j \rangle_L)\, P_L \right] + \frac{1}{2}\, C_0\, \varepsilon\, \frac{\partial^2 P_L}{\partial V_i \partial V_i}. \tag{25}$$

There are two constants in Eq. (25). While the first one, C_ε, is expected to be filter size dependent,[26] the second one, C_0, is equal to 2.1 for very high Reynolds number flows according to Obukhov-Kolmogorov hypotheses.[42–46] For finite Reynolds number flows the value of C_0 can vary between 0 and 6 based on theoretical works and RAS simulations.[40,47–49]

V Monte Carlo solution of the VFDF

The solution of the VFDF transport equation (Eq. (25)) provides all the statistical information pertaining to the velocity vector $U(\mathbf{x}, t)$. This equation can be solved most effectively via the Monte Carlo schemes which can be utilized in both Eulerian[50] and Lagrangian[40,51] contexts. The advantages of Lagrangian numerical methods in reducing the amount of numerical diffusion are well-recognized.[52–57] The basis of the Lagrangian solution of the VFDF transport equation relies upon the principle of *equivalent systems*.[37,41] Two systems with different instantaneous behaviors may have identical statistics and satisfy the same VFDF transport equation. In the Lagrangian Monte Carlo procedure each of the particles obeys certain equations which govern its transport. These particles undergo motion in the physical space by convection due to the velocity vector and diffusion due to the molecular viscosity. The evolution of the velocity vector is governed by the cumulative effects of the local pressure gradient and velocity dissipation rate at the resolved and subgrid scales. The spatial and velocity diffusion of the particles are represented in a stochastic manner by the following system of stochastic differential equations (SDE)[37,58–60]

$$dX_i(t) = D_i(\mathbf{X}(t), \mathbf{V}(t); t)\, dt + B(\mathbf{X}(t), \mathbf{V}(t); t)\, dW_i^x(t),$$
$$dV_i(t) = M_i(\mathbf{X}(t), \mathbf{V}(t); t)\, dt + E(\mathbf{X}(t), \mathbf{V}(t); t)\, dW_i^v(t) \tag{26}$$
$$+ F_{ij}(\mathbf{X}(t), \mathbf{V}(t); t)\, dW_j^x(t).$$

where X_i is the Lagrangian position of a stochastic particle with velocity U_i. The coefficients D_i and M_i are known as the "drift" in spatial and velocity coordinates respectively. B and E are the "diffusion" coefficients for physical and velocity spaces respectively, and W_i^x and W_i^v denote independent Wiener-Levy processes.[61] The tensor F_{ij} represents the dependency between the velocity and physical spaces for this process.

The corresponding Fokker-Planck equation for this Lagrangian process is,

$$\begin{aligned}\frac{\partial f^*}{\partial t} + \frac{\partial}{\partial x_k}\left[\langle D_k|\boldsymbol{V},\boldsymbol{X}\rangle f^*\right] = &-\frac{\partial}{\partial V_k}\left[\langle M_k|\boldsymbol{V},\boldsymbol{X}\rangle f^*\right] + \frac{1}{2}\frac{\partial^2}{\partial x_k \partial x_k}\left[\langle B^2|\boldsymbol{V},\boldsymbol{X}\rangle f^*\right] \\ &+ \frac{1}{2}\frac{\partial^2}{\partial V_k \partial V_k}\left[\langle E^2|\boldsymbol{V},\boldsymbol{X}\rangle f^*\right] + \frac{\partial^2}{\partial x_k \partial V_i}\left[\langle F_{ik}B|\boldsymbol{V},\boldsymbol{X}\rangle f^*\right] \\ &+ \frac{1}{2}\frac{\partial^2}{\partial V_i \partial V_j}\left[\langle F_{ik}F_{jk}|\boldsymbol{V},\boldsymbol{X}\rangle f^*\right].\end{aligned} \tag{27}$$

where $f^* = f^*(\boldsymbol{V}, \boldsymbol{X}; t)$, is the PDF of the process, $\langle A\rangle$ is the "*expected value of* A", and $\langle A|\boldsymbol{V},\boldsymbol{X}\rangle \equiv \langle A|\mathbf{U}(t)=\mathbf{V}, X(t)=\mathbf{X}\rangle$. The PDF of $\boldsymbol{X}$, f_x^*, is obtained by integrating Eq. (27) over the velocity space,[58,62]

$$\frac{\partial f_x^*}{\partial t} + \frac{\partial}{\partial x_k}\left[\langle D_k|\boldsymbol{X}\rangle f_x^*\right] = \frac{1}{2}\frac{\partial^2}{\partial x_k \partial x_k}\left[\langle B^2|\boldsymbol{X}\rangle f_x^*\right]. \tag{28}$$

Proper initial and boundary conditions for Eq. (28) ensures that $f_x^*(\boldsymbol{X};t) = C^{st}$ (non zero). If this is satisfied one can divide Eq. (27) by f_x^* and derive the Eulerian transport equation.[60,63]

By comparison of the Eulerian transport equation corresponding to Eq. (26) with the modeled VFDF transport equation (25) one can determine a set of appropriate values for the coefficients. For example,

$$\begin{aligned}&M_i \equiv -\frac{\partial\langle p\rangle_L}{\partial x_i} + 2\nu\frac{\partial^2\langle u_i\rangle_L}{\partial x_k \partial x_k} - G_{ij}(U_j - \langle u_j\rangle_L), \quad D_i \equiv U_i, \\ &B \equiv \sqrt{2\nu}, \quad E \equiv \sqrt{C_0\varepsilon}, \quad F_{ij} \equiv \sqrt{2\nu}\,\frac{\partial\langle u_i\rangle_L}{\partial x_j}, \quad \langle u_i\rangle_L \equiv \langle U_i\rangle,\end{aligned} \tag{29}$$

is one convenient set of relationships but is not unique. With the equalities given in Eq. (29) f_x^* is non zero as it should be, if the proper initial and boundary conditions are applied. Note that the diffusion coefficient, $B = \sqrt{2\nu}$ is selected consistently with the one used by Einstein,[64] Wiener[65] and Lévy[66] to describe Brownian motions. Thus the chosen SDE's which represent the transport of the modeled VFDF are

$$\begin{aligned} dX_i(t) &= U_i(t)\,dt + \sqrt{2\nu}\,dW_i^x(t), \\ dU_i(t) &= \left[-\frac{\partial\langle p\rangle_L}{\partial x_i} + 2\nu\frac{\partial^2\langle u_i\rangle_L}{\partial x_k\partial x_k} + G_{ij}\left(U_j(t) - \langle u_j\rangle_L\right)\right] dt + \sqrt{C_0\varepsilon}\,dW_i^u(t) \\ &\quad + \sqrt{2\nu}\,\frac{\partial\langle u_i\rangle_L}{\partial x_j}\,dW_j^x(t). \end{aligned} \tag{30}$$

This stochastic system reduces to the one developed for RAS calculations[60,67] when the filter operation is assimilated to an ensemble averaging operation.

It has been shown by Pope[37] that the stochastic system yields identical statistics as the fluid particles (to a first order approximation in time) if and only if the time increment, dt, is much smaller than the characteristic time of the large scale turbulent motions, τ, and much larger than the Kolmogorov time scale τ_η:

$$\tau_\eta \ll dt \ll \tau. \tag{31}$$

Under the previous constraints and to a first order approximation in time, the statistics obtained from the stochastic process evolve as:

$$\begin{aligned} &\langle dX_i\rangle = \langle u_i\rangle_L\,dt, \quad \langle dU_i\rangle = \left[-\frac{\partial\langle p\rangle_L}{\partial x_i} + 2\nu\frac{\partial^2\langle u_i\rangle_L}{\partial x_k\partial x_k}\right] dt \\ &\langle dX_i dX_j\rangle = 2\nu\,\delta_{ij}\,dt, \quad \langle dU_i dU_j\rangle = 2\nu\frac{\partial\langle u_i\rangle_L}{\partial x_k}\frac{\partial\langle u_j\rangle_L}{\partial x_k}\,dt + C_0\varepsilon\,\delta_{ij}\,dt, \\ &\langle dX_i dU_j\rangle = 2\nu\frac{\partial\langle u_j\rangle_L}{\partial x_i}\,dt. \end{aligned} \tag{32}$$

In the numerical implementation, the VFDF is represented by a set of Monte Carlo particles, each with a velocity vector $\mathbf{U}^{(n)}(\mathbf{X}^{(n)}(t),t)$ and a Lagrangian position vector $\mathbf{X}^{(n)}$. The simplest means of simulating Eq. (30) is via the Euler-Maruyamma approximation[68]

$$\begin{aligned} X_i^n(t_{k+1}) &= X_i^n(t_k) + D_i^n(t_k)\Delta t + B^n(t_k)(\Delta t)^{1/2}\zeta_i^n(t_k), \\ U_i^n(t_{k+1}) &= U_i^n(t_k) + M_i^n(t_k)\Delta t + E^n(t_k)(\Delta t)^{1/2}\zeta_i^{\prime n}(t_k) \\ &\quad + F_{ij}^n(t_k)(\Delta t)^{1/2}\zeta_j^n(t_k), \end{aligned} \tag{33}$$

where $D_i^n(t_k) = D_i(\mathbf{X}^{(n)}(t_k), \mathbf{U}^{(n)}(t_k); t)$, $B^n(t_k) = B(\mathbf{X}^{(n)}(t_k), \mathbf{U}^{(n)}(t_k); t)$, ... and $\zeta_i^{\prime n}(t_k)$, $\zeta_j^n(t_k)$

are samples from two independent Gaussian white noises at time t_k. This formulation preserves the Markovian character of the diffusion processes[69–71] and facilitates affordable computations. Higher order numerical schemes for solving Eq. (30) are available,[68] but one must be very cautious in using them for LES.[28] Since the diffusion term in Eq. (26) strongly depends on the stochastic processes $\mathbf{U}(t)$ and $\mathbf{X}(t)$, the numerical scheme must preserve the Itô-Gikhman[72,73] nature of the process. Equation (33) exhibits this property.

The LES of the first hydrodynamic moments is conducted with the "compact parameter" finite difference scheme of Carpenter.[74] This is a variant of the McCormack[75] scheme in which a fourth order compact differences are used to approximate the spatial derivatives, and a second order symmetric predictor-corrector sequence is employed for time discretization. The computational scheme is based on a hyperbolic solver which considers a fully compressible flow. Here, the simulations are conducted with a low Mach number ($M \approx 0.3$) to minimize compressibility effects. The procedure involved in the finite difference discretization is dependent of the Monte Carlo solver through the SGS. All the finite difference operations are conducted on fixed and equally sized grid points. Thus, all the filtered values of the hydrodynamic variables are determined on these grid points. The transfer of information from these points to the location of the Monte Carlo particles is conducted via interpolation. Second-order (bilinear) interpolation scheme is considered, as no significant difference in statistics were observed when higher orders were used.[29]

The SGS necessary to the finite difference LES solver (or higher order moments of the VFDF) at a given point are estimated by consideration of particles within some volume centered at the point of interest. Effectively, this finite volume constitutes an "ensemble domain" characterized by the length scale Δ_E in which the VFDF is represented discretely by stochastic particles. This is necessary as, with probability one, no particle will coincide with the point as considered.[40] Here, a box of size Δ_E is used to construct the ensemble mean variances and covariances of the velocity vector from which the ensemble mean values are subtracted to yield the SGS at the finite difference nodes. These values are used in the finite difference LES solver of Eq. (4). The subgrid kinetic energy dissipation rate and the subgrid mixing frequency are also obtained from the SGS. From the numerical standpoint, determination of the size of the ensemble domain is an important issue as it determines the time evolution of the LES solver through the values of the SGS. Ideally, it is desired to obtain the statistics from the Monte Carlo solution when the size of sample domain is infinitely small (*i.e.* $\Delta_E \to 0$) and the number of particles within this domain is infinitely large. With a finite number of particles, if Δ_E is too small there may not be enough particles to construct the statistics. A larger ensemble domain decreases the statistical errors, but may increase the dispersion errors which manifest themselves in "artificially diffused" statistical results. This compromise between the statistical accuracy and dispersive accuracy as pertaining to Lagrangian Monte Carlo schemes implies that the optimum magnitude of Δ_E cannot, in general, be specified *a priori*.[37] This does not diminish the capability of the procedure, but exemplifies the importance of the parameters governing the statistics. A better understanding of the sample size impact is obtained through consistency simulations as illustrated in the results section.

VI Results

VI.1 Flows simulated

In this section results are presented to demonstrate the effectiveness of the VFDF method. Spatially developing jet configurations are considered for the LES simulations. $2D$ planar jet simulations are used for consistency assessment of the previously described methodology and for comparisons with existing closures. $3D$ round jet simulations allow validation of the new approach and pre-existing closures via experimental data.

All of these flows are dominated by large scale coherent structures. The formation of these structures are expedited by imposing low amplitude perturbations at the inflow boundary. In the figures presented below, x, y correspond to the streamwise and cross-stream directions, respectively. In 3D, z denotes the spanwise direction. Finally $r = \sqrt{y^2 + z^2}$ is the radial direction. The size of the domain in the $2D$ jet flow is $0 \leq x \leq 14D,\ -3.5D \leq y \leq 3.5D$. The ratio of the inlet jet velocity to that of coflowing stream is kept fixed at 0.5 for the consistency analysis and 0.2 for comparative results between closures. For the $3D$ jet the domain consists of a rectangular box of dimensions $0 \leq x \leq 14D,\ -3.5D \leq y \leq 3.5D,\ -3.5D \leq z \leq 3.5D$.

All the flow configurations are simulated via LES. The procedure in LES is based on the Monte Carlo solution of the modeled VFDF transport equation (Eq. (25)) for the velocity vector augmented by the finite difference solution of the filtered hydrodynamic modeled equations (Eqs. (4)). In the presentation below, these results are identified by the abbreviation VFDF. In addition, another LES is conducted in which the modeled transport equations for the filtered velocity and the generalized subgrid stresses are simulated with the finite difference scheme. In these simulations, the hydrodynamic solver and the models for the SGS are consistent with those employed in the VFDF (i.e. Eqs. (7), (8) and imposing Eq. (24)). The effects of the turbulent subgrid transport, $\tau_L(u_i, u_j, u_k)$, are obtained from the VFDF in the case of the consistency simulations. The results based on this procedure are referred to as LES-FD. No attempt is made here to determine the magnitudes of the constants appearing in these models in a dynamic manner.[14] However, different values are considered for C_0 in order to compare the predictions obtained from the VFDF with other deterministic closures.

VI.2 Numerical specifications

The primary parameter is the flow Reynolds number (Re). All finite difference simulations are conducted on equally-spaced square grids ($\Delta x = \Delta y = \Delta z(\text{for 3D}) = \Delta$). Since the size of the computational domain is fixed, the number (and the size) of the grids depends on the type of simulation being conducted.

The VFDF and LES-FD runs are conducted on grids coarser than those in DNS. Unless otherwise specified, the LES resolutions in the consistency simulations of the planar jet are 201×101 and 181×91, with $Re = 4,000$ (based on the inlet jet diameter). The planar jet configurations used for comparisons of the various closures use 161×81 points with $Re = 10,000$. The $3D$ grid is composed of $161 \times 81 \times 81$ grid points for a Reynolds numbers of $Re = 10,000$ based on the inner stream velocity and jet diameter. A low speed coflow corresponding to a 0.2 ratio with respect to the inner flow is maintained in order to stabilize the solver.

When required (inlet conditions, DNS) a top-hat filter function[33] of the form below is used

$$G(\mathbf{x}' - \mathbf{x}) = \prod_{i=1}^{N_D} \tilde{G}(x'_i - x_i)$$

$$\tilde{G}(x'_i - x_i) = \begin{cases} \frac{1}{\Delta_G} & |x'_i - x_i| \le \frac{\Delta_G}{2}, \\ 0 & |x'_i - x_i| > \frac{\Delta_G}{2}, \end{cases} \tag{34}$$

in which N_D denotes the number of dimensions, and $\Delta_G = 2\Delta$. No attempt is made to investigate the sensitivity of the results to the filter function[34] or the size of the filter.[76]

In VFDF, the Monte Carlo particles should initially be distributed at $t = 0$ throughout the domain. For the jet simulations the particles are supplied only in the region $-1.75D \leq y \leq 1.75D$ in $2D$. This procedure seems to be sufficient to yield accurate results, at least for the velocity ratios under study. The particle density is monitored at all times to ensure an approximately uniform particle density through the domain of interest.

In the spatial jets, new particles are introduced through the inlet boundary at a rate proportional to the local flow velocity and with a compositional makeup dependent on the y, (and z in 3D) coordinate and yielding identical statistics regardless of the ensemble domain size Δ_E. The density of the Monte Carlo particles is determined by the initial number of particles per grid cell (NPG) of dimension $\Delta \times \Delta (\times \Delta)$. The magnitude of NPG is varied to evaluate its affect on statistical convergence of the Monte Carlo results. This assessment is demonstrated in 2D simulations of the spatially developing planar jet. The simulations of 3D spatial jet are based on $NPG = 40$. The size of the "ensemble domain" in the VFDF simulations is also varied in order to quantify its influence on the statistical convergence. The following sizes are used, $\Delta_E = 2\Delta, \Delta, \Delta/2$ in the consistency simulations and $\Delta_E = \Delta$ otherwise. The number of sample particles used to construct the VFDF statistics is thus controlled by the values of NPG and Δ_E.

An additional parameter which influences the numerical accuracy is the magnitude of the incremental time step. The stability criterion for the finite difference scheme requires $CFL \leq 1/\sqrt{3}$[74] and is more stringent than the criterion for the Fourier number. The effect of the time increment on the accuracy of the Euler-Maruyamma scheme is not investigated here. The Δt value (CFL numbers) equal to the value from Colucci *et al.*[28] is adopted.

The simulated results are analyzed both "instantaneously" and "statistically." In the former, the instantaneous contours (snap-shots) of the vorticity and scatter plots of the redundant variables are considered. In the latter, the "Reynolds-averaged" statistics constructed from the instantaneous data are considered. In these spatially developing flows this averaging procedure is conducted via sampling in time. All Reynolds averaged results are denoted by an overbar.

VI.3 Consistency of VFDF and convergence of the Monte Carlo procedure

The objective of this subsection is to demonstrate the consistency of the VFDF formulation and the convergence of the Monte Carlo simulations. For this purpose, the LES results via VFDF and LES-FD are compared against each other in a planar-jet configuration under different conditions. Since the accuracy of the finite difference procedure is well-established (at least for the first order filtered quantities), this comparative analysis provides a good means of assessing the performance of the Monte Carlo solution of the VFDF and allows identification of the governing parameters. For simplicity and a clear understanding of the methodology, the model is simplified by neglecting the spatial diffusion of the VFDF due to the molecular term. This assumption results in the neglect of the molecular transport in the SGS equations (Eq. (23)). The Generalized Langevin model in turns models the expression,

$$\frac{\partial}{\partial V_i}\left[\left(\left\langle\frac{\partial p}{\partial x_i}|\boldsymbol{V}\right\rangle_L - \frac{\partial\langle p\rangle_L}{\partial x_i} - \left\langle\frac{\partial\sigma_{ik}}{\partial x_k}|\boldsymbol{V}\right\rangle_L + \frac{\partial\langle\sigma_{ik}\rangle_L}{\partial x_k}\right)P_L\right]. \tag{35}$$

This simplification is equivalent to an assumed high Reynolds number at the subgrid level since only Eqs.(22) are fully recovered. This approximation reduces the degrees of freedom of the stochastic process. The new equivalent stochastic system therefore reads,

$$\begin{aligned} dX_i(t) &= U_i(t)\,dt \\ dU_i(t) &= \left[\left(-\frac{\partial\langle p\rangle_L}{\partial x_i} + \frac{\partial\langle\sigma_{ik}\rangle_L}{\partial x_k}\right) - G_{ij}\left(U_j(t) - \langle u_j\rangle_L\right)\right]dt + \sqrt{C_0\varepsilon}\,dW_i^u(t). \end{aligned} \tag{36}$$

and has statistics evolving (to a first order in time) as,

$$\begin{aligned} \langle dX_i\rangle = \langle u_i\rangle_L\,dt, \quad \langle dU_i\rangle = \left[-\frac{\partial\langle p\rangle_L}{\partial x_i} - \frac{\partial\langle\sigma_{ik}\rangle_L}{\partial x_k}\right]dt, \\ \langle dX_i dX_j\rangle = 0., \quad \langle dU_i dU_j\rangle = C_0\varepsilon\,\delta_{ij}\,dt, \quad \langle dX_i dU_j\rangle = 0. \end{aligned} \tag{37}$$

The third order term in Eq. (7), $\tau_L(u_i, u_j, u_k)$, is obtained from the VFDF and used into LES-FD.[37] This ensure a fully consistent approach between LES-FD and the VFDF. The model's coefficients are taken to be $C_0 = 1$[48] and $C_\varepsilon = 1$.[77,78] Eq. (36) model could be used for LES in particular cases but the reader has to recognize that the proper behavior of the VFDF is not fully recovered.[79]

In Fig. 1, results are presented of the LES of the spatially developing planar-jet. Shown in the figure is the instantaneous vorticity contour plots via (a) VFDF and (b) LES-FD. This figure provides a simple visual demonstration of the consistency of the VFDF as the results via the particle method are in agreement with those obtained by LES-FD. In fact, the Monte Carlo results are even more attractive due the Lagrangian nature of the solution procedure. While the LES-FD results suffer from slight over- and under-shoots, there are no such errors in the Monte Carlo scheme. The visual agreement is confirmed by the scatter plots of the redundant variables $\langle u\rangle_L$ and $\langle v\rangle_L$ shown in Fig. 2(a) and (b). The correlation and regression coefficients for the first filtered moments were found to be rather insensitive to Δ_E ($\pm 0.5\%$) as seen in Tables (1) and (2).

Another rigorous means of assessing the VFDF results is via consideration of the Reynolds averaged results. Figure 3 shows such results in which the sensitivity of the VFDF predictions to several parameters is assessed. Figure 3(a) shows the comparison of VFDF and LES-FD results for the cross-stream variation of $\overline{\langle u\rangle_L}$ at a distance of 7.5 inlet diameters from the inflow boundary. The results are qualitatively identical at all y locations in the flow field. Several values of Δ_E are taken under consideration for a unique number of particles per ensemble ($NPG = 10, 40, 160$). It is shown that the first filtered moment of the VFDF agrees very well with those obtained by LES-FD, even for large Δ_E values. The differences between the VFDF and LES-FD results are more significant in Fig. 3(b) where the stream-wise variation of $\overline{\langle u\rangle_L}$ is shown for several values of Δ_E. This figure also indicates that the difference between VFDF and LES-FD predictions diminishes as Δ_E decreases.

The differences observed in the first order filtered quantities are directly correlated to the contribution of the subgrid second order filtered moments. Significant differences observed at various instantaneous times between the subgrid moments from LES-FD and from the VFDF would result in distinct evolutions of the flow field in time. It is therefore necessary to have a better understanding of the effect of Δ_E on the subgrid quantities. Figure 4(a,b,c) shows scatter plots at a given time for (a) $\tau_L(u,u)$, (b) $\tau_L(v,v)$ and (c) $\tau_L(u,v)$, for various Δ_E. The corresponding correlation and regression coefficients are shown in Table (1). Convergence at the subgrid level is clearly obtained as $\Delta_E \to 0$. Note nonetheless the large difference between LES-FD and VFDF when $\Delta_E = 2\Delta$. Time averaged quantities corroborate these last results as observed in Fig. 5(a,b,c) where (a) $\overline{\tau_L(u,u)}$, (b) $\overline{\tau_L(v,v)}$ and (c) $\overline{\tau_L(u,v)}$ are shown.

The other parameter which influences the accuracy of the Monte Carlo results is the number of Monte Carlo particles per grid cell (NPG). Figures 6(a,b) and 7(a,b,c) show that $\overline{\langle u\rangle_L}$ and $\overline{\langle v\rangle_L}$

are totally insensitive to NPG for the range considered and that $\overline{\tau_L(u_i, u_j)}$ values do not vary significantly for $NPG > 40$ with a given Δ_E. More important figures 6 and 7 illustrate the greater influence of the size of the ensemble domain than NPG. Consistency simulations with no third order subgrid terms in the LES-FD scheme were conducted and significant drops in the correlation coefficients were observed especially for $\Delta_E = 2\Delta$ (cases not shown). The Reynolds averaged subgrid stresses did not depict such drastic behaviors but differences could still be observed stressing the importance of the third order terms for any LES-FD/deterministic approach. This problem is avoided with the VFDF. Therefore in the general case even smaller NPG values can be used as long as Δ_E is properly chosen. This last statement is advanced based on the observation that the third order subgrid quantity $\tau_L(u_i, u_j, u_k)$ is required for consistency simulations which is not the case for the general approach.

The convergence of the Monte Carlo solution and the independence to NPG and Δ_E are demonstrated by these results (at least for the first filtered moments). The size of the ensemble average is nonetheless important as it influences the general behavior of the LES solver through the predictions of the SGS. It seems necessary to keep Δ_E reasonably small in accordance with the theoretical point of view to estimate the subgrid quantities correctly.

VI.4 Qualitative study of the VFDF: comparison with existing closures

Deterministic closures were presented in Section II. The first one referred to as the "Smagorinsky model", Eq. (5), assumes equilibrium between the production and dissipation rates at the subgrid scales yielding a zeroth order closure. The second closure, Eq. (6), referred to as the "k-eqn model",[20] suppresses the previous equilibrium assumption by solving a modeled transport equation for $k = \frac{1}{2}\tau_L(u_k, u_k)$ which, to some extent, allows resolution of the present desequilibrium in the subgrid scales. Both of these models are nonetheless unable to resolve the anisotropy of SGS which is expected to increase in low resolution LES simulations of practical engineering flows. The last deterministic model corresponding to Eqs. (7,8,9) and referred to as the "SGS-eqns model"[25,27] theoretically predicts anisotropy of the SGS as well as the desequilibrium process. The VFDF model, Eq. (30), has all the properties of the "SGS-eqns model". These last two models are not fully consistent in this subsection. The third order quantities, $\tau_L(u_i, u_j, u_k)$, being implied in the VFDF closure have to be modeled with "SGS-eqns model", Eq.(9). These term contributions were already found to be critical in the previous subsection and are further studied for the second order closures. The coefficient C_0 found in the VFDF and "SGS-eqns" models is varied in order to evaluate its effect on the flow predictions. Only the Reynolds averaged quantities are considered here as they are illustrative of the instantaneous behavior of the studied dynamic systems. Our objective is to illustrate through numerical simulations the fundamental differences between the dynamic systems composed of the LES governing equations plus the LES model and quantify the closure coefficient significance.

Figure 8(a) shows the values of $\overline{\langle u\rangle_L}$ along the center line as obtained from the different models. The Smagorinsky and k-eqn models predict roughly the same slope of decay of the streamwise velocity. The higher order models on the other hand predict different behaviors depending on the value of C_0. This observation allows us to stipulate on the importance of this coefficient in predicting the strength of the diffusive effect of the SGS scales. Also to notice from Fig. 8(a) are the different locations of the starting velocity decay from one model to another. The deterministic models predict the transition to occur at $x = 7.5D \pm 0.5D$. The VFDF produces two distinct regimes. The first regime depicts a slowly decaying $\overline{\langle u\rangle_L}$ until $x \approx 8D$ where transition to a fast decay occurs. In the second regime the slopes are similar to the values obtained with the SGS-eqns closures. Shown in Fig. 8 (b) is the cross-stream variation along $x = 8D$ for the streamwise velocity component non-dimensionalized by its value at the center line. Clearly the level of diffusion in the profiles decreases as one uses the Smagorinsky, the k-eqn model, the SGS-eqns or VFDF models. Note that results obtained without model are adjoined to the figures to illustrate the importance of the SGS in the present simulations.

The decay rate of the center line velocity is related to the large structures behavior which is essentially governed by the subgrid production rate of kinetic energy, $-\tau_L(u_i, u_k)\frac{\partial\langle u_k\rangle_L}{\partial x_i}$. This last quantity transfers the mechanical energy contained in the large structures to the internal energy and is dissipated by the viscous forces. The Reynolds averaged production rate and subgrid kinetic energy are shown in Fig. 9(a,b). The choice of LES model defines the mechanism of energy tranfer between scales. The Smagorinsky and k-eqn models predict roughly the same level of energy transfer while the other models predict more than twice the amount of subgrid kinetic energy production rate. Here again C_0 is found to be an important parameter for the second order type of closures (SGS-eqns and VFDF). For approximately the same levels of subgrid turbulent kinetic energy, Fig. 9(b), the subgrid production rate differs quite much for various C_0 values. In Fig. 9(a,b) the subgrid quantities as obtained from the VFDF models show two regimes as observed in Fig. 8(a). The subgrid production rate and turbulent kinetic energy first grow slowly at two different rates until $x \approx 8D$. Within this potential core energy is slowly removed from the large scales increasing the energy in the small scales. This transfer of energy results in a slowly decaying center line velocity component as observed in Fig. 8(a). At $x \approx 8D$, k and its production rate suddenly increase to the levels obtained with the SGS-eqns model. This two regime behavior observed with the VFDF in Figs. 8(a)-9(a,b) can only find its source in the third order term as it is not predicted with the deterministic models which ignore $\tau_L(u_i, u_j, u_k)$ or supply a more or less ***ad hoc*** modelisation. Finally, differences observed between VFDF simulations can only result from the values of C_0 as $NPG = 40$ and $\Delta_E = \Delta$ are kept identical.

Equation (23) demonstrates that C_0 influences only the anisotropy of the SGS. Hence, the observations formulated from Fig. 9(a,b) are explained through the level of anisotropy in the SGS as predicted by the models. The third order term, $\tau_L(u_i, u_j, u_k)$, can aslo be at the origin of these differences, but only to some limited extent. Anisotropy in the normal SGS are shown in Fig. 10(a,b) for the cross-stream direction along $x = 8D$. The effect of C_0 is clearly illustrated at the subgrid level in these last figures. Because of the importance of the SGS in Eqs. (4) and in the evolution equation of k, Fig. 8, C_0 plays a crucial role in predicting the desired behavior of the LES dynamic system.

The final part of this subsection considers the VFDF equations obtained in Eq. (30) and Eq. (36). These models are respectively referred to as "VFDF1" and "VFDF2" in the figures. The comparison is conducted for the same conditions as above and aim to study the differences between the two stochastic systems given in Eqs. (32) and Eqs. (37). The two models essentially differ in the presence or not of the resolved disspation rate in the time evolution of the incremental velocity correlations. Figure 10(a,b) validates the approximation made in Eq. (36) for the flow configuration studied. The resolved part of the dissipation rate is still found to have effects on the predictions and use of the original model, Eq. (30), is still advised as LES usually deals with $3D$, transient flows of finite Re number in which resolved scale contributions are of critical importance.

The comparative study of the behavior of various LES systems (i.e: LES solver plus SGS model) underscores fundamental differences in the dynamics of the systems inherited from the SGS models. More specifically, the third order filtered correlations are found to be of importance for the second order closure systems. The C_0 coefficient, necessary for the VFDF closure, seems critical in estimating the anisotropy in the SGS as well as the proper decay rate and energy transfer between scales. The choice of coefficient in the VFDF model will therefore result in a specific dynamic evolution of the LES solver as observed in this subsection. As a consequence, gathering informations about C_0 for different flow configurations is necessary for validation of the VFDF approach.

References

[1] Lilly, D. K., The Representation of Small-Scale Turbulence in Numerical Simulation Experiments, in *Proceedings of IBM Scientific Computing Symposium Environmental Sciences*, pp. 195–210, IBM Form No. 320-1951, 1967.

[2] Ferziger, J. H., Higher Level Simulations of Turbulent Flows, Stanford University Report TF-16, Department of Mechanical Engineering, Stanford University, Stanford, CA, 1981.

[3] Voke, P. R. and Collins, M. W., Large Eddy Simulation: Petrospect and Prospect, *Physico-Chemical Hydrodynamics*, **4**(2):119–161 (1983).

[4] Rogallo, R. S. and Moin, P., Numerical Simulation of Turbulent Flow, *Ann. Rev. Fluid Mech.*, **16**:99–137 (1984).

[5] Jou, W.-H. and Riley, J. J., Progress in Direct Numerical Simulations of Turbulent Reacting Flows, *AIAA J.*, **27**(11):1543–1556 (1989).

[6] Givi, P., Model Free Simulations of Turbulent Reactive Flows, *Prog. Energy Combust. Sci.*, **15**:1–107 (1989).

[7] Lumley, J. L., editor, *Whither Turbulence? Turbulence at the Crossroads, Lecture Notes in Physics*, Vol. 357, Springer-Verlag, 1990.

[8] Oran, E. S. and Boris, J. P., editors, *Numerical Approaches to Combustion Modeling, Progress in Astronautics and Aeronautics*, Vol. 135, AIAA Publishing Co., New York, NY, 1991.

[9] McMurtry, P. A. and Givi, P., Spectral Simulations of Reacting Turbulent Flows, in Oran, E. S. and Boris, J. P., editors, *Numerical Approaches to Combustion Modeling, Progress in Astronautics and Aeronautics*, Vol. 135, chapter 9, pp. 257–303, AIAA Publishing Co., Washington, D.C., 1991.

[10] Gao, F. and O'Brien, E., A large-eddy simulation scheme for turbulent reacting flows, *Phys. Fluids A*, **5**:1282 (1993).

[11] Givi, P., Spectral and random vortex methods in turbulent reacting flows, in Libby, P. A. and Williams, F. A., editors, *Turbulent Reacting Flows*, pp. 475–572, Academic, 1994.

[12] Smagorinsky, J., General Circulation Experiments With the Primitive Equations. I. The Basic Experiment, *Monthly Weather Review*, **91**(3):99–164 (1963).

[13] Lilly, D. K., On the Computational Stability of Numerical Solutions of Time-Dependent Non-Linear Geophysical Fluid Dynamics Problems, *Monthly Weather Review*, **93**(1):11–26 (1965).

[14] Germano, M., Turbulence: The filtering approach, *J. Fluid Mech.*, **238**:325 (1992).

[15] Germano, M., Piomelli, U., Moin, P., and Cabot, W., A dynamic subgrid-scale eddy viscosity model, *Phys. of Fluids*, **A3**:1760 (1991).

[16] Moin, P., Squires, K., Cabot, W., and Lee, S., A dynamic subgrid-scale model for compressible turbulence and scalar transport, Technical Report CTR Manuscript 124, NASA Ames Research Center, Stanford, CA 94305-3030, 1991.

[17] Moin, P., A New Approach for Large Eddy Simulation of Turbulence and Scalar Transport, in Birkhäuser, editor, *Proc. Monte Veritá Coll. on Turbulence*, pp. 1–9, Bale, 1991, Dracos, T and Tsinober, A.

[18] Wong, V., A proposed statistical-dynamic closure method for the linear or nonlinear subgrid-scale stresses, *Phys. Fluids A*, **4**(5):1080–1082 (1992).

[19] Wong, V. and Lilly, D., A comparison of two dynamic subgrid closure methods for turbulent themal convection, *Phys. Fluids*, **6**(2):1016–1023 (1994).

[20] Menon, S. and Kim, W., High Reynolds Number Flow Simulation Using the Localized Dynamic Subgrid-Scale Model, in *34th Aerospace Sciences Meeting and Exhibit*, pp. 1–11, Reno, NV, 1996, AIAA.

[21] Menon, S., Yeung, P., and Kim, W., Effect of subgrid models on the computed interscale energy transfer in isotropic tubrulence, *Computers and Fluids*, **25**(2):165–180 (1996).

[22] Chakravarthy, V. and Menon, S., On Large Eddy Simulation of non-homogeneous flows, in *35th Aerospace Sciences Meeting and Exhibit*, pp. 1–8, Reno, NV, 1997, AIAA.

[23] Kim, W. and Menon, S., A New Dynamic One-Equaiton Subgrid-Scale Model for Large Eddy Simulations, in *33rd Aerospace Sciences Meeting and Exhibit*, pp. 1–9, Reno, NV, 1995, AIAA.

[24] Ghosal, S., Lund, T., Moin, P., and Akselvoll, K., A dynamic localization model for large-eddy simulation of turbulent flows, *JFM*, **286**:229–255 (1995).

[25] Deardorff, J., The Use of Subgrid Transport Equations in a Three-Dimensional Model of Atmospheric Turbulence, *Journal of Fluids Engineering*, pp. 429–438 (1973).

[26] Fureby, C., Tabor, G., Weller, H., and Gosman, A., A comparative study of subgrid scale models in homogeneous isotropic turbulence, *Phys. of Fluids*, pp. 1416–1429 (1997).

[27] Fureby, C., Tabor, G., Weller, H., and Gosman, A., Differential subgrid models in large eddy simulations, *Phys. of Fluids*, pp. 3578–3580 (1997).

[28] Colucci, P., Jaberi, F., Givi, P., and Pope, S., Filtered density function for large eddy simulation of turbulent reacting flows, *Physics of Fluids*, **10**(2):499–515 (1998).

[29] Colucci, P., Filtered density function for large eddy simulation of turbulent reactive flows, PhD Thesis, Department of Mechanical and Aerospace Engineering, State University of New-York at Buffalo, Buffalo, NY, 1998.

[30] FMDF, pp. – (1998).

[31] Zang, Y., Street, R., and J.R., K., A dynamic mixed subgrid-scale model and its application to turbulent recirculating flows, *Phys. Fluids A*, **5**:3186–3196 (1993).

[32] Kerr, R., Domaradzki, J., and Barbier, G., Small-scales properties of nonlinear interactions and subgrid-scale energy transfer in isotropic turbulence, *Phys. Fluids*, **8**:197 (1996).

[33] Aldama, A. A., *Filtering Techniques for Turbulent Flow Simulations, Lecture Notes in Engineering*, Vol. 49, Springer-Verlag, New York, NY, 1990.

[34] Vreman, B., Geurts, B., and Kuerten, H., Realizability conditions for the turbulent stress tensor in large-eddy simulation, *J. Fluid Mech.*, **278**:351 (1994).

[35] Rotta, J., notitle, *J. Zeitsch fur Physik*, **129**:547 (1951), Translation in English available in NASA TM-14560 (1982).

[36] O'Brien, E. E., The Probability Density Function (PDF) Approach to Reacting Turbulent Flows, in Libby, P. A. and Williams, F. A., editors, *Turbulent Reacting Flows*, chapter 5, pp. 185–218, Springer-Verlag, Heidelberg, 1980.

[37] Pope, S. B., PDF Methods for Turbulent Reacting Flows, *Prog. Energy Combust. Sci.*, **11**:119–192 (1985).

[38] Haworth, D. and Pope, S., A generalized Langevin model for turbulent flows, *Physics of Fluids*, **29**(2):387–405 (1986).

[39] Pope, S., Consistency conditions for random-walk models of turbulent dispersion, *Physics of Fluids*, **30**(8):2374–2378 (1987).

[40] Pope, S., Lagragian PDF methods for turbulent flows, *Annu. Rev. Fluid Mech*, **26**:23–63 (1994).

[41] Pope, S., On the relationship between stochastic Lagrangian models of turbulence and second-moment closures, *Physics of Fluids*, **6**(2):973–985 (1994).

[42] Kolmogorov, A., Local structure of turbulence in an incompressible fluid at very high Reynolds numbers, *Dokl. Akad. Nauk. SSSR*, **30**:299–303 (1941).

[43] Kolmogorov, A., Equations of turbulent motion of an incompressible fluid, *Izv. Acad. Sci. USSR phys.*, **6**:56–58 (1942).

[44] Kolmogorov, A., A refinement of previous hypotheses concerning the local structure of turbulence in a viscous incompressible fluid at high Reynolds number, *JFM*, **13**:82–85 (1962).

[45] Obukhov, A., On the theory of atmospheric turbulence, *Izv. Akad. Nauk. SSSR Ser. Fiz.*, **6**:59–63 (1942).

[46] Obukhov, A., Some specific features of atmospheric turbulence, *J. Geophys. Res.*, **67**:311–314 (1962).

[47] Frisch, U., *TURBULENCE*, Cambridge, New York, 1995.

[48] Sawford, B., Reynolds number effects in Lagrangian stochastic models of tubulent dispersion, *Phys. of Fluids*, **A3**:1577 (1991).

[49] George, W., The decay of homogeneous isotropic turbulence, *Phys. Fluids A*, 4(7):1492–1509 (1992).

[50] Pope, S. B., Transport Equation for the Joint Probability Density Function of Velocity and Scalars in Turbulent Flow, *Phys. Fluids*, **24**(4):588–596 (1981).

[51] Pope, S., PDF METHODS FOR TURBULENT REACTIVE FLOWS, *Prog. Energy Combust. Sci.*, **11**:119–192 (1985).

[52] Chorin, A. J. and Marsden, J. E., *A Mathematical Introduction to Fluid Mechanics*, Springer-Verlag, New York, NY, 1979.

[53] Leonard, A., Vortex Methods for Flow Simulation, *J. Comp. Phys.*, **37**(3):289–335 (1980).

[54] Majda, A., Vortex Dynamics: Numerical Analysis, Scientific Computing, and Mathematical Theory, in McKenna, J. and Temam, R., editors, *ICIAM '87*, pp. 153–182, Society for Industrial and Applied Mathematics, Philadelphia, 1988.

[55] Sarpkaya, T., Computational Methods with Vortices - The 1988 Freeman Scholar Lecture, *Journal of Fluids Engineering*, **111**:5–52 (1989).

[56] Ghoniem, A. F., Vortex Simulation of Reacting Shear Flow, in Oran, E. S. and Boris, J. P., editors, *Numerical Approaches to Combustion Modeling, Progress in Astronautics and Aeronautics*, Vol. 135, chapter 10, pp. 305–348, AIAA Publishing Co., Washington, D.C., 1991.

[57] Gustafson, K. E. and Sethian, J. A., editors, *Vortex Methods and Vortex Motion*, SIAM, Philadelphia, PA, 1991.

[58] Risken, H., *The Fokker-Planck Equation*, Methods of Solution and Applications, Springer, New York, 1989.

[59] Gardiner, C., *Handbook of Stochastic Methods*, Springer, New York, 1990.

[60] Dreeben, T. and Pope, S., Probability density function/Monte Carlo simulation of near-wall turbulent flows, *J. Fluid Mech.*, **357**:141–166 (1998).

[61] Karlin, S. and H.M, T., *A secon course in Stochastic Processes*, Academic, New York, 1981.

[62] Soong, T. and Grigoriu, M., *Random Vibration of Mechanical and Structural Systems*, PTR Prentice Hall, Englewoods Cliffs, New Jersey 07632, 1992.

[63] Dreeben, T. and Pope, S., Wall-function treatment in pdf methods for turbulent flows, *Physics of Fluids*, **9**(9):2692–2703 (1997).

[64] Einstein, A., *Investigations on the Theory of the Brownian Movement*, Methuen and Co. Ltd., Translation by A.D. Cowper, r. furth edition, 1926.

[65] Wiener, N., Differential Space, *J. Math. and Phys.*, **2**:131–174 (1923).

[66] Lévy, P., *Processus Stochastiques et Mouvement Brownien*, Gauthier-Villars, Paris, 1948.

[67] Dreeben, T. and Pope, S., Probability density function and Reynolds-stress modeling of near-wall turbulent flows, *Physics of Fluids*, **9**(1):154–163 (1997).

[68] Kloeden, P. and Platen, E., *Numerical Solution of Stochastic Differential Equations, Applications of Mathematical Stochastic Modelling and Applied Probability*, Vol. 23, Springer, New York, 1995.

[69] Billingsly, P., *Probability and Measure*, Wiley, New York, 1979.

[70] Helfand, E., Numerical integration of stochastic differential equations, *Bell Syst. Tech. J.*, **58**:2289 (1979).

[71] Gillespie, D., *Markov Processes*, An Introduction for Physical Scientists, Academic, New York, 1992.

[72] Itô, K., *Differential Equations, Memoirs of the American Mathematical Society*, Vol. 4, American Math Society, Providence, 1951.

[73] Gikhman, I. and A.V., S., *Stochastic Differential Equations*, Academic, New York, 1972.

[74] Carpenter, M. H., A High-Order Compact Numerical Algorithm for Supersonic Flows, in Mortron, K. W., editor, *Proc. 12th International Conference on Numerical Methods in Fluid Dynamics, Lecture Notes in Physics*, Vol. 371, pp. 254–258, Springer-Verlag, 1990.

[75] MacCormack, R. W., The Effect of Viscosity in Hypervelocity Impact Catering, AIAA paper AIAA-69-354, 1969.

[76] Erlebacher, G., Hussaini, M. Y., Speziale, C. G., and Zang, T. A., Toward the Large Eddy Simulation of Compressible Turbulent Flows, *J. Fluid Mech.*, **238**:155–185 (1992).

[77] Yoshizawa, A., Statistical theory for compressible shear flows, with the application to subgrid modelling, *Phys. Fluids*, **29**:2162 (1986).

[78] Schumann, U., Subgrid scale model for finite difference simulation of turbulent flows in plane channels and annuli, *J. Comput. Phys.*, **18**:376 (1975).

[79] Minier, J. and Pozordki, J., Derivation of a PDF model for turbulent flows based on principles from statistical physics, *Physics of Fluids*, **9**(6):1748–1753 (1997).

Figures and Tables

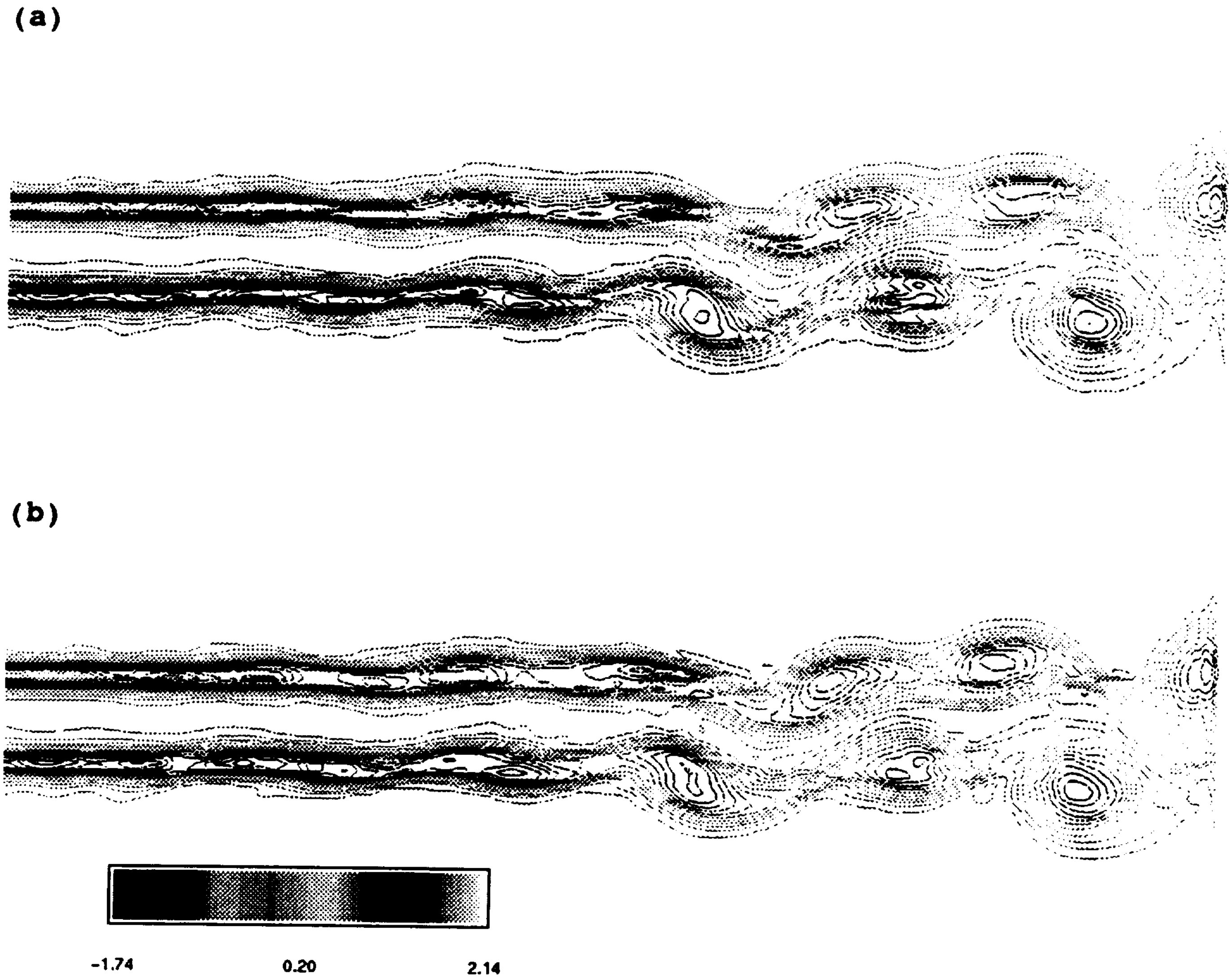

Figure 1: Instantaneous snapshot of the vorticity field: (a) VFDF, (b) LES-FD.

VFDF/LES-FD		$\Delta_E = \Delta/2$	$\Delta_E = \Delta$	$\Delta_E = 2\Delta$
$\langle u \rangle_L$	ρ_{EF}	0.9997	0.9997	0.9995
	r_{EF}	0.9995	0.9977	0.9947
$\langle v \rangle_L$	ρ_{EF}	0.9826	0.9806	0.9688
	r_{EF}	0.9879	0.9900	0.9726
$\tau_L(u,u)$	ρ_{EF}	0.9233	0.9131	0.6954
	r_{EF}	0.9516	1.2334	1.8474
$\tau_L(v,v)$	ρ_{EF}	0.8992	0.8867	0.7059
	r_{EF}	0.8943	1.1900	1.8666
$\tau_L(u,v)$	ρ_{EF}	0.8930	0.8784	0.5137
	r_{EF}	0.9351	1.0894	0.9236

Table 1: Regression, r_{EF}, and correlation, ρ_{EF}, coefficients as a function of Δ_E for Fig. (4). Planarjet configuration: 201×101.

VFDF/LES-FD		$\Delta_E = \Delta/2$	$\Delta_E = \Delta$	$\Delta_E = 2\Delta$
$\langle u \rangle_L$	ρ_{EF}	0.9995	0.9994	0.9995
	r_{EF}	0.9962	0.9974	0.9942
$\langle v \rangle_L$	ρ_{EF}	0.9838	0.9869	0.9871
	r_{EF}	0.9987	0.9930	0.9857
$\tau_L(u,u)$	ρ_{EF}	0.8724	0.8563	0.6879
	r_{EF}	1.1204	1.0594	1.5074
$\tau_L(v,v)$	ρ_{EF}	0.8244	0.8295	0.6836
	r_{EF}	1.0853	1.0272	1.5082
$\tau_L(u,v)$	ρ_{EF}	0.8279	0.7994	0.8958
	r_{EF}	1.0738	0.9547	0.8958

Table 2: Regression, r_{EF}, and correlation, ρ_{EF}, coefficients as a function of Δ_E. Planarjet configuration: 181×91.

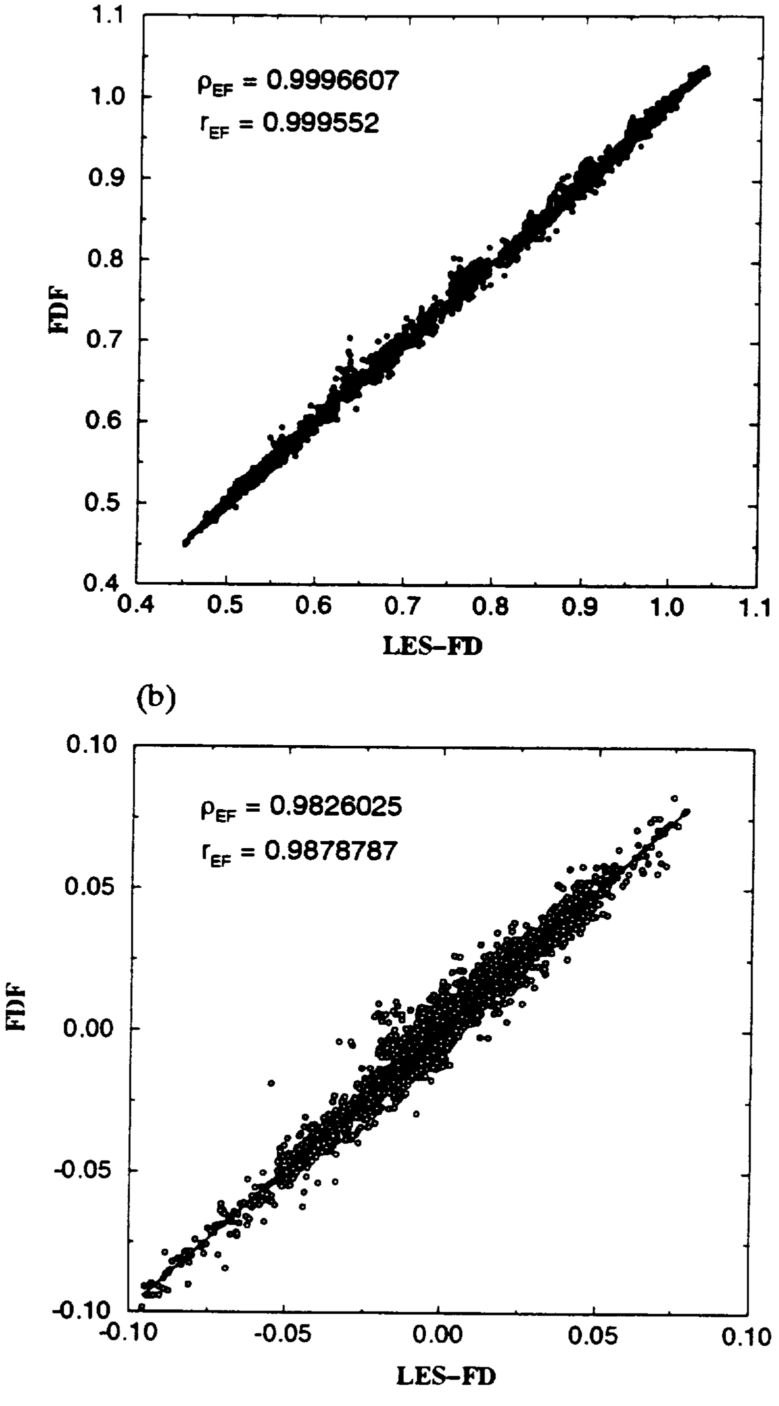

Figure 2: Scatter Plots, r_{EF} and ρ_{EF} are the regression and correlation coefficients, respectively - (a) $\langle u \rangle_L$, (b) $\langle v \rangle_L$.

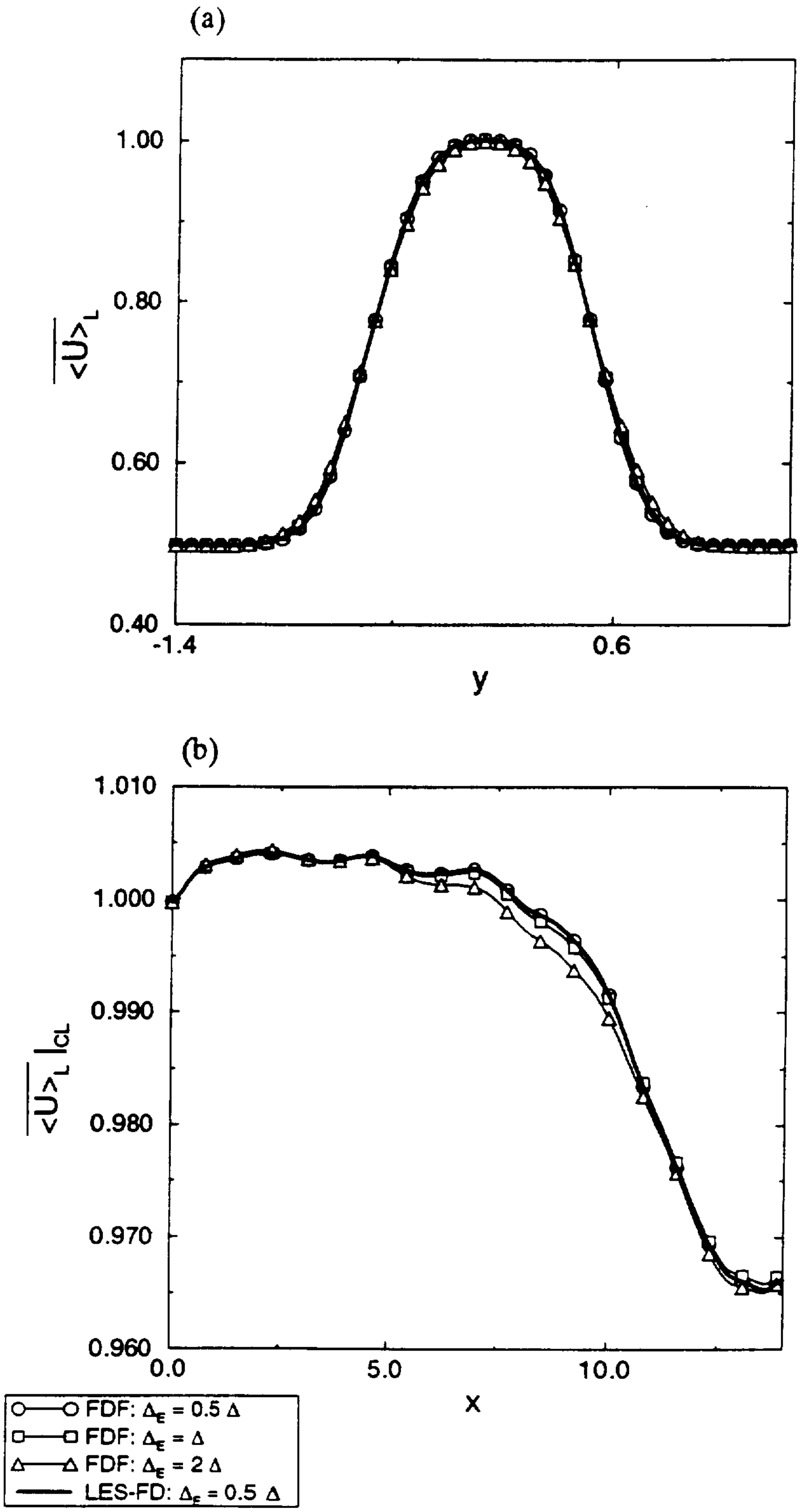

Figure 3: (a) Cross stream variation of $\overline{\langle u\rangle_L}$ at $x = 7.5D$, (b) Streamwise variation of $\overline{\langle u\rangle_L}|_{CL}$.

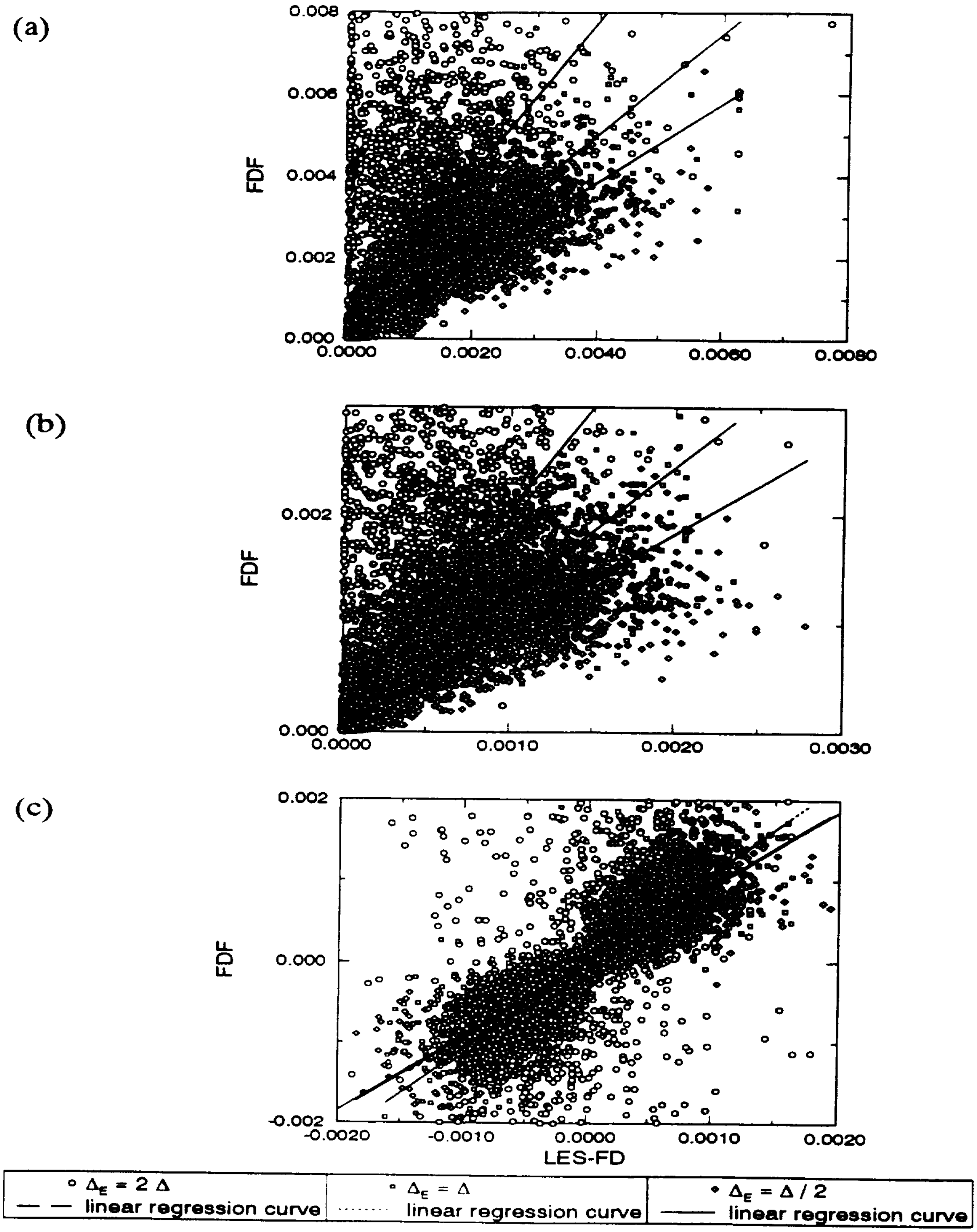

Figure 4: (a) $\tau_L(u,u)$ scatter plot, (b) $\tau_L(v,v)$ scatter plot and (c) $\tau_L(u,v)$ scatter plot.

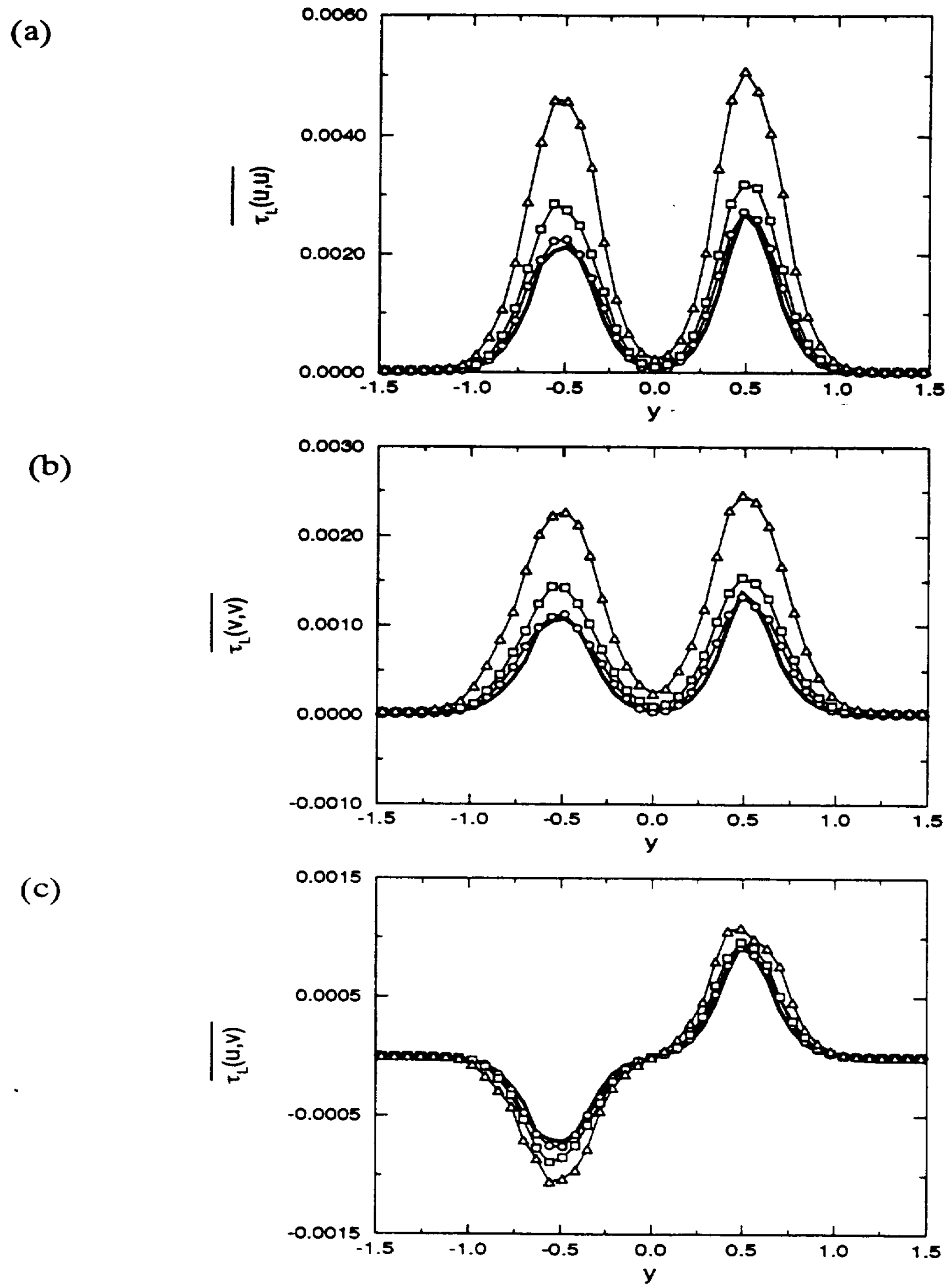

Figure 5: Cross stream variations of the time averaged SGS at $x = 7.5D$ (similar symbols as Fig. (3)).

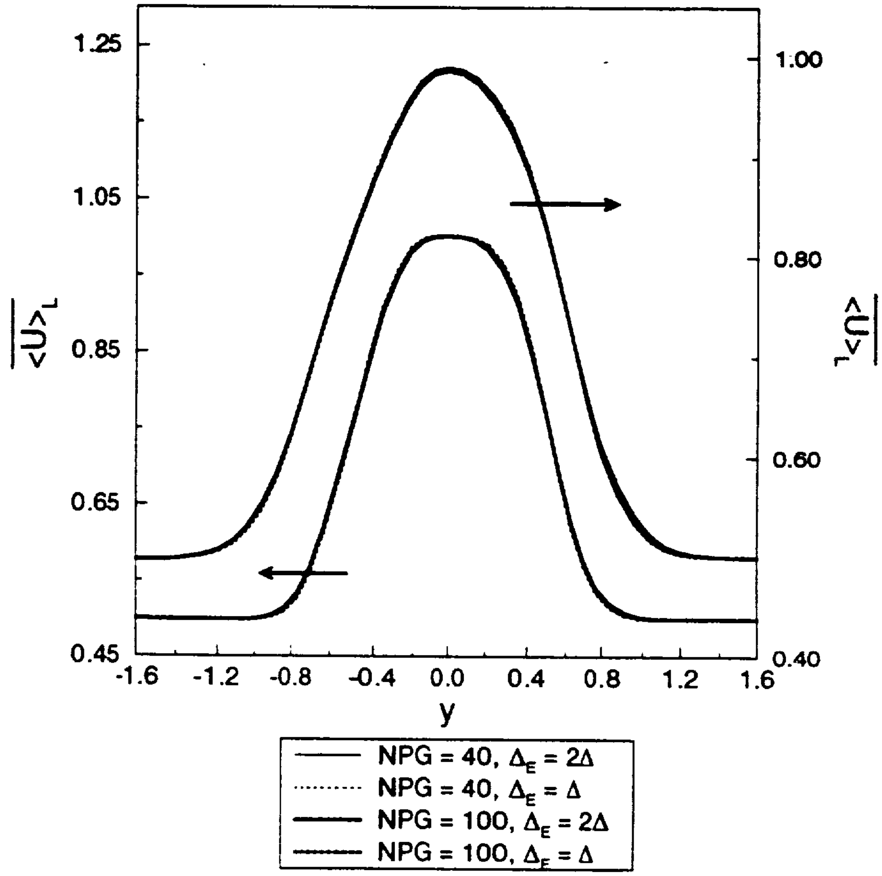

Figure 6: Cross stream variations of (a) $\overline{\langle u\rangle_L}$, (b) $\overline{\langle v\rangle_L}$ as a function of NPG ($x = 5D, 9D$).

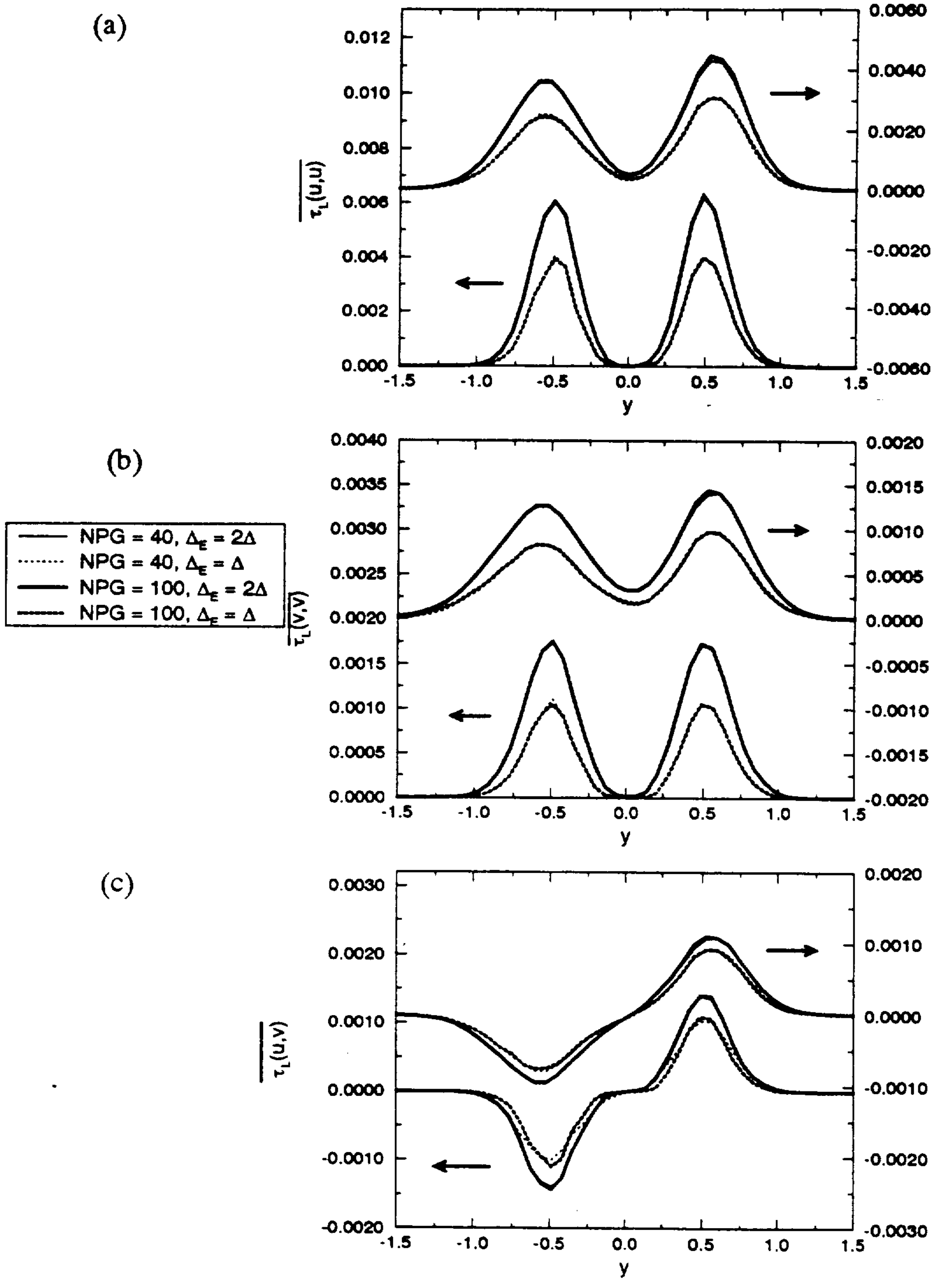

Figure 7: Cross stream variations of (a) $\overline{\tau_L(u,u)}$, (b) $\overline{\tau_L(v,v)}$ and (c) $\overline{\tau_L(u,v)}$ as a function of NPG ($x = 5D, 9D$).

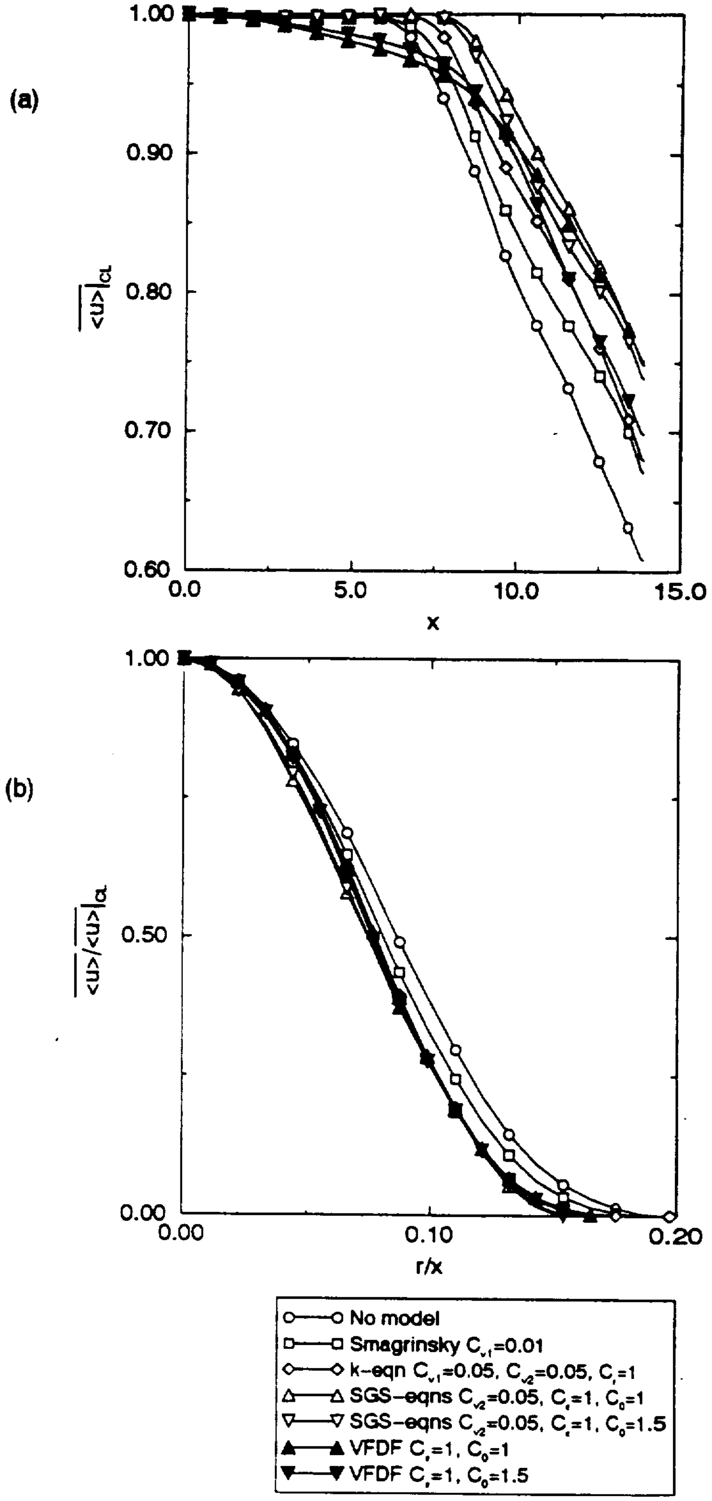

Figure 8: (a) Streamwise and (b) cross stream variations at $x = 8D$ for $\overline{\langle u \rangle_L}$ obtained with various LES models.

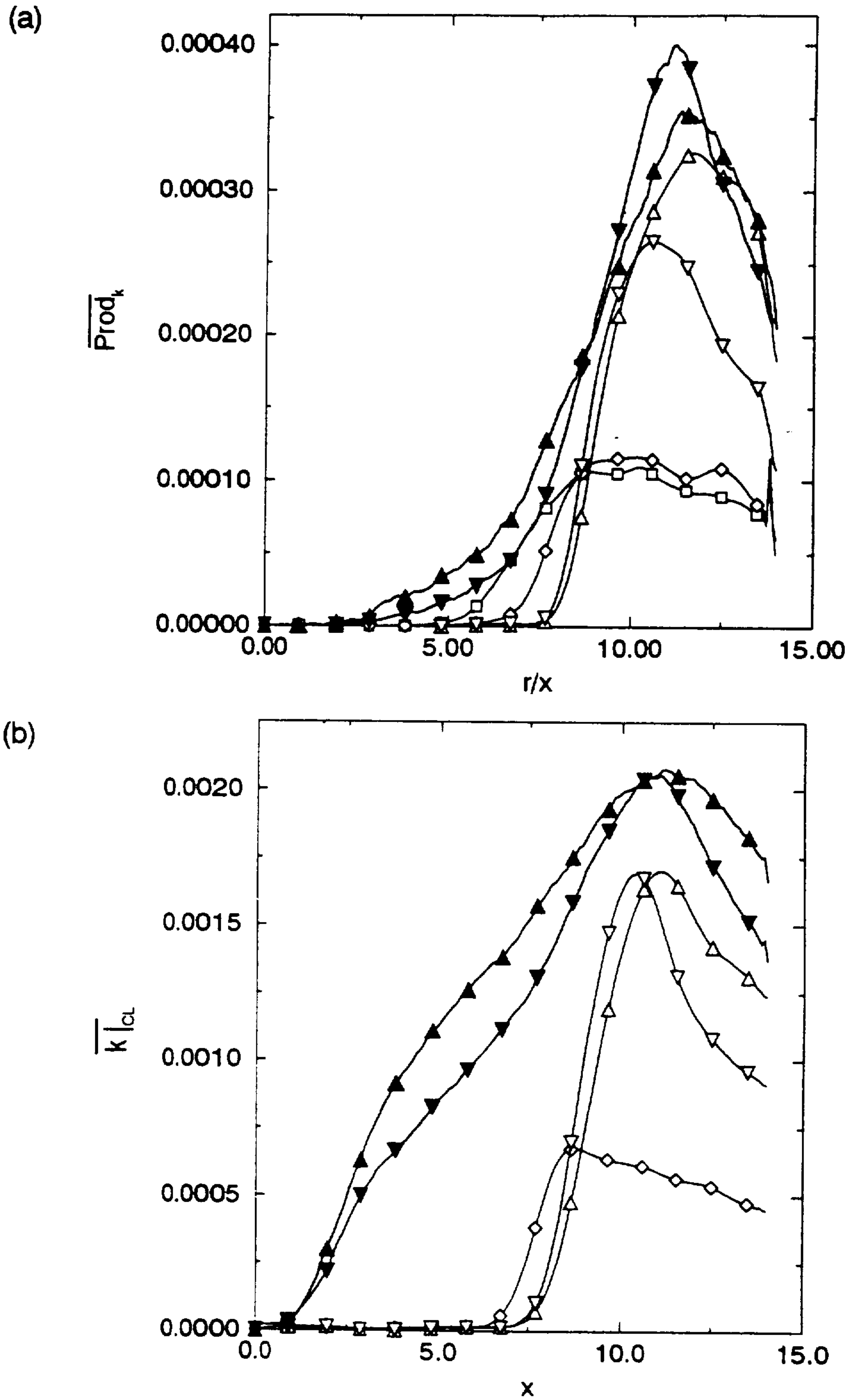

Figure 9: (a) Streamwise variations of $\overline{Prod_k}$ and (b) $\overline{k}$ from different LES models (symbols identical to Fig. (8)).

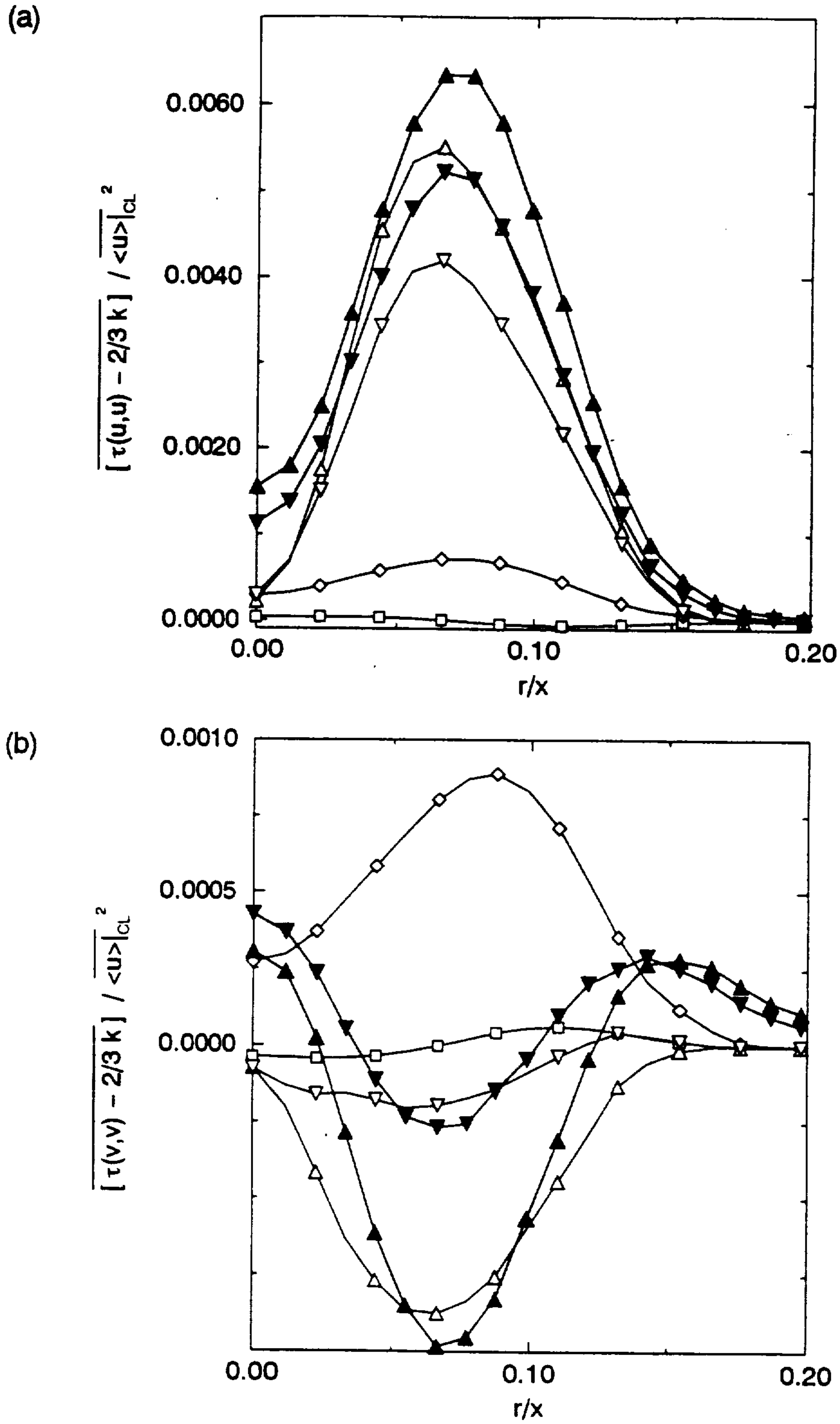

Figure 10: Cross-stream variation of the anisotropic component of the normal SGS, (a) $\overline{\tau_L(u,u) - \frac{2}{3}k}$ and (b) $\overline{\tau_L(v,v) - \frac{2}{3}k}$ (symbols identical to Fig. (8)).

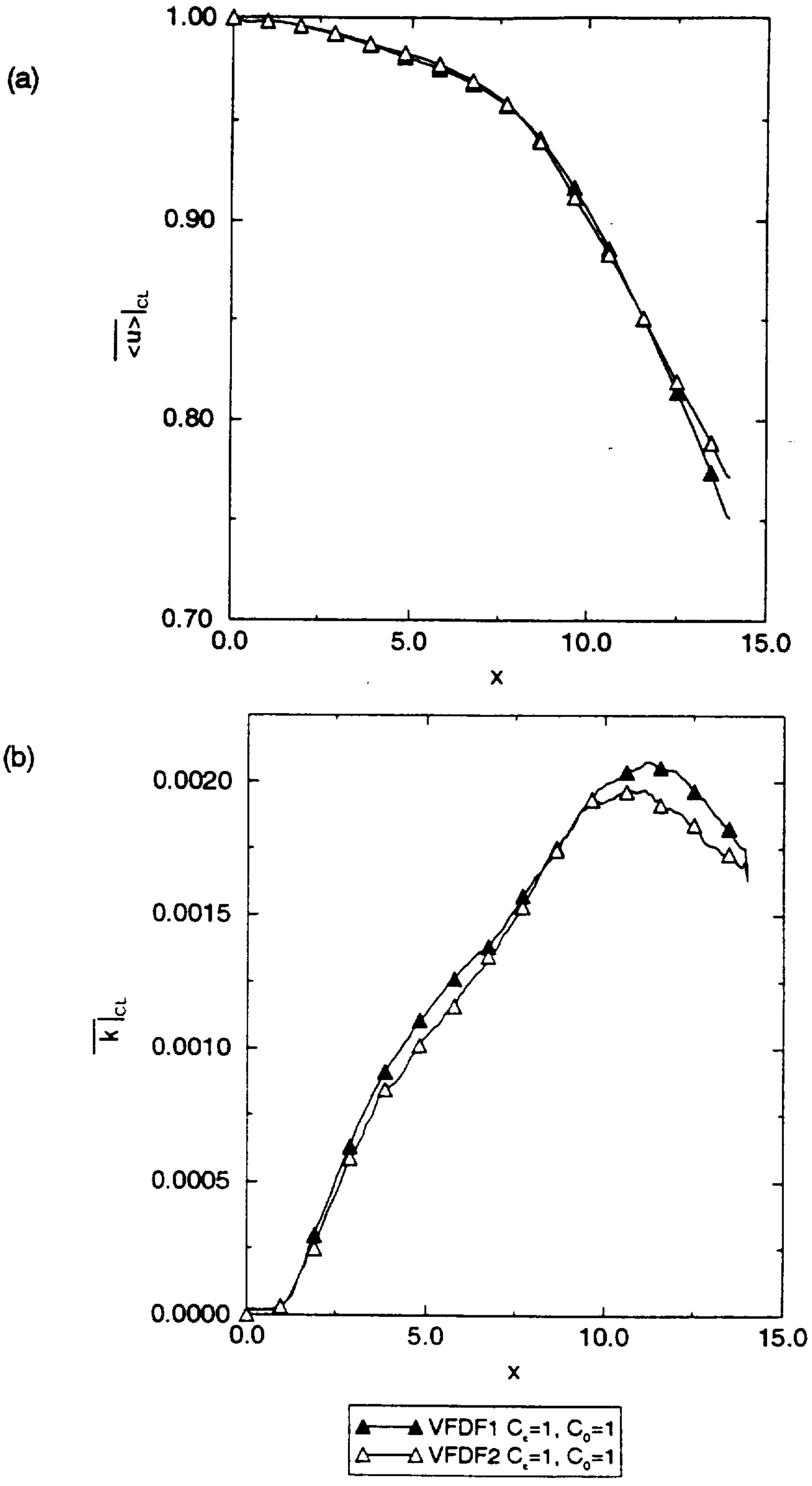

Figure 11: Streamwise variation of (a) $\overline{\langle u \rangle_L}$ and (b) $\overline{k}$ along the center line for the models "VFDF 1" and "VFDF 2".

Appendix V

Explicit Algebraic Scalar-Flux Models for Turbulent Reacting Flows

Reprinted from AICHE JOURNAL, AUGUST 1997

Explicit Algebraic Scalar-Flux Models for Turbulent Reacting Flows

V. Adumitroaie, D. B. Taulbee, and P. Givi
Dept. of Mechanical and Aerospace Engineering, State University of New York at Buffalo, Buffalo, NY 14260

Explicit algebraic scalar-flux models that are valid for three-dimensional turbulent flows are derived from a hierarchy of second-order moment closures. The mathematical procedure is based on the Cayley–Hamilton theorem and is an extension of the scheme developed by Taulbee. Several closures for the pressure–scalar gradient correlations are considered and explicit algebraic relations are provided for the velocity–scalar correlations in both nonreacting and reacting flows. In the latter, the role of the Damköhler number is exhibited in isothermal turbulent flows with nonpremixed reactants. The relationship between these closures and traditional models based on the linear gradient-diffusion approximation is theoretically established. The results of model predictions are assessed by comparison with available laboratory data in turbulent jet flows.

Introduction

Despite extensive recent contributions in direct and large eddy simulations of turbulent reacting flows, the application of such simulations is limited to "simple flows" (Givi, 1994). Based on this fact, it is now widely recognized that the "statistical" approach is *still* the most practical means in computational turbulence, and future capabilities in predictions of engineering turbulent combustion systems depend on the extent of developments in statistical modeling.

The literature on computational prediction of nonreactive turbulent transport is rich with schemes based on single-point statistical closures for moments up to the second order (Taulbee, 1989). Referred to as Reynolds stress models (RSM), these schemes are based on transport equations for the second-order velocity correlations and lead to determination of "nonisotropic eddy-diffusivities." This methodology is more advantageous than the more conventional models based on the Boussinesq approximations with isotropic eddy diffusivities (such as the $k-\epsilon$ type of closures). However, the need for solving additional transport equations for the higher-order moments could potentially make RSM less attractive, especially for practical applications. For example, it has been recently demonstrated (Höfler, 1993) that the computational requirement associated with RSM for predictions of three-dimensional (3-D) engineering flows is significantly higher than that required to implement the $k-\epsilon$ model. The increase is naturally higher for second-order modeling of chemically reacting flows due to the additional length and time scales that have to be considered (Toor, 1991; Jones, 1994; Libby and Williams, 1994).

A modality to reduce the large number of equations associated with RSM is to utilize "algebraic" closures. Such closures are either derived directly from the RSM transport equations, or other types of representations (Speziale, 1991; Yoshizawa, 1988) that lead to anisotropic eddy diffusivities. One of the original contributions in the development of algebraic Reynolds stress models (ARSM) is due to Rodi (1976). In this work, all the stresses are determined from a set of "implicit" equations that must be solved in an iterative manner. A somewhat similar method was applied to the heat-flux equation by Gibson and Launder (1976). Pope (1975) offers an improvement of the procedure by providing an "explicit" solution for the Reynolds stresses. This solution is generated by the use of the Cayley–Hamilton theorem, but is only applicable for predictions of two-dimensional (2-D) mean flows. The extension of this formulation has been recently done by Taulbee (1992) and Gatski and Speziale (1993). In these efforts, the Cayley–Hamilton is used to generate explicit algebraic Reynolds stress models that are valid in both 2-D and 3-D flows.

The objective of this work is to expand upon the formulation developed by Taulbee (1992) (also see Taulbee et al., 1993) for predictions of turbulent flows involving scalar quantities (Brodkey, 1981). The specific objective is to provide explicit algebraic relations for the turbulent flux of scalar vari-

---

Current address of V. Adumitroaie: CFD Research Corp., Huntsville, AL 35805.

ables. Both nonreacting and reacting flows are considered. In the latter, a second-order, irreversible chemical reaction of the type $A + B \rightarrow P$ is considered in isothermal turbulent flows with initially segregated reactants (Brodkey, 1975; Toor, 1975). The closure explicitly accounts for the influence of the Damköhler number and includes the mixing solution in the limit of zero Damköhler number. Similar to previous contributions, the starting equations are the currently available differential equations for the second-order moments. Accordingly, several previously suggested closures for the pressure–scalar gradients correlations are considered. The final results are compared with available experimental data in turbulent jet flows.

Theoretical Background

With the convention that the angle brackets $\langle\,\rangle$ represent the ensemble mean value of a transport variable and the prime denotes its fluctuations from the mean, the nondimensionalized averaged equations in space (x_i, $i = 1, 2, 3$) and time (t) for incompressible, isothermal turbulent reacting flows are:

$$\frac{\partial\langle u_j\rangle}{\partial x_j} = 0, \tag{1}$$

$$\frac{\partial\langle u_i\rangle}{\partial t} + \frac{\partial\langle u_i\rangle\langle u_j\rangle}{\partial x_j} = -\frac{\partial\langle u_i'u_j'\rangle}{\partial x_j} - \frac{1}{\langle\rho\rangle}\frac{\partial\langle p\rangle}{\partial x_i} + \frac{1}{Re}\frac{\partial^2\langle u_i\rangle}{\partial x_j\partial x_j}, \quad i,j = 1,2,3 \tag{2}$$

$$\frac{\partial\langle Y_\alpha\rangle}{\partial t} + \frac{\partial\langle Y_\alpha\rangle\langle u_j\rangle}{\partial x_j} = -\frac{\partial\langle u_j'\rangle\langle Y_\alpha'\rangle}{\partial x_j} + \frac{1}{ScRe}\frac{\partial^2\langle Y_\alpha\rangle}{\partial x_j\partial x_j} + \langle\dot\omega_\alpha\rangle, \quad \alpha = A,B. \tag{3}$$

Here u_i, p, ρ, Y_α, Re, and Sc denote the ith component of the velocity vector, the pressure, fluid density, mass fraction of species α, the Reynolds number, and the Schmidt number, respectively, while $\langle\dot\omega_\alpha\rangle$ represents the rate of chemical reaction ($\langle\dot\omega_A\rangle = \langle\dot\omega_B\rangle$):

$$\langle\dot\omega_\alpha\rangle = -Da(\langle Y_A\rangle\langle Y_B\rangle + \langle Y_A'Y_B'\rangle), \tag{4}$$

where Da is the Damköhler number. The algebraic formulation entails a two-equation scheme in which the Reynolds stresses and the scalar fluxes are expressed by nonlinear functions of the mean gradients and the time scales of the flow (Wang and Tarbell, 1993). The mechanical time scale is determined by the solution of transport equations for the turbulent kinetic energy $\langle k\rangle = \langle u_i'u_i'\rangle/2$ and for the turbulent dissipation

$$\langle\epsilon\rangle = \frac{1}{Re}\left\langle\frac{\partial u_i'}{\partial x_j}\frac{\partial u_i'}{\partial x_j}\right\rangle.$$

For shear flows, these equations are (Pope, 1978):

$$\frac{\partial\langle k\rangle}{\partial t} + \frac{\partial\langle k\rangle\langle u_j\rangle}{\partial x_j} = -\frac{\partial}{\partial x_j}\left[\langle u_j'k\rangle + \frac{1}{\langle\rho\rangle}\langle p'u_j'\rangle\right] + \frac{1}{Re}\frac{\partial^2\langle k\rangle}{\partial x_j\partial x_j} - \langle u_i'u_j'\rangle\frac{\partial\langle u_i\rangle}{\partial x_j} - \frac{1}{Re}\left\langle\frac{\partial u_i'}{\partial x_j}\frac{\partial u_i'}{\partial x_j}\right\rangle, \tag{5}$$

$$\frac{\partial\langle\epsilon\rangle}{\partial t} + \frac{\partial\langle\epsilon\rangle\langle u_j\rangle}{\partial x_j} = -\frac{\partial}{\partial x_j}\left[\langle u_j'\epsilon\rangle + \frac{2}{Re}\left\langle\frac{\partial p'}{\partial x_k}\frac{\partial u_j'}{\partial x_k}\right\rangle\right] + \frac{1}{Re}\frac{\partial^2\langle\epsilon\rangle}{\partial x_j\partial x_j} - C_{\epsilon_1}\frac{\langle\epsilon\rangle}{\langle k\rangle}\langle u_i'u_j'\rangle\frac{\partial\langle u_i\rangle}{\partial x_j} - C_{\epsilon_2}'\frac{\langle\epsilon\rangle^2}{\langle k\rangle}, \tag{6}$$

with $C_{\epsilon_1} = 1.44$ and $C_{\epsilon_2}' = 1.92 - C_{\epsilon_3}\chi$. The parameter χ represents the correction for the dissipation equation in round jets and is given by $\chi = (\langle k\rangle/\langle\epsilon\rangle)^3\{\Omega\Omega\mathrm{S}\}$, where $\{\}$ denotes the trace, S represents the mean-flow strain-rate tensor, $S_{ij} = [\partial\langle u_i\rangle/\partial x_j + \partial\langle u_j\rangle/\partial x_i]/2$, and Ω denotes the mean flow rotation-rate tensor, $\Omega_{ij} = [\partial\langle u_i\rangle/\partial x_j - \partial\langle u_j\rangle/\partial x_i]/2$. With $C_{\epsilon_3} = 0.89$, the spreading rate of jet flows is correctly predicted with the nonlinear stress–strain relation.

Treatment of the scalar variable requires the solution of additional transport equations (Chakrabarti et al., 1995) for the reactants' covariance $\langle Y_\alpha'Y_\beta'\rangle$, and dissipations

$$\langle\epsilon_{\alpha\beta}\rangle = \frac{1}{ScRe}\left\langle\frac{\partial Y_\alpha'}{\partial x_j}\frac{\partial Y_\beta'}{\partial x_j}\right\rangle.$$

For the former we have

$$\frac{\partial\langle Y_\alpha'Y_\beta'\rangle}{\partial t} + \frac{\partial\langle Y_\alpha'Y_\beta'\rangle\langle u_j\rangle}{\partial x_j} = -\frac{\partial\langle u_j'Y_\alpha'Y_\beta'\rangle}{\partial x_j} + \frac{1}{ScRe}\frac{\partial^2\langle Y_\alpha'Y_\beta'\rangle}{\partial x_j\partial x_j} - \langle u_j'Y_\alpha'\rangle\frac{\partial\langle Y_\beta\rangle}{\partial x_j} - \langle u_j'Y_\beta'\rangle\frac{\partial\langle Y_\alpha\rangle}{\partial x_j} - \frac{2}{ScRe}\left\langle\frac{\partial Y_\alpha'}{\partial x_j}\frac{\partial Y_\beta'}{\partial x_j}\right\rangle + \langle\dot\omega_\alpha Y_\beta'\rangle + \langle\dot\omega_\beta Y_\alpha'\rangle. \tag{7}$$

By neglecting the third-order mass-fraction correlations, the chemical-source terms in the expanded form read (no summation on Greek indexes in all subsequent equations) $\langle\dot\omega_\alpha Y_\beta'\rangle + \langle\dot\omega_\beta Y_\alpha'\rangle = -Da[(\langle Y_\alpha'Y_A'\rangle + \langle Y_\beta'Y_A'\rangle)\langle Y_B\rangle + (\langle Y_\alpha'Y_B'\rangle + \langle Y_\beta'Y_B'\rangle)\langle Y_A\rangle]$. Full resolution of the nonlinear interactions in the chemical scalar fields requires significant computational effort in practical applications (Hill, 1976; Givi, 1989; Fox, 1996). The neglect of the higher-order scalar fluctuations for the configurations considered here is justified (Givi, 1989), but cannot be recommended for general applications (Wang and Tarbell, 1993). In such applications, the single-point probability density function (PDF) or the joint PDF of the scalar variable provides the required information (Toor, 1962; O'Brien, 1980; Dopazo, 1994; Fox, 1996). The inclusion of the PDF is not attempted here.

There are several methods for evaluating the scalar covariance dissipation (Jones, 1994; Newman et al., 1981; Jones and Musonge, 1988; Borghi, 1990). By using the first-order term in the two-scale direct-interaction approximation, Yoshizawa (1988) develops a generic model for the scalar dissipation. An equivalent functional expression is obtained from Yoshizawa's results by making use of the time-scales ratios $r_\alpha = 2\langle k\rangle\langle\epsilon_\alpha\rangle/(\langle\epsilon\rangle\langle Y_\alpha'^2\rangle)$ (hereinafter $\epsilon_\alpha \equiv \epsilon_{\alpha\alpha}$) and replacing the diffusion effect term by the inherent gradient of the turbulent flux. The equivalent form of this equation including the effects of chemical reaction is (Adumitroaie, 1997):

$$\frac{\partial\langle\epsilon_{\alpha\beta}\rangle}{\partial t}+\frac{\partial\langle\epsilon_{\alpha\beta}\rangle\langle u_j\rangle}{\partial x_j}=-\frac{\partial}{\partial x_j}\langle u_j'\epsilon_{\alpha\beta}\rangle+\frac{1}{ScRe}\frac{\partial^2\langle\epsilon_{\alpha\beta}\rangle}{\partial x_j\partial x_j}$$
$$-C_{y_1}\frac{\langle\epsilon\rangle}{\langle k\rangle}\frac{1}{2}\left(\langle u_j'Y_\alpha'\rangle\frac{\partial\langle Y_\beta\rangle}{\partial x_j}+\langle u_j'Y_\beta'\rangle\frac{\partial\langle Y_\alpha\rangle}{\partial x_j}\right)$$
$$-C_{y_2}\frac{\langle\epsilon_{\alpha\beta}\rangle}{\langle k\rangle}\langle u_i'u_j'\rangle\frac{\partial\langle u_i\rangle}{\partial x_j}-C_{y_3}\frac{\langle\epsilon_{\alpha\beta}\rangle^2}{\langle Y_\alpha'Y_\beta'\rangle}$$
$$-C_{y_4}\frac{\langle\epsilon\rangle\langle\epsilon_{\alpha\beta}\rangle}{\langle k\rangle}+\mathcal{S}_{\alpha\beta}, \quad (8)$$

in which the chemical-source term is of the form

$$\mathcal{S}_{\alpha\beta}=-Da[(\langle\epsilon_{A\alpha}\rangle+\langle\epsilon_{A\beta}\rangle)\langle Y_B\rangle+(\langle\epsilon_{B\beta}\rangle+\langle\epsilon_{\alpha B}\rangle)\langle Y_A\rangle]. \quad (9)$$

To determine the magnitudes of the model constants the transport equation for r_α as derived from Eqs. 5–8 can be used in the limiting case of mixing:

$$\frac{\langle k\rangle}{\langle\epsilon\rangle}\frac{1}{r_\alpha}\frac{dr_\alpha}{dt}=(C_{y_1}-r_\alpha)\frac{P_\alpha}{\epsilon_\alpha}+(1-C_{\epsilon_1}+C_{y_2})\frac{P}{\epsilon}$$
$$+\left(1-\frac{C_{y_3}}{2}\right)r_\alpha+(C_{\epsilon_2}'-1-C_{y_4}) \quad (10)$$

where the production terms are $P=-\langle u_i'u_j'\rangle\partial\langle u_i\rangle/\partial x_j$ and $P_\alpha=-\langle u_j'Y_\alpha'\rangle\partial\langle Y_\alpha\rangle/\partial x_j$. In the experiments of Warhaft and Lumley (1978) on decaying heated-grid turbulent flows it has been observed that the magnitude of r_α is in the range $0.6 \leq r_\alpha \leq 2.4$. In the experiments of Beguier et al. (1978) on thermal turbulence in several thin shear flows it is indicated that $r_\alpha \approx 2$. Based on this information, using the procedure detailed by Jones and Musonge (1988) it is possible to estimate the magnitudes of the model constants: $C_{y_1}=r_\alpha=2.0$, $C_{y_3}=2.0$, $C_{y_4}=C_{\epsilon_2}'-1=0.92-C_{\epsilon_3}\chi$, $C_{y_2}=0.5$.

To complete the closure formulation, all the third-order transport terms are described by the gradient diffusion hypothesis. Denoting by Ξ any of the fluctuation products on which the second-order correlations rest, we have:

$$\langle u_i'\Xi\rangle=-C_s\frac{\langle k\rangle}{\langle\epsilon\rangle}\langle u_i'u_j'\rangle\frac{\partial\langle\Xi\rangle}{\partial x_j}, \quad (11)$$

where C_s is taken to be equal to 0.22 for all nongradient correlations ($\Xi \equiv k$ and $\Xi \equiv Y_\alpha'^2$), whereas for the dissipations ($\Xi \equiv \epsilon$ and $\Xi \equiv \epsilon_\alpha$), $C_s = 0.18$. Also, the molecular transport terms are neglected under the assumption of high Reynolds–Peclet numbers flow.

Explicit Algebraic Models

An improved explicit ARSM for 3-D flow has been derived by Taulbee (1992) from the modeled transport equation for the Reynolds stresses. This model is based on the general linear pressure–strain closure given by Launder et al. (1975). The improvement is due to an extended range of validity; the model is valid in both small and large mean strain fields and time scales of turbulence. The nonlinear stress–strain relation for 3-D mean flows is of the form (Taulbee, 1992; Taulbee et al., 1993) $\mathbf{a}=\mathbf{a}(\mathrm{S}, \mathbf{\Omega})$, where $\mathbf{a}$ is the anisotropic stress tensor, $a_{ij}=[\langle u_i'u_j'\rangle/\langle k\rangle-2\delta_{ij}/3]$. The ARSM depends on key turbulence parameters such as the turbulence time scale $\tau=\langle k\rangle/\langle\epsilon\rangle$; the production-to-dissipation ratio $P/\langle\epsilon\rangle$, where $P=-\langle k\rangle a_{ij}S_{ji}$ is the production of the turbulent kinetic energy; the invariants of the strain rate and rotation rate tensors $\sigma^2=(S_{ij}S_{ji})$, $\omega^2=(\Omega_{ij}\Omega_{ij})$; and the model coefficients of the pressure–strain correlation and the modeled dissipation equation.

A similar line of reasoning is followed to obtain a 3-D algebraic closure for the velocity–scalar correlations. The transport equations governing these correlations are transformed into algebraic expressions by making two assumptions: (1) existence of a "near-asymptotic" state, and (2) the difference in the transport terms is negligible. The starting equations for the convective scalar fluxes are described by

$$\frac{\partial\langle u_i'Y_\alpha'\rangle}{\partial t}+\frac{\partial\langle u_i'Y_\alpha'\rangle\langle u_j\rangle}{\partial x_j}=-\frac{\partial(\langle u_j'u_i'Y_\alpha'\rangle+\langle p'Y_\alpha'\rangle/\langle\rho\rangle\delta_{ij})}{\partial x_j}$$
$$+\frac{1}{\langle\rho\rangle}\left\langle p'\frac{\partial Y_\alpha'}{\partial x_i}\right\rangle-\left(\langle u_j'u_i'\rangle\frac{\partial\langle Y_\alpha\rangle}{\partial x_j}+\langle u_j'Y_\alpha'\rangle\frac{\partial\langle u_i\rangle}{\partial x_j}\right)$$
$$-Da(\langle u_i'Y_\alpha'\rangle\langle Y_\beta\rangle+\langle u_i'Y_\beta'\rangle\langle Y_\alpha\rangle+\langle u_i'Y_\alpha'Y_\beta'\rangle)$$
$$+\frac{1}{Re}\left[\frac{\partial}{\partial x_j}\left\langle Y_\alpha'\frac{\partial u_i'}{\partial x_j}+\frac{u_i'}{Sc}\frac{\partial Y_\alpha'}{\partial x_j}\right\rangle\right]-\frac{1+Sc}{ScRe}\left\langle\frac{\partial u_i'}{\partial x_j}\frac{\partial Y_\alpha'}{\partial x_j}\right\rangle. \quad (12)$$

On the RHS of this equation, the following terms are identified: turbulent transport, pressure–scalar gradient correlation, production by the mean velocity and the mean scalar gradients, chemical reaction effects, molecular transport (assumed negligible at high Peclet numbers), and viscous dissipation. Based on the Poisson equation satisfied by the pressure fluctuations one can arguably split the pressure-scalar gradient correlation into two parts corresponding to so-called rapid and slow terms (Lumley, 1978). The rapid term represents an inner product between the velocity gradient tensor and a third-order tensor, the last one subject to symmetry, continuity, and normalization constraints. As suggested by Lumley (1978), since the slow pressure–scalar gradient term and the viscous dissipation term are functions only of turbulent quantities, they can be incorporated into a single closure. The ensemble of the entire pressure-gradient term and viscous-dissipation term enjoys a general relation encompassing some of the formulations proposed in precedent contributions. Consequently, this is written

$$\Phi_{i\alpha} = \frac{1}{\langle\rho\rangle}\left\langle p'\frac{\partial Y_\alpha'}{\partial x_i}\right\rangle - \frac{1+Sc}{ScRe}\left\langle\frac{\partial u_i'}{\partial x_j}\frac{\partial Y_\alpha'}{\partial x_j}\right\rangle$$

$$= -\frac{\mathcal{C}_{1\alpha}}{2}\frac{\langle\epsilon\rangle}{\langle k\rangle}\langle u_i'Y_\alpha'\rangle + \left[c_1\frac{\partial\langle u_i\rangle}{\partial x_j}\langle u_j'Y_\alpha'\rangle + c_2\frac{\partial\langle u_j\rangle}{\partial x_i}\langle u_j'Y_\alpha'\rangle\right.$$

$$+ c_3\frac{\partial\langle u_j\rangle}{\partial x_k}a_{ij}\langle u_k'Y_\alpha'\rangle + c_4\frac{\partial\langle u_k\rangle}{\partial x_j}(a_{ij}\langle u_k'Y_\alpha'\rangle + a_{jk}\langle u_i'Y_\alpha'\rangle)$$

$$\left. + c_5\frac{\partial\langle u_i\rangle}{\partial x_j}a_{jk}\langle u_k'Y_\alpha'\rangle + c_6\frac{\partial\langle Y_\alpha\rangle}{\partial x_j}a_{ij}\langle k\rangle\right]. \quad (13)$$

The model coefficients in this equation are taken from Launder (1975):

$$\mathcal{C}_{1\alpha} = 6.4, \quad c_1 = 0.5, \quad c_i = 0; \quad i = 2,6, \quad (14)$$

Jones and Musonge (1988):

$$\mathcal{C}_{1\alpha} = 6/\left[1 + 1.5(a_{jk}a_{jk})^{1/2}\right], \quad c_1 = 1.09, \quad c_2 = 0.51,$$

$$c_i = 0; \quad i = 3,5; \quad c_6 = 0.12, \quad (15)$$

Rogers et al. (1989):

$$\mathcal{C}_{1\alpha} = 18\left(1 + \frac{130}{ScRe_t}\right)^{0.25}\left(1 + \frac{12.5}{Re_t^{0.48}}\right)^{-2.08} - \left(\frac{P}{\langle\epsilon\rangle} - 1\right)$$

$$- r_\alpha\left(\frac{P_\alpha}{\langle\epsilon_\alpha\rangle} - 1\right), \quad c_i = 0; \quad i = 1.6, \quad (16)$$

where $Re_t = 4\langle k\rangle^2/(\langle\epsilon\rangle\nu)$, and Shih et al. (1990):

$$\mathcal{C}_{1\alpha} = \psi + r_\alpha - \frac{(\psi - 1)II_d}{\left(II_d + 3a_{jk}d_{jk}^2/2 - 3a_{jk}d_{jk}/2\right)} + HF_D^{1/2},$$

$$c_1 = 4/5, \quad c_2 = -1/5, \quad c_3 = 1/10,$$

$$c_4 = -3/10, \quad c_5 = 1/5, \quad c_6 = 0, \quad (17)$$

where $H = 1.1 + 0.55(2\psi - 1)\tanh[4(r_\alpha - 1)]$; $\psi = 1 + F/18\exp(-7.77/Re_l^{1/2})\{72/Re_l^{1/2} + 80.1\log[1 + 15.6(-II + 1.15III)]\}$, with $F = 1 + 27III/8 + 9II/4$, a parameter involving the second invariant $II = -1/2a_{ij}a_{ji}$ and the third invariant $III = -1/3a_{ij}a_{jk}a_{ki}$ of the Reynolds stress anisotropy tensor; $Re_l = 4\langle k\rangle^2/(9\langle\epsilon\rangle\nu)$ denotes the turbulence Reynolds number: $d_{jk} = (\langle u_j'Y_\alpha'\rangle\langle u_k'Y_\alpha'\rangle - \langle u_j'u_k'\rangle\langle Y_\alpha'^2\rangle)/(\langle u_p'Y_\alpha'\rangle\langle u_p'Y_\alpha'\rangle - 2\langle k\rangle\langle Y_\alpha'^2\rangle)$; $F_D = 9/2 - 27d_{jj}^2/2 + 9d_{jj}^3$; II_d is the second invariant of the tensor d_{jk}; $d_{jj}^2 = d_{jl}d_{lj}$; and $d_{jj}^3 = d_{jl}d_{lm}d_{mj}$.

To proceed, let us denote the mechanical–chemical correlation coefficient (normalized scalar flux) by:

$$\varphi_{i\alpha} = \frac{\langle u_i'Y_\alpha'\rangle}{(\langle k\rangle\langle Y_\alpha'^2\rangle)^{1/2}}. \quad (18)$$

The transport equation for the correlation coefficient $\varphi_{i\alpha}$ ($\alpha \neq \beta$) is of the form:

$$\frac{D\varphi_{i\alpha}}{Dt} = \frac{1}{(\langle k\rangle\langle Y_\alpha'^2\rangle)^{1/2}}$$

$$\times\left[\frac{\partial T_{ij}^\alpha}{\partial x_j} - \frac{\varphi_{i\alpha}}{2}\left(\frac{\langle k\rangle}{\langle Y_\alpha'^2\rangle}\right)^{1/2}\frac{\partial T_j^\alpha}{\partial x_j} - \frac{\varphi_{i\alpha}}{2}\left(\frac{\langle Y_\alpha'^2\rangle}{\langle k\rangle}\right)^{1/2}\frac{\partial T_j}{\partial x_j}\right]$$

$$-\left[\frac{\varphi_{i\alpha}\langle\epsilon_\alpha\rangle}{\langle Y_\alpha'^2\rangle}\left(\frac{P_\alpha}{\langle\epsilon_\alpha\rangle} - 1 + \frac{\mathcal{S}_\alpha}{\langle\epsilon_\alpha\rangle}\right) + \frac{\varphi_{i\alpha}}{2\tau}\left(\frac{P}{\langle\epsilon\rangle} - 1\right)\right]$$

$$+ \bar{P}_{i\alpha} + \bar{\Phi}_{i\alpha} + \bar{\mathcal{S}}_{i\alpha}, \quad (19)$$

where the notation D/Dt indicates the convective transport, and T_{ij}^α, T_j^α, and T_j denote turbulent transports of the scalar flux, the scalar variance, and the kinetic energy, respectively. Moreover $P_\alpha = -(\langle k\rangle\langle Y_\alpha'^2\rangle)^{1/2}\varphi_{j\alpha}\partial\langle Y_\alpha\rangle/\partial x_j$ is the production of scalar variance; $\mathcal{S}_\alpha = \langle\dot{\omega}_\alpha Y_\alpha'\rangle$ is the chemical source term in the $\langle Y_\alpha'^2\rangle$ equation; and the remaining quantities are the normalized production, pressure-gradient, and the chemical-source term:

$$\bar{P}_{i\alpha} = -\left(\frac{\langle k\rangle}{\langle Y_\alpha'^2\rangle}\right)^{1/2}\left(a_{ij} + \frac{2}{3}\delta_{ij}\right)\frac{\partial\langle Y_\alpha\rangle}{\partial x_j} - \varphi_{j\alpha}(S_{ij} + \Omega_{ij}) \quad (20)$$

$$\bar{\Phi}_{i\alpha} = -\frac{\mathcal{C}_{1\alpha}}{2\tau}\varphi_{i\alpha} + [(c_1 + c_2)S_{ij}\varphi_{j\alpha}$$

$$+ (c_1 - c_2)\Omega_{ij}\varphi_{j\alpha} + (c_3 + c_4)a_{ij}S_{jk}\varphi_{k\alpha} + c_5a_{jk}S_{ij}\varphi_{k\alpha}$$

$$+ (c_3 - c_4)a_{ij}\Omega_{jk}\varphi_{k\alpha} + c_5a_{jk}\Omega_{ij}\varphi_{k\alpha} + c_4a_{jk}S_{jk}\varphi_{i\alpha}]$$

$$+ c_6\left(\frac{\langle k\rangle}{\langle Y_\alpha'^2\rangle}\right)^{1/2}a_{ij}\frac{\partial\langle Y_\alpha\rangle}{\partial x_j} \quad (21)$$

$$\bar{\mathcal{S}}_{i\alpha} = -Da\left(\varphi_{i\alpha}\langle Y_\beta\rangle + \varphi_{i\beta}\langle Y_\alpha\rangle + \gamma_{i\alpha\beta}\langle Y_\beta'^2\rangle^{1/2}\right). \quad (22)$$

Here $\gamma_{i\alpha\beta} = \langle u_i'Y_\alpha'Y_\beta'\rangle/(\langle k\rangle\langle Y_\alpha'^2\rangle\langle Y_\beta'^2\rangle)^{1/2}$ is the normalized covariance flux vector.

The results of direct numerical simulations (DNS) of nonreacting passive scalar mixing in homogeneous turbulent shear flow (Rogers et al., 1989) suggest the existence of an asymptotic state for the normalized correlation coefficient $\varphi_{i\alpha}$, but not for the scalar flux itself. This observation justifies the first assumption, at least for reacting flows near the frozen limit. The second approximation is yet to be substantiated and its assessment requires future DNS or laboratory experiments. Under these assumptions the term representing the convective transport is set to zero and the difference in turbulence diffusion terms is discarded. This procedure leads to an algebraic system of equations for the two unknown vectors $\varphi_{i\alpha}$ and $\varphi_{i\beta}$:

$$\begin{cases} \varphi_\alpha + D_\alpha\mathbf{A}\varphi_\alpha + B_\alpha\varphi_\beta + \mathbf{C}_\alpha = 0 \\ \varphi_\beta + D_\beta\mathbf{A}\varphi_\beta + B_\beta\varphi_\alpha + \mathbf{C}_\beta = 0, \end{cases} \quad (23)$$

where the coefficients are

$$D_\alpha = \frac{2\tau h_\alpha}{1+2Da\tau h_\alpha \langle Y_\beta \rangle}, \qquad D_\beta = \frac{2\tau h_\beta}{1+2Da\tau h_\beta \langle Y_\alpha \rangle}, \tag{24}$$

$$B_\alpha = Da \langle Y_\alpha \rangle D_\alpha, \qquad B_\beta = Da \langle Y_\beta \rangle D_\beta, \tag{25}$$

with

$$h_\alpha = \left[\mathcal{C}_{1\alpha} - 1 + (1+2c_4)\frac{P}{\langle \epsilon \rangle} + r_\alpha \left(\frac{P_\alpha}{\langle \epsilon_\alpha \rangle} - 1 + \frac{\mathcal{S}_\alpha}{\langle \epsilon_\alpha \rangle} \right) \right]^{-1}, \tag{26}$$

$$h_\beta = \left[\mathcal{C}_{1\beta} - 1 + (1-2c_4)\frac{P}{\langle \epsilon \rangle} + r_\beta \left(\frac{P_\beta}{\langle \epsilon_\beta \rangle} - 1 + \frac{\mathcal{S}_\beta}{\langle \epsilon_\beta \rangle} \right) \right]^{-1}, \tag{27}$$

and the vector terms read:

$$C_{i\alpha} = D_\alpha \left\{ \left(\frac{\langle k \rangle}{\langle Y_\alpha'^2 \rangle} \right)^{1/2} \left[(1-c_6)a_{ki} + \frac{2}{3}\delta_{ki} \right] \times \frac{\partial \langle Y_\alpha \rangle}{\partial x_k} + Da \langle Y_\beta'^2 \rangle^{1/2} \gamma_{i\alpha\beta} \right\}, \tag{28}$$

$$C_{i\beta} = D_\beta \left\{ \left(\frac{\langle k \rangle}{\langle Y_\beta'^2 \rangle} \right)^{1/2} \left[(1-c_6)a_{ki} + \frac{2}{3}\delta_{ki} \right] \times \frac{\partial \langle Y_\beta \rangle}{\partial x_k} + Da \langle Y_\alpha'^2 \rangle^{1/2} \gamma_{i\alpha\beta} \right\}. \tag{29}$$

Finally, the anisotropy of the turbulent diffusivity is ensured by the properties of the second-order tensor **A**:

$$A_{ik} = [(1-c_1-c_2)S_{ik} + (1-c_1+c_2)\Omega_{ik} - (c_3+c_4)a_{ij}S_{jk} - c_5 a_{kj}S_{ji} - (c_3-c_4)a_{ij}\Omega_{jk} + c_5 a_{kj}\Omega_{ji}]. \tag{30}$$

This tensor turns out to be traceless ($A_{ii} = 0$) as a consequence of incompressibility and of the particular values taken by the constants, c_i's. Now, the solution of the system of Eqs. 23 is conveniently represented in the form:

$$\begin{cases} \varphi_\alpha = -\mathbf{M}^{-1}[(\boldsymbol{\delta} + D_\beta \mathbf{A})\mathbf{C}_\alpha - B_\alpha \mathbf{C}_\beta] \\ \varphi_\beta = -\mathbf{M}^{-1}[(\boldsymbol{\delta} + D_\alpha \mathbf{A})\mathbf{C}_\beta - B_\beta \mathbf{C}_\alpha], \end{cases} \tag{31}$$

where **M** denotes the matrix $[(1-B_\alpha B_\beta)\boldsymbol{\delta} + (D_\alpha + D_\beta)\mathbf{A} + D_\alpha D_\beta \mathbf{A}^2]$. The expressions for the turbulent fluxes of reacting scalars exhibit the influence of the Damköhler number *Da*. Also, the coupling between the reactants is reflected by the nonlinear dependence on the mean scalars and the presence of the covariance flux.

To provide a computationally efficient algorithm, the matrix **M** is inverted analytically. This is achieved by the use of the Cayley–Hamilton theorem and yields an expansion defining a natural basis for this problem:

$$\varphi_\alpha = \sum_{n=0}^{2} a_n \mathbf{A}^n C_\alpha + \sum_{n=0}^{2} a'_n \mathbf{A}^n C_\beta. \tag{32}$$

In the Appendix the inversion procedure via the Cayley–Hamilton theorem is outlined and the coefficients a_n and a'_n are listed. The final results provide an explicit solution for the scalar fluxes. In the limit $Da \to \infty$, the use of the mixing solution ($Da = 0$) for the transport of a Shvab–Zel'dovich variable (Toor, 1962; Williams, 1985) is recommended.

Illustrative Examples

In this section, we present some sample results of numerical calculations based on the models given earlier. There are two primary reasons for conducting these simulations: (1) model assessments via comparisons with laboratory data, (2) demonstration of the model capabilities in comparison to traditional closures based on the linear gradient-diffusion approximation. The flow configurations considered consist of turbulent-plane and round-jet flows for which laboratory data are available. The mean flow motion in these shear flows is assumed 2-D or axisymmetric. The space coordinates are identified by $\mathbf{x} = [x, y]$, where x is the streamwise coordinate denoting the direction of the flow's principal evolution, and y represents the cross-stream direction. The velocity field is identified by $\mathbf{u} = [u, v]$. In nonreacting flow simulations the mass fraction of one conserved species, Y_A, is considered. In the jet configurations, $Y_A = 1$ is issued at the inlet into a surrounding of $Y_A = 0$. For the reactive case, $Y_A = 1$ is issued at the inlet into a surrounding of $Y_B = 1$. These species are assumed thermodynamically identical, and there is no trace of one of these species at the feed of the other one; that is, complete initial segregation. Also, the heat generated by the reaction is assumed negligible.

The transport equations governing the velocity and the scalar fields are of parabolic type with the thin-shear layer approximation. For 2-D mean flows, the ARSM (Taulbee, 1992) is of the form:

$$\mathbf{a} = -2C_\mu \tau \left[\mathbf{S} + b_1 g \tau \sigma^2 \left(\frac{2}{3}\boldsymbol{\delta} - \boldsymbol{\delta}^{(2)} \right) + b_2 g \tau (\mathbf{S}\boldsymbol{\Omega} - \boldsymbol{\Omega}\mathbf{S}) \right], \tag{33}$$

where $\boldsymbol{\delta}^{(2)} \equiv [\delta_{ij}^{(2)}] = 1$ for $i = j = 1, 2$ and 0 otherwise. The parameters C_μ and g are given by

$$C_\mu = \frac{4g/15}{1 - \frac{2}{3}(b_1 g \tau)^2 \sigma^2 + 2(b_2 g \tau)^2 \omega^2},$$

$$g = \left[C_1 + C_{\epsilon_2} - 2 + (2 - C_{\epsilon_1})P/\langle \epsilon \rangle + \frac{\tau}{\sigma}\frac{D\sigma}{Dt} \right]^{-1}, \tag{34}$$

where C_1, b_1, and b_2 are constants from the pressure–strain correlation model ($C_1 = 1.8$, $b_1 = (5 - 9C_2)/11$, $b_2 = (1 + 7C_2)/11$, $C_2 = 0.45$). In the self-preserving regions of turbulent shear flows, the convective term $D\sigma/Dt$ can be neglected. For 2-D mean flows, with zero rate of reaction the scalar-flux model is expressed as

$$\langle u_i' Y_\alpha' \rangle = -\frac{2\tau h_\alpha \langle k \rangle}{1+II_G} \Delta_{ij} \frac{\partial \langle Y_\alpha \rangle}{\partial x_j}, \tag{35}$$

which has the gradient form, but with an anisotropic diffusivity. With the thin-shear layer approximation,

$$II_G = [(c_2 + c_4 a_{22})(1 - c_1 - c_3 a_{11} - c_5 a_{22}) - c_3^2 a_{12}^2] \times \left(2h_\alpha \tau \frac{d\langle u \rangle}{dy} \right)^2 \tag{36}$$

and the nonzero components of the diffusivity tensor, Δ_{ij}, are

$$\Delta_{11} = \left(1 - 2c_3 \tau h_\alpha a_{12} \frac{d\langle u \rangle}{dy} \right) \left[(1-c_6) a_{11} + \frac{2}{3} \right] - 2\tau h_\alpha (1-c_6) a_{21} \frac{d\langle u \rangle}{dy} (1 - c_1 - c_3 a_{11} - c_5 a_{22}) \tag{37}$$

$$\Delta_{22} = \left(1 + 2c_3 \tau h_\alpha a_{12} \frac{d\langle u \rangle}{dy} \right) \left[(1-c_6) a_{22} + \frac{2}{3} \right] + 2\tau h_\alpha (1-c_6) a_{12} \frac{d\langle u \rangle}{dy} (c_2 + c_4 a_{22}) \tag{38}$$

$$\Delta_{33} = (1 + II_G) \left[(1-c_6) a_{33} + \frac{2}{3} \right] \tag{39}$$

$$\Delta_{12} = \left(1 - 2c_3 \tau h_\alpha a_{12} \frac{d\langle u \rangle}{dy} \right) (1-c_6) a_{12} - 2\tau h_\alpha \left[(1-c_6) a_{22} + \frac{2}{3} \right] \frac{d\langle u \rangle}{dy} (1 - c_1 - c_3 a_{11} - c_5 a_{22}) \tag{40}$$

$$\Delta_{21} = \left(1 + 2c_3 \tau h_\alpha a_{12} \frac{d\langle u \rangle}{dy} \right) (1-c_6) a_{21} + 2\tau h_\alpha \left[(1-c_6) a_{11} + \frac{2}{3} \right] \frac{d\langle u \rangle}{dy} (c_2 + c_4 a_{22}). \tag{41}$$

These anisotropic diffusivities are determined directly from the velocity gradient, the components of anisotropic Reynolds stress tensor, and the model coefficients.

The numerical algorithm for the solution of the transport equations augmented by the algebraic closures is based on a first-order upwind differencing for the convection terms and a second-order central differencing scheme for all the other terms. Due to the anisotropic character of the algebraic closures, it is possible to evaluate all the components of the Reynolds stress tensor and the scalar-flux vectors. In this evaluation, the terms appearing as model coefficients (e.g., $P/\langle \epsilon \rangle$ in Eq. 26) are treated in an iterative procedure. The implementation of the boundary conditions is similar to that in many previous simulations of parabolic shear flows (e.g., Taulbee, 1989). In the results presented below, the spatial coordinates are presented by $\eta = y/(x - x_0)$ for hydrodynamic and

$$\eta^* = \frac{y}{y(\langle Y_A \rangle = 0.5 \langle Y_A \rangle_{CL})}$$

for the scalar variables. x_0 denotes the virtual origin of the jets. In the nonreacting jets, the subscript CL denotes values at the center line (i.e., $y = 0$). In the reacting jets, the corresponding profile of Y_A under no chemical reaction is employed in the normalization. In all the figures below, the transverse variations of the statistical variables are presented.

The experimental results pertaining to the velocity fields of planar jets as reported by Gutmark and Wygnanski (1976), Bradbury (1965), and Heskestad (1965) are compared with the model predictions in Figure 1. The agreement is reasonable for the mean streamwise velocity and also for the components of the Reynolds stress tensor. The predicted spreading rate $(dy_{\langle u \rangle / \langle u \rangle_{CL} = 0.5}/dx)$ is 0.105, which is within the range suggested by experimental measurements. In Figure 2, the predicted results for the mean and the variance of the nonreacting scalar are compared with the experimental data reported by Browne et al. (1984), Bashir and Uberoi (1975), Uberoi and Singh (1975), Jenkins and Goldschmidt (1973), and Antonia et al. (1983). Figure 2 indicates that the models based on the coefficients proposed by Launder (1975), Jones and Musonge (1988), and Shih et al. (1990) predict the mean scalar values in these experiments reasonably well. These models also yield good predictions of the experimental data

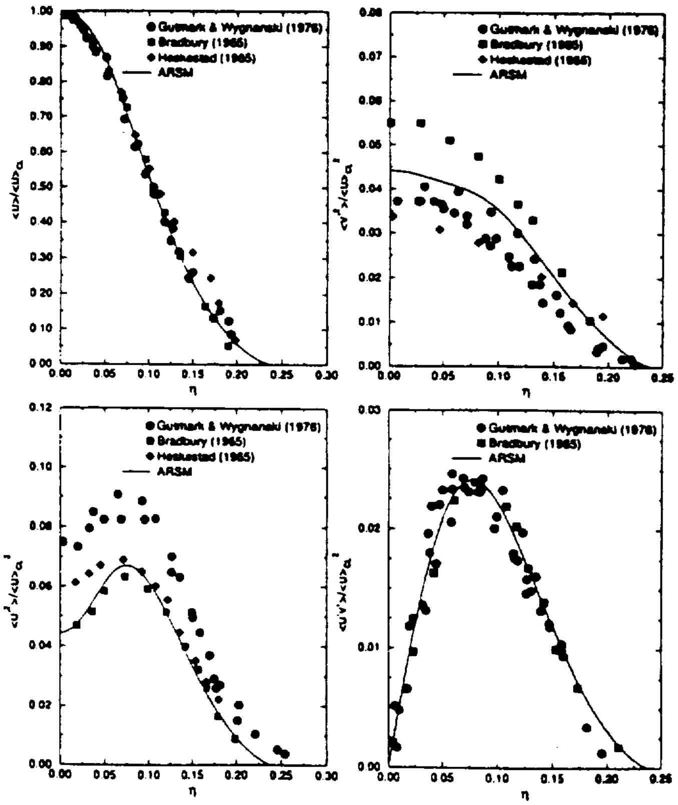

Figure 1. Cross-stream variation of $\langle u \rangle / \langle u \rangle_{CL}$, $\langle u'^2 \rangle / \langle u \rangle_{CL}^2$, $\langle v'^2 \rangle / \langle u \rangle_{CL}^2$, and $\langle u'v' \rangle / \langle u \rangle_{CL}^2$ for the planar jet.

of Uberoi and Singh (1975) for the scalar variance. All the other experimentally measured variance profiles are better predicted by the model with the coefficients of Rogers et al. (1989).

The procedure by which the Reynolds stress tensor and the scalar-flux vector are determined by our explicit solution allows a direct comparison of the calculated fluxes with data. This comparison is made in Figure 2 and indicates that the models with coefficients of Launder (1975), Jones and Musonge (1988), and Shih et al. (1990) yield results in reasonable agreements with the experimental data of Jenkins (1976), but overpredict the experimental data of Antonia (1985) and Browne et al. (1984). These data are in better agreement with the predicted fluxes based on the model of Rogers et al. (1989). The lower spreading rates predicted by the model of Rogers et al. (1989) are primarily due to the relatively large values adopted by the parameter $\mathcal{C}_{1\alpha}$. In this model, the proposed form of $\mathcal{C}_{1\alpha}$ and its correlation with the turbulence Reynolds number are determined with comparative assessments by DNS results of homogeneous turbulent shear flows. In the jet-flow experiments, as considered here, a direct application of the model yields relatively large values for $\mathcal{C}_{1\alpha}$, and thus small turbulent diffusivities. Consequently, the predicted scalar spreading rate is lower than that measured experimentally. Nevertheless, in the core region, the results predicted by this model are closer to the majority of available experimental data compared to predictions based on other models.

With these results it is possible to perform an *a posteriori* appraisal of the closures based on conventional linear gradient-diffusion hypotheses. For example, the parameters C_μ and Sc_t as given by

$$\langle u'v'\rangle = -\nu_t \frac{\partial\langle u\rangle}{\partial y}, \qquad \nu_t = C_\mu \frac{\langle k\rangle^2}{\langle \epsilon\rangle}, \tag{42}$$

$$\langle v'Y'_\alpha\rangle = -\frac{\nu_t}{Sc_t}\frac{\partial\langle Y_\alpha\rangle}{\partial y}, \tag{43}$$

can be directly evaluated. The explicit algebraic relation for C_μ is given by Eq. 34; the relation for the turbulent Schmidt number is

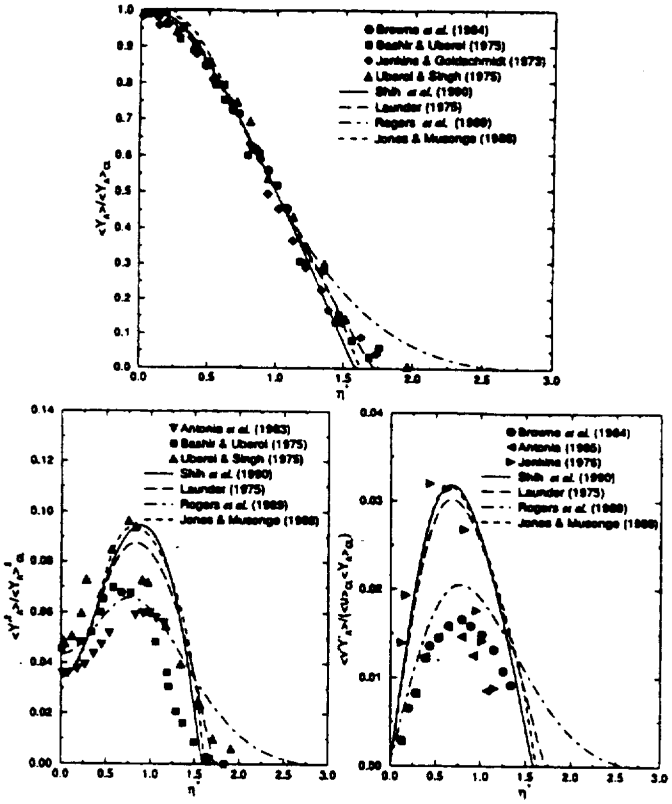

Figure 2. Cross-stream variation of $\langle Y_A\rangle/\langle Y_A\rangle_{CL}$, $\langle Y_A'^2\rangle/\langle Y_A\rangle^2_{CL}$, and $\langle v'Y'_A\rangle/(\langle u\rangle_{CL}\langle Y_A\rangle_{CL})$ for the planar jet.

for all these parameters near the free stream. The amplitude of the parameters at the free streams can be controlled by modifications of the boundary conditions. An extract specification of these conditions requires inputs from laboratory measurements.

Some of the influences of the chemical reaction on the scalar field in the turbulent plane jet are presented in Figures 4 and 5. In the calculations pertaining to these figures, the model coefficients of Launder (1975) are employed. The influence of reaction in modifying the amplitudes of the scalars' means (Figure 1), variances (not shown), and turbulent fluxes are captured by the model (Dutta and Tarbell, 1989; Gao and O'Brien, 1991). In accord with the physics of turbulent flows with segregated reactants, the unmixedness is negative throughout the layer (Shenoy and Toor, 1989; Leonard and Hill, 1991; Wang and Tarbell, 1993). The same is true in the limit of no chemistry; in that case, the amplitude is slightly larger (Leonard and Hill, 1988; Frankel et al., 1993, 1995).

$$Sc_t = \frac{1-4\left[c_3^2a_{12}^2-(c_2+c_4a_{22})(1-c_1-c_3a_{11}-c_5a_{22})\right]\left(h_\alpha\tau\dfrac{d\langle u\rangle}{dy}\right)^2}{h_\alpha\left\{\left(1+2c_3\tau h_\alpha a_{12}\dfrac{d\langle u\rangle}{dy}\right)\left[(1-c_6)a_{22}+\dfrac{2}{3}\right]+2\tau h_\alpha(1-c_6)a_{12}\dfrac{d\langle u\rangle}{dy}(c_2+c_4a_{22})\right\}}\times\frac{2g}{15\left[1+\left(b_2^2-\dfrac{b_1^2}{3}\right)\left(g\tau\dfrac{d\langle u\rangle}{dy}\right)^2\right]}. \tag{44}$$

Figure 3 shows the cross-stream variations of C_μ and of Sc_t and r_α based on the pressure–scalar gradient model in Shih et al. (1990). These results can be compared with $C_\mu = 0.09$ and $Sc_t = 0.7$, typically employed in the linear gradient-diffusion approximations. Also, the ratio of the velocity to scalar time scales (r_α) indicates that an approximate constant value can be used at the central region of the layer. This is in accord with the results of Beguier et al. (1978) and Tavoularis and Corrsin (1981). As expected, there are large variations

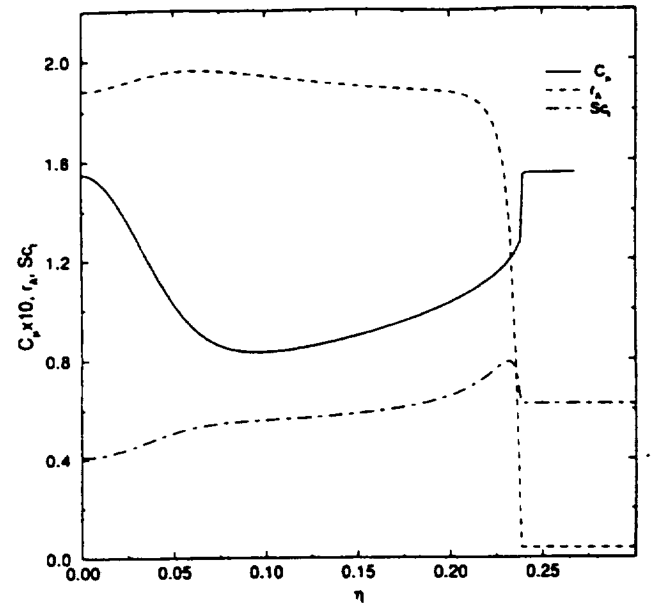

Figure 3. Cross-stream variation of C_μ, Sc_t, and r_A for the planar jet.

The comparison between the full second-order model (Eq. 12) and the algebraic closure in predicting the scalar fluxes is presented in Figure 5, and indicates that the transverse flux as predicted by the algebraic closure is in close agreement with that by the transport-equation model. However, there are differences between the two predictions of the streamwise flux near the jet center line. The zero value of this flux in the algebraic model is due to the thin-shear-layer approximation. The neglect of the axial diffusion in this approximation combined with the gradient diffusion nature of the algebraic model can only yield zero flux values at the axis of symmetry. While the thin-shear-layer approximation is also invoked in the transport equation model, the inclusion of the streamwise convective effects in the transport equations can, and does, yield nonzero flux values. If the thin-layer assumption is relaxed in the algebraic model, the inclusion of axial scalar gradients would generate nonzero scalar-flux values at the center line, thus reducing the disagreement. It must be noted that for this class of flows the cross-stream scalar flux is more dominant than the streamwise flux in influencing the mean scalar distribution and the production terms. Thus, the agreement observed in Figure 5 is encouraging in support of the algebraic approximation. Nevertheless, this is demonstrated here only for a "simple" flow configuration. The im-

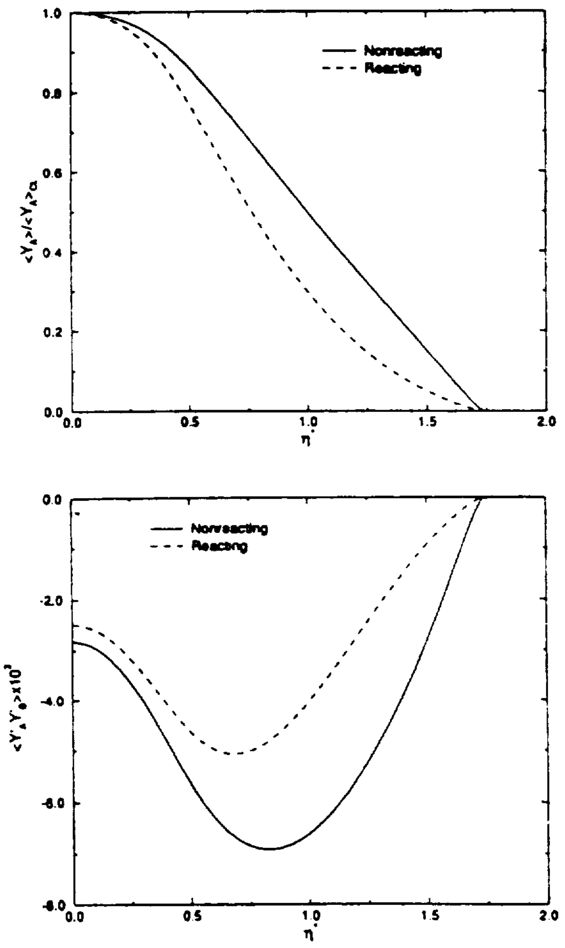

Figure 4. Cross-stream variation of $\langle Y_A \rangle / \langle Y_A \rangle_{CL}$ and $\langle Y_A' Y_B' \rangle$ for the nonreacting and reacting planar jets.

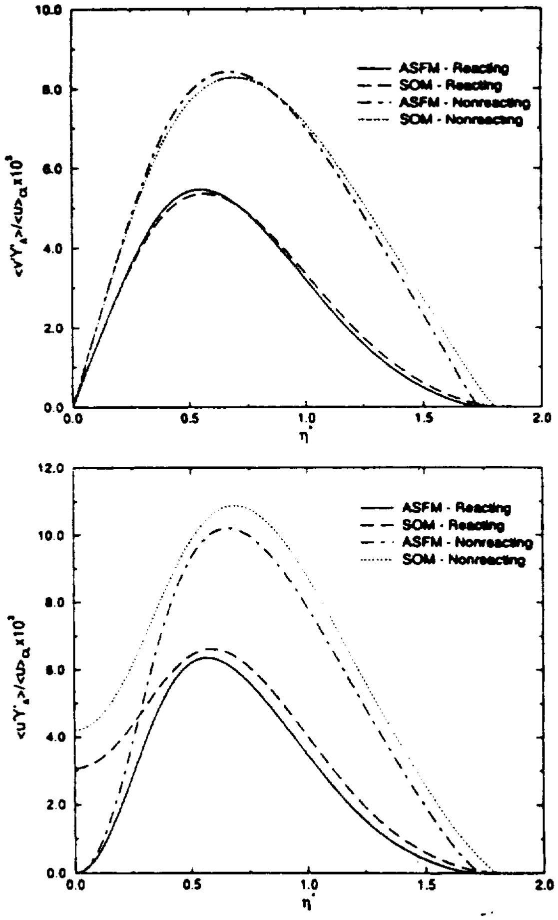

Figure 5. Cross-stream variation of $\langle v'Y_A' \rangle / \langle u \rangle_{CL}$ and $\langle u'Y_A' \rangle / \langle u \rangle_{CL}$ for the nonreacting and reacting planar jets.

It was computed via the algebraic scalar-flux model (ASFM) and the full second-order transport-equation model (SOM).

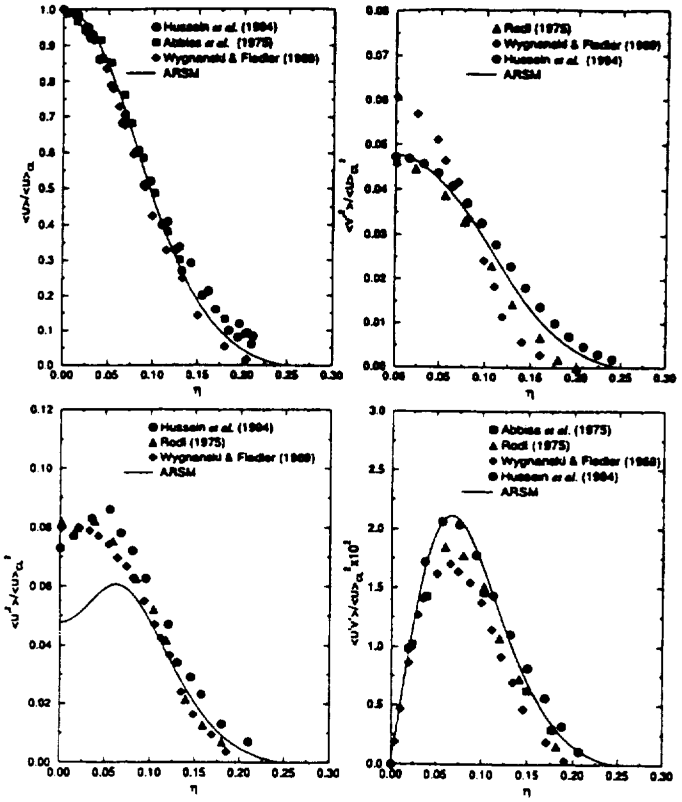

Figure 6. Cross-stream variation of $\langle u\rangle/\langle u\rangle_{CL}$, $\langle u'^2\rangle/\langle u\rangle_{CL}^2$, $\langle v'^2\rangle/\langle u\rangle_{CL}^2$, and $\langle u'v'\rangle/\langle u\rangle_{CL}^2$ for the round jet.

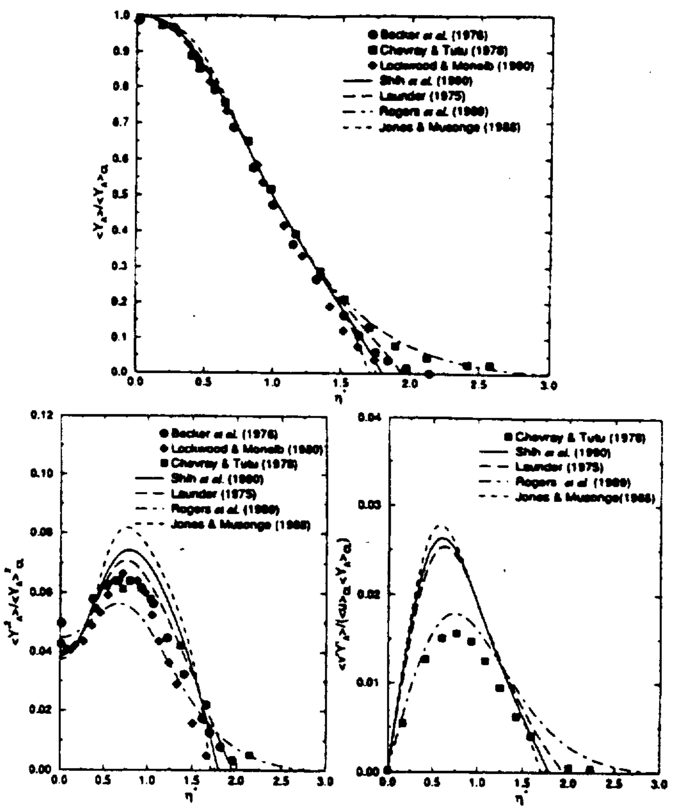

Figure 7. Cross-stream variation of $\langle Y_A\rangle/\langle Y_A\rangle_{CL}$, $\langle Y_A'^2\rangle/\langle Y_A\rangle_{CL}^2$, and $\langle v'Y_A'\rangle/(\langle u\rangle_{CL}\langle Y_A\rangle_{CL})$ for the round jet.

plementation of the model for complex flows would be very useful in further assessment of the algebraic approximation.

The performance of the models for prediction of axisymmetric jet flows is assessed in Figures 6 and 7 where the experimental data of Hussein et al. (1994), Abbiss et al. (1975), Wygnanski and Fiedler (1969), and Rodi (1975) are used for hydrodynamics variables, and those of Chevray and Tutu (1978), Becker et al. (1976), and Lockwood and Moneib (1980) for the scalar variables. The predicted hydrodynamic spreading rate with the axisymmetric correction is 0.094, and is in agreement with the experimental results of Hussein et al. (1994). Again, all the mean values are reasonably well predicted. The same is true for the Reynolds stresses, except for the streamwise normal stress in the central region for which an improvement of about 30% can be obtained if all the components of the rate of deformation tensor are considered. Consistent with the planar-jet results, the model with coefficients of Rogers et al. (1989) results in lower scalar diffusivities. This model also yields lower values for the second-order moments in the core. The model predictions based on the coefficients of Launder (1975), Jones and Musonge (1988), and Shih et al. (1990) overpredict the experimentally measured scalar's covariance and turbulent fluxes. The predictions based on the model of Rogers et al. (1989) again yield better agreement for the scalar fluxes. It is important, however, to indicate that the experiments of Chevray and Tutu (1978) are not conducted in the self-preserving regions of the jet. Therefore a definite assessment cannot be made without comparisons with further data.

From the preceding comparisons, it can be concluded that the algebraic model developed here provides an effective means of predicting the second-order moments in reacting turbulent flows. Because of their anisotropic feature, these algebraic schemes are more general than the conventional linear gradient-diffusion schemes (Toor, 1991). The explicit nature of the relations is particularly convenient for applications in practical flows of the type considered by Höfler (1993). With the reasonable agreement of the model results with experimental data in simple configurations, the methodology is recommended for predictions of more complex flows. Even so, the restrictions stemming from the assumptions involved in the development of the models have to be clearly underscored. The results shown here indicate the need for refinement of current pressure-gradient correlation closures. Moreover, the modeled transport equations for the passive scalar dissipations have known inconsistencies (Pope, 1983). These and the nature of the pressure-correlation models might raise realizability concerns, which can be considerably alleviated by implementing some of the techniques developed by Shih and Shabbir (1994). The present models are devised for high Reynolds–Peclet number flows; therefore some corrections might be required for modeling of the near-wall regions. In flows with important nonlocal effects such as the action of diffusion over long distances, rapidly varying flows, or other kind of flows far from equilibrium, the results by algebraic models are expected to have a larger departure from those by the full second-order moment formulation. In flows with very large strain fields there is a potential for singular behavior of the scalar-flux models. This issue requires further investigations of complex flows. Further improvements are recommended by considering low Reynolds–Peclet number effects, the higher-order moments of the scalar–scalar fluctuations in reacting flows, and the effects of exothermicity in nonequilibrium chemically reacting systems.

Acknowledgment

This work is part of a research program sponsored by the NASA Langley Research Center under Grant NAG-1-1122. Dr. J. Philip Drummond is the Technical Monitor. Computational resources are provided by the SEAS Computing Center at SUNY-Buffalo.

Literature Cited

Abbiss, J. B., L. J. S. Bradbury, and M. P. Wright, "Measurements in an Axisymmetric Jet Using a Photon Correlator," *Proc. LDA Symp.*, Copenhagen, Denmark (1975).

Adumitroaie, V., PhD Thesis, Dept. of Mechanical and Aerospace Engineering, State Univ. of New York at Buffalo, Buffalo (1997).

Antonia, R. A., L. W. Browne, A. J. Chambers, and S. Rajagopalan, "Budget of Temperature Variance in a Turbulent Plane Jet," *Int. J. Heat Mass Transfer*, **26**, 41 (1983).

Antonia, R. A., "On a Heat Transfer Model for a Turbulent Plane Jet," *Int. J. Heat Mass Transfer*, **28**, 1805 (1985).

Bashir, J., and M. S. Uberoi, "Experiments on Turbulent Structure and Heat Transfer in a Two Dimensional Jet," *Phys. Fluids*, **18**, 405 (1975).

Becker, H. A., H. C. Hottel, and G. C. Williams, "The Nozzle Fluid Concentration Field of the Round Turbulent Free Jet," *J. Fluid Mech.*, **30**, 285 (1976).

Beguier, C., I. Dekeyser, and B. E. Launder, "Ratio of Scalar and Velocity Dissipation Time Scales in Shear Flow Turbulence," *Phys. Fluids*, **21**, 307 (1978).

Borghi, R., "Turbulent Premixed Combustion: Further Discussions on the Scales of Fluctuations," *Combust. Flame*, **80**, 304 (1990).

Bradbury, L. J. S., "The Structure of Self-Preserving Turbulent Plane Jet," *J. Fluid Mech.*, **23**, 31 (1965).

Brodkey, R. S., ed., *Turbulence in Mixing Operation*, Academic Press, New York (1975).

Brodkey, R. S., "Fundamental of Turbulent Motion," *Chem. Eng. Commun.*, **8**, 1 (1981).

Browne, L. W. B., A. R. Antonia, and A. J. Chambers, "The Interaction Region of a Turbulent Plane Jet," *J. Fluid Mech.*, **149**, 355 (1984).

Chakrabarti, M., R. M. Kerr, and J. C. Hill, "Direct Numerical Simulation of Chemical Selectivity in Homogeneous Turbulence," *AIChE J.*, **41**, 2356 (1995).

Chevray, R., and N. K. Tutu, "Intermittency and Preferential Transport of Heat in a Round Jet," *J. Fluid Mech.*, **88**, 133 (1978).

Dopazo, C., "Recent Developments in PDF Methods," *Turbulent Reacting Flows*, Chap. 7, P. A. Libby and F. A. Williams, eds., Academic Press, New York, p. 375 (1994).

Dutta, A., and J. M. Tarbell, "Closure Models for Turbulent Reacting Flows," *AIChE J.*, **35**, 2013 (1989).

Fox, R. O., "Computational Methods for Turbulent Reacting Flows in Chemical Process Industry," *Rev. Inst. Fr. Pet.*, **51**, 215 (1996).

Frankel, S. H., C. K. Madnia, and P. Givi, "Comparative Assessment of Closures for Turbulent Reacting Flows," *AIChE J.*, **39**, 899 (1993).

Frankel, S. H., P. A. McMurtry, and P. Givi, "Linear Eddy Modeling of Reactant Conversion and Selectivity in Homogeneous Turbulence," *AIChE J.*, **41**, 258 (1995).

Gao, F., and E. E. O'Brien, "Direct Numerical Simulations of Reacting Flows in Homogeneous Turbulence," *AIChE J.*, **37**, 1459 (1991).

Gatski, T. B., and C. G. Speziale, "On Explicit Algebraic Stress Models for Complex Turbulent Flows," *J. Fluid Mech.*, **254**, 59 (1993).

Gibson, M. M., and B. E. Launder, "On the Calculation of Horizontal, Turbulent, Free Shear Flows under Gravitational Influence," *ASME J. Heat Transfer*, **98C**, 81 (1976).

Givi, P., "Model Free Simulations of Turbulent Reactive Flows," *Prog. Energy Combust. Sci.*, **15**, 1 (1989).

Givi, P., "Spectral and Random Vortex Methods in Turbulent Reacting Flows," *Turbulent Reacting Flows*, Chap. 8, P. A. Libby and F. A. Williams, eds., Academic Press, London, p. 475 (1994).

Gutmark, E., and I. Wygnanski, "The Planar Turbulent Jet," *J. Fluid Mech.*, **73**, 465 (1976).

Heskestad, G., "Hot Wire Measurements in a Plane Turbulent Jet," *J. Appl. Mech.*, **32**, 721 (1965).

Hill, J. C., "Homogeneous Turbulent Mixing with Chemical Reaction," *Ann. Rev. Fluid Mech.*, **8**, 135 (1976).

Höfler, T., "Reynolds Stress Model (RSM) in FIRE," *FIRE Newsl.*, **5**, 1 (1993).

Hussein, H. J., S. P. Capp, and W. K. George, "Velocity Measurements in a High-Reynolds-number, Momentum-Conserving, Axisymmetric, Turbulent Jet," *J. Fluid Mech.*, **258**, 31 (1994).

Jenkins, P. E., and V. W. Goldschmidt, "Mean Temperature and Velocity in a Plane Turbulent Jet," *ASME J. Fluids Eng.*, **95**, 581 (1973).

Jenkins, P. E., "Some Measured Temperature Characteristics in a Two Dimensional Heated Jet of Air," *AMS J. Eng. Power*, **98**, 501 (1976).

Jones, W. P., and P. Musonge, "Closure of the Reynolds Stress and Scalar Flux Equations," *Phys. Fluids*, **31**, 3589 (1988).

Jones, W. P., "Turbulence Modelling and Numerical Solution Methods for Variable Density and Combusting Flows," *Turbulent Reacting Flows*, Chap. 6, P. A. Libby and F. A. Williams, eds., Academic Press, London, p. 309 (1994).

Launder, B. E., G. J. Reece, and W. Rodi, "Progress in the Development of a Reynolds-Stress Turbulence Closure," *J. Fluid Mech.*, **68**, 537 (1975).

Launder, B. E., "On the Effects of a Gravitational Field on the Turbulent Transport of Heat and Momentum," *J. Fluid Mech.*, **67**, 569 (1975).

Leonard, A. D., and J. C. Hill, "Direct Numerical Simulation of Turbulent Flows with Chemical Reaction," *J. Sci. Comput.*, **3**, 25 (1988).

Leonard, A. D., and J. C. Hill, "Scalar Dissipation and Mixing in Turbulent Reacting Flows," *Phys. Fluids A.*, **3**, 1286 (1991).

Libby, P. A., and F. A. Williams, eds., *Turbulent Reacting Flows*, Academic Press, London (1994).

Lockwood, F. C., and H. A. Moneib, "Fluctuating Temperature Measurement in a Heated Round Free Jet," *Combust. Sci. Technol.*, **22**, 63 (1980).

Lumley, J. L., "Computational Modeling of Turbulent Flows," *Adv. Appl. Mech.*, **18**, 123 (1978).

Newman, G. R., B. E. Launder, and J. L. Lumley, "Modelling the Behaviour of Homogeneous Scalar Turbulence," *J. Fluid Mech.*, **111**, 217 (1981).

O'Brien, E. E., "The Probability Density Function (PDF) Approach to Reacting Turbulent Flows," *Turbulent Reacting Flows*, Chap. 5, P. A. Libby and F. A. Williams, eds., Springer-Verlag, Heidelberg, p. 185 (1980).

Pope, S. B., "A More General Effective-Viscosity Hypothesis," *J. Fluid Mech.*, **72**, 331 (1975).

Pope, S. B., "An Explanation of the Turbulent Round-jet/Plane-jet Anomaly," *AIAA J.*, **16**, 279 (1978).

Pope, S. B., "Consistent Modeling of Scalars in Turbulent Flows," *Phys. Fluids*, **26**, 404 (1983).

Rodi, W., "A New Method of Analyzing Hot-wire Signals in Highly Turbulent Flow and Its Evaluation in Round Jet," Disa Information 17 (1975).

Rodi, W., "A New Algebraic Relation for Calculating the Reynolds Stresses," *ZAMM*, **56**, T219 (1976).

Rogers, M. M., N. N. Mansour, and W. C. Reynolds, "An Algebraic Model for the Turbulent Flux of a Passive Scalar," *J. Fluid Mech.*, **203**, 77 (1989).

Shenoy, U. V., and H. L. Toor, "Turbulent Micromixing Parameters from Reactive Mixing Measurements," *AIChE J.*, **35**, 1692 (1989).

Shih, T.-H., and A. Shabbir, "Methods of Ensuring Realizability for Non-realizable Second Order Closures," ICOMP 94-14, NASA Lewis Research Center, Cleveland, OH (1994) (also available as *NASA TM 106681*).

Shih, T.-H., J. L. Lumley, and J.-Y. Chen, "Second-Order Modeling of Passive Scalar in a Turbulent Shear Flow," *AIAA J.*, **28**, 610 (1990).

Speziale, C. G., "Analytical Methods for the Development of Reynolds Stress Closures in Turbulence," *Ann. Rev. Fluid Mech.*, **23**, 107 (1991).

Taulbee, D. B., J. R. Sonnenmeier, and K. W. Wall, "Stress Relation for Three-Dimensional Turbulent Flows," *Phys. Fluids*, **6**, 1399 (1993).

Taulbee, D. B., "Engineering Turbulence Models," *Advances in Turbulence*, W. K. George and R. Arndt, eds., Hemisphere, New York, p. 75 (1989).

Taulbee, D. B., "An Improved Algebraic Reynolds Stress Model and Corresponding Nonlinear Stress Model," *Phys. Fluid A*, **4**, 2555 (1992).

Tavoularis, S., and S. Corrsin, "Experiments in Nearly Homogeneous Turbulent Shear Flow with a Uniform Mean Temperature Gradient. Part 1," *J. Fluid Mech.*, **104**, 311 (1981).

Toor, H. L., "Mass Transfer in Dilute Turbulent and Nonturbulent Systems with Rapid Irreversible Reactions and Equal Diffusivities," *AIChE J.*, **8**, 70 (1962).

Toor, H. L., "The Non-premixed Reaction: $A + B \rightarrow$ Products," *Turbulence in Mixing Operation*, R. S. Brodkey, ed., Academic Press, New York, p. 123 (1975).

Toor, H. L., "Turbulent Diffusivities in Reacting Systems," *AIChE J.*, **37**, 1737 (1991).

Uberoi, M. S., and P. I. Singh, "Turbulent Mixing in a Two Dimensional Jet," *Phys. Fluids*, **18**, 764 (1975).

Wang, D. M., and J. M. Tarbell, "Closure Models for Turbulent Reacting Flows with a Non-homogeneous Concentration Field," *Chem. Eng. Sci.*, **48**, 3907 (1993).

Warhaft, Z., and J. L. Lumley, "An Experimental Study of the Decay of Temperature Fluctuations in Grid-Generated Turbulence," *J. Fluid Mech.*, **88**, 659 (1978).

Williams, F. A., *Combustion Theory*, 2nd ed., Benjamin/Cummings, Menlo Park, CA (1985).

Wygnanski, I., and H. Fiedler, "Some Measurements in the Self-Preserving Jet," *J. Fluid Mech.*, **38**, 577 (1969).

Yoshizawa, A., "Statistical Modelling of Passive-Scalar Diffusion in Turbulent Shear Flows," *J. Fluid Mech.*, **195**, 541 (1988).

Appendix

The procedure leading to explicit solutions for the scalar-flux vector, as governed by Eq. 23 is described here.

Consider an arbitrary 3-D second-order tensor $Q \equiv [Q_{ij}]$, and the corresponding Kronecker tensor $\delta \equiv [\delta_{ij}]$. According to the Cayley–Hamilton theorem, this matrix satisfies its own characteristic polynomial:

$$Q^3 - I_Q Q^2 + II_Q Q - III_Q \delta = 0, \qquad \text{(A1)}$$

where $I_Q = \{Q\} = Q_{ii}$, $II_Q = 1/2[\{Q\}^2 - \{Q^2\}] = 1/2[Q_{ii}Q_{jj} - Q_{ij}Q_{ji}]$, $III_Q = 1/6[\{Q\}^3 - 3\{Q\}\{Q^2\} + 2\{Q^3\}] = 1/6[Q_{ii}Q_{jj}Q_{kk} - 3Q_{ii}Q_{jk}Q_{kj} + 2Q_{ij}Q_{jk}Q_{ki}]$ are the three tensorial invariants. Multiplying the characteristic polynomial with Q^{-1} and solving for the inverse, we obtain

$$Q^{-1} = \frac{1}{III_Q}\left(Q^2 - I_Q Q + II_Q \delta\right). \qquad \text{(A2)}$$

This relation can be used now to find explicit solutions to the problem considered here. For example, for the case with $Da = 0$ (pure mixing), we can write

$$\varphi_\alpha = -(\delta + G)^{-1} C, \qquad \text{(A3)}$$

where $G = D_\alpha A$. Hence

$$(\delta + G)^{-1} = \frac{1}{III_{\delta+G}}[G^2 + (2 - I_{\delta+G})G + (1 - I_{\delta+G} + II_{\delta+G})\delta]. \qquad \text{(A4)}$$

It is easy to show that $I_{\delta+G} = I_G + \{\delta\}$, $II_{\delta+G} = 2I_G + II_G + \{\delta\}$, $III_{\delta+G} = I_G + II_G + III_G + (\{\delta\}/3)$. Therefore the normalized scalar flux vector takes the form:

$$\varphi_\alpha = a_0 C + a_1 G C + a_2 G^2 C \qquad \text{(A5)}$$

with the coefficients:

$$a_0 = -\frac{1 + I_G + II_G}{1 + I_G + II_G + III_G} \qquad \text{(A6)}$$

$$a_1 = \frac{1 + I_G}{1 + I_G + II_G + III_G} \qquad \text{(A7)}$$

$$a_2 = -\frac{1}{1 + I_G + II_G + III_G}. \qquad \text{(A8)}$$

In a solenoidal velocity field the pressure–scalar gradient correlation includes a rapid term that satisfies the zero-divergence constraint. This further translates into $\{A\} = 0$; thus,

$$a_0 = -\frac{1 - \frac{1}{2}\{G^2\}}{1 - \frac{1}{2}\{G^2\} + \frac{1}{3}\{G^3\}} \qquad \text{(A9)}$$

$$a_1 = \frac{1}{1 - \frac{1}{2}\{G^2\} + \frac{1}{3}\{G^3\}} \qquad \text{(A10)}$$

$$a_2 = -\frac{1}{1 - \frac{1}{2}\{G^2\} + \frac{1}{3}\{G^3\}} \qquad \text{(A11)}$$

The reacting case is somewhat more complex. Nonetheless, by following the same procedure explicit solutions are obtained:

$$\varphi_\alpha = a_0 C_\alpha + a'_0 C_\beta + a_1 A C_\alpha + a'_1 A C_\beta + a_2 A^2 C_\alpha + a'_2 A^2 C_\beta \qquad \text{(A12)}$$

$$\varphi_\beta = b_0 C_\alpha + b'_0 C_\beta + b_1 A C_\alpha + b'_1 A C_\beta + b_2 A^2 C_\alpha + b'_2 A^2 C_\beta, \qquad \text{(A13)}$$

with the coefficients:

$$a_0 = -\frac{F_\beta\left(F_\alpha + D_\alpha^2\frac{\{A^3\}}{3}\right) + B_\alpha B_\beta\left[\frac{\{A^3\}}{3}(D_\beta F_\alpha - ED_\alpha)D_\beta - E\left(E + \frac{\{A^3\}}{3}D_\alpha D_\beta\right)\right]}{(1 - B_\alpha B_\beta)\left(F_\alpha F_\beta - E^2 B_\alpha B_\beta\right)}, \quad \text{(A14)}$$

$$a'_0 = B_\alpha \frac{F_\alpha\left(F_\beta + D_\beta^2\frac{\{A^3\}}{3}\right) + D_\alpha\frac{\{A^3\}}{3}(D_\alpha F_\beta - ED_\beta) - EB_\alpha B_\beta\left(E + \frac{\{A^3\}}{3}D_\alpha D_\beta\right)}{(1 - B_\alpha B_\beta)\left(F_\alpha F_\beta - E^2 B_\alpha B_\beta\right)}, \quad \text{(A15)}$$

$$a_1 = \frac{B_\alpha B_\beta[E(D_\beta - D_\alpha) + F_\alpha D_\beta] - D_\alpha F_\beta}{D_\alpha\left(F_\alpha F_\beta - E^2 B_\alpha B_\beta\right)} \quad \text{(A16)}$$

$$a'_1 = \frac{B_\alpha}{D_\alpha}\,\frac{D_\alpha F_\beta - D_\beta F_\alpha - E(D_\beta - D_\alpha B_\alpha B_\beta)}{F_\alpha F_\beta - E^2 B_\alpha B_\beta} \quad \text{(A17)}$$

$$a_2 = \frac{D_\alpha F_\beta - ED_\beta B_\alpha B_\beta}{F_\alpha F_\beta - E^2 B_\alpha B_\beta} \quad \text{(A18)}$$

$$a'_2 = -B_\alpha \frac{D_\alpha F_\beta - ED_\beta}{F_\alpha F_\beta - E^2 B_\alpha B_\beta}, \quad \text{(A19)}$$

with the shorthand notations:

$$F_\alpha = (1 - B_\alpha B_\beta)\left(D_\alpha\frac{\{A^2\}}{2} - \frac{1}{D_\alpha} - \frac{B_\alpha B_\beta}{D_\beta}\right) - D_\alpha^2\frac{\{A^3\}}{3} \quad \text{(A20)}$$

$$F_\beta = (1 - B_\alpha B_\beta)\left(D_\beta\frac{\{A^2\}}{2} - \frac{1}{D_\beta} - \frac{B_\alpha B_\beta}{D_\alpha}\right) - D_\beta^2\frac{\{A^3\}}{3} \quad \text{(A21)}$$

$$E = \left(\frac{1}{D_\alpha} + \frac{1}{D_\beta}\right)(1 - B_\alpha B_\beta) - D_\alpha D_\beta\frac{\{A^3\}}{3}. \quad \text{(A22)}$$

The coefficients b_i are obtained from the a_i's through the permutations $\alpha \to \theta$, $\beta \to \alpha$, $\theta \to \beta$, $a_0 \to b'_0$, $a'_0 \to b_0$, $a_1 \to b'_1$, $a'_1 \to b_1$, $a_2 \to b'_2$, and $a'_2 \to b_2$.

Manuscript received Dec. 16, 1996, and revision received Mar. 14, 1997.

Appendix VI

Progress in Favré-Reynolds Stress Closures for Compressible Flows

Progress in Favré-Reynolds Stress Closures for Compressible Flows

V. Adumitroaie [1]
Department of Mechanical and Aerospace Engineering
State University of New York at Buffalo, Buffalo, NY 14260-4400.

J.R. Ristorcelli [2]
Institute for Computer Applications in Science and Engineering
NASA Langley Research Center, Hampton, VA, 23681-0001.

D.B. Taulbee
Department of Mechanical and Aerospace Engineering
State University of New York at Buffalo, Buffalo, NY 14260-4400.

A closure for the compressible portion of the pressure-strain covariance is developed. It is shown that, within the context of a pressure-strain closure assumption linear in the Reynolds stresses, an expression for the pressure-dilatation can be used to construct a representation for the pressure-strain. Additional closures for the unclosed terms in the Favré-Reynolds stress equations involving the mean acceleration are also constructed. The closures accommodate compressibility corrections depending on the magnitude of the turbulent Mach number, the mean density gradient, the mean pressure gradient, the mean dilatation, and, of course, the mean velocity gradients. The effects of the compressibility corrections on the Favré-Reynolds stresses are consistent with current DNS results. Using the compressible pressure-strain and mean acceleration closures in the Favré-Reynolds stress equations an algebraic closure for the Favré-Reynolds stresses is constructed. Noteworthy is the fact that, *in the absence of mean velocity gradients*, the mean density gradient produces Favré-Reynolds stresses in accelerating mean flows. Computations of the mixing layer using the compressible closures developed are described. Favré-Reynolds stress closure and two-equation algebraic models are compared to laboratory data for the mixing layer. Experimental data from diverse laboratories for the Favré-Reynolds stresses appears inconsistent and, as a consequence, comparison of the Reynolds stress predictions to the data is not conclusive. Reductions of the kinetic energy and the spread rate are consistent with the sizable decreases seen in these classes of flows.

PACS: 47.27.Ak (Fundamentals), 47.27.Eq (Turbulence simulation and modeling), 47.27.Wg (Jets), 45.10.Na (Geometrical and tensorial methods), 02.10.Sp (Matrix theory).

---

[1] Current address: CFD Research Corporation, 215 Wynn Drive, Huntsville, AL 35805. Telephone: (256) 726-4845; Fax: (256) 726-4806. E-mail: va@cfdrc.com.

[2] Current address: Institute for Geophysical and Planetary Physics, MS C305, Los Alamos National Laboratory, POB 1663, Los Alamos, NM 87545. E-mail: jrrj@lanl.gov.

I. Introduction

There has been a resurgence of interest in effects of compressibility on turbulent flows related to the design of high-speed/high-altitude engines. Although experimental and numerical information is growing (for reviews see Refs. 1–3), rational theoretical and modeling efforts are in a preliminary stage of development. This is consistent with the fact that what is understood of the relative importance of many of the different physical effects of compressibility is very much in flux — changing as more numerical simulation information becomes available. While several issues regarding the effects of the compressibility of turbulent fluctuations have been recognized, progress in incorporating the physics responsible for these new compressibility effects in single-point turbulence closures has been slow. One of the major impediments to progress has been the absence of a procedure that would allow for the inclusion of the effects of compressibility on the pressure-strain covariance appearing in the second-order moment equations. A method of including compressibility effects as they appear in the pressure-strain covariance and also the variable inertia effects are the subject of the present study.

Several earlier studies have obtained closures for diverse effects of compressibility. Researchers have, in general, exploited a decomposition of the compressible field into solenoidal and dilatational parts. This has been done using a dimensional analysis in physical space[4] or in Fourier space,[5] asymptotic analysis,[6] rapid-distortion theory,[7] and a singular perturbation method.[8] All such approaches have generated models for the *scalar* compressible terms, the pressure-dilatation and the dilatational dissipation. These scalar terms appear in the kinetic energy equation for high-speed flows. Such an approach to compressible turbulence modeling has been called, very sensibly, an "energetic" approach to the effects of compressibility.[9] The models resulting from the "energetic" approach to compressibility have been applied as compressibility corrections to the standard $k-\epsilon$ model,[10] and their generalizations,[5] or to standard incompressible second-order moment [Reynolds stress] closures.[11–13] Such a procedure implies, of course, a tacit assumption that compressible effects do not manifest themselves in either the pressure-strain or in the dissipation of enstrophy. Which is to say the effects of compressibility occur only in those terms explicitly linked to the dilatational field. Thus, energetic approaches to the problem of compressible turbulence, as pointed out in Simone *et al.*,[9] are incomplete.

At one time, the pressure-dilatation and the compressible dissipation, on which modeling effort has been expended, were believed to be the primary physical effects contributing to the reduced growth rate of the compressible mixing layer. Recent studies[14,15] have demonstrated that the dilatational effects on the mixing layer are, in fact, much smaller than once believed. In addition, more recent direct numerical simulations (DNS) suggest that the pressure-dilatation covariance is nominally more important than the compressible dissipation, contrary to early proposals.[4,6] The pressure-dilatation does not, however, account for the reduced growth of the mixing layer. It appears, as suggested in Ref. 16, that the phenomena responsible for the reduced growth rate of the turbulent shear flows is due to the reduction in the Reynolds shear stress anisotropy; this effect is thought to be due to the effects of compressibility on the pressure-strain covariance. This viewpoint is consistent with the earlier numerical studies.[17] The article[13] and the later[18] studied Reynolds stress closures in the context of the DNS of the homogeneous shear. The study showed that the inclusion of the [then] current compressible dissipation and pressure-dilatation models in the Reynolds stress turbulence closures led to improved predictions for the turbulent kinetic energy. However, there were no changes in the anisotropy consistent with that seen in DNS. The authors concluded that the [then] current models were deficient primarily in the modeling of the pressure-strain covariance which controls the level of Reynolds stress anisotropy.

It should be noted that the improved agreement for the time evolution of the kinetic energy,[13,18] when using such models for the scalar compressible terms cannot be taken to indicate that such flows were rationally predicted. The models current at that time, designed with erroneous assumptions regarding the importance of the dilatational effects, were providing dissipative behavior by a mechanism that did not reflect actual flow physics. This has since been substantiated numerically in the studies;[9,14–16] all of which indicate the lack of significance of both the pressure-dilatation and the compressible dissipation. The fact that the compressible dissipation and the pressure-dilatation are nominal effects is also consistent with the analytical development of Ristorcelli.[8] In Ref. 8 the pressure-dilatation is shown to vanish as turbulence approaches equilibrium; the simulations mentioned are quasi-equilibrium flows for which the pressure dilatation is expected to be small. It should be mentioned that in the homogeneous shear simulations, arguably the most non-equilibrium of the benchmark flows, the pressure-dilatation is small but non-negligible; it is some 5-10% of the dissipation. Our position is the same as the position of Vreman *et al.*[14] as pithily summarized in their conclusion. To paraphrase, turbulence models constructed using the dilatational dissipation or pressure-dilatation to explain the suppression of the turbulence [in the mixing layer] do not appear to be reflecting the correct physics.

Thus, if it is assumed that the primary source of the reduced mixing rate in the mixing layer is due to the reduction in the shear stress anisotropy as indicated by DNS then a closure of the second-moment or Reynolds stress equations is in order: the pressure-strain covariance appearing in the second-moment equations is the only possible mechanism for such behavior. This is a substantially more difficult problem than that treated using the energetic approach; the quantities requiring closure are no longer scalars but second-order tensors. As one might expect, true compressible second-order modeling attempts are few.[7,19]

This article describes the development of a closure for the compressible aspects of pressure-strain covariance appearing in the Favré-Reynolds stress equations. [As is clear from the material, the phrase Reynolds stresses will be used to refer to the Favré-Reynolds stresses.] Closures for the unclosed terms involving the mean acceleration are also constructed. In as much as many engineering calculations are done with lower order closures this article therefore also includes the additional development of the second-order moment closure into an algebraic Reynolds stress closure, used for flows near structural equilibrium, following established procedures.[20–28]

The algebraic Reynolds stress closure is noteworthy for the fact that it indicates that, even in the absence of mean deformation, the mean density gradient is a source of turbulence stresses in accelerating mean flows. As a consequence, for flows with large arbitrary mean density and pressure gradients an eddy viscosity representation for the Reynolds stresses is, from first principles, inappropriate. In the next section, Sec. II, the Favré averaged nondimensional form of the governing equations are given. Both first and second-order moment equations for a compressible medium, with no combustion, are given. Issues related to moment closures for compressible turbulence are also outlined.

The development of closures for the effects of compressibility in the Reynolds stress equations is described in Sec. III. It is shown that, within the context of a pressure-strain closure *linear* in the Reynolds stresses, an expression for the pressure-dilatation covariance can be used to construct the off-diagonal components of the pressure-strain covariance. In this way the results of previous "energetic" approaches,[9] to the effects of compressibility can be built into the deviatoric portion of an expression for the pressure-strain. It is hoped that such a procedure would allow one to avoid the development of a whole new theory and methodology for the compressible pressure-strain tensor.

Closures for the effects of the mean acceleration, which involve the mass flux, are also developed. The new closures account for the influence of the turbulent Mach number, and the mean density and pressure gradients through a new quantity, the baroclinic dyad. The effects of the bulk dilatation are also included. Section III is concluded with a summary of models for the compressible dissipation; given the acknowledged lack of importance of the compressible dissipation in weakly compressible aerodynamic turbulence, as discussed above and in Sec. III, no development of models for the compressible dissipation is pursued.

Starting with the closure for the second-order moment equations developed in Sec. III, Sec. IV develops an algebraic closure for the Reynolds stresses. The physics of compressibility, as captured by the full second-moment closure, are built into the simpler and more widely used two-equation $k-\epsilon$ platform. The tensor polynomial representation techniques employed produce both two-dimensional and three-dimensional versions of an algebraic turbulence stress closure. Given the complexity of the three-dimensional algebraic closure and the current status of single-point turbulence models for three-dimensional flow only the two-dimensional model is developed into a working closure.

Section V focuses on a numerical investigation of the closures. The numerical method used to simulate the free-shear flows of interest is sketched. The theory and results presented in earlier sections are implemented in simulations in the mixing layer.

Simulations using second-order moment (SOM) closures as well as the algebraic models are conducted. The numerical experiments are constructed with the intention of investigating several very different issues of relevance to the prediction of compressible turbulent flows for engineering purposes. Foremost in importance is the success of an algebraic stress model to reflect the compressible physics of the full SOM closures.

The pressure-strain methodology developed for the SOM equations in Sec. III are general and depend on a choice of closures for the pressure-dilatation. As consequence it follows that it is necessary to understand sensitivity of the formulation to different models for the pressure-dilatation. In this context two pressure-dilatation models are investigated.

In addition to assessing the sensitivity of the pressure-strain model to different pressure-dilatation models and the suitability of the algebraic stress closure, we compare the computational results to what is seen in numerical and laboratory experiments. Of particular interest is the well known effect of compressibility on the reduction of the spread rate of the mixing layer. In as much as the reduction in the spread rate is due to changes in the principal axes of the Reynolds stress tensor the effects of compressibility on the anisotropy tensor are investigated. Given that the anisotropy of the Reynolds stresses is dependent on the pressure-strain, the effects of compressibility on the different components of the pressure-strain tensor are also investigated.

II. Governing equations

The problem formulation is now described. This includes a statement of the governing equations – the first and second-moment equations. Indications of the modeling issues to be addressed in subsequent sections are also given. The Favré averaging procedure is first described.

The conservation equations for mass, momentum and energy in a Favré setting are now derived. The dependent variables used are the density ρ, the velocity u_i and the total energy $e_t = h -$

$p/\rho + u_i u_i/2$. The fluid is assumed to be Newtonian fluid satisfying the Stokes relation with zero bulk viscosity and a constant molecular Prandtl number. Although real gas effects are of interest for industrial applications there are a sufficient number of unresolved and more important issues associated with compressibility that justify limiting the study to ideal gases. Consequently, the pressure p is obtained from the equation of state $p = \rho RT$.

The Favré averaging procedure is now described: denote by an over-bar the ensemble (or time) average and by the brackets the density weighted ensemble (or time) average:

$$\langle X \rangle = \frac{\overline{\rho X}}{\overline{\rho}} \tag{1}$$

The ensemble average obeys the following decomposition rules:

$$X = \overline{X} + X', \quad \overline{X'} = 0. \tag{2}$$

The Favré average obeys the following decomposition rules:

$$X = \langle X \rangle + X'', \quad \langle X'' \rangle = 0, \quad \overline{X''} = \overline{X} - \langle X \rangle. \tag{3}$$

The application of the above averaging procedure on the instantaneous transport equations, decomposing the variables Favré mean and fluctuating components, produces the Favré averaged equations. The equations of motion are first rewritten in nondimensional form (with respect to reference values taken in the high speed stream: ρ_∞, u_∞, T_∞, μ_∞ and the inlet value of the vorticity thickness δ_ω). Using these reference quantities, we define the relevant nondimensional parameters: the Reynolds number $Re = \rho_\infty u_\infty \delta_\omega / \mu_\infty$, the Prandtl number $Pr = c_p \mu_\infty / \lambda$, the mean flow Mach number $M = u_\infty / \sqrt{\gamma R T_\infty}$. γ is c_p/c_v. For this study, $Pr = 1$.

A. First moment equations

The mass conservation equation reads:

$$\frac{\partial \overline{\rho}}{\partial t} + \frac{\partial \overline{\rho} \langle u_j \rangle}{\partial x_j} = 0 \tag{4}$$

and the conservation of momentum is:

$$\frac{\partial \overline{\rho} \langle u_i \rangle}{\partial t} + \frac{\partial \overline{\rho} \langle u_i \rangle \langle u_j \rangle}{\partial x_j} = -\frac{\partial \overline{\rho} \langle u_i'' u_j'' \rangle}{\partial x_j} - \frac{\partial \overline{p}}{\partial x_i} + \frac{\partial \overline{\sigma}_{ji}(u)}{\partial x_j}. \tag{5}$$

Note that the stress tensor notation is changed to $\sigma_{ji}(u) = \frac{2\mu}{Re}[S_{ij}(u) - \frac{1}{3} S_{pp}(u) \delta_{ij}] = 2\mu S^{\star}_{ij}(u)/Re$. For the strain rate $S_{ij}(u) = \frac{1}{2}(\frac{\partial u_i}{\partial x_j} + \frac{\partial u_j}{\partial x_i})$ and for all the other linear differential operators, this new notation is more suitable when investigating compressible flows. In these instances the two types of averages, having different properties with respect to the linear differential operators, are naturally encountered. Hereafter any tensor with a star superscript will indicate the deviator – the traceless portion of that tensor.

Two supplementary hypotheses pertaining to the molecular transport of momentum are set forth: the viscosity fluctuations are unimportant and the mean viscosity $\langle \mu \rangle$ is described by the Maxwell-Rayleigh law, *i.e.*, it varies with the mean temperature as $\langle \mu \rangle / \mu_{ref} = (\langle T \rangle / T_{ref})^m$, $m =$

0.76. The fluctuations of the viscosity and their correlation with other variables are neglected. Within the current notation the averaged stress $\overline{\sigma}_{ji}(u)$ is equal to $\sigma_{ji}(\langle u\rangle) + \sigma_{ji}(\overline{u''})$.

The Favré mean of the total energy of the fluid $e_t = T/[\gamma(\gamma-1)M^2] + u_j u_j/2$ obeys:

$$\frac{\partial \overline{\rho}\langle e_t\rangle}{\partial t} + \frac{\partial \overline{\rho}\langle e_t\rangle\langle u_j\rangle}{\partial x_j} = -\frac{\partial \overline{q}_j(T)}{\partial x_j} - \frac{\partial \overline{\rho}\langle u''_j e''_t\rangle}{\partial x_j} + \frac{\partial}{\partial x_j}(\overline{u_i\sigma_{ji}(u)} - \overline{pu_j}). \tag{6}$$

As is the situation with the momentum equation, the molecular flux term in the energy equation introduces the other type of mean quantity present in the Favré formulation - the plain ensemble mean. Using the new notation, the heat flux

$$q_j(T) = -\frac{\mu}{(\gamma-1)RePrM^2}\frac{\partial T}{\partial x_j}$$

has the resulting averaged expression:

$$\overline{q}_j(T) = q_j(\langle T\rangle) + q_j(\overline{T''}).$$

The remaining terms on the right-hand side of the energy equation can be expanded by using the equation of state in the average sense

$$\overline{p} = \frac{1}{\gamma M^2}\overline{\rho}\langle T\rangle. \tag{7}$$

Then the pressure work term is of the form

$$\overline{pu}_j = \overline{p}\langle u_j\rangle + \frac{1}{\gamma M^2}\overline{\rho}\langle u''_j T''\rangle,$$

the viscous work term reads

$$\overline{u_i\sigma_{ji}(u)} = \langle u_i\rangle\sigma_{ji}(\langle u\rangle) + \langle u_i\rangle\sigma_{ji}(\overline{u''}) + \overline{u''}\sigma_{ji}(\langle u\rangle) + \overline{u''_i\sigma_{ji}(u'')}$$

and the turbulent total energy flux is

$$\overline{\rho}\langle u''_j e''_t\rangle = \frac{1}{\gamma(\gamma-1)M^2}\overline{\rho}\langle u''_j T''\rangle + \overline{\rho}\langle u''_j u''_i\rangle\langle u_i\rangle + \overline{\rho}\frac{\langle u''_j u''_i u''_i\rangle}{2}.$$

The fluctuations of transported quantities in turbulent flows are sustained via interaction between the mean gradients and the turbulence. The fluctuations will be characterized by length and time scales of the order of those of the mean flow and which, provided the Reynolds number is large, will be many orders of magnitude larger than the fine scales at which the molecular diffusion is important. Thus the form of the moment equations carried in the closure development for the computation of free shear flows will not include viscous transport effects.

B. Second-order moment equations

The average of the first moment of the Favré decomposed Navier-Stokes equations produces the following second moment equations:

$$\begin{aligned}\frac{\partial\overline{\rho}\langle u_i''u_j''\rangle}{\partial t}+\frac{\partial\overline{\rho}\langle u_i''u_j''\rangle\langle u_k\rangle}{\partial x_k}&=-\frac{\partial}{\partial x_k}\left[\overline{\rho}\langle u_i''u_j''u_k''\rangle+\overline{p'u_j''}\delta_{ik}+\overline{p'u_i''}\delta_{jk}-\overline{u_i''\sigma_{kj}(u'')}-\right.\\ &\left.\overline{u_j''\sigma_{ki}(u'')}\right]-\overline{\rho}\langle u_i''u_k''\rangle\frac{\partial\langle u_j\rangle}{\partial x_k}-\overline{\rho}\langle u_k''u_j''\rangle\frac{\partial\langle u_i\rangle}{\partial x_k}+\overline{p'\left(\frac{\partial u_i''}{\partial x_j}+\frac{\partial u_j''}{\partial x_i}\right)}-\overline{u_i''}\frac{\partial\overline{p}}{\partial x_j}-\overline{u_j''}\frac{\partial\overline{p}}{\partial x_i}\\ &+\overline{u_j''}\frac{\partial\sigma_{ki}(\langle u\rangle)}{\partial x_k}+\overline{u_i''}\frac{\partial\sigma_{kj}(\langle u\rangle)}{\partial x_k}-\left[\overline{\sigma_{jk}(u'')\frac{\partial u_i''}{\partial x_k}}+\overline{\sigma_{ki}(u'')\frac{\partial u_j''}{\partial x_k}}\right]\end{aligned}\tag{8}$$

It is necessary to provide a closure for two compressible quantities: the pressure-strain correlation and the mass flux/pressure gradient (the last three terms in the second line). The molecular diffusion terms are generally small in high Reynolds number flows and will be negligible for problems addressed here. It should be pointed out that, depending on how the derivation is done, the mass flux terms multiply the acceleration of the mean flow. For this reason the mass flux terms are often called acceleration terms: they appear to be important in accelerating mean flows.

Various tensors are divided into their traces and their deviators. The production of the Reynolds stresses becomes,

$$P_{ij}^{*}=P_{ij}-\frac{2}{3}P\delta_{ij}=-\overline{\rho}\left[\langle u_i''u_k''\rangle\frac{\partial\langle u_j\rangle}{\partial x_k}+\langle u_k''u_j''\rangle\frac{\partial\langle u_i\rangle}{\partial x_k}-\frac{2}{3}\langle u_k''u_l''\rangle\frac{\partial\langle u_l\rangle}{\partial x_k}\delta_{ij}\right]\tag{9}$$

where P is the production of $\langle k\rangle$. The pressure-strain covariance is written as

$$\Pi_{ij}^{*}=\Pi_{ij}-\frac{2}{3}\overline{p'd}\delta_{ij}=\overline{p'\left(\frac{\partial u_i''}{\partial x_j}+\frac{\partial u_j''}{\partial x_i}\right)}-\frac{2}{3}\overline{p'\frac{\partial u_k''}{\partial x_k}}\delta_{ij}.\tag{10}$$

The viscous and pressure acceleration terms are written, respectively, as

$$\mathcal{V}_{ij}^{*}=\mathcal{V}_{ij}-\frac{2}{3}\mathcal{V}\delta_{ij}=\overline{u_j''}\frac{\partial\sigma_{ki}(\langle u\rangle)}{\partial x_k}+\overline{u_i''}\frac{\partial\sigma_{kj}(\langle u\rangle)}{\partial x_k}-\frac{2}{3}\overline{u_l''}\frac{\partial\sigma_{kl}(\langle u\rangle)}{\partial x_k}\delta_{ij}\tag{11}$$

and

$$\mathcal{M}_{ij}^{*}=\mathcal{M}_{ij}-\frac{2}{3}\mathcal{M}\delta_{ij}=-\left[\overline{u_i''}\frac{\partial\overline{p}}{\partial x_j}+\overline{u_j''}\frac{\partial\overline{p}}{\partial x_i}-\frac{2}{3}\overline{u_k''}\frac{\partial\overline{p}}{\partial x_k}\delta_{ij}\right].\tag{12}$$

Note that the mean pressure gradient appearing in M_{ij} and the mean viscous stress appearing in $\mathcal{V}_{ij}$ can be replaced using the mean momentum equations. In which case they are written in terms of the mean flow Lagrangian acceleration. Both of these terms involve the mass flux; any closure for these two acceleration terms requires a closure for the mass flux. The dissipation is rewritten as

$$\overline{\rho}\,\epsilon_{ij}^{*}=\overline{\rho}\left(\overline{\epsilon}_{ij}-\frac{2}{3}\overline{\epsilon}\delta_{ij}\right)=\overline{\sigma_{jk}(u'')\frac{\partial u_i''}{\partial x_k}}+\overline{\sigma_{ki}(u'')\frac{\partial u_j''}{\partial x_k}}-\frac{2}{3}\overline{\sigma_{lk}(u'')\frac{\partial u_l''}{\partial x_k}}\delta_{ij}\tag{13}$$

In turbulent free shear flows the viscous diffusion part is overlooked owing to high Reynolds numbers which are characteristic to these flows. The present analysis can accommodate the discarded viscous terms when necessary; the tensor $\mathcal{V}_{ij}$ will be carried for generality. Furthermore, the turbulent transport terms are considered together:

$$T_{ijk} = -\left[\overline{\rho}\langle u_i''u_j''u_k''\rangle + \overline{p'u_j''}\delta_{ik} + \overline{p'u_i''}\delta_{jk} - \overline{u_i''\sigma_{kj}(u'')} - \overline{u_j''\sigma_{ki}(u'')}\right]. \tag{14}$$

The Reynolds stress or second-order moment equations are then written

$$\begin{aligned}\frac{\partial\overline{\rho}\langle u_i''u_j''\rangle}{\partial t} + \frac{\partial\overline{\rho}\langle u_i''u_j''\rangle\langle u_k\rangle}{\partial x_k} = \frac{\partial}{\partial x_k}T_{ijk} + P_{ij}^\star + \Pi_{ij}^\star + \mathcal{M}_{ij}^\star + \mathcal{V}_{ij}^\star - \overline{\rho}\ \epsilon_{ij}^\star \\ +\frac{2}{3}\left[P + \overline{p'd} + \mathcal{M} + \mathcal{V} - \overline{\rho}\ \overline{\epsilon}\right]\delta_{ij}\end{aligned} \tag{15}$$

The equation for the anisotropy The single-point anisotropy tensor, **a**, is defined

$$a_{ij} = \langle u_i''u_j''\rangle/\langle k\rangle - \frac{2}{3}\delta_{ij}. \tag{16}$$

The anisotropy has zero trace. Note that the Reynolds stress has been normalized by $\langle k\rangle$ and not $2\langle k\rangle$; in which case this version of the anisotropy is related to an older definition by $a_{ij} = 2b_{ij}$. The turbulence time scale is $\tau = \langle k\rangle/\overline{\epsilon}_s$ where $\overline{\epsilon}_s$ is the solenoidal dissipation. The second invariants of the mean strain and rotation are denoted by $\sigma^2 = S_{ij}^\star(\langle u\rangle)S_{ji}^\star(\langle u\rangle)$ and $\omega^2 = \Omega_{ij}(\langle u\rangle)\Omega_{ij}(\langle u\rangle)$.

In order to derive the algebraic stress closure in Sec. IV the second-order moment transport equations are replaced with the equation for $\langle k\rangle$ and an equation for the anisotropy tensor. For the algebraic stress closure the modeling procedure of Taulbee,[21] discussed further in Sec. IV, is employed. Taulbee's procedure, in order to be consistent with observed asymptotic behavior, chooses as dependent variable the ratio $a_{ij}/(\tau\sigma)$. The relevant form of the anisotropy equation is

$$\begin{aligned}\tau\sigma\overline{\rho}\frac{D\,a_{ij}/(\tau\sigma)}{Dt} = \frac{1}{\langle k\rangle}\left[\frac{\partial T_{ijk}}{\partial x_k} - \frac{\langle u_i''u_j''\rangle}{\langle k\rangle}\frac{\partial T_k}{\partial x_k}\right] - \frac{a_{ij}}{\langle k\rangle}\left[\frac{\partial T_k}{\partial x_k} - \tau\frac{\partial T_k^\epsilon}{\partial x_k}\right] \\ +\frac{1}{\langle k\rangle}\left[P_{ij}^\star + \Pi_{ij}^\star + \mathcal{M}_{ij}^\star + \mathcal{V}_{ij}^\star - \overline{\rho}\ \epsilon_{ij}^\star\right] - \\ \overline{\rho}\frac{a_{ij}}{\tau}\left[C_{\epsilon_2} - 2 + (2 - C_{\epsilon_1})\frac{P}{\overline{\rho}\ \overline{\epsilon}_s} + \frac{\tau}{\sigma}\frac{D\sigma}{Dt} + 2\frac{\mathcal{M} + \mathcal{V} + \overline{p'd} - \overline{\rho}\ \overline{\epsilon}_c}{\overline{\rho}\ \overline{\epsilon}_s}\right]\end{aligned} \tag{17}$$

where D/Dt indicates the mean Lagrangian derivative, $D/Dt = \frac{\partial}{\partial t} + \langle u_j\rangle\frac{\partial}{\partial x_j}$.

The kinetic energy equation The equation for the turbulent kinetic energy $\langle k\rangle = \langle u_i''u_i''\rangle/2$ is

$$\begin{aligned}\frac{\partial\overline{\rho}\langle k\rangle}{\partial t} + \frac{\partial\overline{\rho}\langle k\rangle\langle u_j\rangle}{\partial x_j} = -\frac{\partial}{\partial x_j}\left[\overline{\rho}\langle u_j''k\rangle + \overline{p'u_j''} - \overline{u_i''\sigma_{ji}(u'')}\right] - \overline{\rho}\langle u_i''u_j''\rangle\frac{\partial\langle u_i\rangle}{\partial x_j} \\ + \overline{p'\frac{\partial u_i''}{\partial x_i}} - \overline{u_j''}\frac{\partial\overline{p}}{\partial x_j} + \overline{u_j''}\frac{\partial\sigma_{ji}(\langle u\rangle)}{\partial x_j} - \overline{\sigma_{ji}(u'')\frac{\partial u_i''}{\partial x_j}}.\end{aligned} \tag{18}$$

The additional terms reflecting the compressible nature of the turbulence are on the last line; they are, respectively, the pressure-dilatation covariance, the mass flux – mean acceleration, and

the compressible dissipation. Note that neither the pressure-strain nor the mass flux/pressure acceleration terms, $\mathcal{M}_{ij}$, appear in the $\langle k \rangle$ equation. The effects of the pressure-strain and the $\mathcal{M}_{ij}$, appears only in the Reynolds stress equations. Any classical two-equation turbulence model cannot, as a consequence, account for the physics associated with these two unknown covariances that lead to changes in the Reynolds stress structure. Early approaches accounting for the effects of compressibility have focussed only on the effects of compressibility as they occur in the energy equation. This so-called "energetic" approach, to use the phrase of Simone *et al.*,[9] for the effects of compressibility misses the changes in the Reynolds stresses due to compressibility and inertia. It is for this reason that, in Sec. III, the second-order equations are closed. An algebraic Reynolds stress closure is then derived in Sec. IV. In this way the structural effects of compressibility, for a certain class of flows, can be accounted for within the context of a two-equation single-point closure.

The dissipation equation The dissipation appearing in the kinetic energy equation is typically written, for locally homogeneous flows,[4,6,29]

$$\overline{\sigma_{ji}(u'')\frac{\partial u_i''}{\partial x_j}} = \overline{\rho}\,\overline{\epsilon} = \overline{\rho}(\overline{\epsilon}_s + \overline{\epsilon}_c) = 2\overline{\mu\Omega_{ij}(u'')\Omega_{ij}(u'')} + \frac{4}{3}\overline{\mu S_{kk}^2(u'')} \tag{19}$$

with $\Omega_{ij}(u) = \frac{1}{2}(\frac{\partial u_i}{\partial x_j} - \frac{\partial u_j}{\partial x_i})$ as the rotation rate. It is customary to compute the solenoidal dissipation from the incompressible $k - \epsilon$ model extended to variable density flows:

$$\frac{\partial \overline{\rho}\,\overline{\epsilon}_s}{\partial t} + \frac{\partial \overline{\rho}\,\overline{\epsilon}_s \langle u_j \rangle}{\partial x_j} = -\frac{\partial}{\partial x_j}\left[\overline{\rho}\langle u_j'' \epsilon_s \rangle - \frac{\mu}{Re}\frac{\partial \overline{\epsilon}_s}{\partial x_j}\right] - - C_{\epsilon_1}\overline{\rho}\frac{\overline{\epsilon}_s}{\langle k \rangle}\langle u_i'' u_j'' \rangle \frac{\partial \langle u_i \rangle}{\partial x_j} - C_{\epsilon_2}\overline{\rho}\frac{\overline{\epsilon}_s^2}{\langle k \rangle}, \tag{20}$$

where $C_{\epsilon_1} = 1.44$ and $C_{\epsilon_2} = 1.92$.

In the present closure formulation turbulent transport of the second order quantities are all closed using a gradient diffusion model. Thus the turbulent transport of the product of fluctuating quantities, Ξ, is written

$$\langle u_i'' \Xi \rangle = -C_s \frac{\langle k \rangle}{\overline{\epsilon}_s} \langle u_i'' u_j'' \rangle \frac{\partial \langle \Xi \rangle}{\partial x_j}, \tag{21}$$

where C_s is taken to be equal to 0.22 for all non-gradient correlations (*e.g.*, $\Xi \equiv \langle k \rangle$ or $\Xi \equiv \langle u_k'' u_l'' \rangle$), whereas for the dissipation ($\Xi \equiv \overline{\epsilon}_s$), $C_s = 0.18$.

III. Compressible closures for the second-order moment equations

This section describes the development of closures for the unknown terms in the second-order equations. The pressure-strain covariance appearing in the Reynolds stress equations is closed using a linear tensor polynomial representation in the Reynolds stress following well established procedures similar to Launder *et al.*[30] In recognition of the minor role viscosity plays in high Reynolds number free shear flows, only pressure-strain and pressure-acceleration closures are addressed. The pressure-acceleration terms are closed using a leading order [isotropic] gradient transport expression for the mass flux. The following section, Sec. IV, uses the results of the present section to obtain an algebraic closure for the Reynolds stresses.

A. A closure for the pressure-strain covariance

In incompressible turbulence the closure of the pressure-strain covariance by a tensor polynomial linear in the Reynolds stresses is used with notable success for simple two-dimensional mean flows. The procedure is standard; a popular early reference is Launder *et al.*[30] An updated version of the linear[30] rapid pressure-strain modeling is given in Speziale *et al.*[31] As the ultimate goal is to devise an algebraic Reynolds stress model only pressure-strain models linear in the Reynolds stresses will be considered. A discussion of nonlinear rapid-pressure-strain model and the need for realizability can be found in Ref. 32. Additional discussion of the physical assumptions underlying such methodologies can be found in Refs. 33–35.

The compressible correction to the pressure-strain covariance representation is obtained using established linear procedures. As in the incompressible situation,[30,34,32] the pressure strain-covariance closure can be written as:

$$\Pi_{ij} - \overline{\rho}\, \epsilon^{*}_{ij} = \mathcal{A}_{ij} + 2\overline{\rho}\,[\mathcal{I}_{piqj} + \mathcal{I}_{pjqi}][S_{pq}(\langle u\rangle) + \Omega_{pq}(\langle u\rangle)]. \tag{22}$$

Such an expression is possible if the supplementary compressible terms appearing in the Poisson equation for the pressure (see Appendix) are, in the weakly compressible limit, of higher order. This will be the case if the evanescent wave portion of the initial value problem is not important as is the case for aerodynamic applications.[36] The tensors in the above decomposition are modeled as:

$$\begin{aligned}
\mathcal{A}_{ij} &= -C_1\overline{\rho}\,\overline{\epsilon}a_{ij} + \mathcal{A}_{pp}\frac{\delta_{ij}}{3} && (23)\\
\frac{\mathcal{I}_{pjqi}}{\langle k\rangle} &= \alpha_1\delta_{qi}\delta_{pj} + \alpha_2(\delta_{pq}\delta_{ij} + \delta_{qj}\delta_{pi}) + \beta_1\delta_{pj}a_{qi} \\
&+ \beta_2(\delta_{pq}a_{ij} + \delta_{pi}a_{qj} + \delta_{ij}a_{pq} + \delta_{jq}a_{pi}) + \beta_3\delta_{qi}a_{pj} && (24)
\end{aligned}$$

Here $\mathcal{I}_{pjqi}$, following precedent, is linear in the Reynolds stresses satisfying necessary symmetry requirements. There are five unknowns. To determine the coefficients in $\mathcal{I}_{pjqi}$ additional constraints are required. As is the usual procedure, the normalization constraint,[30,32] requires

$$\mathcal{I}_{ppqi} = [(3\alpha_1 + 2\alpha_2)\delta_{qi} + (3\beta_1 + 4\beta_2)a_{qi}]\langle k\rangle = \langle u''_q u''_i\rangle \tag{25}$$

which can be satisfied if

$$\begin{aligned}
3\alpha_1 + 2\alpha_2 &= 2/3\\
3\beta_1 + 4\beta_2 &= 1.
\end{aligned}$$

There are now three unknowns and additional information is required to obtain them.

In incompressible turbulence modeling the trace of the pressure-strain is zero, $\mathcal{I}_{pkqk} = 0$, and this provides the additional information to determine the unknowns. In compressible turbulence the trace of the pressure-strain is the pressure-dilatation and the so-called continuity constraint becomes

$$\mathcal{A}_{kk} + 4\overline{\rho}\,\mathcal{I}_{pkqk}[S_{pq} + \Omega_{pq}] = 2\overline{p'd}. \tag{26}$$

As the right hand side, $\overline{pd}$, is known from earlier energetic approaches to the compressible turbulence modeling problem, the continuity constraint, Eq. (26), becomes a constraint that determines the coefficients in the pressure-strain closure. Note that as $\overline{pd}$ vanishes with turbulent Mach number the incompressible limit, $\mathcal{A}_{kk} + 4\bar{\rho}\,\mathcal{I}_{pkqk}[S_{pq} + \Omega_{pq}] = 0$, is recovered for vanishing compressibility.

As a consequence of the continuity constraint a certain combination of coefficients appears in the final model. These are readily defined by a portion of Eq. (26) such that

$$\mathcal{I}_{piqi}/\langle k\rangle = (\alpha_1 + 4\alpha_2)\delta_{pq} + (\beta_1 + 5\beta_2 + \beta_3)a_{pq} = d_1\delta_{pq} + d_2 a_{pq}. \tag{27}$$

The final model for the compressible portions of the pressure-strain is then written in terms of d_1 and d_2. The values of d_1 and d_2, as will be indicated shortly, are then determined by the expression for the pressure-dilatation. The values of the α_i can be related to the d_i:

$$\begin{aligned} \alpha_1 &= -d_1/5 + 4/15, \quad & \alpha_2 &= 3d_1/10 - 1/15 \\ \beta_1 &= (15 + 6C_2)/33, \quad & \beta_2 &= -(2 + 3C_2)/22 \\ \beta_3 &= d_2 + C_2/2. \end{aligned}$$

and $C_3 = (5 - 9C_2)/11$, $C_4 = (1 + 7C_2)/11$.

Application of the normalization and continuity constraints then allows the linear pressure-strain model to be written as

$$\begin{aligned} \Pi^\star_{ij} - \bar{\rho}\ \epsilon^\star_{ij} = -C_1\bar{\rho}\ \bar{\epsilon}a_{ij} + \bar{\rho}\langle k\rangle \Bigg[\left(\frac{4}{5} + \frac{2}{5}d_1\right) S^\star_{ij}(\langle u\rangle) + \\ [1 - C_3 + 2d_2]\left[a_{ip}S^\star_{pj}(\langle u\rangle) + S^\star_{ip}(\langle u\rangle)a_{pj} - \frac{2}{3}S^\star_{pq}(\langle u\rangle)a_{pq}\delta_{ij}\right] - \\ [1 - C_4 - 2d_2][a_{ip}\Omega_{pj}(\langle u\rangle) - \Omega_{ip}(\langle u\rangle)a_{pj}] + \frac{4}{3}d_2 S_{pp}(\langle u\rangle)a_{ij}\Bigg] \end{aligned} \tag{28}$$

which follows from Eq. (22) after subtracting the pressure-dilatation from the left side and the pressure-dilatation model from the right side of Eq. (22). All terms involving the d_i represent corrections due to the compressibility of the fluctuations; the d_i vanish as the turbulent Mach number vanishes. The terms involving the C_i come from the incompressible pressure-strain model. In which case the choice of the C_i allow one's favorite incompressible pressure-strain model to be used. The above expression for the pressure-strain, reflecting the choice $C_2 = 0.45$, is used in all the calculations presented in this paper. In more complex flows realizability corrections may need to be incorporated, in which case C_2 would be a variable. A realizable form of the model is given in an Appendix; more details can be found in Ref. 37.

1. Commentary

It has been seen that the knowledge of one invariant of the pressure-strain, the pressure-dilatation, *and* the assumption of a form linear in the Reynolds stress allows one to obtain a model for the deviatoric components of the pressure-strain tensor. In this way an independent new theory for the compressible pressure-strain can be avoided by using the results of developments for the scalar pressure-dilatation. The results of previous so-called energetic approaches, Simone *et al.*,[9] to the effects of compressibility is built into the deviatoric portion of an expression for the pressure-strain.

This point merits consideration from another point of view. Consider, for the moment, the following partition of the pressure-strain:

$$\overline{ps_{ij}} = \overline{ps^*_{ij}} + \frac{2}{3}\overline{pd}\delta_{ij}. \tag{29}$$

For this subsection, the primes on p have been dropped. Here by s^*_{ij} we now mean the deviatoric portion of the fluctuating strain, $s^*_{jj} = 0$, which contains solenoidal and compressible contributions $s^*_{ij} = s^{*I}_{ij} + s^{*C}_{ij}$, where, of course, $s^{*I}_{ij} = s^I_{ij}$. This is done for ease of presentation; in the nomenclature of Sec. II these quantities would, of course, be represented by $S^*_{ij}(u'')$ a precision unnecessary for the present discussion. Thus one can write

$$\overline{ps_{ij}} = \overline{ps^*_{ij}}^{\,I} + \overline{ps^*_{ij}}^{\,C} + \frac{2}{3}\overline{pd}\,\delta_{ij}. \tag{30}$$

The term $\overline{ps^*_{ij}}^{\,I}$ is closed using standard incompressible pressure-strain closures. The pressure-dilatation is closed using models already in the literature, see Sec. III.B below. In Sec. III.A an expression for $\overline{ps^{*C}_{ij}}$ has been obtained.

As has already been discussed in energetic approaches, the pressure-dilatation cannot account for the suppression of the turbulence by the reduction in the shear stress as is seen in compressible flows. A straightforward extension of the energetic approach to the second-order closure level implies

$$\overline{ps_{ij}} = \overline{ps^*_{ij}}^{\,I} + \frac{2}{3}\overline{pd}\,\delta_{ij}. \tag{31}$$

Such an expression, as is consistent with Refs. 13,18, is likewise unsuccessful in reducing the turbulence shear stress. As will be discussed further in Sec. V the pressure-dilatation is a small quantity and has a nominal effect, for $\alpha \approx 1$, on the turbulence stresses and energy when it is included in the spherical portion of the pressure-strain. Our procedure, using the pressure-dilatation, produces an expression for the compressible contribution to the deviatoric portions of the pressure strain, $\overline{ps^*_{ij}}^{\,C}$. In fact, as was born out by computational experiments, had the expression

$$\overline{ps_{ij}} = \overline{ps^*_{ij}}^{\,I} + \overline{ps^*_{ij}}^{\,C} \tag{32}$$

[without $\overline{pd}$ on the diagonal] been used in the numerical investigations reported in Sec. V, our results would not have changed much, for $\alpha < 1$.

2. Pressure-dilatation models

To obtain the final form of the pressure-strain an expression for $\overline{pd}$ is required. There are some choices. Some proposals for $\overline{pd}$ require the solution of transport equations for the density variance[5] or pressure variance.[7] There are two pressure-dilatation models[8,38] that do not require separate equations. The model of Sarkar[38] is:

$$\frac{1}{2}\Pi_{pp} = \overline{p'd} = -3\chi_1 M_t^2\left[\frac{2}{3}\left(\frac{1}{\sqrt{3}M_t} - 8\frac{\chi_3}{\chi_1}\right)\overline{\rho}\langle k\rangle S_{pp} + \frac{P}{\sqrt{3}M_t} - \frac{\chi_2}{\chi_1}\overline{\rho}\,\overline{\epsilon}_s\right] \tag{33}$$

where $\chi_1 = 0.15$, $\chi_2 = 0.2$, and $\chi_3 = 0$ (still to be determined by the author). Note that the model as we have grouped the terms makes it appear as if it is singular in M_t; it is most definitely not singular. The model of Ristorcelli[8] is

$$\overline{p'd} = -\chi M_t^2[P - \overline{\rho}\,\overline{\epsilon} + T_k - \frac{3}{4}M_t^2\gamma(\gamma-1)(P_T + \overline{\rho}\,\overline{\epsilon} + T_T)] \\ -\overline{\rho}\langle k\rangle M_t^2\chi'\frac{D(3\sigma^2+5\omega^2)}{Dt} \tag{34}$$

where

$$\chi = \frac{2I_{pd}}{1+2I_{pd}M_t^2+\frac{2}{3}I_{pd}M_t^4\gamma(\gamma-1)}, \quad \chi' = \frac{I_{pd}^r}{1+2I_{pd}M_t^2+\frac{2}{3}I_{pd}M_t^4\gamma(\gamma-1)}, \\ I_{pd} = \frac{2}{3}I_1^s + I_{pd}^r\left[3\sigma^2+5\omega^2\right], \qquad I_{pd}^r = \frac{1}{30}\left(\frac{2}{3}\right)^3\alpha^2 I_1^r. \tag{35}$$

Here α is the proportionality constant in the Kolmogorov scaling; we return to this in more detail below. In the above expression, T_T is the transport of the mean temperature including effects such as heat flux and the turbulent or pressure transport. The production term P_T, contains the mean pressure dilatation and the mean dissipation with positive sign (heat release term). These two models, as well as a third (the Aupoix model), have been discussed in Ref. 39.

The d_i are determined by the pressure-dilatation model. For the Sarkar model, one requires that

$$d_1 = \frac{8\chi_3 M_t^2}{3},\ d_2 = \frac{\chi_1 M_t}{2} \tag{36}$$

$$\frac{\mathcal{A}_{pp}}{2} = \chi_2 M_t^2\overline{\rho}\,\overline{\epsilon}_s. \tag{37}$$

For the Ristorcelli model one requires that

$$d_1 = \frac{\chi M_t^2}{3},\ d_2 = \frac{\chi M_t^2}{2} \tag{38}$$

$$\frac{\mathcal{A}_{pp}}{2} = \chi M_t^2[\overline{\rho}\,\overline{\epsilon} + \frac{3}{4}M_t^2\gamma(\gamma-1)(P_T+\overline{\rho}\,\overline{\epsilon})] - \overline{\rho}\langle k\rangle M_t^2\chi'\frac{D(3\sigma^2+5\omega^2)}{Dt}. \tag{39}$$

Transport terms have been neglected; this is necessary to obtain an algebraic closure [which requires homogeneity]. The compressibility of the turbulence will only be important where the turbulence energy is large [and thus also M_t], which is typically in regions of large production and where transport is not as important. Which is to say that transport is only of importance in the peripheral regions of simple flows – regions where the turbulence intensity is low, production low, and [therefore] the fluctuations are essentially incompressible.

B. The mass flux and pressure-acceleration closures

The models for mass fluxes have not undergone much development and their importance in a general flow is not fully understood. Judging from the equations one can infer that the mass flux will be important in accelerating flows with large density gradients. There has been some research on the mass flux: Taulbee and VanOsdol[5] solved its transport equations and Ristorcelli [40] showed how an algebraic model for the mass flux can be obtained from its transport equation:

$$\bar{\rho}\ \overline{u_i''} = \tau_u \left[\nu_0 \delta_{ij} + \nu_1 \tau_u \frac{\partial \langle u_i \rangle}{\partial x_j} + \nu_2 \tau_u^2 \frac{\partial \langle u_i \rangle}{\partial x_k} \frac{\partial \langle u_k \rangle}{\partial x_j} \right] \langle u_j'' u_p'' \rangle \frac{\partial \bar{\rho}}{\partial x_p} \tag{40}$$

where $\tau_u = M_t \tau / [1 + \frac{M_t \bar{\epsilon}}{2\bar{\epsilon}_s}(P/(\bar{\rho}\ \epsilon) - 1)]$. Here ν_0, ν_1 and ν_2 are the coefficients retrieved from the inversion of the matrix $G_{ij} = \delta_{ij} + \tau_u \frac{\partial \langle u_i \rangle}{\partial x_j}$: $\nu_0 = -(1 + I_{\mathbf{G}} + II_{\mathbf{G}})\nu_2$, $\nu_1 = (1 + I_{\mathbf{G}})\nu_2$, $\nu_2 = (1 + I_{\mathbf{G}} + II_{\mathbf{G}} + III_{\mathbf{G}})^{-1}$, the Roman numbers representing the invariants of **G**. Note that the leading order term is a gradient transport model. For an isotropic turbulence, an eddy viscosity formulation is possible. For the present set of simple benchmark shear flows, one does not expect the mass flux terms to be very important – the mean flow does not accelerate much. We shall use, for the sake of simplicity, the eddy viscosity form of the mass flux – the lowest order contribution in the polynomial given above. This is consistent with the gradient transport model used in Ref. 11.

The baroclinic dyad, a tensor product formed from the mean density and pressure gradients, is defined as

$$\mathcal{R}_{ij} = \frac{\partial \bar{\rho}}{\partial x_i} \frac{\partial \bar{p}}{\partial x_j} \tag{41}$$

and the mass flux/acceleration terms in the second-moment equations can then be written, using the leading order portion of Eq. (40) - equivalent to replacing the Reynolds stress by two thirds of turbulent kinetic energy times the Kronecker tensor, as

$$\mathcal{M}_{ij}^{*} = -\frac{1}{\bar{\rho}} \frac{2}{3} \tau_u \nu_0 \langle k \rangle (\mathcal{R}_{ij} + \mathcal{R}_{ji} - \frac{2}{3} \mathcal{R}_{pp} \delta_{ij}) = -\frac{1}{\bar{\rho}} \frac{2}{3} \tau_u \nu_0 \langle k \rangle R_{ij}^{*} \tag{42}$$

where $R_{ij}^{*} = \mathcal{R}_{ij} + \mathcal{R}_{ji} - \frac{2}{3} \mathcal{R}_{pp} \delta_{ij}$.

C. The compressible dissipation

There are several models available for the compressible dissipation.[4–6,8] Many of these models reflect certain assumptions regarding the importance of the compressible dissipation observed in early DNS of compressible turbulence. The compressible dissipation has since been found to be less important than originally believed. In fact, the low turbulent Mach number asymptotics[8] indicate it varies inversely with the Reynolds number and as a consequence is negligible in engineering flows, though perhaps not in low Reynolds number DNS. Compressible dissipation models are nonetheless included for completeness.

As the Taulbee and VanOsdol[5] compressible dissipation model requires additional transport equations, in the spirit of computational simplicity, that model will not be used. The closure proposed by Sarkar *et al.*[6] is based on ideas from linear acoustics and appears related to the initial value problem.[36] It can be written as

$$\overline{\epsilon}_c = 3\alpha_s \overline{\epsilon}_s M_t^2 \tag{43}$$

with $\alpha_s = 1.0$ from DNS of decaying compressible turbulence; unfortunately this arrangement was deemed to lack universality.[19] Zeman[4] provides a model on the grounds that eddy shocklets occur in high speed flow and relating this assumption to the dilatational dissipation:

$$\overline{\epsilon}_c = 0.75(1 - \exp\{-[(\frac{3}{2}(1+\gamma)M_t - 0.1)/0.6]^2\})\epsilon_s \tag{44}$$

It has been shown by Blaisdell *et al.*[41] that Zeman's model gives incorrect scaling between ϵ_s and ϵ_c. Besides, the exponential dependence on M_t^2 delivers a steeper growth rate reduction compared to other models.

As has been mentioned in more recent DNS studies,[9,14,15,42] have demonstrated that dilatational covariance closures with a M_t^2 scaling predict effects of compressibility when they are, in fact, very small. In an asymptotic analysis, Ristorcelli[8] has found that the compressible dissipation has an M_t^4 dependence and is inversely proportional to the turbulent Reynolds number:

$$\begin{aligned}\overline{\epsilon}_c = \Bigg\{ &\frac{16}{3\alpha_r^2}\left[I_2^s + 6I_1^s I_3^s\right] + \left(\frac{2}{5}\right)^5 \tau^2 \left[3\sigma^2 + 5\omega^2\right] \cdot \\ &\left[\frac{3}{5}I_3^r + \left(\frac{1}{15}\right)^2 \left[13\sigma^2 + 15\omega^2\right] \tau^2 \alpha_r^2 I_1^r\right]\Bigg\} \frac{M_t^4}{R_t}\overline{\epsilon}_s .\end{aligned} \tag{45}$$

The parameters are $I_1^s = 0.3$, $I_2^s = 13.768$, $I_3^s = 2.623$, $I_1^r = 1.392$, $I_3^r = 3$ and $\alpha_r = 0.4 - 4$ is the Kolmogorov scaling coefficient. Also, M_t denotes the turbulent Mach number, that is $M_t^2 = \frac{2}{3}\langle k\rangle/c^2$ and R_t the turbulent Reynolds number $R_t = \overline{\rho}4\langle k\rangle^2/(9\epsilon_s\mu)Re$. The local speed of sound is given by $c^2 = T/M^2$. For high Reynolds number flows, in the absence of wall effects, viscous diffusion is negligible.

As this article focuses on a closure for the Reynolds stresses, the turbulent temperature flux and its transport equation modeling is not presented here. The reader is referred to the thesis of Adumitroaie[37] for a treatment of the thermodynamic modeling issues. It should be made clear that the findings, for the classes of flows with which we are concerned with in this article, are insensitive to the turbulent temperature flux modeling. For simple unidirectional shear flows without strong heat transfer effects the difference between a second-order closure and an eddy viscosity closure is negligible. This cannot be expected to be true for more complex flows.

At this point the Reynolds stress equations have been closed and it is possible to compute the flow using a second-order closure. Such computations are the subject of Sec. V. There are, however, a wide class of engineering flows that can be computed using simple algebraic Reynolds stress models. An algebraic closure for the Reynolds stresses is now developed.

IV. A compressible algebraic Reynolds stress model

A quasi-explicit algebraic model for the Reynolds stresses is now derived. An algebraic Reynolds stress model comes from the fixed point solution of the evolution equations for the anisotropy tensor. These equations can be thought of as describing a turbulence in a state of structural equilibrium:

the fixed point solution corresponds to an exact solution of the Reynolds stress equations.

Several permutations of quasi-explicit algebraic Reynolds stress expressions exist.[20-28] The qualifier "quasi-explicit" is used to indicate that, as the fixed point equations are nonlinear, the solution is given implicitly. A notable exception is the recent explicit algebraic model of Girimaji[28] who has found the exact *nonlinear* solution to the fixed point equations. The inception of our work predates[28] and our procedure follows precedents set by.[20,21,26] The polynomial representation methods will be used to obtain two-dimensional and three-dimensional versions of the algebraic turbulent stress models.

The method of algebraic stress modeling introduced by Taulbee[21] is used. This involves the *ansatz*

$$\frac{D}{Dt}\left[\frac{a_{ij}}{\tau\sigma}\right] = 0, \tag{46}$$

which allows relaxation effects to be built into the Reynolds stress model. Equation (46) allows a relaxation of the anisotropy to its equilibrium value at the same rate that the relative strain reaches its equilibrium value.[21] The major improvement due to the formulation in Eq. (46) comes at small applied strains. It can be shown that Eq. (46) produces a stress model consistent with the weak strain expansion of the Reynolds stress equations; the usual algebraic stress modeling *ansatz*, $\frac{D}{Dt}\, a_{ij} = 0$ does not.

The combination of transport terms in Eq. (17) is set to zero following established algebraic stress modeling procedures:

$$\frac{1}{\langle k\rangle}\left[\frac{\partial T_{ijk}}{\partial x_k} - \frac{\langle u_i'' u_j''\rangle}{\langle k\rangle}\frac{\partial T_k}{\partial x_k}\right] - \frac{a_{ij}}{\langle k\rangle}\left[\frac{\partial T_k}{\partial x_k} - \tau\frac{\partial T_k^{\epsilon}}{\partial x_k}\right] = 0. \tag{47}$$

Applying these approximations results in a quasi-linear tensor expression for the anisotropy.

If $b_1 = \frac{8}{5} - \frac{2}{5}d_1$, $b_2 = \frac{1}{\overline{\rho}^2}\frac{2}{3}\tau_u\nu_0$, $b_3 = C_3 - 2d_2$, $b_4 = C_4 + 2d_2$, and

$$g = \left[C_1\frac{\overline{\epsilon}}{\overline{\epsilon}_s} + C_{\epsilon_2} - 2 + (2 - C_{\epsilon_1})\frac{P}{\overline{\rho}\,\overline{\epsilon}_s} + \frac{\tau}{\sigma}\frac{D\sigma}{Dt} + \frac{2\tau}{3}(1 - 2d_2)S_{pp}(\langle u\rangle) + 2\frac{\mathcal{M} + \overline{p'd} - \overline{\rho}\,\overline{\epsilon}_c}{\overline{\rho}\,\overline{\epsilon}_s}\right]^{-1} \tag{48}$$

the algebraic fixed point form of the Reynolds stress anisotropy equation is written

$$\mathbf{a} = -g\tau\left[b_1\mathbf{S}^* + b_2\mathbf{R}^* + b_3\left(\mathbf{a}\mathbf{S}^* + \mathbf{S}^*\mathbf{a} - \frac{2}{3}\{\mathbf{a}\mathbf{S}^*\}\delta\right) - b_4(\mathbf{a}\boldsymbol{\Omega} - \boldsymbol{\Omega}\mathbf{a})\right] \tag{49}$$

where the curly braces signify the trace. From this expression it is seen that the anisotropy tensor

$$a_{ij} = a_{ij}(\mathbf{S}^*, \boldsymbol{\Omega}, \mathbf{R}^*) \tag{50}$$

is dependent on three second order tensors, two symmetric and one skew-symmetric.

A. A three-dimensional algebraic Reynolds stress model

Standard representation theory methods can be applied to obtain the solution $a_{ij} = a_{ij}(\mathbf{S}^*, \boldsymbol{\Omega}, \mathbf{R}^*)$ to Eq. (49). In contrast to the incompressible case the solution of Eq. (49) is now much more difficult inasmuch as the procedure now involves an additional tensor. Following standard methods the solution can be expressed as a finite 3-D tensor polynomial,

$$\mathbf{a} = \sum_{\lambda} C^{\lambda} T^{\lambda} \tag{51}$$

comprised of a linear combination of all the independent tensor products (generators) formed from the three primary tensors. The coefficients in the polynomial are functions of the independent invariants of the tensors. For this problem the dimension of the [minimal] tensor base is $\lambda = 41$ (cf. Spencer[43]). This is very large and is unlikely to be used in practice.

The complexity presented by such a large tensor basis can be side stepped by simplifying approximation regarding the b_3 term. It has been argued[21,27] that for the range of values used for the constant C_2 the inequality $C_3 \ll C_4$ holds and thus the term multiplied by C_3 will only have a small effect on the solution. This approximation decouples the contributions of $\mathbf{S}^*$ and $\mathbf{R}^*$ to $\mathbf{a}$. As the equation is linear the solution is determined using the superposition principle. This one allows to split the problem into two equations of lower tensor base dimension:

$$\mathbf{a} = \mathbf{a}^S + \mathbf{a}^R \tag{52}$$

where $\mathbf{a}^S$ stands for the solution dependent on $\mathbf{S}^*$,

$$\mathbf{a}^S = -g\tau \left[b_1 \mathbf{S}^* - b_4 (\mathbf{a}^S \boldsymbol{\Omega} - \boldsymbol{\Omega} \mathbf{a}^S) \right] \tag{53}$$

and $\mathbf{a}^R$ denoting the solution dependent on $\mathbf{R}^*$

$$\mathbf{a}^R = -g\tau \left[b_2 \mathbf{R}^* - b_4 (\mathbf{a}^R \boldsymbol{\Omega} - \boldsymbol{\Omega} \mathbf{a}^R) \right]. \tag{54}$$

The decomposition of $\mathbf{a}$ into portions dependent on $\mathbf{S}^*$ and $\mathbf{R}^*$ is unique.

Applying the results from Ref. 21 the strain dependent portion of the solution for the anisotropy tensor can be written

$$\begin{aligned} \mathbf{a}^S = & -2C_\mu \tau \mathbf{S}^* - 4\alpha_2 \tau^2 (\mathbf{S}^* \boldsymbol{\Omega} - \boldsymbol{\Omega} \mathbf{S}^*) - 8\alpha_3 \tau^3 (\boldsymbol{\Omega}^2 \mathbf{S}^* + \mathbf{S}^* \boldsymbol{\Omega}^2 - \frac{2}{3} \{\mathbf{S}^* \boldsymbol{\Omega}^2\} \boldsymbol{\delta}) \\ & -16\alpha_4 \tau^4 (\boldsymbol{\Omega} \mathbf{S}^* \boldsymbol{\Omega}^2 - \boldsymbol{\Omega}^2 \mathbf{S}^* \boldsymbol{\Omega}) - 32\alpha_5 \tau^5 \{\mathbf{S}^* \boldsymbol{\Omega}^2\} (\boldsymbol{\Omega}^2 - \frac{1}{3} \{\boldsymbol{\Omega}^2\} \boldsymbol{\delta}) \end{aligned} \tag{55}$$

where $C_\mu = b_1 g (1 + \frac{7}{2} h_0^2 \omega^2) h_1$, $\alpha_2 = \frac{1}{2} b_1 b_4 g^2 h_2$, $\alpha_3 = \frac{3}{4} b_1 b_4^2 g^3 h_1$, $\alpha_4 = -\frac{3}{8} b_1 b_4^3 g^4 h_1$, $\alpha_5 = \frac{3}{8} b_1 b_4^4 g^5 h_1$, $h_0 = b_4 g \tau$, $h_1 = h_2 [1 + 2h_0^2 \omega^2]^{-1}$ and $h_2 = [2 + h_0^2 \omega^2]^{-1}$.

Using a similar procedure the portion of the Reynolds stress anisotropy dependent on the baroclinic dyad is written

$$\begin{aligned} \mathbf{a}^R = & -2C_\mu \tau \mathbf{R}^* - 4\alpha_2 \tau^2 (\mathbf{R}^* \boldsymbol{\Omega} - \boldsymbol{\Omega} \mathbf{R}^*) - 8\alpha_3 \tau^3 (\boldsymbol{\Omega}^2 \mathbf{R}^* + \mathbf{R}^* \boldsymbol{\Omega}^2 - \frac{2}{3} \{\mathbf{R}^* \boldsymbol{\Omega}^2\} \boldsymbol{\delta}) \\ & -16\alpha_4 \tau^4 (\boldsymbol{\Omega} \mathbf{R}^* \boldsymbol{\Omega}^2 - \boldsymbol{\Omega}^2 \mathbf{R}^* \boldsymbol{\Omega}) - 32\alpha_5 \tau^5 \{\mathbf{R}^* \boldsymbol{\Omega}^2\} (\boldsymbol{\Omega}^2 - \frac{1}{3} \{\boldsymbol{\Omega}^2\} \boldsymbol{\delta}) \end{aligned} \tag{56}$$

in which the coefficients have the same form as those in $\mathbf{a}^S$ with the exception that b_1 is replaced by b_2. To obtain the full anisotropy tensor the two complex expressions Eq. (55) and Eq. (56) need to be added. In the light of the complexity of the three-dimensional formalism a two-dimensional formalism is developed.

B. A two-dimensional algebraic Reynolds stress model

A simpler and tractable two-dimensional treatment is possible. In many engineering flows the mean flow and the statistics of the turbulence are two-dimensional. The two-dimensional problem is less complicated as the number of tensor products necessary to express the solution is substantially reduced. The symbols $\mathbf{S}, \mathbf{\Omega}, \mathbf{R}$ now denote two-dimensional tensors.

It is necessary to recast the equation for the anisotropy in terms of the traceless 2-D tensors: $\underline{S}^\star_{ij}(\langle u\rangle) = S_{ij}(\langle u\rangle) - \frac{1}{2}S_{pp}(\langle u\rangle)\delta^{(2)}_{ij}$, $\underline{R}^\star_{ij}(\overline{\rho}, \overline{p}) = R_{ij}(\overline{\rho}, \overline{p}) - \frac{1}{2}R_{pp}(\overline{\rho}, \overline{p})\delta^{(2)}_{ij}$. Here, the two-dimensional Kronecker symbol is $\delta^{(2)} \equiv [\delta^{(2)}_{ij}] = 1$ for $i = j = 1, 2$ and 0 otherwise. The pressure-strain model is then written:

$$
\begin{aligned}
\Pi^\star_{ij} - \overline{\rho}\ \epsilon^\star_{ij} = -C_1\overline{\rho}\ \overline{\epsilon} a_{ij} + \overline{\rho}\langle k\rangle \Bigg[\left[\frac{4}{5} + \frac{2}{5}d_1\right] \underline{S}^\star_{ij}(\langle u\rangle) + \\
[1 - C_3 + 2d_2]\left[a_{ip}\underline{S}^\star_{pj}(\langle u\rangle) + \underline{S}^\star_{ip}(\langle u\rangle)a_{pj} - \frac{2}{3}\underline{S}^\star_{pq}(\langle u\rangle)a_{pq}\delta_{ij}\right] - \\
[1 - C_4 - 2d_2][a_{ip}\underline{\Omega}_{pj}(\langle u\rangle) - \underline{\Omega}_{ip}(\langle u\rangle)a_{pj}] + \\
\frac{4}{3}d_2 S_{pp}(\langle u\rangle)a_{ij} - \left[\frac{4}{5} + \frac{2}{5}d_1\right] S_{pp}(\langle u\rangle)\left[\frac{\delta_{ij}}{3} - \frac{\delta^{(2)}_{ij}}{2}\right] - \\
2[1 - C_3 + 2d_2]\left[a_{ip}\left(\frac{\delta_{pj}}{3} - \frac{\delta^{(2)}_{pj}}{2}\right) - \frac{1}{3}a_{pq}\left(\frac{\delta_{pq}}{3} - \frac{\delta^{(2)}_{pq}}{2}\right)\delta_{ij}\right] S_{kk}(\langle u\rangle)\Bigg].
\end{aligned} \tag{57}
$$

The pressure acceleration is written

$$
\mathcal{M}^\star_{ij} = -\frac{1}{\overline{\rho}}\frac{2}{3}\tau_u\nu_0\langle k\rangle \underline{R}^\star_{ij} + \frac{1}{\overline{\rho}}\frac{2}{3}\tau_u\nu_0\langle k\rangle R_{pp}\left[\frac{\delta_{ij}}{3} - \frac{\delta^{(2)}_{ij}}{2}\right]. \tag{58}
$$

The fact that both 2D and 3D expressions of the pressure-strain correlation model must give the same result when applied to two-dimensional mean flows will be used for our simplifications. Recasting the model in 2D is done to take advantage of the simplifications that result from the 2D structure.

Inserting the closures for the pressure-strain and mean acceleration terms, Eqs. (57), (58) into the Reynolds stress equation, using the same *ansatz* regarding transport at a fixed point, the 2D analog of Eq. (49) is obtained:

$$
\begin{aligned}
\mathbf{a} = -g\tau\Bigg[b_1\underline{\mathbf{S}}^\star + b_2\underline{\mathbf{R}}^\star + b_3\left(\mathbf{a}\underline{\mathbf{S}}^\star + \underline{\mathbf{S}}^\star\mathbf{a} - \frac{2}{3}\{\mathbf{a}\underline{\mathbf{S}}^\star\}\boldsymbol{\delta}\right) - b_4\left(\mathbf{a}\underline{\mathbf{\Omega}} - \underline{\mathbf{\Omega}}\mathbf{a}\right) \\
-b_5\left(\frac{\boldsymbol{\delta}}{3} - \frac{\boldsymbol{\delta}^{(2)}}{2}\right) - b_6\left(\mathbf{a}\left(\frac{\boldsymbol{\delta}}{3} - \frac{\boldsymbol{\delta}^{(2)}}{2}\right) - \frac{1}{3}\left\{\mathbf{a}\left(\frac{\boldsymbol{\delta}}{3} - \frac{\boldsymbol{\delta}^{(2)}}{2}\right)\right\}\boldsymbol{\delta}\right)\Bigg]
\end{aligned} \tag{59}
$$

with

$$b_1 = \frac{8}{5} - \frac{2}{5}d_1, \quad b_2 = \frac{1}{\overline{\rho}^2}\frac{2}{3}\tau_u\nu_0, \quad b_3 = C_3 - 2d_2, \quad b_4 = C_4 + 2d_2,$$
$$b_5 = b_1 S_{pp}(\langle u\rangle) + b_2 R_{pp}(\overline{\rho}, \overline{\mathrm{p}}), \quad b_6 = 2b_3 S_{pp}(\langle u\rangle) \tag{60}$$

and g having the same expression as in the 3-D algebraic equation. The two-dimensional polynomial solution of Eq. (59) is, as before, also written as

$$\mathbf{a} = \sum_{\lambda} C^{\lambda} T^{\lambda}. \tag{61}$$

Unlike the three-dimensional solution, however, the generators now consist of only five tensor groups:

$$\mathbf{T}^0 = \frac{\delta}{3} - \frac{\delta^{(2)}}{2}, \quad \mathbf{T}^1 = \underline{\mathbf{S}}^*, \quad \mathbf{T}^2 = \underline{\mathbf{S}}^*\underline{\boldsymbol{\Omega}} - \underline{\boldsymbol{\Omega}}\underline{\mathbf{S}}^*, \quad \mathbf{T}^3 = \underline{\mathbf{R}}^*, \quad \mathbf{T}^4 = \underline{\mathbf{R}}^*\underline{\boldsymbol{\Omega}} - \underline{\boldsymbol{\Omega}}\,\underline{\mathbf{R}}^* \tag{62}$$

for which there are five non-zero independent invariants,

$$\sigma^2 = \{\underline{\mathbf{S}}^{*2}\}, \quad \omega^2 = -\{\underline{\boldsymbol{\Omega}}^2\}, \quad \{\underline{\mathbf{R}}^{*2}\}, \quad \{\underline{\mathbf{R}}^*\underline{\mathbf{S}}^*\}, \quad \{\underline{\mathbf{S}}^*\underline{\mathbf{R}}^*\underline{\boldsymbol{\Omega}}\}. \tag{63}$$

The fact that there are no other independent tensor generators [or invariants] can be verified using the 2 × 2 matrix identity:

$$\begin{aligned} 2\mathbf{abc} = \mathbf{bc}\{\mathbf{a}\} + \mathbf{a}\{\mathbf{bc}\} + \mathbf{ac}\{\mathbf{b}\} - \mathbf{b}\{\mathbf{ac}\} + \mathbf{ab}\{\mathbf{c}\} + \mathbf{c}\{\mathbf{ab}\} - \\ \mathbf{c}\{\mathbf{a}\}\{\mathbf{b}\} - \mathbf{a}\{\mathbf{b}\}\{\mathbf{c}\} + (\{\mathbf{ac}\}\{\mathbf{b}\} - \{\mathbf{acb}\})\delta^{(2)}. \end{aligned} \tag{64}$$

To obtain the solution to the algebraic equations for the anisotropy tensor, Eq. (59), a procedure similar to the one devised by Pope[20] is used. Three 5 × 5 matrices $\mathcal{H}_{\eta}^{\lambda}$, $\mathcal{J}_{\eta}^{\lambda}$, $\mathcal{I}_{\eta}^{\lambda}$, are defined:

$$\begin{aligned} \mathbf{T}^{\eta}\underline{\mathbf{S}}^* + \underline{\mathbf{S}}^*\mathbf{T}^{\eta} - \frac{2}{3}\{\mathbf{T}^{\eta}\underline{\mathbf{S}}^*\}\delta &= \sum_{\lambda} \mathcal{H}_{\eta}^{\lambda}\mathbf{T}^{\lambda} \\ \mathbf{T}^{\eta}\underline{\boldsymbol{\Omega}}^* - \underline{\boldsymbol{\Omega}}^*\mathbf{T}^{\eta} &= \sum_{\lambda} \mathcal{J}_{\eta}^{\lambda}\mathbf{T}^{\lambda} \\ \mathbf{T}^{\eta}\left(\frac{\delta}{3} - \frac{\delta^{(2)}}{2}\right) - \frac{2}{3}\left\{\mathbf{T}^{\eta}\left(\frac{\delta}{3} - \frac{\delta^{(2)}}{2}\right)\right\}\delta &= \sum_{\lambda} \mathcal{I}_{\eta}^{\lambda}\mathbf{T}^{\lambda} \end{aligned} \tag{65}$$

for which $\lambda = 0 - 4$. The elements of the matrices are determined from the above equations by making use of matrix relations stemming from the Cayley-Hamilton theorem. The 2-D tensor polynomial $\mathbf{a} = \sum_{\lambda} C^{\lambda} T^{\lambda}$ is introduced in both sides of Eq. (59). By making use of the above matrix identities the coefficients of the tensor polynomials are found to satisfy the following system of equations:

$$C^{\lambda} = -g\tau\left[b_1\delta_{1\lambda} + b_2\delta_{3\lambda} + b_3\sum_{\eta} C^{\eta}\mathcal{H}_{\lambda}^{\eta} - b_4\sum_{\eta} C^{\eta}\mathcal{J}_{\lambda}^{\eta} - b_5\delta_{0\lambda} - b_6\sum_{\eta} C^{\eta}\mathcal{I}_{\lambda}^{\eta}\right]. \tag{66}$$

The solution of this system of equations determines the model coefficients in the following algebraic expression for the anisotropy tensor

$$\mathbf{a} = -2C_\mu \tau \left[\mathcal{Q}_2 \underline{\mathbf{S}}^\star + (\mathcal{Q}_1 + \mathcal{Q}_3) b_3 g f_2 \tau \sigma^2 \left(\frac{2}{3}\delta - \delta^{(2)} \right) + \mathcal{Q}_2 b_4 g f_1 \tau (\underline{\mathbf{S}}^\star \underline{\mathbf{\Omega}} - \underline{\mathbf{\Omega}}\ \underline{\mathbf{S}}^\star) \right]$$
$$-2C'_\mu \tau \left[\underline{\mathbf{R}}^\star + b_4 g f_1 \tau (\underline{\mathbf{R}}^\star \underline{\mathbf{\Omega}} - \underline{\mathbf{\Omega}}\ \underline{\mathbf{R}}^\star) \right] \tag{67}$$

suitable for two-dimensional mean flows. The eddy viscosities, C_μ and C'_μ, are given by:

$$C_\mu = \frac{b_1 g f_1 / 2}{1 - \frac{2}{3}(b_3 g \tau)^2 \sigma^2 f_1 f_2 + 2(b_4 g f_1 \tau)^2 \omega^2} \tag{68}$$

$$C'_\mu = \frac{b_2 g f_1 / 2}{1 + 2(b_4 g f_1 \tau)^2 \omega^2}. \tag{69}$$

The $\mathcal{Q}_i$ coefficients are given by

$$\mathcal{Q}_1 = 1 + \frac{b_2}{b_1} \left[\frac{\{\underline{\mathbf{S}}^\star \underline{\mathbf{R}}^\star\}}{\sigma^2} + 2 g f_1 \tau b_4 \frac{\{\underline{\mathbf{S}}^\star \underline{\mathbf{R}}^\star \underline{\mathbf{\Omega}}\}}{\sigma^2} \right] \tag{70}$$

$$\mathcal{Q}_2 = 1 + \frac{2}{3} \frac{(b_3 g \tau)^2 \sigma^2 f_1 f_2}{1 + 2(b_4 g f_1 \tau)^2 \omega^2} (\mathcal{Q}_1 - 1) - \frac{b_3 b_5}{3 b_1} g f_2 \tau \tag{71}$$

$$\mathcal{Q}_3 = -\frac{b_5}{b_1 b_3} \frac{1 + 2(b_4 g f_1 \tau)^2 \omega^2}{2 g f_1 \tau \sigma^2} \tag{72}$$

with $f_1 = (1 + b_6 g \tau / 6)^{-1}$ and $f_2 = (1 - b_6 g \tau / 6)^{-1}$. Note that the direct effect of compressibility as reflected in the baroclinic dyad occurs in $\mathcal{Q}_1$ and $\mathcal{Q}_2$.

The high order of nonlinearity of the algebraic equations does not permit, in general, the construction of a fully explicit solution. Instead, an iterative approach is employed during the computations to generate the correct values. The algebraic solution is linearized by lagging the turbulence production term which contains the nonlinearity.

C. Discussion

To conclude this section some general statements regarding the behavior of the algebraic closure derived for the Reynolds stresses are highlighted. In Sec. III a closure for the Reynolds stress equations was obtained. In the present section the fixed point solution of the modeled second moment equations, under the condition of structural equilibrium, was obtained. For two-dimensional mean flows the compressible algebraic stress model can be symbolically written as

$$\mathbf{a} = -\nu_{t0} \underline{\mathbf{S}}^\star - \nu_{t1} [\underline{\mathbf{S}}^\star \underline{\mathbf{\Omega}} - \underline{\mathbf{\Omega}}\ \underline{\mathbf{S}}^\star] - \nu_{t2} [\frac{2}{3}\delta - \delta^{(2)}] - \nu^c_{t0} \underline{\mathbf{R}}^\star - \nu^c_{t1} [\underline{\mathbf{R}}^\star \underline{\mathbf{\Omega}} - \underline{\mathbf{\Omega}}\ \underline{\mathbf{R}}^\star]. \tag{73}$$

Note that products of the mean strain and the baroclinic dyad do not appear. This is due, for two-dimensional flows, to the relation $\mathbf{T}^\eta \underline{\mathbf{S}}^\star + \underline{\mathbf{S}}^\star \mathbf{T}^\eta - \frac{2}{3}\{\mathbf{T}^\eta \underline{\mathbf{S}}^\star\}\delta = -2\{\mathbf{T}^\eta \underline{\mathbf{S}}^\star\}\mathbf{T}^0$; the generator comprised of the mean strain and baroclinic dyad product is redundant. Examining the above expression, the following observations can be made:

1. The first two terms are the same terms obtained in algebraic stress closure for two-dimensional [in the mean] incompressible flows.

2. The first two eddy coefficients are functions of the relative strain and the relative rotation as is the case in incompressible flows. They are now also functions of the turbulent Mach number and the gradient Mach number.
3. Neither of these eddy coefficients depend on baroclinic effects.
4. It is seen that in the absence of mean velocity gradients that the turbulence is anisotropic due to the mean baroclinic dyad. This anisotropy manifests itself in the deviatoric as well as diagonal terms.

It is useful to construct a simple example to see how the new effects influence the anisotropy. Consider a simple shear flow with a streamwise acceleration: let the Favré mean velocity, the mean density and the mean pressure gradients be represented by $U_{1,2}$, $U_{1,1}$, $\nabla\bar{\rho} = \bar{\rho}_{,2}$, and $\nabla P = P_{,1}$.

$$\begin{aligned}
a_{11} &= -\frac{2}{3}\nu_{t0}\,U_{1,1} + \frac{1}{2}\nu_{t1}\,U_{1,2}^2 + \frac{1}{3}\nu_{t2} + \nu_{t1}^c\,U_{1,2}\,\bar{\rho}_{,2}\,P_{,1} && (74)\\
a_{22} &= \frac{1}{3}\nu_{t0}\,U_{1,1} - \frac{1}{2}\nu_{t1}\,U_{1,2}^2 + \frac{1}{3}\nu_{t2} - \nu_{t1}^c\,U_{1,2}\,\bar{\rho}_{,2}\,P_{,1} && (75)\\
a_{33} &= \frac{1}{3}\nu_{t0}\,U_{1,1} - \frac{2}{3}\nu_{t2} && (76)\\
a_{12} &= -\frac{1}{2}\nu_{t0}\,U_{1,2} - \frac{1}{2}\nu_{t1}\,U_{1,2}\,U_{1,1} - \nu_{t0}^c\,\bar{\rho}_{,2}\,P_{,1} && (77)
\end{aligned}$$

Several observations regarding the above algebraic expression for the anisotropy can be made:

1. The expression is the first [that we know of] rigorous indication of the direct role the baroclinic dyad plays in determining the Reynolds stresses.
2. The expression indicates that, for arbitrary mean deformation, the mean baroclinic dyad contributes to the deviatoric portions of the Reynolds stress.
3. The expression also indicates that the baroclinic dyad also changes the relative magnitude of the normal stresses. This effect only occurs for mean deformations that are rotational. For an irrotational mean deformation the baroclinic dyad makes no contributions to the normal stresses.
4. For a uniform mean velocity the baroclinic dyad is a source contributing only to the deviatoric portions of the anisotropy tensor.
5. The expression indicates the inapplicability of any heuristic gradient transfer arguments for the Reynolds stresses in flows with important gradients of mean density and pressure.

While these results indicate the inapplicability of any form of eddy viscosity model for the stresses in compressible flows with arbitrary large density and pressure gradients some qualifications are in order. The presence of the baroclinic dyad is likely to be important only in rapidly accelerating aerodynamic flows or in combusting flows where one can expect the mass fluxes to be important. In the absence of these effects it appears that the parameterization of the Reynolds stresses in terms of powers of the mean deformation with modifications according to the compressibility of the fluctuations as those indicated in Sec. III is appropriate.

V. Computational investigations of free shear flows

The theory and results presented in the previous sections are now implemented over a very wide range of mean flow Mach numbers in the simulation of free shear flows. Simulations using second-order moment (SOM) closures as well as the quasi-explicit algebraic models are conducted. The numerical experiments are constructed with the intention of investigating several different issues of relevance to the prediction of compressible turbulent flows for engineering purposes.

In addition to assessing the sensitivity of the pressure-strain model to the different pressure-dilatation models we compare the computational results to what is expected from laboratory and numerical experiments. Of particular interest is the well known effect of compressibility on reduction of the spread rate of the mixing layer. The main objective is to assess the effectiveness of the compressibility corrections in reproducing the reduced growth rate of the free-shear layers with increasing Mach number - a phenomenon which is well documented experimentally.[44] We also study the adequacy of the algebraic stress closure with the results of the SOM simulations. In particular the Reynolds stresses and the anisotropy computed using both of these procedures are compared to solutions without the compressible corrections in order to assess the effects of the new pressure-strain closure on the anisotropy. Our intention is to further investigate the notion that the dramatic reduction of the mixing layer growth rate is due to the effects of compressibility on the pressure-strain and, consequently, its effect on the reduction of the turbulence shear stress.

A. Numerical method

The simulations are conducted using a finite difference scheme[45] second-order accurate in time and fourth-order accurate in space. The governing equations are integrated explicitly in time using the predictor-corrector finite difference scheme developed by Gottlieb and Turkel.[46] The Gottlieb-Turkel scheme is a higher order accurate variant of the MacCormack[47] predictor-corrector method. During a numerical sweep, the inviscid fluxes are alternatively differenced backward in the predictor step and forward in the corrector step. Fourth-order central differences are used for the viscous and heat flux terms as well as for the derivatives in the source vector. To maintain stability, it is required that the CFL number be less than 2/3. To prevent numerical oscillations in regions of large gradients a smoothing scheme devised by MacCormack and Baldwin[48] is employed. The method, as outlined in Ref. 45, adds artificial viscosity that is very small everywhere except in the regions where the pressure oscillates.

All simulations are conducted on a uniformly spaced grid in the computational domain. By means of a coordinate transformation the mesh is transversally compressed in the physical domain in the region corresponding to the mixing layer.

The physical domain is a rectangular box defined by the set of points (x, y), in which x represents the streamwise coordinate and y the transversal coordinate. The grid overlaying the computational domain of size $x\delta_\omega \times y\delta_\omega$ has 100×60 points, where the vorticity thickness $\delta_\omega = (u_1 - u_2)/(\partial\langle u\rangle/\partial y)_{max}$. In this nondimensionalization, the reference length scale is the magnitude of the vorticity thickness at the inlet. The initial profile for the mean axial velocity is adjusted such that the resulting nondimensional vorticity thickness at the inlet is equal to one. The values of the physical dimensions are $(x, y) = [80, 20]$ for the mixing layer. To evaluate the grid sensitivity the number of grid points is increased by a factor of 1.5. The change in the steady-state values of the peak of the turbulent stresses is less than 2 percent.

To accelerate convergence to the stationary state, a local time stepping technique is used. The convergence criterion is imposed so that the global averaged residual profile attained is stationary for each dependent variable. Although more stringent criteria can be sought, it is known,[49] that predictor-corrector schemes are limited in their ability to achieve very high rates of residual reduction.

Due to the nonlinearity of the destruction terms, the $k-\epsilon$ equations display a stiffness which can either generate numerical instabilities or increase the computational time. In order to avoid these inconveniences the turbulence source terms are treated implicitly. The $k-\epsilon$ destruction terms are decoupled by suitable manipulation of the ϵ/k ratio, treated as a known quantity from the previous time step.

Initial and boundary conditions The initial fields are obtained by propagating the inflow conditions throughout the entire domain; hence, the flow has to sweep the domain at least one time to obtain meaningful results. For ease of computation, the inflow initial conditions (IC) for the flow variables are assumed to be a smoothed step (hyperbolic tangents for the axial velocity or species) or a smoothed hat profile (for turbulence quantities). Uniform profiles are assigned at the inlet to the static pressure, to the static temperature and, by virtue of the equation of state, to the static density.

The boundary conditions (BC) are set according to the elliptic nature of the problem on all four boundaries. The inflow BC are fixed (Dirichlet) for all primary variables in the supersonic and subsonic regions with one exception. For the portions where the flow is subsonic the pressure is allowed to adjust to the characteristic waves through a Neumann boundary condition. At the outflow and outer boundaries zero gradient (Neumann) conditions are applied due to their non-reflective properties in relation with the outgoing waves. In the mixing layer, the static pressure, temperature and density in the two free stream layers are matched. This isolates the contributions to the layer growth to those due solely to the variation of the reference Mach number.

Free-shear flow parameters The magnitude of the effects of compressibility are often parameterized by the convective Mach number.[50] In our formulation the expression for the convective Mach number is $M_c = M(1-r_v)/2$, where $r_v = u_2/u_1$ is the axial velocity (u) ratio. A wide range of values of M_c including both subsonic and supersonic regimes are considered: $0.2 < M_c < 2.0$. The convective Mach number is varied by keeping the velocity ratio constant, $r_v = 1/2$, and varying the reference Mach number M. The reference Reynolds number is $Re = 5 \times 10^6$, while all other nondimensional parameters are kept constant. The subscript 1 refers to the high-speed stream value, while the subscript 2 refers to the low-speed stream value in the mixing layer. In the results presented, the spatial coordinate, for the hydrodynamic variables, is given by $\eta = \frac{y - y(\hat{u}=0.5)}{x}$, where $\hat{u} = \frac{\langle u \rangle - u_2}{u_1 - u_2}$. Only the mixing layer simulations are presented in this article. Simulations for the jet configuration can be found in Ref. 37.

After an initial period of flow development a linear growth rate of the shear layers is attained. In the fully developed regime, when a linear growth rate has been established, the mean velocity and the normalized Reynolds stresses display self-similar behavior. The spread rate of a turbulent shear layer, in the self-similar region, is conventionally expressed as $d\delta_u/dx = C_\delta(1-r_v)/(1+r_v)$ where δ_u could be either the 10 percent visual thickness of the shear layer based on the normalized velocity profile or the vorticity thickness, and C_δ is a constant (approximately). As the present article is concerned with compressible corrections to the turbulence moment equations no plots of the mean flow quantities are given; the mean field variables are quite typical and can be seen in the literature.[11,51,52]

Model calculations Computations are performed with several different forms of closures. The presentation of the results is much clearer if we designate precisely what equations are used for what calculations. The central methodology is based on the models of Ristorcelli.[8] Thus KE-Rist represents the $k-\epsilon$ model equations Eqs. (4, 5, 6, 7, 18, 20), with the Ristorcelli compressible closures Eqs. (34, 45). KE-Sarkar denotes the $k-\epsilon$ model equations, with the Sarkar compressible closures Eqs. (33, 43). KE-Zeman is the $k-\epsilon$ model equations, with the Zeman compressible closure Eq. (44). ARSM denotes the $k-\epsilon$ model equations Eqs. (4, 5, 6, 7, 18, 20), with the 2-D ARSM compressible closures Eqs. (38, 48, 60, 67-72). ARSM-Sarkar denotes the $k-\epsilon$ model equations, with the 2-D ARSM compressible closures Eqs. (36, 48, 60, 67-72). SOM represents the second order model equations Eqs. (4, 5, 6, 7, 15, 20), with the compressible closures Eqs. (28, 38, 42).

B. Mixing layer simulations

The primary concerns of this article are with 1) a representation of the effects of compressibility as they appear in the pressure-strain covariance and 2) the construction of an algebraic Reynolds stress model useful for engineering calculations. Studies related to both these issues, for the $M_c = 1.07$ mixing layer configuration, are shown in the first two figures. The Reynolds stresses and the production/dissipation ratio obtained for ARSM and SOM calculations are shown in Figs. 1 and 2. Also shown, as a double check, are curves based on an *a priori* evaluation of the algebraic stress model; the data from a SOM calculation is used as input to the ARSM. The neglect of turbulent transport in the algebraic stress model is reflected in differences in the normal stresses at the centerline. In general the *a priori* evaluated ARSM curves follow closely the computed ARSM values indicating that for this flow the neglect of transport in the moment transport equations is justified. The algebraic approximation is, as has been verified at several different convective Mach numbers, suitable for an investigation of trends in this flow configuration.

Also shown in Figs. 1 and 2 is the SOM computation without compressibility corrections [NC - no compressibility], *i.e.* d_1 and d_2 are set to zero. The effect of the compressibility corrections manifest themselves as decreases in the centerline values of $\langle uu\rangle, \langle uv\rangle$ and $\langle vv\rangle$ of approximately 16%, 25% and 24% respectively. This is consistent with that seen in DNS. In addition, the streamwise normal stress suffers a smaller reduction than the other Reynolds stresses. This, as will be seen, will manifest itself in an increase in the streamwise normal anisotropy.

The production/dissipation ratio is shown in the bottom of Fig. 2. The average level of P/ϵ for the compressible case is smaller than the incompressible case; this is consistent with the reduced turbulent kinetic energy of the compressible flow. While the overall level of the production is smaller it is interesting to note that at one location in the mixing layer, the centerline, P/ϵ is nominally higher. It has been conjectured that this might be due to the higher relative strain rates compressible flows may be able to sustain. This is an issue that further DNS may resolve.

Figure 3 displays the vorticity thickness. Vorticity thickness spread rates as predicted by the SOM simulations, with and without (NC) the compressibility correction, are shown on the top of Fig. 3. It is seen, that even with such modest contributions from compressibility, scaling as they do with M_t^2, a sizable change in growth rate is seen. The variation of M_t with M_c is shown in Fig. 5.

Figure 3 also displays the different components of the pressure-strain tensor computed from the SOM simulation with and without (NC) the compressibility correction. The different components of the pressure-strain are all reduced by about the same amount. This is precisely the behavior seen, in both direction and magnitude, in the recent DNS[15] – see figure 4.18 from Ref. 15.

Reynolds stress anisotropy In Fig. 4 the computed values of the centerline Reynolds stress anisotropies are shown. At low values of compressibility the anisotropy has values similar to that of simple incompressible shears. At higher levels the anisotropy behaves very much like the compressible shear DNS; more of the energy of the turbulence is in the streamwise component as made clear by the increase in a_{11}. This is at the expense of the crosstream component, $\langle vv \rangle$, which is reduced. This is, as shall be discussed further, due to the reduction of intercomponent energy transfer due to the compressible aspect of the pressure-strain. There is also a reduction in the shear stress as is seen in compressible DNS.

Comparison with laboratory Reynolds stresses The effects of the new compressible models on the anisotropy is shown in Fig. 4. Unfortunately, in the laboratory situation, the spanwise Reynolds stresses are rarely measured. As a consequence the anisotropy is not known and one returns to primitive variables.

The maximum values of diverse Reynolds stresses in the mixing layer are plotted as function of the convective Mach number in Fig. 4. In this figure σ_u and σ_v represent, respectively, the $\langle uu \rangle$ and $\langle vv \rangle$ Reynolds stresses nondimensionalized by the square of the velocity difference across the layer. Also shown are the experimental results of Elliot and Samimy.[53] Underlying this comparison is, of course, the implicit assumption of self-similarity. The maximum Reynolds stresses decrease with compressibility. In the present simulations, however, the peak values of the turbulence intensities (axial and transverse) do not vary as strongly as in the laboratory findings of Goebel and Dutton.[54] In fact the present simulations are closer to the results of either Ref. 54 or Ref. 53 than either Ref. 54 or Ref. 53 *are to each other.*

There appears to be a discrepancy. A survey of the diverse compressible DNS indicates that a_{11} increases with compressibility. This implies that $\langle uu \rangle$ decreases more slowly than $\langle vv \rangle$. [Figure 9 of Ref. 14 is the most comprehensive presentation of this trend.] This does not appear to be the case in all laboratory experiments. In the mixing layer of Ref. 53 $\langle uu \rangle$ decreases more rapidly than $\langle vv \rangle$ for all M_c implying that a_{11} decreases with increasing compressibility contrary to DNS results. In Ref. 54 $\langle uu \rangle$ decreases more rapidly than $\langle vv \rangle$ for low M_c; while at moderate M_c, $\langle uu \rangle$ decrease less rapidly than $\langle vv \rangle$ in accord with DNS results. No explanation for this discrepancy between laboratory and numerical data is known.

The pressure-strain tensor The effects of compressibility on the Reynolds stresses are believed to be the source of the dramatic influence on the spread rate as the convective Mach number increases. The physical mechanisms responsible for these phenomena were once believed to be the compressible dissipation and pressure-dilatation which caused a decrease in the Reynolds stresses due to an overall decrease in k. This was accompanied by no substantial changes in the anisotropy. As discussed in Sec. I, recent simulations suggest that compressibility causes a turbulent shear stress reduction due to a reduction in its associated anisotropy. This is a statement that compressibility manifests itself structurally, not energetically. The reduction in the anisotropy leads, of course, to a reduction in k and ultimately in the mixing layer growth rate.

More recent simulations,[9,14–16] all seem to indicate that the major changes in the shear stress are due to the effect of compressibility on the pressure-strain covariance. Figure 6 is an illustration of this idea: Fig. 6 depicts the different components of pressure-strain tensor and its trace [the pressure dilatation] at the centerline of the mixing layer. Figure 6 is patterned after Vreman *et al.'s*[14] figures 3 and 9. The behavior of all the components of the pressure-strain, shown in Fig. 6, are very much in accord with the figures of Ref. 14. The only notable difference is the relative levels of Π_{22} and Π_{33}. The trends are very much the same and the relative behavior – a commensurate across the board reduction with M_c – is very much in accord with Ref. 15.

The behavior of the pressure-strain illustrated in Fig. 6 is very much in keeping with the current understanding of the mechanism for the reduction of the turbulence energy by the reduction of the shear stress: the only source for the kinetic energy is in the $\langle uu \rangle$ component and its production is proportional to $\langle uv \rangle$. The reduction [in magnitude] of Π_{11} and Π_{22} means that less energy generated in the $\langle uu \rangle$ equation is transferred to $\langle vv \rangle$ [by Π_{22}]. As $\langle vv \rangle$ has no production $\langle vv \rangle$ is much smaller. As consequence of the fact that the production of $\langle uv \rangle$ is proportional $\langle vv \rangle$ much less $\langle uv \rangle$ is produced and much less $\langle uu \rangle$ is produced. This can be seen by the considering the truncated forms of the second-order moment equations:

$$\frac{D}{Dt}\langle uu \rangle \sim -\langle uv \rangle U_{1,2} + \Pi_{11} + \dots \tag{78}$$

$$\frac{D}{Dt}\langle vv \rangle \sim \Pi_{22} + \dots \tag{79}$$

$$\frac{D}{Dt}\langle uv \rangle \sim -\langle vv \rangle U_{1,2} + \Pi_{12} + \dots \ . \tag{80}$$

The thesis of Freund[15] provides a schematic of the above process. The behavior of the Reynolds stresses and the pressure-strain indicated by Figs. 2 and 6 is consistent with the mechanism for the reduction just delineated. Specifically, the fact that less of the $\langle uu \rangle$ energy is transferred to the other components of the Reynolds stress means that the anisotropy, $a_{11} = 2b_{11}$, must increase as seen in all the DNS. Note also, as might be expected for a quasi-equilibrium flow, that the pressure-dilatation as derived by the asymptotic procedure in Ref. 8 is very small; negligible in comparison to the pressure-strain. Yet its use to obtain the deviatoric portions of the pressure-strain produces a very sizable reduction in the shear stress and the growth rate.

Gradient Mach number Sarkar[16] and earlier work cited therein have drawn attention to the gradient Mach number as a potentially useful parameterization of the effects of compressibility. Many of the effects of compressibility, as indicated by diverse DNS, have been observed to become more apparent as the gradient Mach number increases. Shown in the bottom of Fig. 5 is the gradient Mach number using the definition $M_g = \frac{2}{3} M_t \sigma \langle k \rangle / \epsilon_s$. The definition of the gradient Mach reflects the fact that the Kolmogorov scaling, $\epsilon \sim \langle k \rangle^{3/2}/\ell$ has been used to eliminate the length scale in the definition $M_g = \sigma \ell / c$. In DNS, the length scale ℓ is determined from the two-point correlation; no such opportunity occurs in single-point closures. Both the DNS, for example figure 4.29 in Ref. 15, and the SOM simulation indicate a similar decrease in rate of increase of M_g with M_c. The decrease seems to occur at lower M_c in the DNS. This is likely to be related to the different length scales used.

One of the noteworthy observations made of the effects of compressibility is their tendency to saturate.[11] In the bottom of Fig. 5 the rate of increase of the maximum turbulent Mach decreases at higher convective Mach numbers. This is in line with other observations.[11]

Kolmogorov scaling While in DNS a length can be determined from the two-point correlation, no such possibility exists for single-point closures. Yet a length scale, reflecting the two-point nature of the turbulence problem, as seen analytically in Ref. 8, is required. The length scale appearing in the Kolmogorov inertial range scaling, $\epsilon \sim \langle k \rangle^{3/2}/\ell$, was used in Ref. 8.

There is a proportionality coefficient, α, in the Kolmogorov scaling $\alpha = \bar{\epsilon}_s \ell/(2\bar{k}/3)^{3/2}$. For infinite Reynolds number isotropic turbulence $\alpha \sim 1$. For finite but large Reynolds number anisotropic turbulence undergoing deformation the Kolmogorov scaling is likely to be useful but α is likely to be a flow dependent quantity. Sreenivasan[55] has made some studies of the variation of the Kolmogorov scaling coefficient: he has found values of α ranging between $0.4 - 2$ for diverse incompressible simple shear flows. To allow for the expected variability of α two different values of are used in many of the simulations. The value of α does not change any of the trends and does not seem to have too strong an effect on the energy at the centerline (see Figs. 4 and 5). It does however effect the mixing layer spread rate as can be seen in Fig. 8.

Mixing layer growth rates Settles and Dodson[44] have compiled a very large number of experimental results.[50,54,56–61] These are shown in Figs. 7 and 8. The scatter in the data reflects the fact that different experiments are done in different wind tunnels, with different inlet configurations and with different reservoirs. The computational curves shown in Figs. 7 and 8 reflect two different but complementary investigations. As the "Langley curve"[62] has been a popular benchmark it has also been included. The well known reduction in the mixing rate with increasing M_c is seen in all the data.

Figure 7 reflects computations using the "energetic" approaches. A $k - \epsilon$ scheme has been used to calculate the mixing layer growth and the only compressible corrections are in the k equation; the Reynolds stresses are closed with the usual incompressible eddy viscosity [Boussinesq] approximation. Figure 7 indicates that the results based on the KE-Zeman and KE-Sarkar schemes capture the mixing layer reduction. The reduction of the mixing layer growth rate has been captured by similar mechanisms in both models; most of the suppression is provided by a substantial amount of additional dissipation that comes from the compressible dissipation models. As was pointed out in Sec. I, the compressible dissipation, as indicated by several DNS and by asymptotic analysis,[8] does not play an important role in these classes of flows. Any arbitrarily dissipative term added to the k equation, appropriately calibrated and scaled, can produce very good agreement for the mixing layer growth. Moreover, as with all energetic approaches, there is no possibility of accounting for the very important structural changes that appear in the anisotropy.

As indicated by Fig. 7 the pressure-dilatation model of Ristorcelli[8] by itself, with $\alpha = 2$, accounts for a nominal suppression of the growth rate. The compressible dissipation being negligible in analysis of Ristorcelli[8] is not included in this calculation. From incompressible DNS,[63] it can be argued that a value of $\alpha \approx 1$ might be more appropriate. As the pressure dilatation scales with α^2 a value of $\alpha \approx 1$ would decrease the pressure-dilatation effects by a factor of four.

Figure 8 reflects a computation using the compressible algebraic Reynolds stress model. This is exactly the same computation as given in the Fig. 7 with the exception that the algebraic Reynolds stress approximation now includes the effects of compressibility in the pressure-strain covariance. Note that there are substantial changes on the layer growth rate prediction. The change is more drastic for the ARSM modeling than the ARSM-Sarkar modeling; this is to be expected as the majority of the growth rate reduction using the earlier Sarkar modeling was built into a dissipative term (which does not contribute to the modeling of the pressure strain) and the relative change is small.

The algebraic model built upon dilatational closures of Ristorcelli[8] shows improvement over the results from a simple $k - \epsilon$ scheme. Figure 8 depicts the outcomes of the computations with the Ristorcelli [8] based algebraic closures for two values of the Kolmogorov scaling coefficient. The results for $\alpha = 0.4$ with both the pressure-strain and pressure-dilatation provide a modest decrease in the spread rate - matching that predicted with simply the pressure-dilatation with $\alpha = 2$. The ARSM calculation predictions are substantially reduced when $\alpha = 2$. If α were an undefined *ad hoc* constant one might be tempted to set it so as to match the reduction in spread rate indicated by the data. Given that little is known about α [though it is sure to be in the range 0.4-2.0 and most likely $\alpha \approx 1$] these issues must be explained by DNS.

It is concluded that the present pressure-strain modeling method based on the extension of the well-established incompressible procedure, in which the trace-free constraint is relaxed, does rationally account for a significant portion of the reduction in shear stress and growth rate. This procedure is considered a leading order contribution to the compressible turbulence shear stress problem. The possibility that additional compressible corrections to the pressure-strain, addressing physics not able to be accounted for using this constitutive relation methodology, may require consideration.

VI. Some issues in compressible turbulence modeling

In our effort to obtain a closure for the effects of compressibility a few issues, already alluded to, have become clearer. These issues are now highlighted.

The baroclinic dyad The procedure invoked to obtain the algebraic Reynolds model indicates that the baroclinic dyad is a source of turbulence. This, of course, can be anticipated by inspection of the second-order moment equations. The consequence is that an eddy viscosity representation for the Reynolds stresses is, from first principles, inappropriate for classes of flows in which the mass fluxes are important.

The presence of the baroclinic dyad is likely to be important only in rapidly accelerating aerodynamic flows such as through shocks or in hypersonic situations. The baroclinic dyad is also likely to be important in combusting flows where one can expect the mass fluxes to be important. In noncombusting supersonic flows it appears that a parameterization of the Reynolds stresses in terms of the mean deformation with modifications for the compressibility of the fluctuations as derived in Sec. III.A appears appropriate.

A length scale for single-point models of compressible turbulence In Ref. 8 the effects of the non-zero divergence of compressible turbulence was parameterized by several two-point integrals made nondimensional by a length scale. For single-point turbulence closures the length scale chosen is typically that appearing in the Kolmogorov scaling, $\epsilon \sim k^{3/2}/\ell$, which is often taken to be the integral length scale of the longitudinal correlation.

For compressible turbulence of interest to supersonic aerodynamic flows the cascade mechanism will be comprised of the usual nonlinear solenoidal modal interactions. The Kolmogorov scaling is expected to be valid in the weakly compressible limit. However, given the observed effect of compressibility on the length scale seen in simulations (see figure 4.28 of the recent report[15]) one might expect the coefficient of proportionality, α, to be a function of compressibility. That this might be the case is also suggested by the appearance of different instability modes in compressible flows. Studies similar to the incompressible studies shown in Ref. 63 appear to be both interesting and very relevant to issues of compressible turbulence modeling.

It should be understood that the Kolmogorov scaling coefficient, $\alpha = \bar{\epsilon}_s \ell/(2\bar{k}/3)^{3/2}$, is not a free parameter in the sense used in many turbulence model closures. The Kolmogorov constant appears in definite physical relationship having a precise mathematical definition, a clear interpretation in terms of flow physics, and substantial theoretical and numerical substantiation. It is, in principle, measurable for any flow. This in contrast to an *ad hoc* modeling constant; such a constant is often determined by calibrating the results of the model equations to some experimental data. Such a "calibration constant" has neither a precise mathematical definition or a clear interpretation in terms of flow physics and is dependent on the set of model equations used to compute the flow.

Experimental differences in numerical and laboratory data There appears to be a unanimous agreement in the DNS that, with increasing gradient or convective Mach number, a_{11} increases while a_{22} and a_{12} both decrease. This trend does not appear in the laboratory mixing layer experiments. At low M_c, $\langle uu \rangle$ appears to decrease more rapidly, with increasing compressibility, than $\langle vv \rangle$. This implies that a_{11} decreases with compressibility in contradistinction to DNS results. It is crucial to understand the cause for the differences between the DNS and the laboratory flows of the $\langle uu \rangle$ Reynolds stress behavior; turbulence models are based on intuition gleaned from DNS data but are used to predict engineering flows that are more similar to laboratory flows. The present computational results are closer to either of the laboratory experiments of Ref. 53 or Ref. 54 than the laboratory experiments of Ref. 53 or Ref. 54 are to each other. Earnest speculation on the source of the differences in the two experiments and facilities is required.

VII. Summary and conclusions

Progress towards the development of a compressible turbulence closure, starting at the level of second-order moment equations, has been described. Modeling from the second-order level accommodates important structural changes that appear in the anisotropy and are a feature and a function of compressibility. In the second-order moment equations the compressible contributions to the pressure-strain covariance have been obtained. The pressure-strain has been closed by assuming that, as is consistent with the weakly compressible limit, it can be modeled as a tensor polynomial linear in the Reynolds stresses. The difference from the incompressible case is that the trace of the compressible strain is not zero; it is set equal to the pressure-dilatation for which models exist. The compressible pressure-strain closure features a dependence on several turbulence descriptors: the turbulent Mach number, the relative strain, the gradient Mach number, the production and the dissipation. As a consequence the coefficients in the compressible pressure-strain closure are not constants but functions of parameters the turbulence and its compressibility.

In addition to devising a closure for the pressure-strain, a closure for the mean acceleration/mass flux terms appearing in the Reynolds stress equations has also been developed. For the flows studied in this article, limited as they are to the flows for which experimental data are available, the acceleration/mass flux moments are not important. The mass flux terms will be important in the combusting or hypersonic flows which motivated the thesis.[37] Further development of the mean acceleration terms requires experimental data for this class of flows.

Having closed the compressible Reynolds stress equations standard tensor representation theory has been used to produce a compressible algebraic Reynolds stress model useful for flows near structural equilibrium. A noteworthy feature of this portion of the work is that the role that the mean pressure and mean density gradients plays on the Reynolds stresses is immediately seen. As a consequence, it is seen that the baroclinic dyad can, in the absence of mean velocity gradients, contribute to the anisotropy of the turbulence. It is also seen that the mean bulk dilatation contributes to the anisotropy in a way that is quite different from an irrotational mean strain.

The mathematical results developed here have been implemented in mixing layer computations spanning a wide range of mean flow Mach numbers. In this article the discussion has been limited to the compressible mixing layer for which a sizable amount of literature exists. The calculations presented have been organized along two themes: 1) an investigation of the effects of compressibility as related to the compressible pressure-strain and the Reynolds stresses and 2) a validation of the algebraic Reynolds stress model predictions.

The computations with the compressible pressure-strain indicate that the present modeling [which does not have undefined tunable constants] produces precisely the behavior seen in the DNS[14,15]; there is a commensurate reduction, with increasing convective Mach number, of all the components of the compressible pressure-strain tensor. The changes in the pressure-strain lead, as is established by DNS of several different flows,[14-16] to changes in the anisotropy of the Reynolds stresses. The changes predicted by the modeling for the normal and shear anisotropies are very consistent, in trend, with DNS data and especially with the DNS of the mixing layer[14] — the flow configuration most similar to the one treated in this article. Comparison between the computational predictions and laboratory results for the Reynolds stress and their behavior with increasing compressibility is not as good as might be hoped. This is due to unknown experimental issues: the agreement between even the different laboratory experiments is poorer than the agreement between the numerical and experimental results.

All the laboratory data do however agree on the trend, with increasing compressibility, of the mixing layer growth rate and its kinetic energy: it decreases. The computational experiments conducted indicate that sizable reductions in the mixing layer growth rate accompany changes in the anisotropy of the turbulence due to the compressible aspects of the pressure-strain covariance.

Acknowledgments:

This work was performed while the first author was at the State University of New York at Buffalo. The first author is deeply indebted to Prof. Peyman Givi for his patient guidance, constant inspiration and for making this work possible. The financial support for the work at SUNY-Buffalo, provided by the NASA Langley Research Center under Grant NAG-1-1122 with Dr. J. Philip Drummond as the Technical Monitor is gratefully acknowledged. Support for the second author, while he was in residence at ICASE, under NASA Contract No. NAS1-19480 is acknowledged.

Appendix A

The Poisson equation for the fluctuating pressure is obtained by taking the divergence of the Navier-Stokes equations. Both instantaneous and averaged forms of these equations are necessary in the derivation. The subtraction of the mean equations from the instantaneous equations and simple term manipulations involving the continuity relation provide the desired Poisson equation[5]:

$$\frac{\partial^2 p'}{\partial x_i^2} = \frac{\partial^2 \rho'}{\partial t^2} - \frac{\partial^2}{\partial x_i x_j}\left[\rho'\langle u_i\rangle\langle u_j\rangle + \rho u_i'' u_j'' + \rho u_i''\langle u_j\rangle + \rho\langle u_i\rangle u_j'' - \overline{\rho}\langle u_i'' u_j''\rangle\right] + \frac{4}{3}\frac{\partial^2}{\partial x_i^2}\left[\frac{\mu}{Re}\frac{\partial u_k''}{\partial x_k}\right] \quad . \tag{81}$$

The solution for the fluctuating pressure can be determined by using Green's functions or Fourier transforms. With respect to the incompressible counterpart, the compressible Poisson equation is severely complicated. An equivalent form which resembles more to the incompressible equation can be obtained as:

$$\frac{\partial^2 p'}{\partial x_i^2} = \frac{\partial^2 \rho'}{\partial t^2} - 2\frac{\partial^2}{\partial x_i x_j}\rho'\langle u_i\rangle u_j'' - \frac{\partial^2}{\partial x_i x_j}\left[\rho u_i'' u_j'' - \overline{\rho}\langle u_i'' u_j''\rangle\right] - 2\frac{\partial^2}{\partial x_i x_j}\overline{\rho}\langle u_i\rangle u_j'' + \frac{4}{3}\frac{\partial^2}{\partial x_i^2}\left[\frac{\mu}{Re}\frac{\partial u_k''}{\partial x_k}\right] \tag{82}$$

The last term on the right hand side (RHS) converts, when the fluctuating pressure solution is used to determine the pressure-strain correlation, into a viscous interaction tensor whose trace is equal to the dilatational dissipation. In the absence of walls this term can be omitted in high Reynolds number flows. The acoustic term (the first term on the RHS) is difficult to be taken into account in the present analysis. If it is assumed that the pressure fluctuations are caused by turbulence only then this term is negligible. The condition $\rho'/\overline{p} \ll 1$ allows the neglect of the second term on the RHS. The remaining terms are the return-to-isotropy and the rapid part for which known modeling principles can be applied in the limit of low convective Mach numbers.

Appendix B

It well known that for linear pressure strain forms it is impossible to satisfy realizability conditions – the requirement that the eigenvalues of the Reynolds stress tensor remain positive. Satisfying realizability is a very practical computationally stabilizing requirement. Our experience with computations in complex flows indicates that realizability is very useful. The model is now made (weakly) realizable following methods suggested by Schumann[64] and Lumley[34] and detailed by Shih and Shabbir.[65] Let $F = 1 + 27III/8 + 9II/4$ is a parameter involving the second invariant $II = -\frac{1}{2}a_{ij}a_{ji}$ and third invariant $III = -\frac{1}{3}a_{ij}a_{jk}a_{ki}$ of the Reynolds stress anisotropy tensor. Then the following asymptotic behavior for the pressure strain-model ensures that realizability is satisfied:

$$\mathcal{A}_{ee} - \frac{2}{3}\overline{\rho}\,\overline{\epsilon} = CF^a \quad \text{as } F \to 0$$

$$\frac{\partial \langle u_p \rangle}{\partial x_q} \mathcal{I}_{peqe} \to 0 \quad \text{as } F \to 0 \tag{83}$$

where the index e indicates that the relations are written in the principal axes of $\langle u_i'' u_j'' \rangle$. The computational form of the model with the additional parameters necessary to enforce realizability so necessary for computational stability is

$$\begin{gathered}
\Pi^\star_{ij} - \overline{\rho}\ \epsilon^\star_{ij} = -C_1 \overline{\rho}\ \overline{\epsilon} a_{ij} A_r F^{\alpha_r} + \overline{\rho} \langle k \rangle \left[\left(\frac{4}{5} + \frac{2}{5} d_1 \right) S^\star_{ij}(\langle u \rangle) + \right. \\
[1 - C_3 + 2d_2] \left[a_{ip} S^\star_{pj}(\langle u \rangle) + S^\star_{ip}(\langle u \rangle) a_{pj} - \frac{2}{3} S^\star_{pq}(\langle u \rangle) a_{pq} \delta_{ij} \right] - \\
\left. [1 - C_4 - 2d_2][a_{ip} \Omega_{pj}(\langle u \rangle) - \Omega_{ip}(\langle u \rangle) a_{pj}] + \frac{4}{3} d_2 S_{pp}(\langle u \rangle) a_{ij} \right] B_r F^{\beta_r}
\end{gathered} \tag{84}$$

with $C_3 = (5 - 9C_2)/11$ and $C_4 = (1 + 7C_2)/11$. The value for the constant C_2 will be the same as in the incompressible model to preserve consistency in the zero Mach number limit, that is $C_2 = 0.45$. The parameters are $\alpha_r = 0.1$, $\beta_r = 0.5$, $A_r = \min(F^{-\alpha_r},\ 0.1^{-\alpha_r})$ and $B_r = \min(F^{-\beta_r},\ 0.1^{-\beta_r})$.

Using this modified form of the pressure-strain model the ARSM coefficients become: $b_1 = \frac{4}{3} - B_r F^{\beta_r}(\frac{4}{5} + \frac{2}{5} d_1)$, $b_2 = \frac{1}{\overline{\rho}^2} \frac{2}{3} \tau_u \nu_0$, $b_3 = 1 - B_r F^{\beta_r}(1 - C_3 + 2d_2)$, $b_4 = 1 - B_r F^{\beta_r}(1 - C_4 - 2d_2)$, and

$$\begin{gathered}
g = \left[A_r F^{\alpha_r} C_1 \frac{\overline{\epsilon}}{\overline{\epsilon}_s} + C_{\epsilon_2} - 2 + (2 - C_{\epsilon_1}) \frac{P}{\overline{\rho}\ \overline{\epsilon}_s} + \frac{\tau}{\sigma} \frac{D\sigma}{Dt} + \right. \\
\left. \frac{2\tau}{3}(1 - 2d_2 B_r F^{\beta_r}) S_{pp}(\langle u \rangle) + 2 \frac{\mathcal{M} + \overline{p'd} - \overline{\rho}\ \overline{\epsilon}_c}{\overline{\rho}\ \overline{\epsilon}_s} \right]^{-1} .
\end{gathered} \tag{85}$$

References

[1] S. K. Lele, "Compressibility effects on turbulence," Ann. Rev. Fluid Mech. **26**, 211 (1994).

[2] E. J. Gutmark, K. C. Schadow, and K. H. Yu, "Mixing enhancement in supersonic free shear flows," Ann. Rev. Fluid Mech. **27**, 375 (1995).

[3] E. F. Spina, A. J. Smits, and S. K. Robinson, "The physics of supersonic boundary layers," Ann. Rev. Fluid Mech. **26**, 287 (1994).

[4] O. Zeman, "Dilatation dissipation: the concept and application in modelling compressible mixing layers," Phys. Fluids A **2**, 178 (1990).

[5] D. B. Taulbee and J. VanOsdol, "Modeling turbulent compressible flows: the mass fluctuating velocity and squared density," American Institute of Aeronautics and Astronautics, AIAA Paper 91-0524 (1991).

[6] S. Sarkar, G. Erlebacher, M. Y. Hussain, and H. O. Kreiss, "The analysis and modelling of dilatational terms in compressible turbulence," J. Fluid Mech. **227**, 473 (1991).

[7] P. A. Durbin and O. Zeman, "Rapid distorsion theory for homogeneous compressed turbulence with application to modeling," J. Fluid Mech. **242**, 349 (1992).

[8] J. R. Ristorcelli, "A pseudo-sound constitutive relationship for the dilatational covariances in compressible turbulence: An analytical theory," J. Fluid Mech. **347**, 37 (1997).

[9] A. Simone, G. N. Coleman, and C. Cambon, "The effect of compressibility on turbulent shear flow - a rapid-distortion-theory and direct-numerical-simulation study," J. Fluid Mech. **330**, 307 (1997).

[10] J. R. Viegas and M. W. Rubesin, "A comparative study of several compressibity corrections to turbulence models applied to high-speed shear layers," American Institute of Aeronautics and Astronautics, AIAA Paper 91-1783 (1991).

[11] S. Sarkar and B. Lakshmanan, "Application of a Reynolds stress turbulence model to the compressible shear layer," AIAA J. **29**, 743 (1991).

[12] C. G. Speziale and S. Sarkar, "Second order closure models for supersonic turbulent flows," NASA Langley Research Center, Hampton, VA, ICASE Report 91–9 (1991).

[13] R. Abid, "On the prediction of equilibrium states in homogeneous compressible turbulence," NASA Langley Research Center, Hampton, VA, NASA CR 4570 (1994).

[14] A. W. Vreman, N. D. Sandham, and K. H. Luo, "Compressible mixing layer growth rate and turbulence characteristics," J. Fluid Mech. **320**, 235 (1996).

[15] J. B. Freund, P. P. Moin, and S. K. Lele, "Compressibility effects in a turbulent annular mixing layer," Stanford University, Stanford, CA, Department of Mechanical Engineering Report TF-72 (1997).

[16] S. Sarkar, "The stabilizing effect of compressibility in turbulent shear flow," J. Fluid Mech. **282**, 163 (1995).

[17] G. A. Blaisdell and S. S. Sarkar, in *Transitional and turbulent compressible flows*, ASME, Number 151 (1993).

[18] C. G. Speziale, R. Abid, and N. M. Mansour, "Evaluation of reynolds stress turbulence closures in compressible homogeneous shear flows," Z. Angew. Math. Phys. **S717** (1995).

[19] A. M. El Baz and B. E. Launder, in *Engineering Turbulence Modelling and Experiments*, edited by W. Rodi and F. Martelli, Elsevier Publishing Co., North Holland, volume 2, pp. 63–72 (1993).

[20] S. B. Pope, "A more general effective-viscosity hypothesis," J. Fluid Mech. **72**, 331 (1975).

[21] D. B. Taulbee, "An improved algebraic Reynolds stress model and corresponding nonlinear stress model," Phys. Fluids A **4**, 2555 (1992).

[22] W. Rodi, "A new algebraic relation for calculating the Reynolds stresses," ZAMM **56**, 219 (1976).

[23] B. E. Launder, "On the effects of a gravitational field on the turbulent transport of heat and momentum," J. Fluid Mech. **67**, 569 (1975).

[24] W. Rodi, in *Prediction Methods for Turbulent Flows*, edited by W. Kollmann, Hemisphere Publishing Co., New York, NY, pp. 260–349 (1980).

[25] C. G. Speziale, "Analytical methods for the development of Reynolds-stress closures in turbulence," Ann. Rev. Fluid Mech. **23**, 107 (1991).

[26] T. B. Gatski and C. G. Speziale, "On explicit algebraic stress models for complex turbulent flows," J. Fluid Mech. **254**, 59 (1993).

[27] D. B. Taulbee, J. R. Sonnenmeier, and K. M. Wall, "Stress relation for three-dimensional turbulent flows," Phys. Fluids A **6**, 1399 (1994).

[28] S. S. Girimaji, "Fully explicit and self consistent algebraic reynolds stress model," Theoret. Comput. Fluid Dynamics **8**, 387 (1996).

[29] A. Favre, in *Problems of Hydrodynamics and Continuum Mechanics*, SIAM, Philadelphia, pp. 37–44 (1969).

[30] B. E. Launder, G. J. Reece, and W. Rodi, "Progress in the development of a Reynolds-stress turbulence closure," J. Fluid Mech. **68**, 537 (1975).

[31] C. G. Speziale, S. Sarkar, and T. B. Gatski, "Modeling the pressure-strain correlation of turbulence - an invariant dynamical systems approach," J. Fluid Mech. **227**, 245 (1990).

[32] J. R. Ristorcelli, J. L. Lumley, and R. Abid, "A rapid-pressure covariance representation consistent with the taylor-proudman theorem materially-frame-indifferent in the 2D limit," J. Fluid Mech. **292**, 111 (1995).

[33] J. L. Lumley, "Towards a turbulence constitutive relationship," J. Fluid Mech. **41**, 413 (1970).

[34] J. L. Lumley, "Computational modeling of turbulent flows," Adv. Appl. Mech. **18**, 123 (1978).

[35] J. R. Ristorcelli, "Toward a turbulence constitutive relation for geophysical flows," Theoret. Comput. Fluid Dynamics **9**, 207 (1997).

[36]J. R. Ristorcelli, "Some results relevant to the statistical closures for compressible turbulence," NASA Langley Research Center, Hampton, VA, ICASE Report 98–1 (1998).

[37]V. Adumitroaie, "Quasi-explicit algebraic turbulence closures for compressible reacting flows," Ph.D. Thesis, State University of New York at Buffalo, Department of Mechanical and Aerospace Engineering, Buffalo, NY (1997).

[38]S. Sarkar, "The pressure-dilatation correlation in compressible flows," Phys. Fluids A **4**, 2674 (1992).

[39]J. R. Ristorcelli and G. A. Blaisdell, "Validation of a pseudo-sound theory for the pressure-dilatation in the DNS of compressible turbulence," NASA Langley Research Center, Hampton, VA, ICASE Report 97–53 (1997).

[40]J. R. Ristorcelli, "A representation for the turbulent mass flux contribution to Reynolds-stress and two-equation closure for compressible turbulence," NASA Langley Research Center, Hampton, VA, ICASE Report 93–88 (1993).

[41]G. A. Blaisdell, N. N. Mansour, and W. C. Reynolds, "Compressibility effects on the growth and structure of homogeneous turbulent shear flow," J. Fluid Mech. **256**, 443 (1993).

[42]G. N. Coleman, P. Bradshaw, and P. G. Huang, "Compressible turbulent channel flows DNS results and modelling," J. Fluid Mech. **305**, 185 (1995).

[43]A. J. M. Spencer, *Theory of Invariants*, volume 1 of *Continuum Physics*, pp. 240–352, Academic Press (1971).

[44]G. S. Settles and L. J. Dodson, "Hypersonic turbulent boundary-layer and free shear database," NASA Ames Research Center, Moffet Field, CA, NASA Contractor Report 177610 (1993).

[45]P. J. Colucci, "Large eddy simulation of turbulent reacting flows: Stochastic representation of the subgrid scale scalar fluctuations," Ph.D. Thesis, State University of New York at Buffalo, Department of Mechanical and Aerospace Engineering, Buffalo, NY (1997).

[46]D. Gottlieb and E. Turkel, "Dissipative two-four methods for time dependent problems," Math. Comp. **30**, 703 (1976).

[47]R. W. MacCormack, "The effect of viscosity in hypervelocity impact catering," American Institute of Aeronautics and Astronautics, AIAA Paper 69-354 (1969).

[48]R. W. MacCormack and B. S. Baldwin, "A numerical method for solving the Navier-Stokes equations with application to shock-boundary layer interaction," American Institute of Aeronautics and Astronautics, AIAA Paper 75-1 (1975).

[49]J. P. Drummond, "Two-dimensional numerical simulation of a supersonic, chemically reacting mixing layer," NASA Langley Research Center, Hampton, VA, NASA TM 4055 (1988).

[50]D. Papamoschou and A. Roshko, "The compressible turbulent shear layer: An experimental study," J. Fluid Mech. **197**, 453 (1988).

[51]S. Thangam, Y. Zhou, and J. R. Ristorcelli, "Analysis of compressible mixing layers using dilatational covariances model," NASA Langley Research Center, NASA TM 111865 (1996).

[52]S. Thangam, Y. Zhou, and J. R. Ristorcelli, "Development and application of a dilatational covariances model for compressible jets and shear layers," American Institute of Aeronautics and Astronautics, AIAA Paper 97-3544 (1997).

[53]G. S. Elliott and M. Samimy, "Compressibility effects in free shear layers," Phys. Fluids A. **7**, 1231 (1990).

[54]S. G. Goebel and J. C. Dutton, "Experimental study of compressible turbulent mixing layers," AIAA J. **29**, 538 (1991).

[55]K. R. Sreenivasan, in *Developments in Fluid Mechanics and Aerospace Sciences*, edited by S. M. Deshpande, A. Prabhu, K. R. Sreenivasan, and P. R. Viswanath, Interline Publishers, pp. 159–193 (1995).

[56]D. C. Fourguette, M. G. Mungal, R. S. Barlow, and R. W. Dibble, "Concentration measurements in a supersonic shear layer," American Institute of Aeronautics and Astronautics, AIAA Paper 91-0627 (1991).

[57]N. T. Clemens and M. G. Mungal, "Two- and three-dimensional effects in the supersonic mixing layer," AIAA J. **30**, 973 (1992).

[58]D. W. Bogdanoff, "Compressibility effects in turbulent shear layers," AIAA J. **21**, 926 (1983).

[59]M. R. Gruber, N. L. Messersmith, and J. C. Dutton, "Three-dimensional velocity measurements in a turbulent, compressible mixing layer," American Institute of Aeronautics and Astronautics, AIAA Paper 92-3544 (1992).

[60]G. S. Elliott and M. Samimy, "Compressibility effects in free shear layers," American Institute of Aeronautics and Astronautics, AIAA Paper 90-0705 (1990).

[61]J. W. Naughton, L. N. Cattafesta, and G. S. Settles, "Experiments on the enhancement of compressible mixing via streamwise turbulence, Part II - Vortex strength assessment and seed particle dynamics," American Institute of Aeronautics and Astronautics, AIAA Paper 93-0742 (1993).

[62]S. J. Kline, B. J. Cantwell, and G. M. Lilley, in *1980-1981 AFOSR-HTTM-Stanford Conference*, edited by S. J. Kline, B. J. Cantwell, and G. M. Lilley, Stanford University Press, Stanford, CA, pp. 368–380 (1982).

[63]M. M. Rogers, P. Moin, and W. C. Reynolds, "The structure and modeling of the hydrodynamic and passive scalar fields in homogeneous turbulent shear flow," Stanford University, Stanford, CA, Department of Mechanical Engineering TF-25 (1986).

[64]U. Schumann, "Realizability of Reynolds stress turbulence models," Phys. Fluids **20**, 721 (1977).

[65]T.-H. Shih and A. Shabbir, "Methods of ensuring realizability for non-realizable second order closures," NASA Lewis Research Center, Cleveland, OH, ICOMP 94-14 (1994).

Figures

FIG. 1. Comparisons between ARSM and SOM calculations for the mixing layer, $M_c = 1.07$; (a) streamwise normal Reynolds stress; (b) Reynolds shear stress. [$\alpha = 1.2$]

FIG. 2. Comparisons between ARSM and SOM calculations for the mixing layer, $M_c = 1.07$; (a) crosstream normal Reynolds stress; (b) turbulent kinetic energy production over dissipation. [$\alpha = 1.2$]

FIG. 3. Influence of the compressibility correction in SOM calculations for the mixing layer, $M_c = 1.07$; (a) the vorticity thickness; (b) components of the pressure-strain tensor. [$\alpha = 1.2$]

FIG. 4. Variation with convective Mach number in the mixing layer; (a) centerline Reynolds stress anisotropies; (b) centerline Reynolds stresses. [$\alpha = 1.2$]

FIG. 5. Variation with convective Mach number in the mixing layer; (a) maximum turbulent Mach number; (b) maximum gradient Mach number.

FIG. 6. Variation with convective Mach number for the mixing layer; the pressure-strain tensor. [$\alpha = 1.2$]

FIG. 7. Effect of compressibility on normalized thickness growth rate, $k-\epsilon$ calculations of a mixing layer.[$\alpha = 2$]

FIG. 8. Effect of compressibility on normalized thickness growth rate, ARSM calculations of a mixing layer.

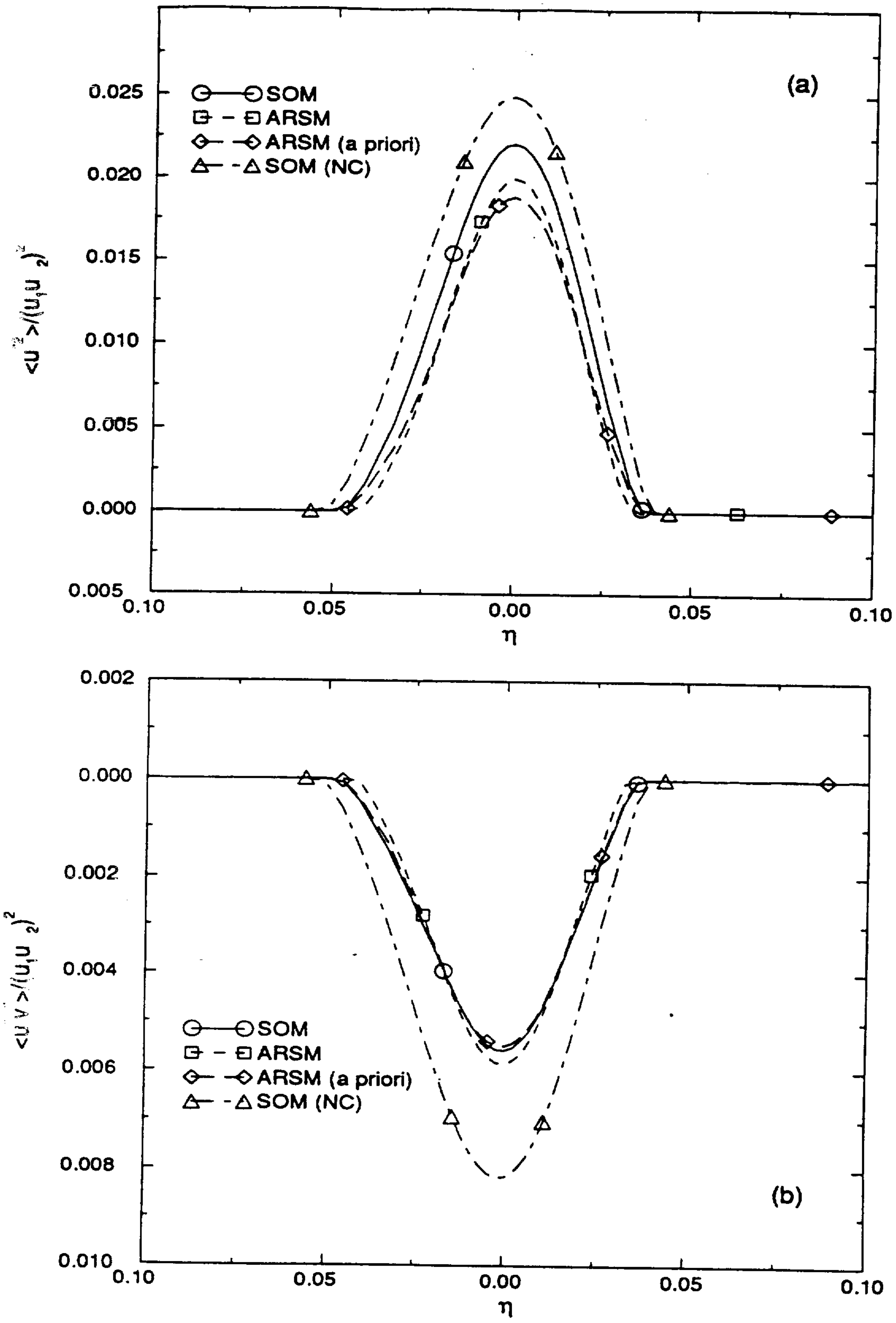
(a)
SOM
ARSM
ARSM (a priori)
SOM (NC)
0.025
0.020
0.015
0.010
0.005
0.000
0.005
<u'2>/(u1u2)2
0.10
0.05
0.00
0.05
0.10
η
0.002
0.000
0.002
0.004
0.006
0.008
0.010
<u'v'>/(u1u2)2
SOM
ARSM
ARSM (a priori)
SOM (NC)
(b)
0.10
0.05
0.00
0.05
0.10
η

FIG. 1.

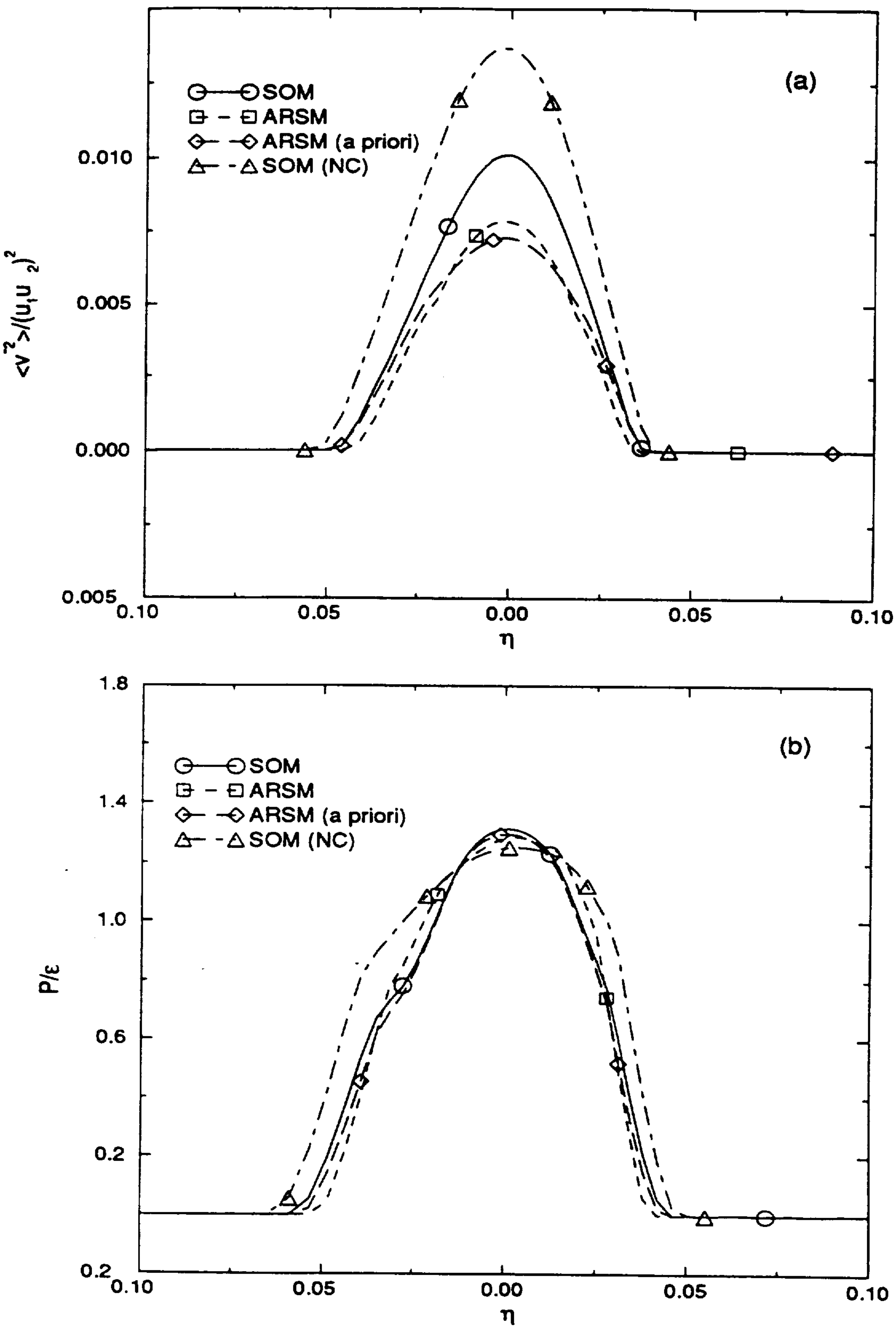
(a)
SOM
ARSM
ARSM (a priori)
SOM (NC)
$<v^2>/(u_t u_2)^2$
0.010
0.005
0.000
0.005
0.10
0.05
0.00
0.05
0.10
η
(b)
SOM
ARSM
ARSM (a priori)
SOM (NC)
P/ε
1.8
1.4
1.0
0.6
0.2
0.2
0.10
0.05
0.00
0.05
0.10
η

FIG. 2.

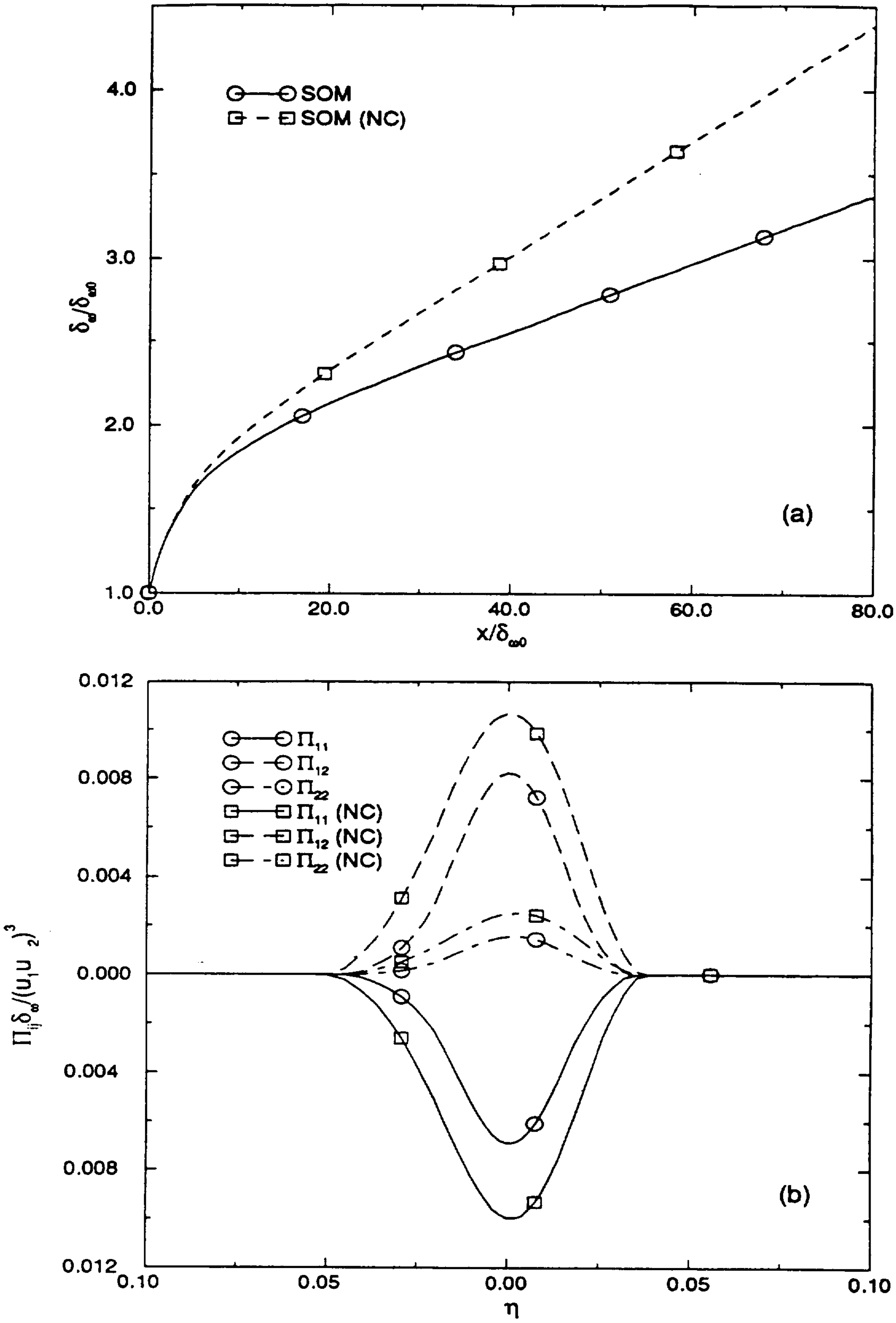
SOM
SOM (NC)
4.0
3.0
2.0
1.0
$\delta_\omega/\delta_{\omega 0}$
0.0
20.0
40.0
60.0
80.0
$x/\delta_{\omega 0}$
(a)
Π_{11}
Π_{12}
Π_{22}
Π_{11} (NC)
Π_{12} (NC)
Π_{22} (NC)
0.012
0.008
0.004
0.000
0.004
0.008
0.012
$\Pi_{ij}\delta_\omega/(u_1 u_2)^3$
0.10
0.05
0.00
0.05
0.10
η
(b)

FIG. 3.

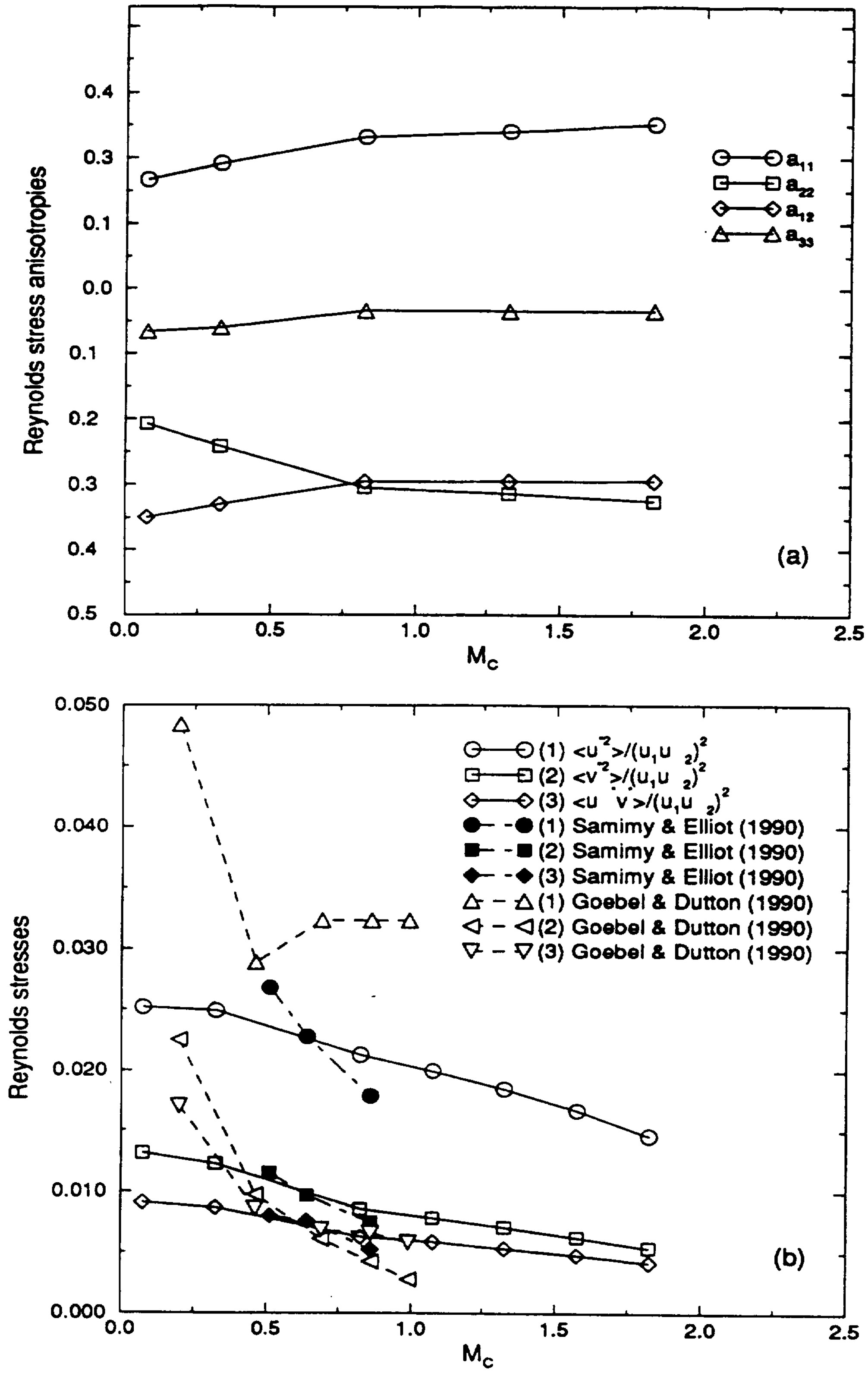

Reynolds stress anisotropies
0.4
0.3
0.1
0.0
0.1
0.2
0.3
0.4
0.5
0.0
0.5
1.0
1.5
2.0
2.5
M_c
a_11
a_22
a_12
a_33
(a)
Reynolds stresses
0.050
0.040
0.030
0.020
0.010
0.000
0.0
0.5
1.0
1.5
2.0
2.5
M_c
(1) <u'²>/(u₁−u₂)²
(2) <v'²>/(u₁−u₂)²
(3) <u'v'>/(u₁−u₂)²
(1) Samimy & Elliot (1990)
(2) Samimy & Elliot (1990)
(3) Samimy & Elliot (1990)
(1) Goebel & Dutton (1990)
(2) Goebel & Dutton (1990)
(3) Goebel & Dutton (1990)
(b)

FIG. 4.

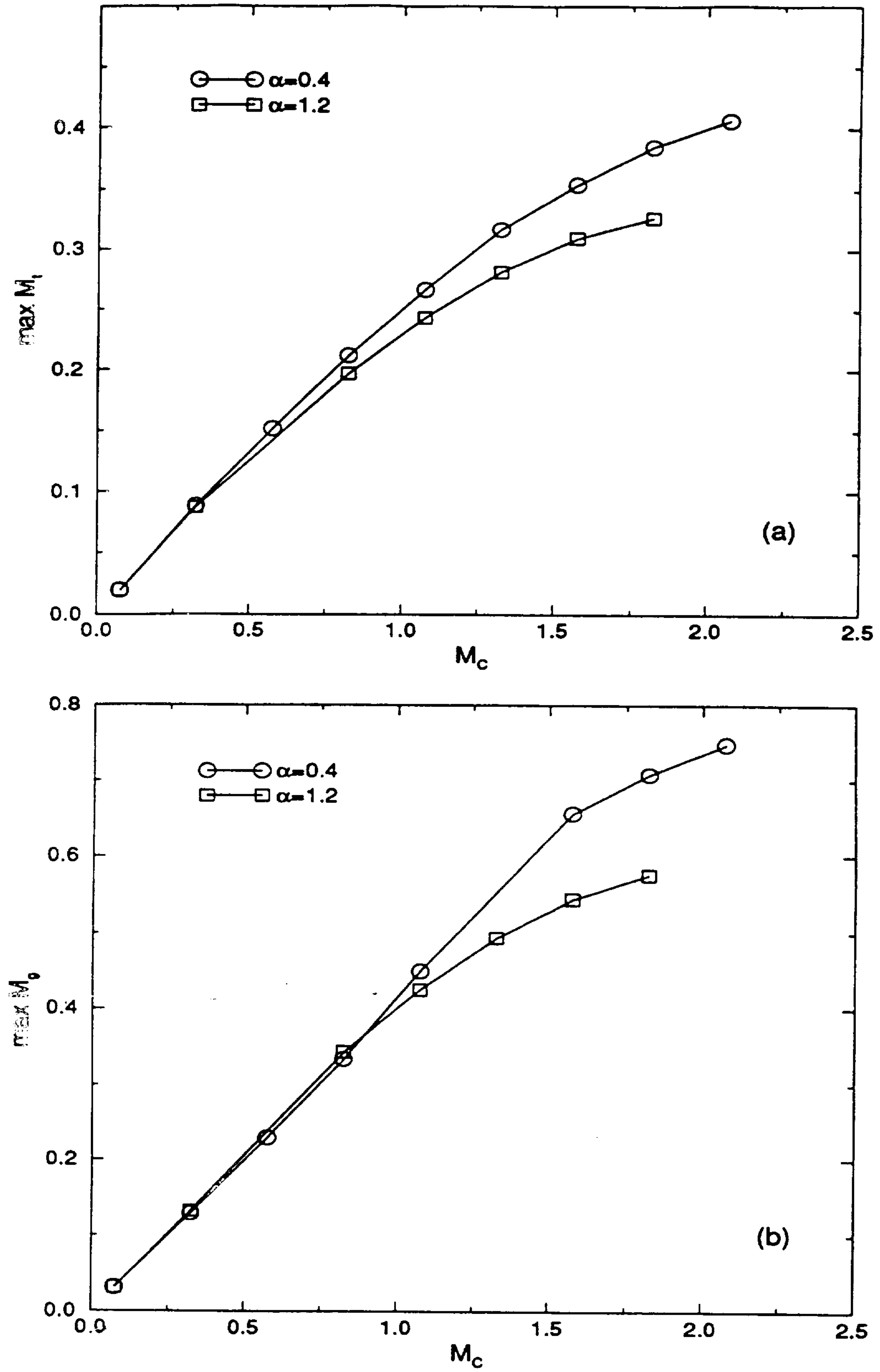
α=0.4
α=1.2
max M_t
0.0
0.1
0.2
0.3
0.4
(a)
0.0
0.5
1.0
1.5
2.0
2.5
M_c
α=0.4
α=1.2
max M_e
0.0
0.2
0.4
0.6
0.8
(b)
0.0
0.5
1.0
1.5
2.0
2.5
M_c

FIG. 5.

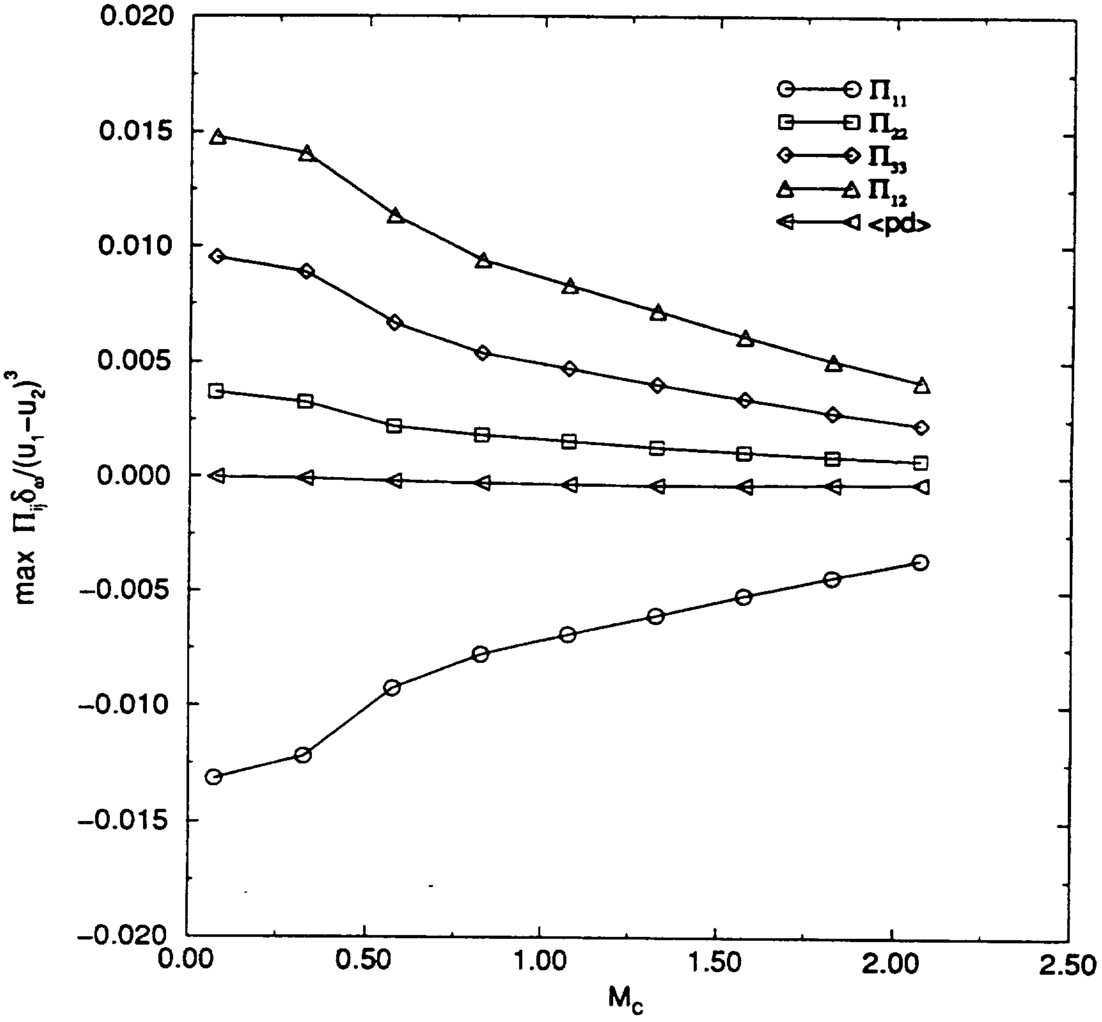0.020
0.015
0.010
0.005
0.000
−0.005
−0.010
−0.015
−0.020
0.00
0.50
1.00
1.50
2.00
2.50
M_c
max $\Pi_{ij}\delta_\omega/(u_1-u_2)^3$
Π_{11}
Π_{22}
Π_{33}
Π_{12}
<pd>

FIG. 6.

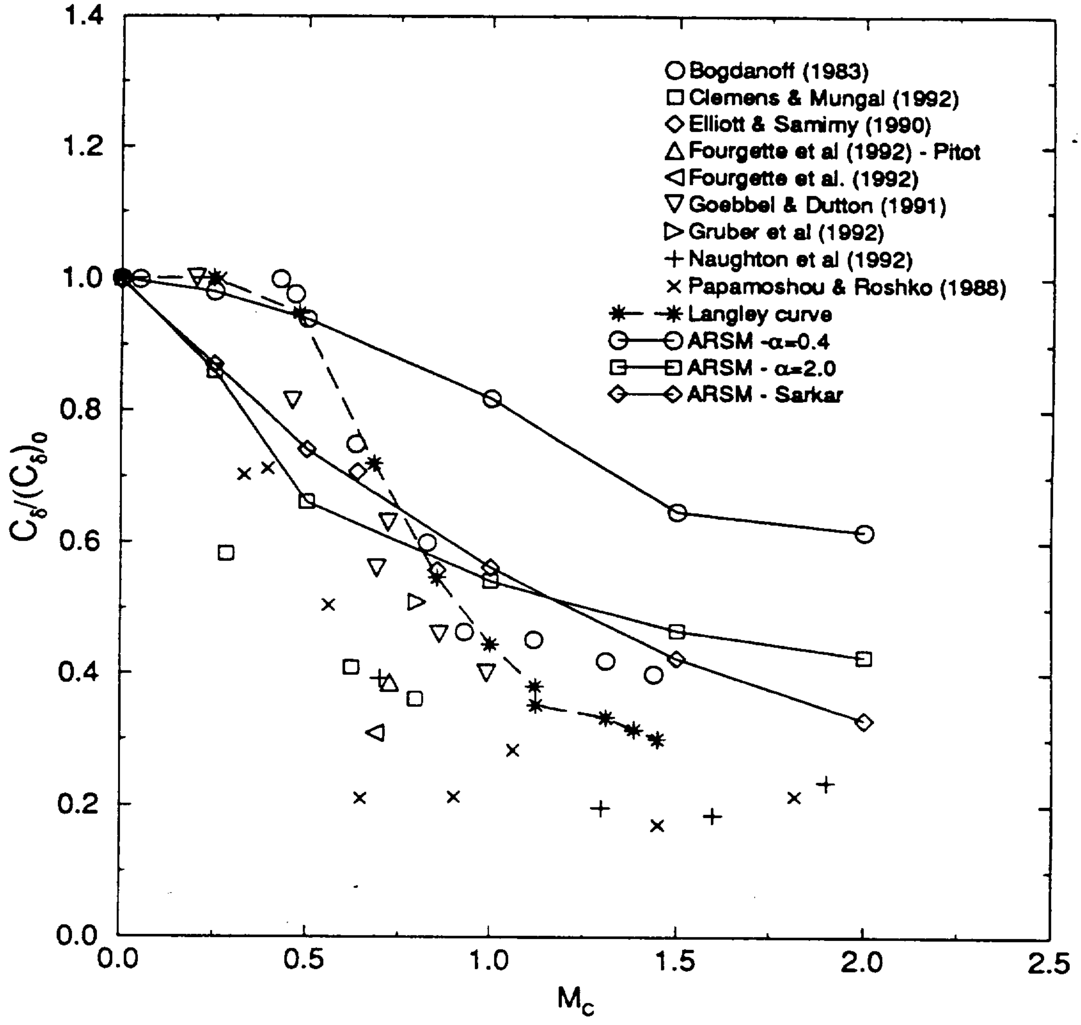

1.4
1.2
1.0
0.8
0.6
0.4
0.2
0.0
0.0
0.5
1.0
1.5
2.0
2.5
$C_\delta/(C_\delta)_o$
M_c
○ Bogdanoff (1983)
□ Clemens & Mungal (1992)
◇ Elliott & Samimy (1990)
△ Fourgette et al (1992) - Pitot
◁ Fourgette et al. (1992)
▽ Goebbel & Dutton (1991)
▷ Gruber et al (1992)
+ Naughton et al (1992)
× Papamoshou & Roshko (1988)
Langley curve
ARSM -α=0.4
ARSM - α=2.0
ARSM - Sarkar

FIG. 7.

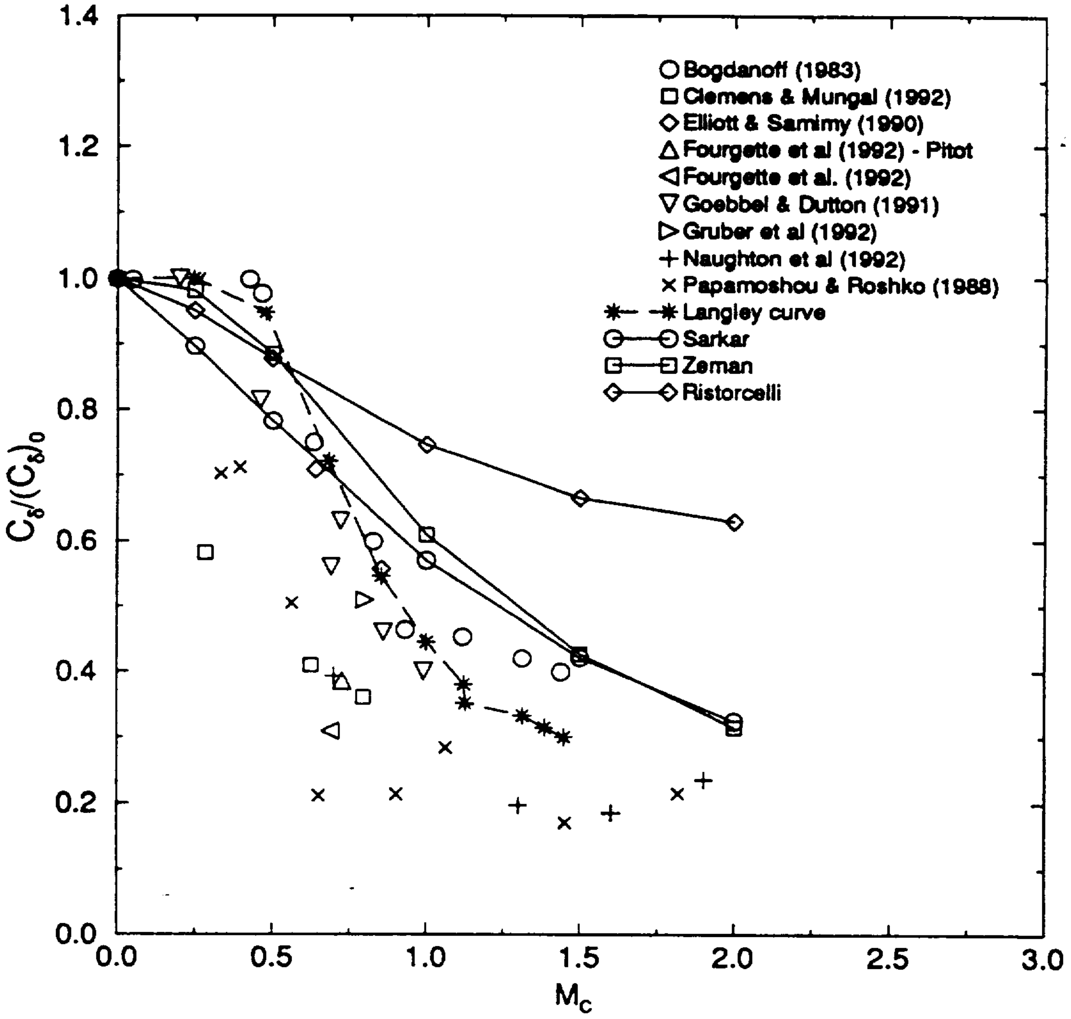

1.4
1.2
1.0
0.8
0.6
0.4
0.2
0.0
$C_\delta/(C_\delta)_0$
0.0
0.5
1.0
1.5
2.0
2.5
3.0
M_c
○ Bogdanoff (1983)
□ Clemens & Mungal (1992)
◇ Elliott & Samimy (1990)
△ Fourgette et al (1992) - Pitot
◁ Fourgette et al. (1992)
▽ Goebbel & Dutton (1991)
▷ Gruber et al (1992)
+ Naughton et al (1992)
× Papamoshou & Roshko (1988)
Langley curve
Sarkar
Zeman
Ristorcelli

FIG. 8.